

First-Principles Investigation of Initial Stages of Surfactant Mediated Growth on the Si(111) Substrate

Von der Fakultät für Mathematik, Informatik und Naturwissenschaften
der Rheinisch-Westfälischen Technischen Hochschule Aachen zur
Erlangung des akademischen Grades eines Doktors der Naturwissenschaften
genehmigte Dissertation

vorgelegt von
Diplom-Physiker
Armin Antons
aus Jülich

Berichter: Professor Dr. K.W. Schroeder
Universitätsprofessor Dr. P.H. Dederichs

Tag der mündlichen Prüfung: 26. November 2001

Abstract

First-Principles Investigation of Initial Stages of Surfactant Mediated Growth on the Si(111) Substrate

The atomic and electronic structure of single adatoms, adatom-clusters and steps on clean or surfactant covered Si(111) surfaces are studied with ab-initio methods. All calculations are performed using the self-developed program package EStCoMPP which is based on density functional theory combined with pseudopotentials.

The paths and energy barriers for diffusion of single Si ad-atoms are studied on the clean (3×3) -reconstructed Si(111), which shows most of the features of the (7×7) -reconstruction. At the most stable position the extra ad-atom sits at a bridge position between the ad-atom and one atom of the second layer. The barrier for diffusion from the faulted to the unfaulted unit half or vice versa is 0.44 eV. The saddle-point is located on the boundary between the unit-halves, close to the dimer. Also the structure of small Si-clusters on this surface is investigated, showing a preferred cluster formation in either one of the unit halves.

The structure and development of small Si-clusters is calculated on surfactant covered Si(111). The investigated cluster sizes range from single ad-atoms to 4 atoms. The results explain the experimentally determined features of the initial stages of homoepitaxial growth. We find that doublelayer growth starts at a cluster size of 4 on As covered Si(111) while no doublelayer growth occurs when Sb is used as surfactant.

The atomic structures of the two closed-packed step-edges on As terminated Si(111) are calculated. The results show that the exposed Si atoms at the step-edges are replaced by As. Thus, the step-edges are fully terminated by surfactant-atoms like the surface. While at the $(11\bar{2})$ step-edge the As atoms are in a naturally threefold coordinated position, the As atoms form dimers at the $(\bar{1}\bar{1}2)$ step-edge. STM-images are simulated to compare the calculated structures with experiments. We can explain the measured step-characteristics with the calculated electronic local density of states. The key-features of the simulated images are in agreement with the experimental findings. The apparent outward relaxation of the upper terrace As atoms at the step-edge can be explained by the higher electronic density of states in the p-channel of these atoms.

The stability of different surface reconstructions of Sb-covered strained Ge(111) is investigated as a function of the lateral lattice constant. We find for high compressive strain the $(\sqrt{3} \times \sqrt{3})$ reconstruction to be stable. Over a large region of lattice constants ($a_{Si}-a_{Ge}$) we find the (2×1) reconstruction to be preferred, and for dilated surfaces the (1×1) reconstruction is favored. This explains the experimentally determined structures of Sb-covered Ge-films grown on Si(111):Sb, and even the peculiar surface structure with (1×1) surface in a $(6\sqrt{3} \times 6\sqrt{3})$ superstructure of overrelaxed islands, which is found for 3 Ge layers.

Contents

1	The Density Functional Theory	11
1.1	The Density as Basic Variable	12
1.2	The Kohn-Sham Equations	15
1.3	Local Density Approximation	17
1.4	Spin-Density Functional Theory	18
2	Pseudopotentials	19
2.1	Pseudopotential Method	19
2.2	Semi-local Pseudopotentials	21
2.3	Separable-Pseudopotentials	22
3	Periodic Supercells	25
3.1	Bloch's Theorem	27
3.2	k -point sampling	29
3.3	Plane-wave basis sets	29
4	The EStCoMPP-Program	31
4.1	Hellmann-Feynman Forces	31
4.2	Minimization of the Energy Functional	33
4.3	Explicit Form of the Equations	34
4.3.1	The kinetic Energy	35
4.3.2	The local Energy	35
4.3.3	The non-local part of the Energy	37
4.3.4	The Ewald-energy	38
4.4	Loop-Structures and Algorithms	39
4.4.1	Iterative Eigenvalue Determination	39
4.4.2	Electronic-Selfconsistency and Molecular- Relaxation Loops	42
5	The EStCoMPP-Visualization Tool	47
5.1	Startup Information Files	55
5.2	Data-File Preparation	55
5.3	Algorithms and Data-Structures	57

5.4	Generating High Quality Output	60
6	Atomistic Processes at Surfaces	63
6.1	Adsorption and Desorption	63
6.2	Diffusion Reactions	65
6.3	Growth Kinetics	66
6.3.1	Kinetic Equations	66
6.3.2	Growth of Stable Islands	67
7	Si Ad-Atoms on Si(111)(7 × 7)	71
7.1	Si(111)(7 × 7)	72
7.2	Si(111)(3 × 3)	74
7.3	Single Ad-Atom Kinetics on Si(111) (3 × 3)	76
7.4	Small Clusters on Si(111) (3 × 3)	81
8	Surfactant modified Growth	87
8.1	Introduction	87
8.2	Surfactant Mechanisms	88
8.2.1	Surfactant enhanced Island Density	89
8.2.2	Surfactant modified Step-Edge Barrier	90
9	Homoepitaxial Growth on Si(111):As/Sb	93
9.1	Surface Structures	93
9.2	Experimental Results	94
9.3	Single Adatom Kinetics	98
9.3.1	Si Ad-Atoms on Si(111):As	99
9.3.2	Si Ad-Atoms on Si(111):Sb	102
9.3.3	Preliminary Conclusions for the growth mechanisms	103
9.4	Island Evolution	105
10	Steps on Si(111):As	119
10.1	Tersoff-Hamann-Approximation	119
10.2	Step Structures and Experimental Results	122
10.3	Calculated STM-images	124
11	Growth of Ge films on Si(111):Sb	135
11.1	Experimental Results	135
11.2	Surface Reconstructions and Stress (Ge(111):Sb)	138
12	Summary	145

A	Tables of Positions and Angles	149
A.1	Clusters on Si(111)(3×3)	150
A.1.1	Si(111)(3×3) without extra ad-atoms	150
A.1.2	One additional Si ad-atom (a)	154
A.1.3	One additional Si ad-atom (b)	158
A.1.4	Two additional Si ad-atoms (c)	162
A.1.5	Two additional Si ad-atoms (d)	166
A.1.6	Three additional Si ad-atoms (f)	170
A.1.7	Four additional Si ad-atoms (g)	174
A.1.8	Five additional Si ad-atoms (h)	178
A.2	Clusters on Si(111):As	182
A.2.1	One exchanged Si atom	182
A.2.2	Two exchanged Si atoms (As-dimer)	186
A.2.3	Three exchanged Si atoms (As-trimer)	190
A.2.4	Four exchanged Si atoms (As/Si-trimer)	194

Introduction

The gradual change from microelectronics to nanoelectronics which is currently underway is a driving force for investigating novel and fundamentally exciting physical, chemical, and biological effects that occur on the nanometer scale. As device miniaturization reaches sub-micrometer and nanometer length scales atomic-level control of the fabrication processes for both novel quantum structures and new materials combinations is becoming crucial [Ler98]. This has motivated efforts to manipulate, control and understand the growth of small structures (e.g. nanowires, quantum-dots or hut-clusters), thin films (e.g. strained Ge/Si heterostructures), and organic/inorganic interfaces on the nanometer scale.

In combination with advanced experimental methods (scanning tunneling microscopy (STM) [BRGW82], scanning tunneling spectroscopy (STS) [Fee94], scanning force microscopy (SFM) [MA88], and atomic resolution electron microscopy) the theoretical modeling of atomic structures has proven to be very successful for the design of new materials or the improvement of materials properties. For structures with length scales larger than 10 nanometers one has to employ empirical or semi-empirical methods using effective parameters whose materials specific values are not known *a priori* and thus are often fitted to experiments. Although such simulations can be of great use, they might miss some essential correlations between the atomic structure of surfaces, interfaces or defects and their electronic functionality, and are of only limited predictive power for new systems.

The realistic modeling of growth phenomena requires the understanding of the underlying atomistic processes which control e.g. the diffusion across terraces, steps or kinks. Surface reconstructions, defects, impurities, vacancies, and possible reactions of deposited atoms have to be identified and taken into consideration. Even today quantitative values for energy barriers or prefactors for diffusion are hardly known. A direct dynamical simulation based on a microscopic quantum mechanical description of the interacting atomic and electronic systems is out of question since the atomic dynamical processes operate on length and time scales of 0.1-10Å and 0.1-1 psec, while the electron dynamics operates on the fsec time scale.

We can contribute to an understanding of the atomic processes by carrying out *ab initio* calculations of the electronic structure, the total energy, and the forces exerted on atoms in order to find equilibrium configurations and energy barriers for different configurations and processes. We basically proceed in two steps: (i) First, we analyze possible atomic structures (ad-atoms, atom clusters, steps on surfaces) and evaluate their relevance by comparing the total energies. (ii) This is succeeded by the calculation of energy barriers, currently only of the simplest processes. The combination of (i) and (ii) defines problems at the cutting edge of super-computing in surface science. Up to now only very few such calculations have been performed.

Usually there is a huge number of relevant atomistic processes: deposition, diffusion on a terrace, diffusion across a step edge, diffusion along a step edge, diffusion around an island, diffusion of dimers, nucleation of islands, exchange of atoms [VSH84]. To model these processes often unit cells containing several hundred atoms are required. The calculation of activation barriers requires the sampling of high-dimensional reaction paths in order to find the trajectories with the minimum energy saddle points. The trend goes to *ab initio* calculations for larger and more inhomogeneous systems which requires a large amount of molecular statics and dynamics calculations using large unit cells. Due to the existence of powerful massively-parallel computers, such as the Cray T3E, this qualitatively new type of calculations comes in reach, opening up new vistas for materials and materials-process simulation.

The basis of *ab initio* calculations is the density functional theory (DFT) [JG89] which states that the ground-state properties of a many-electron system is exclusively determined by the electron density. Kohn and Sham showed that the quantum mechanical many-particle problem can be mapped onto a system of non-interacting electrons moving in an effective potential [KS65]. Using the local density approximation to the exchange-correlation functional [VWN80], the pseudopotential method [BHS82], and iterative numerical methods for solving the single particle equations [Dav75], the *ab initio* methods can be applied to large complex systems like surfaces, clusters or step-edges.

For this purpose we have developed in our group the program package **ESStCoMPP**, an "Electronic Structure Code for Materials Properties and Processes", which is used throughout the thesis [Ber00]. It is a parallelized *ab initio* molecular dynamics program in the spirit of Car and Parrinello based on a plane-wave basis-set [CP85]. It is optimally suited for calculating forces exerted on the atoms and to determine the equilibrium structures of complex systems on semiconductor surfaces. In the chapters 2 - 4 of this thesis we give a short overview of the density functional theory and of the algorithms employed in **ESStCoMPP**.

Further, the **ESStCoMPP** Visualization Tool (**ESStCoMPP-VT**) was developed to extract the informations from the results achieved by the **ESStCoMPP**-program. It allows the visualization of the positions of atoms in the supercell, and the elec-

tron density either as two-dimensional contour-line plots or as three-dimensional surfaces of constant value. Most of the pictures in this thesis, including the theoretical STM-images, were generated by the **ES**t**Co**MPP-VT. A short description of the organization and use of **ES**t**Co**MPP-VT is given in chapter 5.

In this thesis we investigate in detail the initial stages of the surfactant mediated growth process. The “surfactant effect” is a frequently applied experimental method to modify the growth mode for hetero-epitaxial growth of material A on B with lattice mismatch between A and B. E.g. Ge on Si grows in the layer-by-layer mode on As- or Sb-covered Si(111) whereas three-dimensional islands develop on the clean surface (Stranski-Krastanov-mode) [VZ93]. Apart from the reduction of the surface free energy by saturating Si dangling bonds and forming bond saturated surface structures, the surfactant layer has a decisive influence on the ad-atom kinetics during growth. The key issue is the competition between diffusion of ad-atoms on top of the surfactant layer and incorporation into the layer by exchange with a surfactant atom.

High quality growth of epitaxial Si-Ge films has attracted much attention recently. The driving force mainly comes from the potential application of SiGe alloy and Si-Ge strained layer structures in new generation of semiconductor devices such as high-speed transistors and optoelectronic devices. A MOSFET structure with p-type Ge as the active layer has successfully been grown on a Si(111) substrate using an Sb surfactant layer [RKH⁺99].

After giving a description of elemental atomistic processes on surfaces in chapter 6 we describe our investigation of the homoepitaxy of Si on Si(111) without surfactant. Especially, understanding growth on the Si(111)(7 × 7) surface, which involves complicated restructuring processes at the surface, e.g. the conversion of stacking faults to bulk structures remains a challenge. Modern scanning tunneling microscopy (STM) techniques are able to image diffusing atoms at stable or metastable positions, thus revealing a wealth of information on the microscopic atomic motion. As a contribution towards the understanding of growth on Si(111)(7 × 7) the diffusion of single Si ad-atoms on a Si(111)(3 × 3), and the stable configurations for clusters containing up to five deposited Si atoms were investigated. The details of the calculations are presented in Chapter 7.

Although the surfactant mediated Si and Ge epitaxial growth process is under active investigation, the growth mechanism is not well understood yet. A compilation of the currently discussed models and possible mechanisms for the “surfactant effect” can be found in chapter 8 [ZL94, MVV⁺95a, Mar94, Mar96]. To extend our knowledge beyond the behavior of single ad-atoms, the growth of small clusters Si_n of deposited Si atoms ($n \leq 4$) on As terminated (Si(111):As) as well as on Sb terminated (Si(111):Sb) surfaces were studied. A detailed description of the cluster evolution on surfactant-covered surfaces is given in Chapter 9.

The attachment at steps is an important reaction if the diffusion length of ad-atoms on the surface is larger than the terrace width. Our calculations for single Ge ad-atoms on Si(111):As show that Ge diffuses far across the surface and can reach existing steps. Thus, growth takes place by step-flow if the attachment of Ge atoms at the step-edges is easy to achieve. This attachment process is decisively determined by the atomic structure of steps on surfactant covered surfaces. The structure and energetics of several step configurations on Si(111):As were determined by R. Berger in his Ph.D.-thesis. We have now calculated *ab initio* simulations of STM-images for these step-edge structures using the Tersoff-Hamann approximation [TH85]. Our theoretical images and the experimental STM-images recently determined by B. Voigtländer are compared in Chapter 10. They coincide remarkably well.

The growth of Ge on Sb-covered Si(111) surfaces, which is favorable for device production due to the fact that the contamination of the growing Ge-film with Sb atoms is negligible, is much more complicated than Si homoepitaxy on Si(111):Sb or Si(111):As. During growth the surface shows at least three different reconstructions: (i) $(\sqrt{3} \times \sqrt{3})$ on the Sb terminated Si(111) surface before the deposition of Ge. (ii) A $(6\sqrt{3} \times 6\sqrt{3})$ reconstruction of large hexagons where the hexagons itself show a (1×1) reconstruction and, (iii) finally the (2×1) equilibrium reconstruction of Sb-covered Ge [VZ96, The00]. To decide if this reconstructions arise solely due to the relaxation of the Ge-film on Si(111):As with increasing film thickness, we have calculated the energy of the different reconstructions at various lattice constants. In fact, we can explain the appearance of all reconstructions by the stress induced to the Ge film by the Si substrate or the by surfactant atoms as is shown in Chapter 11.

Chapter 1

The Density Functional Theory

The microscopic explanation of materials properties is based on the quantum mechanics for electrons and ions. However, analytic solutions of the Schrödinger equation are possible for only a few very simple systems. For the calculation of the properties of many-particle systems, approximations and numerical solution schemes are necessary.

Due to the large mass difference of electrons and nuclei the two systems can be separated in many cases. In this Born–Oppenheimer or ”adiabatic“ approximation the dynamics of electrons has to be treated in a frozen-in configuration of the nuclei. This leads to electronic energies and wave-functions which contain the nuclear coordinates as external parameters. The nuclear motion is then treated separately. It contains the ground-state energy of the electrons $E_0(\{R_i\})$ for each nuclear configuration $\{R_i\}$ as part of the potential energy. Finding the eigenfunctions and eigenvalues of the electronic system is still impossible without drastic simplifying assumptions. Hartree [Har28] introduced the ”independent electron approximation“ in which the many-electron wave function is reduced to a product of single-particle functions:

$$\Psi(\mathbf{r}_1, \mathbf{r}_2, \dots) = \Psi_1(\mathbf{r}_1) \cdots \Psi_1(\mathbf{r}_1) \quad (1.1)$$

Each of the functions $\Psi_i(\mathbf{r}_i)$ satisfies a one-electron Schrödinger equation with a potential term arising from the average field of the other electrons:

$$\left[-\frac{\hbar^2}{2m} \nabla^2 + V_{ext} + \Phi_i \right] \Psi_i(\mathbf{r}) = \varepsilon_i \Psi_i(\mathbf{r}), \quad (1.2)$$

where V_{ext} is a potential due to the fixed nuclei or other external fields and Φ_i the Coulomb potential due to the electrons which is given by Poissons’s equation

$$\nabla^2 \Phi_i = 4\pi e^2 \sum_{j=1, i \neq j}^N |\Psi_j|^2. \quad (1.3)$$

The Hartree approximation was extended by Fock and Slater in 1930 by replacing the product wave function by a single determinant function:

$$\Phi(\mathbf{r}_1, \mathbf{r}_2, \dots) = \frac{1}{\sqrt{N!}} \begin{vmatrix} \Phi_1(\mathbf{r}_1) & \cdots & \Phi_N(\mathbf{r}_1) \\ \vdots & & \vdots \\ \Phi_1(\mathbf{r}_N) & \cdots & \Phi_N(\mathbf{r}_N) \end{vmatrix} \quad (1.4)$$

Thus the wave function of a many-electron system is antisymmetric under exchange of any two electrons as demanded by the Pauli principle. The spatial separation of two electrons with the same spin reduces the Coulomb energy of the system. The energy difference between the Hartree-Fock and Hartee approximation is the "exchange" energy. The Coulomb energy can be reduced below its Hartree-Fock value at the cost of increasing kinetic energy if electrons with opposite spins are also spatially separated. This introduced additional correlations between the electrons. The energy difference between the true many-electron energy and the Hartree-Fock approximation is the "correlation energy".

In the following all formulas refer to a system where

$$\hbar = 1, \quad m_e = \frac{1}{2}, \quad e^2 = 2, \quad c = \frac{2}{\alpha} = 274.074. \quad (1.5)$$

as is used in the **Electronic Structure Code for Materials Properties and Processes** (EStCoMPP). The energy then is expressed in Rydberg and the length scale is the Bohr radius:

$$1Ry \simeq 13.6058eV, \quad a_B = 0.529177\text{\AA}. \quad (1.6)$$

These units are called "atomic units".

1.1 The Density as Basic Variable

A different approach for simplifying the many-electron problem was taken by Thomas and Fermi who focused on the electron density as the basic variable of the system:

$$n(\mathbf{r}) = 2 \sum_i f_i |\Psi_i(\mathbf{r})|^2 \quad (1.7)$$

The occupation numbers f_i obeys the Fermi distribution and are normalized to the total number of electrons:

$$2 \sum_i f_i = N \quad (1.8)$$

The sum has to be taken over all normalized one-electron wave functions $\Psi_i(\mathbf{r})$ with the occupation numbers $0 \leq f_i \leq 1$. The factor two accounts for the

spin degeneracy. In this approximation the electrons are treated as independent particles in a homogeneous electron gas, neglecting exchange and correlation. The contributions to the energy are then defined by the electrostatic energy of the electrons, their interaction with an external electrostatic potential and the kinetic energy:

$$E[n] = E_H[n] + E_{ext}[n] + E_{kin}[n] \quad (1.9)$$

The electron-electron interaction energy arises exclusively from the electrostatic energy as in the Hartree approximation

$$E_H[n] = \int d^3\mathbf{r} d^3\mathbf{r}' \frac{n(\mathbf{r})n(\mathbf{r}')}{|\mathbf{r} - \mathbf{r}'|}, \quad (1.10)$$

and the energy due to an external electrostatic potential is given by

$$E_{ext}[n] = \int d^3\mathbf{r} V(\mathbf{r})n(\mathbf{r}). \quad (1.11)$$

Generalizing the results for the homogeneous electron gas, where the average energy per electron is given by

$$\varepsilon = \frac{3}{5} k_F^2, \quad \text{with } k_F = (3\pi n_0)^{2/3} \quad \text{and} \quad n_0 = \frac{N}{V}, \quad (1.12)$$

the kinetic energy for an inhomogeneous electron gas is written as

$$E_{kin}[n(\mathbf{r})] = \int d^3\mathbf{r} n(\mathbf{r})\varepsilon(n(\mathbf{r})) = \left(\frac{3}{5}\right) (3\pi^2)^{2/3} \int d^3\mathbf{r} (n(\mathbf{r}))^{5/3}. \quad (1.13)$$

The Thomas–Fermi method contains all ingredients of a density functional theory. Due to the crude treatment of the kinetic energy, and the neglect of exchange and correlation, it does not yield correct and useful results, e.g. it cannot describe binding of atoms in as solid.

In 1964 Hohenberg and Kohn started a new approach to the density functional theory. They proved two theorems for interacting electrons in an external potential $V(\mathbf{r})$ whose Hamiltonian is

$$H = \sum_{i=1}^N [-\partial_{\mathbf{r}_i}^2 + V(\mathbf{r})] + \sum_{i,j,i \neq j}^N \frac{1}{|\mathbf{r}_i - \mathbf{r}_j|}. \quad (1.14)$$

Hohenberg-Kohn Theorem I: The ground-state of an inhomogeneous interacting many-electron system is a unique functional of the ground-state electron density $n_0(\mathbf{r})$.

Hohenberg-Kohn Theorem II: There exists an energy-functional $E[n]$ which is minimized by the ground-state density $n_0(\mathbf{r})$ under the condition of charge conservation.

While Hohenberg and Kohn proved their Theorems indirect with the assumption that $n(\mathbf{r})$ is uniquely determined by the external potential (V -representation of $n(\mathbf{r})$), Levy [Lev79] showed more precisely that the energy-functional is minimized by $n_0(\mathbf{r})$, using a variational method. He defined the energy-functional as:

$$E[n] := \min \langle \Psi | H | \Psi \rangle \quad (1.15)$$

The expectation value of the Hamilton operator has to be minimized with respect to the norm conserving, antisymmetric many-particle wave-function Ψ , which reproduces a given electron-density $n(\mathbf{r})$ (Ψ representation of $n(\mathbf{r})$). The ground-state density $n_0(\mathbf{r})$ and the ground-state energy $E[n_0]$ is determined by minimizing the energy-functional:

$$\delta E[n] = 0 \quad (1.16)$$

The subsidiary condition of particle conservation

$$\int d^3\mathbf{r} n(\mathbf{r}) = N, \quad (1.17)$$

is taken into account using a Lagrangian-parameter μ . This leads to the minimization of a modified energy-functional

$$\delta \left[E[n] - \mu \left(\int d^3\mathbf{r} - N \right) \right] = 0, \quad (1.18)$$

which yields the following Euler-Lagrange equation:

$$\left. \frac{\delta E[n(\mathbf{r})]}{\delta n(\mathbf{r})} \right|_{n_0(\mathbf{r})} = \mu. \quad (1.19)$$

An explicit form of the energy-functional could not be derived from the approach of Hohenberg and Kohn, nor from Levy's formulation. Thus additional approximations have to be made.

1.2 The Kohn-Sham Equations

To avoid the explicit formulation of the energy-functional, Hohenberg and Kohn developed an approximation method for treating an inhomogeneous system of interacting electrons [KS65]. The contributions to the total energy of the ground state are formally split-up into four parts

$$E[n] = E_{kin}^0[n] + E_{ext}[n] + E_H[n] + E_{xc}[n], \quad (1.20)$$

where E_{kin}^0 is the functional of the kinetic energy of N *non-interacting* electrons. E_{ext} describes the energy of electrons with the density $n(\mathbf{r})$ in an external potential $V(\mathbf{r})$, i.e. the interaction with the nuclei (Eq.1.11). E_H gives the Coulomb energy in the Hartree approximation (see Eq.1.10), and all unknown many-particle effects, including the corrections to the kinetic energy, are contained in the exchange-correlation functional E_{xc} which is defined by Eq.1.20. To find an explicit form of the functional $E[n]$ only $E_{xc}[n]$ has to be approximated. This however is only a small contribution to the total electron energy [JG89].

Minimization of the functional $E[n]$, again under the subsidiary condition that the number of electrons is kept constant ($\int d^3(\mathbf{r}) n(\mathbf{r}) = N$), which is guaranteed with a Lagrangian-parameter μ , yields

$$\frac{\delta E_{kin}}{\delta n(\mathbf{r})} + \frac{\delta E_{ext}}{\delta n(\mathbf{r})} + \frac{\delta E_H}{\delta n(\mathbf{r})} + \frac{\delta E_{xc}}{\delta n(\mathbf{r})} - \mu = 0. \quad (1.21)$$

Since the kinetic energy is formulated for non-interacting electrons, one can parameterize the electron density $n(\mathbf{r})$ by fictitious one-electron wave-functions

$$n(\mathbf{r}) = \sum_{i(occ)}^N |\Psi_i(\mathbf{r})|^2, \quad (1.22)$$

with orthonormalized functions $\Psi_i(\mathbf{r})$, which have to be determined. The variation of the density $n(\mathbf{r})$ is achieved by varying the functions $\Psi_i(\mathbf{r})$ and the particle conservation condition is replaced by a normalization condition for the functions $\Psi_i(\mathbf{r})$:

$$\int d^3(\mathbf{r}) n(\mathbf{r}) - N = \sum_i^N \left[\int d^3(\mathbf{r}) \Psi_i^*(\mathbf{r}) \Psi_i(\mathbf{r}) - 1 \right] \quad (1.23)$$

With the introduction of N independent Lagrangian parameters ε_i one can then minimize the functional

$$\begin{aligned} \tilde{E}[\Psi_i] &= E[n(\mathbf{r})] - \sum_i^N \varepsilon_i \left[\int d^3(\mathbf{r}) \Psi_i^*(\mathbf{r}) \Psi_i(\mathbf{r}) - 1 \right] \\ &\text{using } \frac{\delta E}{\delta \Psi_i} = \frac{\delta E}{\delta n} \cdot \frac{\delta n}{\delta \Psi_i}. \end{aligned} \quad (1.24)$$

This yields a simple equation of motion for each of the functions $\Psi_i(\mathbf{r})$ which has the appearance of a single particle Schrödinger equation where the Lagrangian parameter ε_i takes the role of the eigenvalue:

$$(-\partial_{\mathbf{r}}^2 + U(\mathbf{r})) \Psi_i(\mathbf{r}) = \varepsilon_i \Psi_i(\mathbf{r}) \quad (1.25)$$

The potential $U(\mathbf{r})$ is an effective single particle potential

$$U(\mathbf{r}) = V_{ext}(\mathbf{r}) + V_H(\mathbf{r}) + V_{xc}(\mathbf{r}), \quad (1.26)$$

which contains the contributions:

$$V_{ext}(\mathbf{r}) = \frac{\delta E_{ext}}{\delta n(\mathbf{r})} = V(\mathbf{r}), \quad (1.27)$$

$$V_H = \frac{\delta E_H}{\delta n(\mathbf{r})} = \int d^3\mathbf{r}' \frac{n(\mathbf{r}')}{|\mathbf{r} - \mathbf{r}'|}, \quad (1.28)$$

$$V_{xc} = \frac{\delta E_{xc}}{\delta n(\mathbf{r})}. \quad (1.29)$$

$U(\mathbf{r})$ is density dependent and thus a functional of the function $\Psi_i(\mathbf{r})$. A solution of the Kohn-Sham equations

$$[-\partial_{\mathbf{r}_i}^2 + V_{ext}(\mathbf{r}) + V_H(\mathbf{r}) + V_{xc}(\mathbf{r})] \Psi_i(\mathbf{r}) = \varepsilon_i \Psi(\mathbf{r}) \quad (1.30)$$

has to be found by iterating to self consistency. This Kohn-Sham approach represents a mapping of the interacting many-electron system onto a system of non-interacting electrons moving in an effective potential due to all the other electrons. The self-consistent solution of the Kohn-Sham equation gives the set of wave-function Ψ_i that minimizes the Kohn-Sham energy-functional. If the exchange-correlation energy functional were known exactly, the functional derivative with respect to the density would produce an exchange-correlation potential that includes the effects of exchange and correlation exactly. The eigenvalues of the Kohn-Sham equations are formally one-particle energies. However, since they are only Lagrangian parameters in the density functional theory they have strictly speaking no physical meaning. The same argument holds for the one-particle wave-functions, which have no physical meaning as well. Nevertheless, following Koopmans-theorem, an interpretation of the ε_i and $\Psi_i(\mathbf{r})$ as eigenvalues and one-particle wave-functions is generally possible [JG89]. For delocalized states, where the correlation effects are relatively small, the spectroscopically measured ionization energies and the energies calculated with the density functional theory are indeed in good agreement. This is not true for strong localized states (e.g. atomic states). However, the surface-states which are calculated in this thesis are sufficiently delocalized and can be interpreted as physical states.

1.3 Local Density Approximation

To apply the Kohn-Sham equations, the energy-functional $E[n(\mathbf{r})]$ has to be known. Unfortunately, the Hohenberg-Kohn theorems does not yield the density-functional. Thus, approximations for the exchange-correlation functional, which is the only unknown part of the energy-functional $E[n(\mathbf{r})]$ (Eq.1.20), have to be made. The simplest method of describing the exchange-correlation energy is to use the local-density approximation (LDA), which assumes that the exchange-correlation energy per electron at a point \mathbf{r} in the electron gas $\varepsilon_{xc}(\mathbf{r})$, is equal to the exchange-correlation energy per electron in a homogeneous electron gas that has the same density as the electron gas at point \mathbf{r} . Thus

$$\varepsilon_{xc}^{LDA}[n(\mathbf{r})] = \varepsilon_{xc}^{hom}(n(\mathbf{r})) \quad (1.31)$$

now is a function and not a functional of the density $n(\mathbf{r})$ and spatial integration yields the exchange-correlation energy:

$$E_{xc}^{LDA}[n(\mathbf{r})] = \int d^3\mathbf{r} \varepsilon_{xc}^{LDA}(\mathbf{r}) n(\mathbf{r}) \quad (1.32)$$

The V_{xc} -potential is then calculated as

$$\begin{aligned} V_{xc}^{LDA}[n(\mathbf{r})] &= \frac{\delta E_{xc}^{LDA}[n(\mathbf{r})]}{\delta n(\mathbf{r})} = \frac{\partial [n(\mathbf{r}) \varepsilon_{xc}^{LDA}(n(\mathbf{r}))]}{\partial n(\mathbf{r})} \\ &= \varepsilon_{xc}^{LDA}(n(\mathbf{r})) + n(\mathbf{r}) \left(\frac{d\varepsilon_{xc}^{LDA}(n)}{dn} \right)_{n=n(\mathbf{r})}. \end{aligned} \quad (1.33)$$

The Hartree-Fock equations can be solved exactly for a homogeneous electron gas yielding for the exchange energy $\varepsilon_x(n)$ the result

$$\varepsilon_x(n) = -\frac{3}{2} \left(\frac{3}{\pi} \right) n^{1/3}. \quad (1.34)$$

The ground-state energy as a function of the electron density can be calculated numerically and under the assumption

$$\varepsilon_{xc}(n) = \varepsilon_x(n) + \varepsilon_c(n). \quad (1.35)$$

Ceperley and Alder calculated the correlation-energy density, using a Quantum-Monte-Carlo simulation [CA80]. The parameterization of Vosko *et al.* [VWN80], which is used in this thesis, is based on these results. Several other parameterizations exist for the exchange-correlation energy of a homogeneous electron gas [Wig34, BG80, MJW80], all of which lead to very similar total-energy results. These parameterizations use interpolation formulas using exact results for the exchange-correlation energy of the electron gas at high, intermediate, and low densities. The local-density approximation, in principle, ignores corrections to the exchange-correlation energy at a point \mathbf{r} due to nearby inhomogeneities in

the electron density. Nevertheless the success of the LDA, also for very inhomogeneous system as semiconductor-surfaces, is remarkable. This success can partially be attributed to the fact that the local-density approximation gives the correct sum rule for the exchange-correlation hole and that the exchange-correlation energy depends only the spherical average of the density [JG89].

1.4 Spin-Density Functional Theory

The expansion of the density-functional theory for spin-polarized electrons is straightforward. The spin-density-functional theory allows the investigation of the magnetic properties like ferro- or antiferromagnetism of solids or surface-magnetism. The generalization is achieved by replacing the electron-density $n(\mathbf{r})$ with the spin-densities $n^\uparrow(\mathbf{r})$ and $n^\downarrow(\mathbf{r})$ for electrons with spin-up and spin-down respectively. The electron-density and the magnetization-density are then defined as

$$\begin{aligned} n(\mathbf{r}) &= n^\uparrow(\mathbf{r}) + n^\downarrow(\mathbf{r}), \\ m(\mathbf{r}) &= n^\uparrow(\mathbf{r}) - n^\downarrow(\mathbf{r}). \end{aligned} \quad (1.36)$$

The energy-functional in the Hohenberg-Kohn Theorems is generalized to a functional of two densities

$$E[n] \rightarrow E[n^\uparrow(\mathbf{r}), n^\downarrow(\mathbf{r})]. \quad (1.37)$$

It is minimized by the ground-state densities $n_0^\uparrow(\mathbf{r})$ and $n_0^\downarrow(\mathbf{r})$. The Kohn-Sham equations are obtained by the variation of the energy-functional with respect to the spin-densities. The approximation used most widely is the local spin-density approximation (LSDA), where

$$\varepsilon_{xc}^{LSDA}[n^\uparrow(\mathbf{r}), n^\downarrow(\mathbf{r})] = \varepsilon_{xc}^{hom}(n^\uparrow, n^\downarrow) \quad (1.38)$$

is the exchange and correlation energy per particle of a homogeneous, spin-polarized electron gas [BH72].

Chapter 2

Pseudopotentials

For the application of the density-functional theory, the Kohn-Sham equations have to be solved. The appearing one-electron energies ε_i have a much larger value for the inner closed-shell electrons than for the valence electrons. For example the ground-state energy of an silicon-atom is about $10^5 eV$, while the binding-energy per atom (sublimation energy) in the silicon-crystal is only about $5 eV$. The binding energy is almost exclusively determined by the overlapping outer valence-electrons, whereas the localized core electrons of the inner closed shells are not affected. The aim of the pseudopotential-method (psp-method) is to reduce computational requirements for density-functional theory calculations of solids by treating valence electrons only.

2.1 Pseudopotential Method

Under the assumption that the charge-densities of the core-electrons do not overlap with neighboring atoms, it is possible to treat them as frozen-in. They shield the strong ionic potential, and it should be possible to replace the true potential by a weaker pseudopotential for the valence electrons. Outside the core region, i.e. beyond a cutoff radius r_c , the true all-electron potential and the pseudopotential are identical. The weaker pseudopotential should ideally remove the rapid oscillation of the valence wave-functions in the core region. For density functional calculations one has to construct norm-conserving pseudopotentials, which guarantee the charge conservation. Two contradictory criteria determine the usefulness of a pseudopotential: (i) the pseudopotential should be "soft", i.e. only a small number of plane-wave basis states should be necessary to describe the wave-functions, and (ii) the pseudopotentials should be transferable, which means that the potential should give the correct ground-state energy of the valence electrons in different chemical environments. While the first condition is easy to achieve for large cutoff radii r_c , the second requires small cutoff radii. To obtain meaningful results the cut-off radius for a given atom has to be substantially smaller

than its covalent radius. Otherwise the bonding of the atoms in a solid cannot be described correctly.

The construction of the pseudopotentials is done in two steps: (i) the energy of the valence electrons in an atomic configuration is calculated in an all-electron calculation and, (ii) a pseudopotential is constructed such that the scattering properties of the true potential outside the core-region are preserved. The all-electron potential, the pseudopotential and the corresponding wave functions are shown schematically in Fig. 2.1. Inside the cutoff radius, i.e. in the core region,

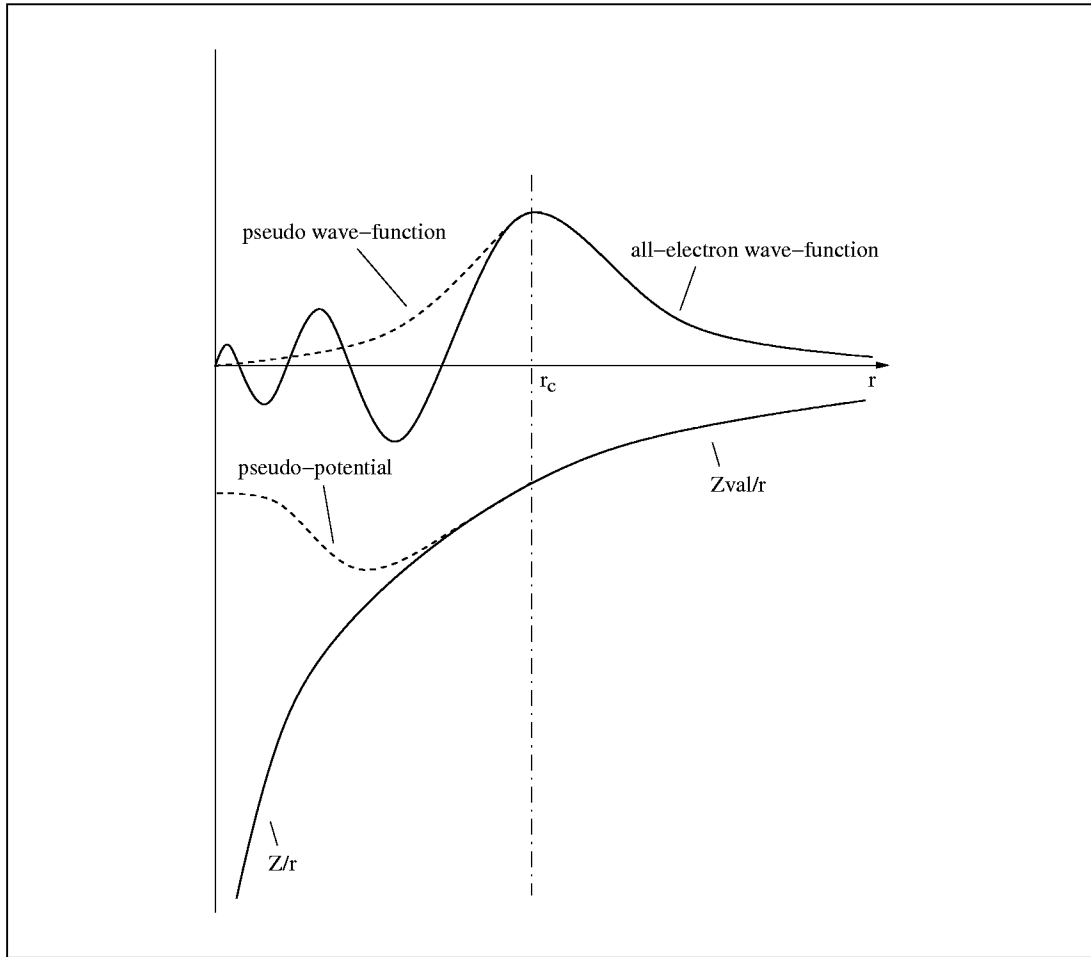


Figure 2.1: Schematic illustration of an all-electron (solid lines) and pseudoelectron (dashed lines) valence wave-function and potentials. Beyond the cutoff-radius r_c the scattering from the two potentials is indistinguishable

the all-electron valence wave function oscillates rapidly due to the strong ionic potential and the orthogonalization to the core states. Outside the cutoff radius the all-electron and pseudo functions coincide and the scattering behavior of the atom is well represented by the pseudopotential.

2.2 Semi-local Pseudopotentials

Generating a norm-conserving pseudopotential proceeds as follows [BHS82]. All-electron calculations for an isolated atom in its ground-state and some excited states are performed. This specifies the all-electron (ae) valence-eigenfunctions $\Psi_{ae,l}(\mathbf{r})$ and eigenvalues ε_l for each l -component. Then one chooses a cutoff radius $r_{c,l}$ and constructs a pseudo (ps) wave-function $\Psi_{ps,l}(\mathbf{r})$ and a pseudopotential $V_{ps,l}(\mathbf{r})$ with adjustable parameters, which deviate from the ae-functions inside of the cutoff radius.

The pseudo wave-functions and pseudopotentials have to match four criteria: (i) The pseudo-eigenvalues have to be equal to the all-electron valence-eigenvalues. (ii) The pseudo wave-functions $\Psi_{ps,l}(\mathbf{r})$ has to be node-less and continuously differentiable. (iii) Charge conservation is guaranteed if $\Psi_{ps,l}(\mathbf{r})$ fulfills the norm-conserving condition $\int_0^{r_c} d\mathbf{r} |\Psi_{ps,l}(\mathbf{r})|^2 = \int_0^{r_c} d\mathbf{r} |\Psi_{ae,l}(\mathbf{r})|^2$. Since outside r_c the wave-functions are identical by construction, norm conservation is then guaranteed in the entire space. (iv) The logarithmic derivatives of the eigenfunctions $\partial(\ln \Psi_{ps,l}(\mathbf{r}, \varepsilon))/\partial r$ have to be identical for the pseudoatom and the all-electron calculations, which ensures that the scattering properties are accurately described. The semi-local pseudopotential then has the form

$$V^{PS}(\mathbf{r}) = \sum_l V_l^{PS}(r) \hat{P}_l, \quad (2.1)$$

where \hat{P}_l is a projection-operator for the angular momentum component l . Since all potentials show the same long-range Coulomb-behavior, a common local potential can be separated:

$$\begin{aligned} V^{PS}(\mathbf{r}) &= \sum_l V_{loc}(r) \hat{P}_l + \sum_l (V_l^{SL}(r) - V_{loc}(r)) \hat{P}_l \\ &= V_{loc}(r) + \sum_l \Delta V_l^{SL}(r) \hat{P}_l \end{aligned} \quad (2.2)$$

The semi-local, l -dependent potentials $\Delta V_l^{SL}(r)$ are limited to the core-region. Using a plane-wave basis, a matrix element of such a semi-local pseudopotential would have the form

$$\begin{aligned} \Delta V_l^{SL}(\mathbf{k} + \mathbf{G}, \mathbf{k} + \mathbf{G}') &:= \frac{1}{\Omega} \left\langle e^{i(\mathbf{k} + \mathbf{G})\mathbf{r}} \left| \Delta V_l^{SL}(r) \hat{P}_l \right| e^{i(\mathbf{k} + \mathbf{G}')\mathbf{r}} \right\rangle \\ &= \frac{4\pi}{\Omega} (2l + 1) P_l(\cos \gamma_{\mathbf{k} + \mathbf{G}, \mathbf{k} + \mathbf{G}'}) \\ &\quad \times \int dr j_l(|\mathbf{k} + \mathbf{G}|r) \Delta V_l^{SL}(r) j_l(|\mathbf{k} + \mathbf{G}'|r) r^2, \end{aligned} \quad (2.3)$$

where Ω is the volume of the cell, j_l a spherical Bessel-function, P_l a Legendre-polynomial and $\gamma_{\mathbf{k} + \mathbf{G}, \mathbf{k} + \mathbf{G}'}$ the angle between $(\mathbf{k} + \mathbf{G})$ and $(\mathbf{k} + \mathbf{G}')$. Thus the pseudopotential contribution to the Hamiltonian is a matrix with the dimension

$N \times N$, where N is the number of plane waves. Since the computational cost for the diagonalization of a matrix scales with N^3 and since N scales with the number of atoms in the system, the size of the systems which can be handled are very limited.

2.3 Separable-Pseudopotentials

Kleinman and Bylander [KB82] proved that each semi-local pseudopotential can be transformed to a non-local pseudopotential

$$\Delta V_l(r) \hat{P}_l \simeq \Delta V_l^{KB} = \sum_{m=-l}^{+l} \frac{|\Delta V_l(r) \Psi_{lm}\rangle \langle \Psi_{lm} \Delta V_l(r)|}{\langle \Psi_{lm} | \Delta V_l(r) | \Psi_{lm} \rangle}, \quad (2.4)$$

where Ψ_{lm} are the pseudo wave-functions which were used for the construction of the semi-local pseudopotential $\Delta V_l(r)$. The application of the Kleinman-Bylander pseudopotential to the pseudo wave-function yields the same results as the application of the semi-local pseudopotential by construction. Using the lm -representation of Ψ_{lm} in the form $\Psi_{lm} = \frac{g_l(r)}{r} Y_{lm}(\theta, \varphi)$, the plane-wave matrix-element of $\Delta V_l(r)$ is given by

$$\begin{aligned} \Delta V_l^{KB}(\mathbf{k} + \mathbf{G}, \mathbf{k} + \mathbf{G}') &:= \frac{1}{\Omega} \left\langle e^{i(\mathbf{k}+\mathbf{G})\mathbf{r}} \left| \Delta V_l^{KB}(r) \hat{P}_l \right| e^{i(\mathbf{k}+\mathbf{G}')\mathbf{r}} \right\rangle \\ &= \frac{4\pi}{\Omega} (2l+1) P_l(\cos \gamma_{\mathbf{k}+\mathbf{G}, \mathbf{k}+\mathbf{G}'}) \\ &\quad \times \frac{T_l^*(|\mathbf{k} + \mathbf{G}|) T_l(|\mathbf{k} + \mathbf{G}'|)}{W_l}, \end{aligned} \quad (2.5)$$

with

$$T_l(|\mathbf{k} + \mathbf{G}|) = \int dr r g_l(r) \Delta V_l(r) j_l(|\mathbf{k} + \mathbf{G}|r), \quad (2.6)$$

and

$$W_l = \int dr g_l(r) \Delta V_l(r) g_l(r). \quad (2.7)$$

If the Legendre-polynomial is also expressed by spherical-harmonics

$$P_l(\cos \gamma_{\mathbf{k}+\mathbf{G}, \mathbf{k}+\mathbf{G}'}) = \frac{4\pi}{2l+1} \sum_{m=-l}^{+l} Y_{lm}^*(\Omega_{\mathbf{k}+\mathbf{G}}) Y_{lm}(\Omega_{\mathbf{k}+\mathbf{G}'}), \quad (2.8)$$

then the pseudopotential is transformed to

$$\begin{aligned} \Delta V_l^{KB}(\mathbf{k} + \mathbf{G}, \mathbf{k} + \mathbf{G}') &= \frac{(4\pi)^2}{\Omega} \sum_m Y_{lm}^*(\Omega_{\mathbf{k}+\mathbf{G}}) Y_{lm}(\Omega_{\mathbf{k}+\mathbf{G}'}) \\ &\quad \times \frac{T_l^*(|\mathbf{k} + \mathbf{G}|) T_l(|\mathbf{k} + \mathbf{G}'|)}{W_l}, \end{aligned} \quad (2.9)$$

where $\Omega_{\mathbf{k}+\mathbf{G}}$ are the angles of $(\mathbf{k} + \mathbf{G})$. Now the pseudopotential is separable in \mathbf{G} and \mathbf{G}' and the computation of the non-local part of the potential scales like $N \cdot \log(N)$ if iterative diagonalization schemes are used. The only drawback for using Kleinman-Bylander potentials is that their construction is not as straightforward as it seems from the short description above. For semi-local potentials it is guaranteed that the energy of the eigenstates increases with increasing number of nodes of the eigenfunctions. For Kleinman-Bylander separable pseudopotentials, unphysical lower energy states with nodes, so-called *ghost-states*, may appear which can be identified due to their poles in the logarithmic derivatives of the eigenfunctions. Since there are no strict rules how to choose the construction parameters of the pseudopotential, generating new, applicable pseudopotentials is still more an art than a simple application of a computational algorithm.

Chapter 3

Periodic Supercells

With the application of the density-functional theory a many-body problem of N interacting particles can be reduced to the calculation of N single-electron equations. We have to define an appropriate basis set to expand the wave-functions, and express the different parts of the Hamiltonian. A particularly simple one to use with soft pseudopotentials is a plane-wave basis-set. The systems we want to describe are usually non-periodic, but in order to use well established band structure methods developed for ideal crystals one approximates the inhomogeneous system by a periodic continuation of a supercell containing the inhomogeneity.

For a crystal lattice the elementary cell is defined as the smallest structure, whose periodical continuation describes the crystal. The elementary cell is defined by three basis-vectors $\mathbf{a}_1, \mathbf{a}_2, \mathbf{a}_3$. Each lattice-vector

$$\mathbf{R}^{\mathbf{n}} = n_1 \mathbf{a}_1 + n_2 \mathbf{a}_2 + n_3 \mathbf{a}_3, \quad \mathbf{n} = (n_1, n_2, n_3), \quad n_i \in \mathbb{Z}, \quad (3.1)$$

points to the position of a different elementary cell and any property of the lattice $f(\mathbf{r})$ ($f(\mathbf{r})$ e.g. potential $V(\mathbf{r})$, electronic density $n(\mathbf{r})$) has to be periodic in $\mathbf{R}^{\mathbf{n}}$:

$$f(\mathbf{r} + \mathbf{R}^{\mathbf{n}}) = f(\mathbf{r}) \quad (3.2)$$

The volume of the elementary cell is

$$\Omega = \mathbf{a}_1 \cdot (\mathbf{a}_2 \times \mathbf{a}_3). \quad (3.3)$$

The basis-vectors of the reciprocal space are defined by

$$\mathbf{b}_i = 2\pi \frac{\mathbf{a}_j \times \mathbf{a}_k}{\Omega}, \quad (3.4)$$

for cyclic i, j, k . The reciprocal space is then spanned by the reciprocal lattice-vectors

$$\mathbf{G}^{\mathbf{g}} = g_1 \mathbf{b}_1 + g_2 \mathbf{b}_2 + g_3 \mathbf{b}_3, \quad (3.5)$$

which ensures that for each $\mathbf{G}^{\mathbf{g}}$ and $\mathbf{R}^{\mathbf{n}}$

$$e^{i\mathbf{G}^{\mathbf{g}} \cdot \mathbf{R}^{\mathbf{n}}} = 1. \quad (3.6)$$

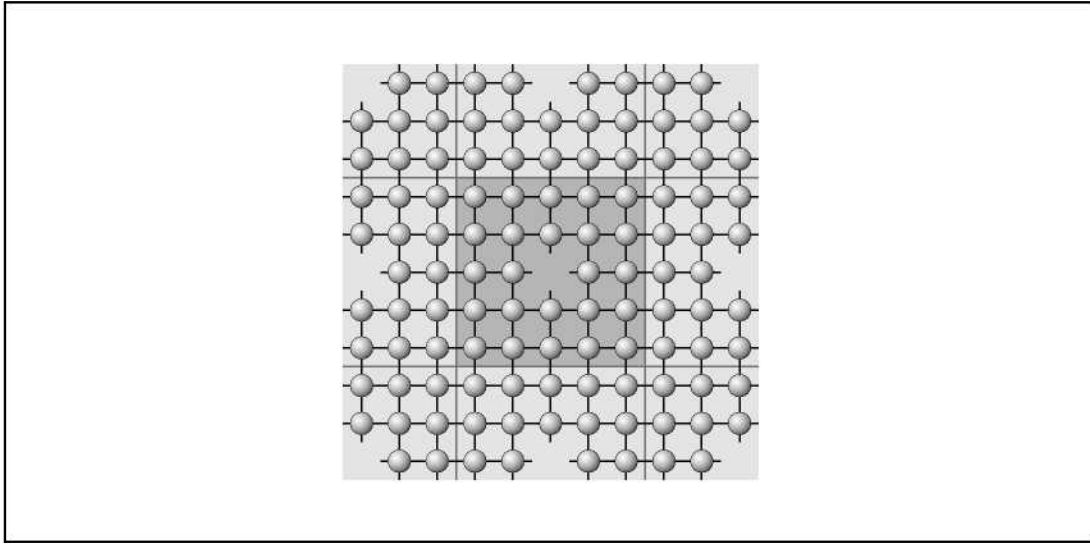


Figure 3.1: Schematic two-dimensional illustration of a supercell geometry for a point defect in a bulk solid. The supercell area is enhanced by the dark grey area.

To describe inhomogeneous systems like point-defects or surfaces of solids, a supercell has to be defined which contains the defect and enough of its neighborhood to be able to describe the required electronic and atomic configuration meaningfully. This supercell is the repeated periodically, as is shown in Fig. 3.1 for a point defect and in Fig. 3.2 for a supercell containing a surface. Thus the energy of a crystal with a periodic arrangement of defects is calculated, rather than the energy of a crystal containing a single defect. It is obvious that the distance between the defects has to be large enough to avoid defect-defect interactions. For point-defect this can be done by including enough bulk solid in the supercell. For surfaces the vacuum-region included in the supercell, which divides the periodic surfaces, has to be sufficiently large. The behavior of the defect-defect interaction can be tested by a series of calculations with varying sizes of the supercell. For increasing size of the supercells the total energy per volume will converge to the single defect energy, since the defect-defect interaction becomes weaker with increasing distances. The vacuum region for surface calculations can easily be tested by plotting the laterally integrated electron-density. In the vacuum, the electron-density will drop exponentially. If the vacuum is sufficiently large, the calculated density will form a plateau of low density before it rises again due to the next surface, which appears because of the periodic continuation of the supercell. Fig. 3.3 shows two systems, of Ge ad-atoms on top of 6 Si(111) double layers covered with As on each side in an inversion-symmetric arrangement, where the vacuum size corresponds to 5 respectively 8 layers of silicon (total height $h = 2.5, 3.0 \times 6$ Si-layers – 10 layers filled with atoms). The bulk region is located on the left and right side of the plot and the vacuum region is in the

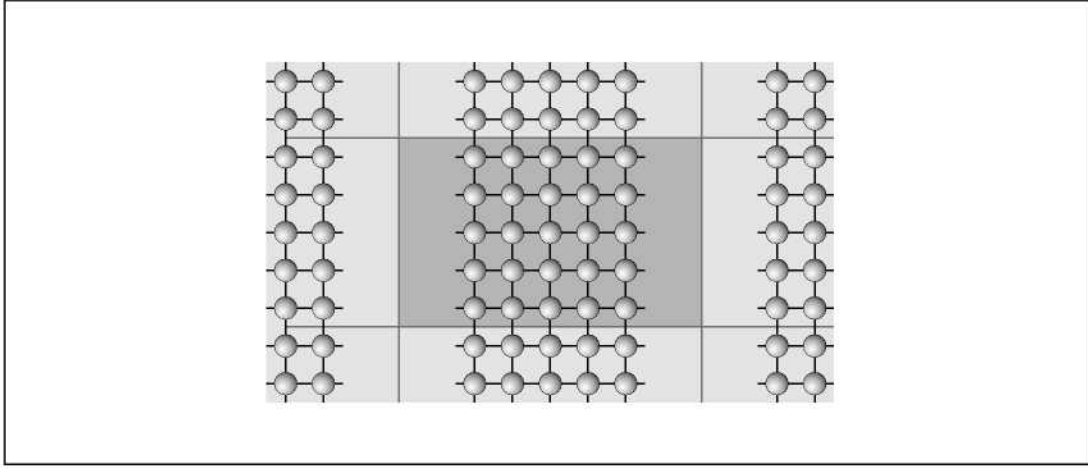


Figure 3.2: Schematic two-dimensional illustration of a supercell geometry for a surface of bulk solid. The supercell area is enhanced by the dark grey area.

middle of the curves. Both systems show an oscillation in the density on the left and right side, which reflects the periodic variations of the density in the atomic layers due to the crystal structure. For the vacuum size of 5 Si-layers ($h = 2.5$) the density does not reach the numerical zero level and increases immediately towards the opposing surface. For $h = 3.0$ a pronounced plateau is achieved, before the density rises again. Thus for the system with $h = 2.5$ the vacuum is not sufficient to separate the surfaces. Obviously each additional point defect on the surface, i.e. an ad-atom, will interact across the vacuum region if the electronic densities overlap. In the case $h = 3.0$ there is enough vacuum to ensure the separation. Even these simple tests, comparing the energy per volume of the supercell for different system sizes or plotting the laterally integrated density for surfaces, are often disregarded in literature.

3.1 Bloch's Theorem

Using the supercell approach, the potential $V(\mathbf{r})$ also has the periodicity of the supercell:

$$V(\mathbf{r} + \mathbf{R}) = V(\mathbf{r}) \quad (3.7)$$

Bloch's theorem states that in a periodic potential each electronic wave-function can be expressed as the product of a cell-periodic part $u_{\nu,\mathbf{k}}(\mathbf{r})$ and a plane-wave part $e^{i\mathbf{k}\mathbf{r}}$

$$\Psi_{\nu,\mathbf{k}}(\mathbf{r}) = e^{i\mathbf{k}\mathbf{r}} u_{\nu,\mathbf{k}}(\mathbf{r}). \quad (3.8)$$

The cell periodic part of the wave function can be expanded using a basis set consisting of a discrete set of plane waves whose wave vectors are the reciprocal

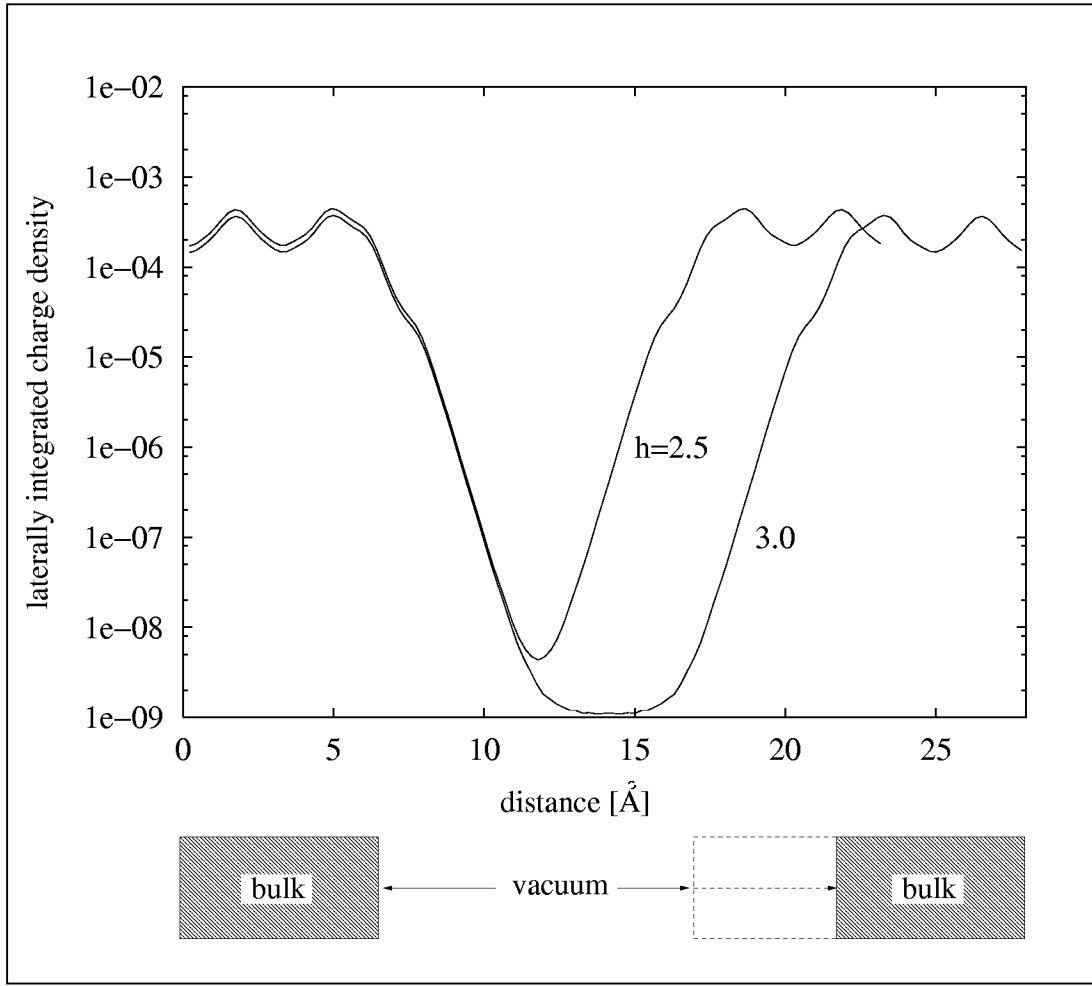


Figure 3.3: Laterally integrated electron-density.

lattice vectors

$$u_{\nu,\mathbf{k}}(\mathbf{r}) = \sum_{\mathbf{G}} c_{\nu,\mathbf{G}} e^{i\mathbf{G}\cdot\mathbf{r}}. \quad (3.9)$$

Therefore each electronic wave-function can be written as a sum of plane waves

$$\Psi_{\nu,\mathbf{k}}(\mathbf{r}) = \sum_{\mathbf{G}} c_{\nu,\mathbf{k}+\mathbf{G}} e^{i(\mathbf{k}+\mathbf{G})\cdot\mathbf{r}}. \quad (3.10)$$

The wave-vector \mathbf{k} can always be confined to the first Brillouin zone (1.BZ), because any \mathbf{k}' outside the 1.BZ can be written as

$$\mathbf{k}' = \mathbf{k} + \mathbf{G}, \quad (3.11)$$

where $\mathbf{G}^{\mathbf{g}}$ is a reciprocal lattice vector and \mathbf{k} lies in the first Brillouin zone. Since there are many solutions for a given \mathbf{k} , the band index ν has to be used to fully characterize the wave-functions.

3.2 k-point sampling

By imposing appropriate boundary conditions (e.g. Born-von Karman [or periodic] boundary conditions) on the wave functions, it can be shown that the wave vector \mathbf{k} must be real, and electronic states are only allowed at a discrete set of \mathbf{k} -points. The density of allowed \mathbf{k} -points is proportional to the volume of the supercell. The electronic wave-functions $\Psi_{\nu\mathbf{k}}$ are continuous functions of \mathbf{k} . Thus it is possible to represent the wave-function over a region of \mathbf{k} -space approximately by the wave-function at a single \mathbf{k} -point. In this case the electronic states at only a finite number of \mathbf{k} -points are required to calculate the electronic potential. The distribution of this \mathbf{k} -points in the first Brillouin-zone, which yield accurate results for the calculation of the electronic potential, have been studied by a number of groups ([CC73, JC73, PM77]). In the **ES**t**Co**MPP-program the Monkhorst-Pack method is used to generate the special \mathbf{k} -point distribution. Using these \mathbf{k} -point sets, BZ integration can be done, yielding an accurate approximation for the electronic potential and the total energy, by calculating the electronic states at only a small number of \mathbf{k} -points. A denser set of \mathbf{k} -points will reduce the error in the total energy due to the inaccurate \mathbf{k} -point sampling. Thus, the convergence of the total energy has to be checked by a series of calculations with increasing \mathbf{k} -point density. With a set of special \mathbf{k} -point the integration over the first Brillouin-zone is replaced by a weighted summation over the \mathbf{k} -points:

$$\int_{1.BZ} d^3\mathbf{k} \dots \rightarrow \sum_{\mathbf{k}} \omega_{\mathbf{k}} \dots \quad (3.12)$$

where $\omega_{\mathbf{k}}$ are the weights of the \mathbf{k} -points, which are also given by the Monkhorst-Pack method.

3.3 Plane-wave basis sets

As stated by Bloch's theorem, the electronic wave-functions at each \mathbf{k} -point can be expanded in terms of discrete plane-wave basis sets:

$$\Psi_{\nu,\mathbf{k}}(\mathbf{r}) = \sum_{\mathbf{G}} c_{\nu,\mathbf{k}+\mathbf{G}} e^{i(\mathbf{k}+\mathbf{G})\cdot\mathbf{r}} \quad (3.13)$$

In principle, an infinite basis set is required to expand the electronic wave-functions. However, since we want to describe rather smooth valence wave-functions the importance of the coefficients $c_{\nu,\mathbf{k}+\mathbf{G}}$ decreases with increasing $|\mathbf{k} + \mathbf{G}|$. Thus, the plane-wave basis set can be truncated to include only plane waves that have kinetic energies less than some particular cutoff-energy $E_{cut} = |\mathbf{k} + \mathbf{G}_{cut}|^2$. The error for the calculation of the total energy with a particular plane-wave basis can be reduced by increasing the cutoff-energy. As for the \mathbf{k} -points, the appropriate cut-off has to be checked by a series of calculations with increasing cutoff-energy.

In summary the \mathbf{k} -point set and the cut-off energy of the plane-wave basis-set determine the accuracy of the representation of the wave-functions, the electronic density, the electronic potential and the total energy. The larger the number of basis-functions, the more accurate the results. On the other hand, the computational effort increases linearly with the number of \mathbf{k} -points and like G_{cut}^3 with the plane-wave cut-off.

Chapter 4

The EStCoMPP-Program

The ***E**lectronic **S**tructure **C**ode for **M**aterials **P**roperties and **P**rocesses:*

EStCoMPP was originally created by S. Blügel and K. Schroeder and developed further by B. Engels, P. Richard, D. Frielinghaus [Eng92b, Ric93, Eng92a, Ric96, Fri98] in the framework of their Masters-Thesis and PHD-Thesis. The EStCoMPP-program was parallelized by R. Berger [Ber01] and a new Projector-Augmented Wave Method (PAW-method), which can handle non-normconserving, ultra-soft pseudopotentials was developed by W. Kromen [Kro01]. In the following chapter a brief introduction into the iterative algorithms for calculating the total energy and the explicit form of the equations is presented.

4.1 Hellmann-Feynman Forces

In the EStCoMPP-program the total energy of the system and the forces on the ions are calculated. In the Born-Oppenheimer approximation the total electronic-energy of the system is explicitly parametric dependent on the coordinates of the ions $\{\tau_\mu\}$. Thus the forces on the ions can be calculated by the derivative of the energy-functional $E_{tot}[n(\mathbf{r}), \{\tau_\mu\}]$ (see below Eq.4.8) with respect to the coordinates of the atoms τ_μ , where μ numbers the ions. In the Born-Oppenheimer approximation the energy-functional consists of the ground-state electronic-energy $E_{el}[n(\mathbf{r}), \tau_\mu]$ and the Coulomb-interaction of the ions¹:

$$E_{ion}[\tau_\mu] = \frac{1}{2} \sum_{\mu'} \frac{Z_\mu Z_{\mu'}}{|\tau_\mu - \tau_{\mu'}|} \quad (4.1)$$

Thus, the forces are given by

$$F = -\partial_{\tau_\mu} E_{el}[n(\mathbf{r}), \tau_\mu] - \partial_{\tau_\mu} E_{ion}[\tau_\mu]. \quad (4.2)$$

¹For a periodic system the Ewald method has to be used to calculate the ion-ion interaction energy and the forces.

While the forces on the ions due to the Coulomb-interaction can easily be calculated analytically

$$F_{ion}(\tau_\mu) = -\frac{1}{2} \partial_{\tau_\mu} \sum_{\mu'} \frac{Z_\mu Z_{\mu'}}{|\tau_\mu - \tau_{\mu'}|}, \quad (4.3)$$

the forces due to the electronic ground-state energy are given by

$$F_{el}(\tau_\mu) = -\partial_{\tau_\mu} \langle \Psi(\tau_\mu) | H | \Psi(\tau_\mu) \rangle, \quad (4.4)$$

where H is the Hamilton-operator (Eq.1.25) of the electronic system. The calculation of this expression is complicated due to the implicit dependency of the wave-functions of the coordinates of the ions. In the Born-Oppenheimer approximation with normalized N -particle wave-functions, i.e. $H|\Psi\rangle = E_0|\Psi\rangle$ and $\langle\Psi|\Psi\rangle = 1$, the expression is reduced to the Hellman-Feynman force

$$\begin{aligned} F_{HF} &= -\partial_{\tau_\mu} \langle \Psi(\tau_\mu) | H | \Psi(\tau_\mu) \rangle \\ &= \langle \Psi(\tau_\mu) | -(\partial_{\tau_\mu} H) | \Psi(\tau_\mu) \rangle - E \partial_{\tau_\mu} \langle \Psi(\tau_\mu) | \Psi(\tau_\mu) \rangle \\ &= \langle \Psi(\tau_\mu) | -(\partial_{\tau_\mu} H) | \Psi(\tau_\mu) \rangle. \end{aligned} \quad (4.5)$$

In the density-functional theory the electronic energy is given by Eq.(1.20). Under the subsidiary condition of charge conservation this functional is minimal for the ground-state density $n(\mathbf{r})$. The functional derivative of the electronic energy-functional with respect to the density yields the chemical potential μ :

$$\mu = \frac{\partial E[n(\mathbf{r}), \tau_\mu]}{\partial n(\mathbf{r})} \quad (4.6)$$

Thus the force resulting from the electronic contribution to the total force is given by:

$$\begin{aligned} F_{el}(\tau_\mu) &= -\partial_{\tau_\mu} E_{el}[n(\mathbf{r}), \tau_\mu] - \int d^3\mathbf{r} \left(\frac{\partial E[n(\mathbf{r}), \tau_\mu]}{\partial n(\mathbf{r})} \right) \partial_{\tau_\mu} n(\mathbf{r}, \tau_\mu) \\ &= -\partial_{\tau_\mu} E_{el}[n(\mathbf{r}), \tau_\mu] - \mu \int d^3\mathbf{r} \partial_{\tau_\mu} n(\mathbf{r}, \tau_\mu) \\ &= -\partial_{\tau_\mu} E_{el}[n(\mathbf{r}), \tau_\mu] - \underbrace{\mu \partial_{\tau_\mu} N}_{=0} \end{aligned} \quad (4.7)$$

As a result the electronic contribution to the forces on the atoms are simply given by the partial derivative of the energy-functional with respect to the coordinates of the atoms

4.2 Minimization of the Energy Functional

As shown in the preceeding chapters, the total energy and thus all single contributions to the total energy are calculated in a periodic supercell. The energy-functional consist of the electronic energy (Eq.1.20) and the Ewald-energy $E_{Ew}[n]$, due to the Coulomb interaction of the ions. There are several contributions due to the Coulomb interaction, i.e. Hartree energy, local pseudopotential energy and ion-ion interaction, which diverge separately. But one can combine the contributions to non-divergent expressions by adding and subtracting appropriate compensating charges. When the energy scale is fixed in such a way that the average electronic potential of the system is set to zero, a constant contribution to the total energy, called $E_{loc}[n]$, has to be taken into account:

$$E_{tot}[n(\mathbf{r})] = E_{kin}[n] + E_{ext}[n] + E_H[n] + E_{xc}[n] + E_{Ew}[n] + E_{loc}[n] \quad (4.8)$$

The potential-energy consists of a local and a non-local part yielding local and non-local potential contributions to the single electron Hamiltonian in the Kohn-Sham equation (1.30). Depending on the functional form of the operators in the Hamiltonian, the matrix-vector products $H|\Psi\rangle$ are either solved in real-space or in \mathbf{k} -space. All contributions to the total energy are finally summed up in \mathbf{k} -space.

Iterative methods are used for solving the eigenvalue-problem and calculating the potentials (Fig.4.1). It is possible that states close to the Fermi-level are occupied in one iteration step and unoccupied in the following one. This leads to oscillations in the density $n(\mathbf{r})$ making the convergence questionable. Oscillations are damped by using a Fermi-distribution at a finite temperature T for the occupation-numbers $f_{\nu,\mathbf{k}}$:

$$f_{\nu,\mathbf{k}} = \frac{1}{\exp(\epsilon_{\nu,\mathbf{k}} - \epsilon_F)/k_B T + 1} \quad (4.9)$$

This ensures a smooth variation of the occupation numbers around the Fermi energy, but introduces a temperature dependent total energy, which can be interpreted as a free energy of the electron system

$$F = E - TS, \quad (4.10)$$

where the entropy-term is defined for independent electrons

$$S = -2k_B \sum_{\nu,\mathbf{k}} \omega_{\mathbf{k}} (f_{\nu,\mathbf{k}} \ln f_{\nu,\mathbf{k}} + (1 - f_{\nu,\mathbf{k}}) \ln(1 - f_{\nu,\mathbf{k}})) , \quad (4.11)$$

with the factor 2 from the spin-degeneracy. The free energy converges faster than the total energy at a given temperature T . For small temperature T the total energy E and the free energy F can be expressed by the ground state energy E_0

$$\begin{aligned} F &= E_0 - \gamma T^2, \\ E &= E_0 + \gamma T^2. \end{aligned} \quad (4.12)$$

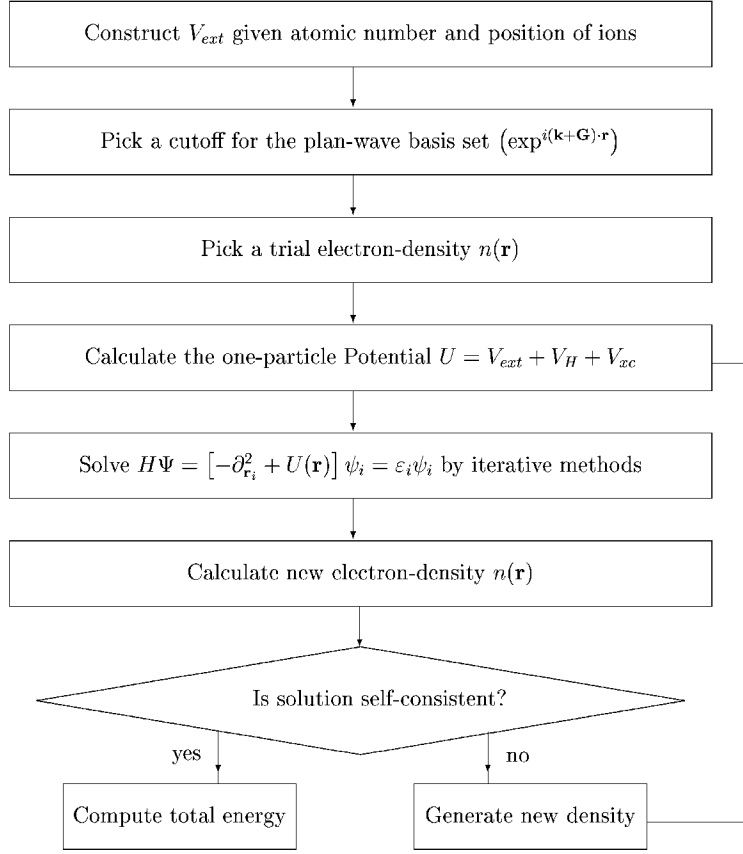


Figure 4.1: Flowchart of the iterative procedure for the calculation of the electronic energy.

An approximation to the ground-state energy at $T = 0$ can be obtained by

$$E_0 = \frac{1}{2} (E + F) . \quad (4.13)$$

1

Initially, the temperature has to be sufficiently large, so that the density and the free energy F smoothly converge. Finally the temperature can be decreased to avoid errors in the ground-state energy extrapolation. The temperature has to be adjusted to the bandgap. As a rule of thumb, a temperature of 1/20 of the bandgap is a good starting point.

4.3 Explicit Form of the Equations

The explicit form of the equations, as programmed in the ESTCoMPP-program are presented shortly in the following subsections. A more detailed description, also for the pseudopotentials and their generation, can be found in the

Masters-Thesis and PHD-Thesis of [Eng92b, Ric93, Eng92a, Ric96, Fri98]. A new Projector-Augmented Wave Method (PAW-method), which can handle non-normconserving, ultra-soft pseudopotentials, was developed by [Kro01].

4.3.1 The kinetic Energy

The kinetic-energy functional is diagonal in \mathbf{k} -space. The application of the Laplacian-operator to the wave-function yields

$$\begin{aligned} E_{kin}[n] &= \langle \Psi | -\partial_{\mathbf{r}}^2 | \Psi \rangle_{\Omega} \\ &= \sum_{\nu, \mathbf{k}} \omega_{\mathbf{k}} f_{\nu, \mathbf{k}} \langle \Psi_{\nu, \mathbf{k}} | -\partial_{\mathbf{r}}^2 | \Psi_{\nu, \mathbf{k}} \rangle_{\Omega} \\ &= \sum_{\nu, \mathbf{k}} \sum_{\mathbf{G}} \omega_{\mathbf{k}} f_{\nu, \mathbf{k}} |\mathbf{k} + \mathbf{G}|^2 u_{\nu, \mathbf{k}}^*(\mathbf{G}) u_{\nu, \mathbf{k}}(\mathbf{G}). \end{aligned} \quad (4.14)$$

The matrix-vector products reveals

$$\begin{aligned} \langle \mathbf{r} | E_{kin} | \Psi_{\nu, \mathbf{k}} \rangle_{\Omega} &= \frac{1}{\sqrt{\Omega}} \sum_{\mathbf{G}} |\mathbf{k} + \mathbf{G}|^2 u_{\nu, \mathbf{k}}(\mathbf{G}) e^{-i(\mathbf{k} + \mathbf{G})\mathbf{r}} \\ \langle \mathbf{k} + \mathbf{G} | E_{kin} | \Psi_{\nu, \mathbf{k}} \rangle_{\Omega} &= |\mathbf{k} + \mathbf{G}|^2 u_{\nu, \mathbf{k}}, \end{aligned} \quad (4.15)$$

and the matrix-elements are given as

$$\langle \mathbf{k}' + \mathbf{G}' | E_{kin} | \mathbf{k} + \mathbf{G} \rangle_{\Omega} = |\mathbf{k} + \mathbf{G}|^2 \delta_{\mathbf{k}, \mathbf{k}'} \delta_{\mathbf{G}, \mathbf{G}'}. \quad (4.16)$$

The operator of the kinetic energy is always applied in \mathbf{k} -space.

4.3.2 The local Energy

The local energy consists of the Hartree part, the exchange-correlation part and the local part of the pseudopotential. Although the local potential have simple expressions in \mathbf{k} -space, they are applied to the wave-function in real-space to avoid the calculation of convolution-equations. The transformation from real-space to reciprocal-space and vice versa is done by fast-fourier transformations (FFT's). The energy scale of the eigenvalue problem is chosen such that the sum of the average Hartree and local pseudopotential is set to zero. The contribution to the total energy of the average potentials is considered separately (see chapter 4.2 and 4.3.5).

The Hartree-potential is determined by Poissons's-equation:

$$\partial_{\mathbf{r}}^2 V_H(\mathbf{r}) = -8\pi n(\mathbf{r}) \quad (4.17)$$

Fourier transformation yields

$$\begin{aligned} V_H(\mathbf{G}) &= \frac{1}{\Omega} \int_{\Omega} d^3\mathbf{r} V_H(\mathbf{r}) e^{i\mathbf{G}\mathbf{r}} \\ &= \frac{1}{\Omega} \frac{8\pi}{\mathbf{G}^2} n(\mathbf{G}). \end{aligned} \quad (4.18)$$

Obviously the Laplacian-operator is diagonal in \mathbf{k} -space. Thus the Hartree-potential is calculated in reciprocal space. The matrix-vector products are given by

$$\langle \mathbf{r} | V_H | \Psi_{\nu, \mathbf{k}} \rangle_{\Omega} = \frac{1}{\sqrt{\Omega}} \sum_{\mathbf{G}} \left(\sum_{\mathbf{G}'} V_H(\mathbf{G}') u_{\nu, \mathbf{k}}(\mathbf{G} - \mathbf{G}') \right) e^{-i(\mathbf{k} + \mathbf{G})\mathbf{r}}, \quad (4.19)$$

with the matrix-elements

$$\langle \mathbf{k}' + \mathbf{G}' | V_H | \mathbf{k} + \mathbf{G} \rangle_{\Omega} = \sum_{\mathbf{G}'} V_H(\mathbf{G}'). \quad (4.20)$$

To avoid the convolution in Eq.(4.19) the Hartree potential is applied in real space.

The exchange-correlation energy in the local density approximation is defined as

$$E_{xc}^{LDA}[n(\mathbf{r})] = \int d^3\mathbf{r} \varepsilon_{xc}^{LDA}(\mathbf{r}) n(\mathbf{r}). \quad (4.21)$$

The matrix-vector products are calculated in real-space as

$$\langle \mathbf{r} | V_{xc} | \Psi_{\nu, \mathbf{k}} \rangle_{\Omega} = V_{xc}(n(\mathbf{r})) \Psi_{\nu, \mathbf{k}}(\mathbf{r}). \quad (4.22)$$

The local part pseudopotential consists of the spherical-symmetric contributions of the atoms at the position $\mathbf{R} + \tau_{\mu}$. Thus the local pseudopotential is given by

$$V_{loc}(\mathbf{r}) = \sum_{\mu} V_{loc}^{\alpha(\mu)}(\mathbf{R} + \tau_{\mu}). \quad (4.23)$$

Here we have used the fact that all chemically identical atoms (of kind α) contribute the same pseudopotential $V_{loc}^{\alpha(\mu)}$. With the Fourier transformation

$$V_{loc}(\mathbf{r}) = \sum_{\mu, \mathbf{G}} S_{\tau_{\mu}}(\mathbf{G}) V_{loc}^{\alpha(\mu)}(\mathbf{G}) e^{-i\mathbf{G}\mathbf{r}}, \quad (4.24)$$

this transforms to

$$V_{loc}(\mathbf{G}) = \sum_{\mu} S_{\tau_{\mu}}(\mathbf{G}) V_{loc}^{\alpha(\mu)}(\mathbf{G}), \quad (4.25)$$

where

$$V_{loc}^{\alpha(\mu)}(\mathbf{G}) = \frac{1}{\Omega} \int_{\infty} d^3\mathbf{r} V_{loc}^{\alpha(\mu)}(\mathbf{r}) e^{-i\mathbf{G}\mathbf{r}}, \quad (4.26)$$

and the structure-factors are

$$S_{\tau_\mu}(\mathbf{G}) = e^{-i\mathbf{G}\tau_\mu}. \quad (4.27)$$

The expressions for the matrix-vector products are

$$\begin{aligned} \langle \mathbf{r} | V_{loc} | \Psi_{\nu, \mathbf{k}} \rangle_\Omega &= \sum_{\mathbf{G}, \mathbf{G}'} \sum_{\mu} \frac{1}{\Omega} S_{\tau_\mu}(\mathbf{G}') V_{loc}^{\alpha(\mu)}(\mathbf{G}) \\ &\quad \times u_{\nu, \mathbf{k}}(\mathbf{G} - \mathbf{G}') e^{-i(\mathbf{k} + \mathbf{G})\mathbf{r}}, \end{aligned} \quad (4.28)$$

$$\langle \mathbf{k} + \mathbf{G} | V_{loc} | \Psi_{\nu, \mathbf{k}} \rangle_\Omega = \sum_{\mathbf{G}'} V_{loc}(\mathbf{G}') u_{\nu, \mathbf{k}}(\mathbf{G} - \mathbf{G}'). \quad (4.29)$$

Again the convolution in Eq.(4.29 is avoided by applying V_{loc} in real space. The integration in Eq.(4.26) is numerically impossible if the local pseudopotential is transformed to \mathbf{k} -space. This is due the Coulomb interaction, which leads to a long-ranged part $\sim -2Z/r$ of the local pseudopotentials. Thus the long-range part is removed and solved analytically. The one-dimensional numerical integration of the rest can easily be done.

4.3.3 The non-local part of the Energy

The non-local part of the pseudopotential consists of the l -dependent contributions $\sum_k \Delta V_{loc}^{\alpha(\mu)}(\mathbf{r}) \hat{P}_l$ of the atoms μ of kind α at the position $\mathbf{R}^n + \tau_\mu$. For the Kleinman-Bylander pseudopotentials (see chapter 2.3) the non-local parts are expressed as follows

$$\begin{aligned} V_{KB} &= \sum_{\mathbf{R}} \sum_{\mu} \sum_{l=0}^{l_{max}} \sum_{m=-l}^{+l} E_{KB}^{l, \alpha(\mu)} T_{\mathbf{R} + \tau_\mu} |t_{l, m, \alpha(\mu)}\rangle \langle t_{l, m, \alpha(\mu)}| \\ &= \sum_{\mu} \sum_{l=0}^{l_{max}} \sum_{m=-l}^{+l} E_{KB}^{l, \alpha(\mu)} T_{\tau_\mu} |t_{l, m, \alpha(\mu)}\rangle \langle t_{l, m, \alpha(\mu)}|, \end{aligned} \quad (4.30)$$

where T_{τ_μ} is the translation-operator, which shifts the non-local part of the pseudopotential to the position τ_μ of the ions. For the matrix-vector products the following expressions are derived

$$\begin{aligned} \langle \mathbf{r} | V_{KB} | \Psi_{\nu, \mathbf{k}} \rangle_\Omega &= \sum_{\mu} \sum_{l=0}^{l_{max}} \sum_{m=-l}^{+l} \left(\sum_{\mathbf{G}'} T_{l, m, \mu}^*(\mathbf{k}, \mathbf{G}') u_{\nu, \mathbf{k}}(\mathbf{G}') \right) E_{KB}^{l, \alpha(\mu)} \\ &\quad \times \frac{1}{\Omega} \sum_{\mathbf{G}} T_{l, m, \mu}(\mathbf{k}, \mathbf{G}) e^{-i(\mathbf{k} + \mathbf{G})\mathbf{r}}, \end{aligned} \quad (4.31)$$

$$\begin{aligned}
\langle \mathbf{k} + \mathbf{G} | V_{KB} | \Psi_{\nu, \mathbf{k}} \rangle_{\Omega} &= \sum_{\mu} \sum_{l=0}^{l_{max}} \sum_{m=-l}^{+l} T_{l, m, \mu}(\mathbf{k}, \mathbf{G}) E_{KB}^{l, \alpha(\mu)} \\
&\times \left(\sum_{\mathbf{G}'} T_{l, m, \mu}^*(\mathbf{k}, \mathbf{G}') u_{\nu, \mathbf{k}}(\mathbf{G}') \right), \quad (4.32)
\end{aligned}$$

with

$$T_{l, m, \mu}(\mathbf{k}, \mathbf{G}) = S_{\tau_{\mu}}(\mathbf{G}) Y_{lm}(\theta_{\mathbf{k}+\mathbf{G}}, \varphi_{\mathbf{k}+\mathbf{G}}) t_{l, \alpha(\mu)}(|\mathbf{k} + \mathbf{G}|), \quad (4.33)$$

and

$$t_{l, \alpha(\mu)}(|\mathbf{k} + \mathbf{G}|) = \frac{4\pi}{\sqrt{\Omega}} \int_{\infty}^0 dr r t_{l, \alpha(\mu)}(r) j_l(|\mathbf{k} + \mathbf{G}|r). \quad (4.34)$$

Due to the dyadic structure of the KB non-local pseudopotentials (see Eq.4.32) the evaluation of expectation values in reciprocal space is favorable.

4.3.4 The Ewald-energy

The Coulomb-interaction of the ions μ of kind α at the positions $\mathbf{R}^n + \tau_{\mu}$ is described by the Ewald-energy E_{Ew} . It can be expressed in real or reciprocal space

$$\begin{aligned}
E_{Ew} &= \frac{1}{2} \sum_{\mathbf{R}^n} \sum_{\mu, \mu'} \frac{Z_{\mu} Z_{\mu'}}{|\tau_{\mu} - (\mathbf{R}^n + \tau_{\mu'})|} \left(1 - \delta_{\tau_{\mu}, \mathbf{R}^n + \tau_{\mu'}} \right) \\
&= \frac{1}{2} \sum_{\mathbf{G} \neq 0} \sum_{\mu, \mu'} Z_{\mu} Z_{\mu'} \frac{1}{\Omega} \frac{4\pi}{\mathbf{G}^2} e^{-i\mathbf{G}(\tau_{\mu} - \tau_{\mu'})}. \quad (4.35)
\end{aligned}$$

A faster convergence of the sums is achieved by applying the Ewald summation formula [Ewa21] yielding a splitting of the sums with contributions from real *and* reciprocal space which include damping factors.

The separately divergent terms for the ($|\mathbf{G}| = 0$) components of the Hartree-energy, the local pseudopotential and the Ewald-energy compensate each other. Since we use an energy scale for the eigenvalue problem where the sum of the average Hartree and local pseudopotential is set to zero we have to consider a constant term [IZC79, Ric96] to the total energy

$$E_{loc}^{const} = \frac{N^v}{\Omega} \sum_{\mu} \int_{\infty}^0 d^3 \mathbf{r} \left(V_{loc}^{\alpha(\mu)}(r) + \frac{2N_{\alpha(\mu)}^v(r)}{r} \right), \quad (4.36)$$

where

$$N^v = \int_{\Omega} d^3 \mathbf{r} n(\mathbf{r}) = n(\mathbf{G})|_{\mathbf{G}=0}. \quad (4.37)$$

4.4 Loop-Structures and Algorithms

In the last chapters the theoretical aspects of the density functional theory and the pseudopotential method were discussed, and in the preceeding sections the explicit form of the equations were introduced. A real calculation of the atomic and electronic structure consists of three parts:

- The calculation of the electronic structure
- The calculation of the forces exerted on the ions
- The relaxation of the ions to the equilibrium positions

In the **EStCoMPP**-program this is done in four encapsulated loops as is shown in Fig.4.2: The iterative procedures will be discussed in more detail in the following.

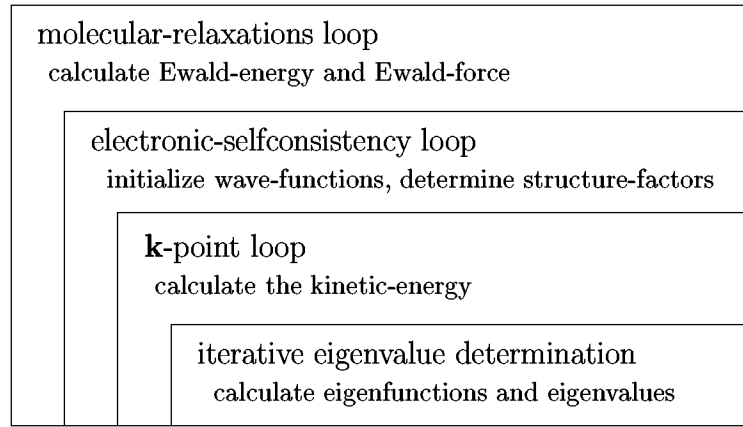


Figure 4.2: Schematic loop-structure of the **EStCoMPP**-program

4.4.1 Iterative Eigenvalue Determination

The large number of basis-functions per atom leads to large eigenvalue problems. For a calculation typical for this PhD-Thesis with 200 atoms per unit cell and 150 basis-functions per atom the Hamilton-matrix has a dimension of 30000×30000 . Because of this large dimension and the fact that only the lowest 2-10% of the eigenvalues ε_i and eigenvectors have to be determined, iterative diagonalization methods are favorable. The iterative procedure consists of four steps:

- guess the starting-vectors $|\psi_i\rangle^{(0)}$
- calculate the matrix-vector products $|H\psi_i\rangle^{(j)} = H|\psi_i\rangle^{(j)}$
- construct the correction-vectors $|\psi_i^{corr}\rangle^{(j)}$

- calculate the new starting-vectors $|\psi_i\rangle^{(j+1)}$

Thus the iteration consists of the construction of correction-vectors and the combination of the starting-vectors and correction-vectors to new, better vectors.

With the definition of the Rayleigh-quotient

$$\rho[\psi] = \frac{\langle \psi | H | \psi \rangle}{\langle \psi | \psi \rangle}, \quad (4.38)$$

which is stationary for the eigenvectors $|\psi_{i0}\rangle$, the eigenvalue-problem can be formulated as an optimization problem. The gradient of the Rayleigh-quotient, which gives the direction of the steepest descent, is defined by:

$$\left| \frac{\delta \rho[\psi]}{\delta \psi} \right\rangle = \frac{2|R[\psi]\rangle}{\langle \psi | \psi \rangle} \quad (4.39)$$

The direction of the gradient is determined by the residuum $|R[\psi]\rangle$ and the norm of the residuum $||R[\psi]||$ is a direct measure for the quality of the approximated eigenvalues and eigenvectors [Ric93]. Thus if the norm of the residuum is lower then a predefined criteria, the eigenvectors are considered to be converged.

To find the minima of the optimization problem, one can follow the negative gradient by a steepest-descent-algorithm. For small steps this procedure is stable but in general extremely slow. This is due to the bad convergence of this method for anisotropic minima. The steepest-descent-algorithm can be used efficiently if the anisotropic minima are mapped on isotropic minima before. This can be done by a pre-conditioning: With the eigenvalue-equation

$$|R[\psi_{i0}]\rangle = (H - \varepsilon_{i0})|\delta\psi\rangle, \quad (4.40)$$

the residuum can be linearized in the vicinity of the eigenvectors $|\psi_{i0}\rangle$ and the eigenvalues ε_{i0} :

$$|R[\psi]\rangle = |R[\psi_{i0} + \delta\psi]\rangle = (H - \varepsilon_{i0})|\delta\psi\rangle + O((\delta\psi)^2) \quad (4.41)$$

For the construction of the correction-vector $|\delta\psi\rangle$ this equation is multiplied with the pre-conditioner, which is an approximation of the matrix $(H - \rho[\psi])^{-1}$.

The Hamiltonian is diagonal dominant in reciprocal space because the diagonal elements of the Hamiltonian are increasing quadratically $\sim (\mathbf{k} + \mathbf{G})^2$ due to the kinetic energy and the fast convergence of local pseudopotentials in \mathbf{k} -space. Thus the inverted diagonal of the matrix $(H - \rho[\psi])$ can be used as the pre-conditioner. The correction-vector in reciprocal space then has the form:

$$c_\nu^{corr}(\mathbf{G}) = - \sum_{\mathbf{G}'} \frac{(\rho[\psi_\nu] \delta_{\mathbf{G}, \mathbf{G}'} - H_{\mathbf{G}, \mathbf{G}'})}{(\rho[\psi_\nu] - H_{\mathbf{G}, \mathbf{G}'})} c_\nu(\mathbf{G}) \quad (4.42)$$

The index \mathbf{k} is omitted since the eigenvalue-problem is solved for each \mathbf{k} -point separately.

Once the correction-vectors are constructed, the new and improved eigenvectors have to be determined. In the Car-Parrinello method [CP85] the new eigenvectors are constructed by adding the correction-vector with a weight (the step-length) to the starting-vector:

$$|\psi_\nu\rangle^{(j+1)} = |\psi_\nu\rangle^{(j)} + \alpha |\psi_\nu^{corr}\rangle^{(j)} \quad (4.43)$$

For small step-length α this method converges very slow while for large α the method diverges. Improvements have been implemented in the spirit of the conjugate gradient method [Ric93].

A different procedure is to diagonalize the Hamiltonian in a sub-space, which contains the starting-vectors as well as the correction-vectors. This can be done with the Rayleigh-Ritz method, where an orthonormalized basis is constructed out of the starting- and correction-vectors with the Gram-Schmidt algorithm. The Hamilton-matrix is then calculated and diagonalized in this orthonormalized basis

The implemented method [Ric93] is based on the Davidson-algorithm [Dav75] which was developed for the calculation of a single eigenvalue and eigenvector. Beginning with a starting-vector, the Davidson-algorithm adds successively one correction-vector in each iteration, and diagonalizes the matrix in the according sub-space, spanned by the starting- and correction-vectors. The eigenvalue problem is solved at the latest, if the complete space is spanned after $N_{\mathbf{G}} - 1$ iterations, but in general the eigenvalue-problem converges much faster.

If more than one eigenvector has to be calculated it is more efficient to use block-algorithms instead of applying the Davidson-algorithm for each eigenvector separately. The generalization of the Davidson-algorithm to a Block-Davidson-algorithm was done by Liu [Liu78]. Instead of one, in the Davidson-algorithm, N_{state} starting-vectors (one for each eigenvector) are needed. A correction-vector for each eigenvector is calculated in each iteration and added to the sub-space. Thus the dimension of the sub-space is in each iteration increased by N_{state} , which leads to memory problems for large matrices.

To avoid this memory problems Kosugi extended the Block-Davidson-algorithm to the Davidson-Kosugi-algorithm, where the dimension of the sub-space N_{sub} is kept fixed. Thus at the beginning one has to choose the dimension of the sub-space. Larger N_{sub} requires larger memory but leads to faster convergence and vice versa. In the **ES**t**Co**MPP-program sub-space dimensions of $2 \times N_{state}$ to $3 \times N_{state}$ turned out to be a good compromise. When the algorithm starts for the first time, the N_{sub} dimensional sub-space is filled with unit-vectors besides the "guessed" N_{state} starting-vectors. The Cartesian unit-vectors are the successively replaced by correction-vectors in each iteration. If all unit-vectors are replaced, the oldest correction-vectors will be replaced instead until the eigenvalue problem is converged.

4.4.2 Electronic-Selfconsistency and Molecular-Relaxation Loops

Within the Born-Oppenheimer approximation the degrees of freedom in the energy-functional can be divided in two classes:

- The electronic degrees of freedom, i.e. the density $n(\mathbf{r})$, resp. the effective potential $V_{eff}[n(\mathbf{r})]$.
- The ionic degrees of freedom, i.e. the positions of the ions τ_μ .

The minimization of the energy-functional can be formulated such that the same algorithms can be used for both classes:

(i) The energy-functional is minimized with respect to the electronic degrees of freedom (and fixed ion-positions) by a selfconsistent calculation, which results in the ground-state density $n_0(\mathbf{r})$ resp. the ground-state potential $V[n_0(\mathbf{r})]$ and the electronic ground state energy $E_0[n_0|\tau]$ for fixed ion positions. Thus starting with a density $n^{(i)}(\mathbf{r})$ resp. a potential $V[n^{(i)}(\mathbf{r})]$ the Kohn-Sham equations are formulated. The new density and potential is determined by solving the Kohn-Sham equations. In general the new density and potential for the next iteration step can be written as $n^{(i+1)}(\mathbf{r}) = F\{n^{(i)}(\mathbf{r})\}$ and $V[n^{(i+1)}(\mathbf{r})] = F'\{V[n^{(i)}(\mathbf{r})]\}$. Thus at the fix-points of $F\{n(\mathbf{r})\}$ and $F'\{V[n(\mathbf{r})]\}$ the energy-functional will be minimized. The fix-points can be formulated zero-points of the modified functionals \hat{F} and \hat{F}' :

$$\begin{aligned}\hat{F}\{n_0\} &= F\{n_0\} - n_0 &= 0 \\ \hat{F}\{V[n_0]\} &= F'\{V[n_0]\} - V[n_0] &= 0\end{aligned}\tag{4.44}$$

(ii) For the molecular-relaxation the energy-functional has to be minimized with respect to the atomic coordinates. Since the electrons are at the Born-Oppenheimer surface, the energy-functional is minimized if:

$$\begin{aligned}\hat{\mathbf{F}}\{\tau\} &= -\frac{d}{d\tau'}E_0[\tau]|_\tau - \frac{dE_{Ew}[\tau]}{d\tau'} \\ \hat{\mathbf{F}}\{\tau_0\} &= 0.\end{aligned}\tag{4.45}$$

The derivative of the electronic energy-functional with respect to the atomic coordinates is given by the Hellmann-Feynman forces.

In the **ES**tCoMPP-program the density resp. the potential is defined on a grid of the dimension $N_{\mathbf{G}}$. Thus the equations 4.44 define a non-linear algebraic system of dimension $N_{\mathbf{G}}$, where the nodes have to be determined. For the determination of the relaxed ion positions the equations 4.45 also define a non-linear algebraic

system of dimension N_τ , where N_τ is the number of the ionic degrees of freedom, i.e. for full relaxation of all atoms: $N_{atoms} \times 3$.

Thus the calculation of the electronic ground-state and the atomic equilibrium positions belong to the same class of problems. In the following the functionals and the fix-points for both classes will be written as $F(x), x_0$ and the dimension as N_x . Thus the non-linear equations look like:

$$F(x) = f(x) - x \quad (4.46)$$

$$F(x_0) = f(x_0) - x_0 = 0 \quad (4.47)$$

In the **EStCoMPP**-program both problems are solved with the iterative Quasi-Newton method. For a better understanding the Newton-Raphson method is described first.

The Newton-Raphson Method

The Taylor-series of a potential $E(\mathbf{x})$ around a position $\mathbf{x}^{(m)}$ close to the minimum is given by:

$$E(\mathbf{x}) = E(\mathbf{x}^{(m)}) - \langle \mathbf{f}^{(m)} | \mathbf{x} - \mathbf{x}^{(m)} \rangle + \frac{1}{2} \langle \mathbf{x} - \mathbf{x}^{(m)} | H | \mathbf{x} - \mathbf{x}^{(m)} \rangle + \dots \quad (4.48)$$

with the "driving force"

$$\mathbf{f}^{(m)} = - \left. \frac{\partial E}{\partial \mathbf{x}} \right|_{\mathbf{x}^{(m)}}. \quad (4.49)$$

The "Hesse"-matrix is defined as the second derivative of the Potential with respect to the coordinates:

$$H^{(m)} = \left. \frac{\partial^2 E}{\partial^2 \mathbf{x}} \right|_{\mathbf{x}^{(m)}} = - \left. \frac{\partial \mathbf{f}}{\partial \mathbf{x}} \right|_{\mathbf{x}^{(m)}}. \quad (4.50)$$

Using only the first two terms of the Taylor-series the derivative of the potential with respect to the coordinates is given by:

$$\left| \frac{\partial E}{\partial \mathbf{x}} \right\rangle = -|\mathbf{f}^{(m)}\rangle + H^{(m)}|\mathbf{x} - \mathbf{x}^{(m)}\rangle \quad (4.51)$$

At the extremal (minimum) position \mathbf{x}_0 , the derivative vanishes

$$\left| \frac{\partial E}{\partial \mathbf{x}}(\mathbf{x}_0) \right\rangle = -|\mathbf{f}^{(m)}\rangle + H^{(m)}|\mathbf{x}_0 - \mathbf{x}^{(m)}\rangle = 0, \quad (4.52)$$

and thus $|\mathbf{x}_0\rangle$ is given by:

$$|\mathbf{x}_0\rangle = |\mathbf{x}^{(m)}\rangle + (H^{(m)})^{-1} |\mathbf{f}^{(m)}\rangle \quad (4.53)$$

This is exact if the truncated Taylor expansion-series is exact, i.e. the potential has a quadratic form. For non-quadratic potentials the last equation can be interpreted as an iteration scheme:

$$|\mathbf{x}^{[m+1]}\rangle = |\mathbf{x}^{(m)}\rangle + (H^{(m)})^{-1} |\mathbf{f}^{(m)}\rangle. \quad (4.54)$$

The convergence is reached if

$$||\mathbf{x}^{[m+1]} - \mathbf{x}^{[m]}|| < \delta, \quad (4.55)$$

where δ is the convergence-criteria.

The Quasi-Newton Method

Instead of calculating the "Hesse"-matrix $H^{(m)}$ from the selfconsistent equation F, and invert $H^{(m)}$ in each iteration, $(H^{(m)})$ can be approximated by a sum over dyadic products $|u_i\rangle$ and $\langle v_i|$ and improved iteratively. There are several possibilities to implement the iteration, which are discussed in [Blü88] and all are implemented in the **ES**t**Co**MPP-code. As example "Broyden's first method" is sketched where the inverse of the "Hesse"-matrix is iterated.

The inverse of the "Hesse"-matrix for the iteration m can be written as

$$(H^{(m)})^{-1} = \alpha \mathbf{1} - \sum_{i=2}^{m-1} |u_i\rangle \langle v_i|, \quad (4.56)$$

with a mixing parameter α . Thus the inverse of the "Hesse"-matrix of the next step is defined by:

$$(H^{(m+1)})^{-1} = (H^{(m)})^{-1} + |u_m\rangle \langle v_m|, \quad (4.57)$$

with

$$(H^{(1)})^{-1} = \alpha \mathbf{1}. \quad (4.58)$$

The vectors of the dyadic product are defined by

$$|u^m\rangle = |\Delta x^m\rangle + (H^{(m)})^{-1} |\Delta f^{(m)}\rangle, \quad (4.59)$$

and

$$\langle v^m| = \frac{1}{||\Delta f^{(m)}||^2} \cdot |\Delta f^{(m)}\rangle, \quad (4.60)$$

where

$$\Delta f^{(m)} = f^{(m)} - f^{(m-1)} = x^{(m)} - x^{(m-2)} \quad (4.61)$$

$$\Delta x^{(m)} = x^{(m)} - x^{(m-1)}. \quad (4.62)$$

Thus the actual inverse of the "Hesse"-matrix can be written in dependence of $(H^{(m)})^{-1}$ in the last iteration step as:

$$\begin{aligned} (H^{(m)})^{-1} &= (H^{(m-1)})^{-1} + [|\Delta x^{(m-1)}\rangle \\ &\quad + (H^{(m-1)})^{-1} |\Delta f^{(m-1)}\rangle] \frac{\langle \Delta f^{(m-1)} |}{\|\Delta f^{(m)}\|^2} \end{aligned} \quad (4.63)$$

If \mathbf{x} are the coordinates of the atoms and \mathbf{f} are the forces then the structural relaxation can be done with the above described Quasi-Newton method. If \mathbf{x} is replaced by the density $n(\mathbf{r})$, $\mathbf{f} = n^{(i+1)} - n^i$ and the "Hesse"-matrix is replaced by the "Jacobian"-matrix $J(n) = -\frac{\partial \mathbf{f}(n)}{\partial n} = -H$, then the Quasi-Newton method is used to minimize the electronic degrees of freedom.

Chapter 5

The EStCoMPP-Visualization Tool

To be able to treat the necessary large supercells containing up to 300 atoms a powerful, parallel version of the **EStCoMPP**-program has been developed by R. Berger [Ber01] which runs on a Cray-T3E parallel-computer. The main topic of ab-initio calculations in our group are the investigation of structural and electronic properties and growth processes on surfaces. Thus, a lot of information is produced by the **EStCoMPP**-program which has to be visualized for a better understanding. For example, the positions of the atoms after relaxation, and the distribution of the electron-density or of wave-functions in space relatively to the atomic positions are of great interest. Existing programs do not have the capabilities to work with three-dimensional data (gnuplot, GLI, etc.) or the data preparation and the handling of the programs is very complicated (BALSAC, AVS, etc).

The **EStCoMPP-Visualization Tool** (**EStCoMPP-VT**) was developed to extract the important information easily from the output generated by the **EStCoMPP**-program and display three-dimensional plots. The capabilities of the program are

- Creating three dimensional plots of
 - atoms
 - atoms with bonds
 - numbered atoms (with bonds)
 - 3D iso-surface of the electron density or of wave-functions (with atoms, bonds)
 - 2D contour-lines electron density (with atoms, bonds)
- Free rotation around all axis and free positioning of the system in real-time
- Free scaling and the choice between parallel or perspective projection
- Producing high quality postscript output

- Runs on any Unix/Linux-system with at least 256 colors.

In principle the program is not limited to draw electron-densities but all data which are stored on a grid relatively to the axis of the coordinate system.

The start-screen is shown in Fig.5.1: In the following a short explanation of

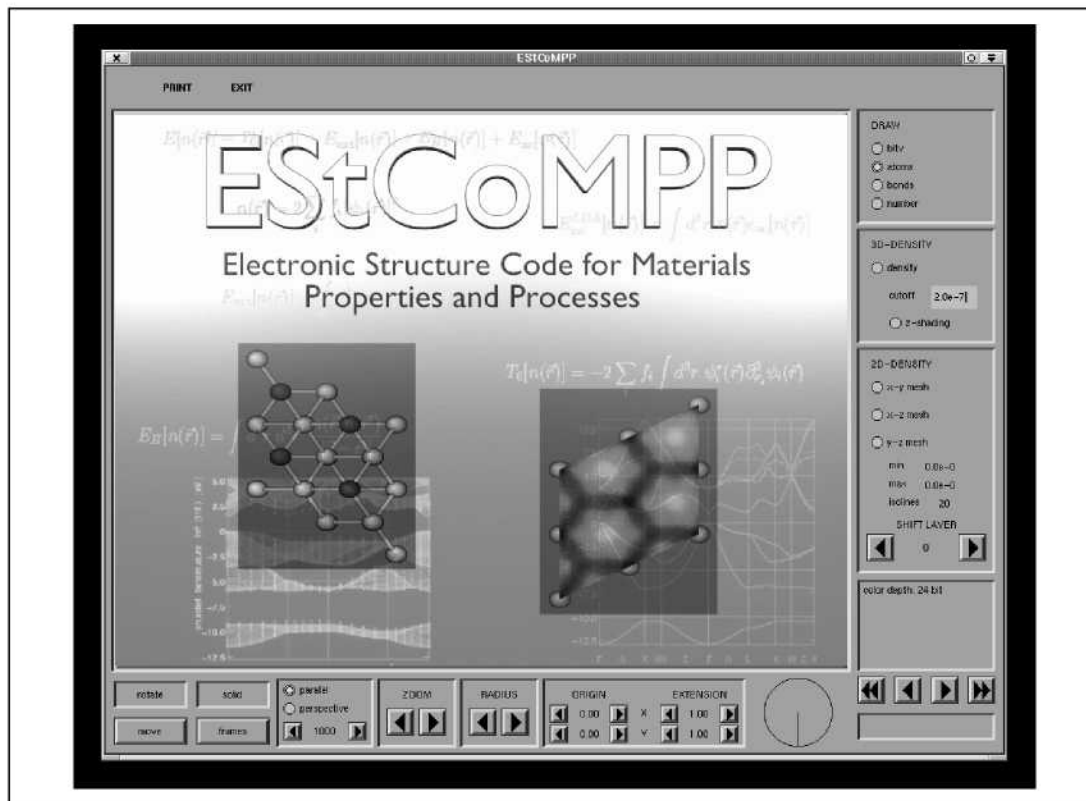


Figure 5.1: Starting screen of the EStCoMPP-VT.

the buttons will be given, starting at the upper left corner and proceeding to the right. On top are the **PRINT**-button for generating postscript files of the actual graphics on screen and the **EXIT**-button to leave the program.

With the first group of buttons on the upper right side the drawing of the bravais lattice vectors **bltv**, the **atoms**, the **bonds**, or the **numbers** can be switched on or off. As default only the atoms are drawn.

In the next group, below the **DRAWING**-buttons, the **3D-density** can be switched on or off. A cutoff-value for the iso-surface of the electron density can entered in the field below. Instead of the three-dimensional shading of the iso-surface the **z-shading** can be switched on which converts the information about the height of the iso-surface into a greyscale, e.g. for generating STM-images.

The next group below handles the two dimensional contour-plots of the electron densities. One can choose between the **x-y**, **x-z** and **y-z** planes, according to the given coordinate system. The minimum and maximum value of the density

which should be considered, and how many equidistant contour lines should be drawn can be entered in the fields below. Since only one layer of density is cut out of a three dimensional data-set, the layer can be shifted along the third axis by the **SHIFTLAYER**-buttons.

In the text-window below information the computer activity is displayed.

If, for example, a diffusion path was calculated, all positions of the atoms on this path can be included in one file. With the four buttons below the text window one can move through these positions on the path back and forth with the two innermost buttons or go directly to the initial or final position with the outermost buttons. The density, which is stored in a separate file, can only be displayed for one of the configuration. The last window in the right column is a small status-window which indicates the reading of files.

The circular window to the left is a kind of clock indicating the computer activity for long lasting procedures, e.g. the calculation of 3-dimensional iso-surfaces.

Further to the left are buttons for changing the **origin** and **extension** of the displayed cell. Since in our ab-initio calculations all atoms are defined in supercells, the origin of this supercell can be shifted laterally and the supercell can be continued periodically in space along the lateral axes to find the best overall view of specific sections.

Further to the left are buttons for changing the **RADIUS** of the atoms and accordingly the width of the bonds, and to **ZOOM** in and out of the displayed system.

A choice between a parallel or a perspective view can be made in the next window to the left. In the numerical input field the distance of the camera to the scene can be defined, which is only meaningful in perspective view.

If the scene is rotated or shifted the program automatically switches to the **frames** mode to ensure that all operations can be performed in real-time. **frames** mode means that all atoms are only drawn as circles and the bonds are not filled. To go back to the shaded view, one has to press the **solid** button.

Rotation and shifting is done with the mouse. Moving the mouse with the left mouse button pressed rotates the system around the two axes parallel to the screen. Moving the mouse with the right mouse button pressed rotates the system around the axis perpendicular to the screen. The middle mouse button can be used to shift the position of the scene. This only works if the **rotate** button is activated, which is the default. For owner of two-button mice one can shift around with the left mouse button by activating the **move** button in the window first. A few examples how the **EStCoMPP-VT** screen looks and what kind of output is generated if the **PRINT** button is pressed is shown below.

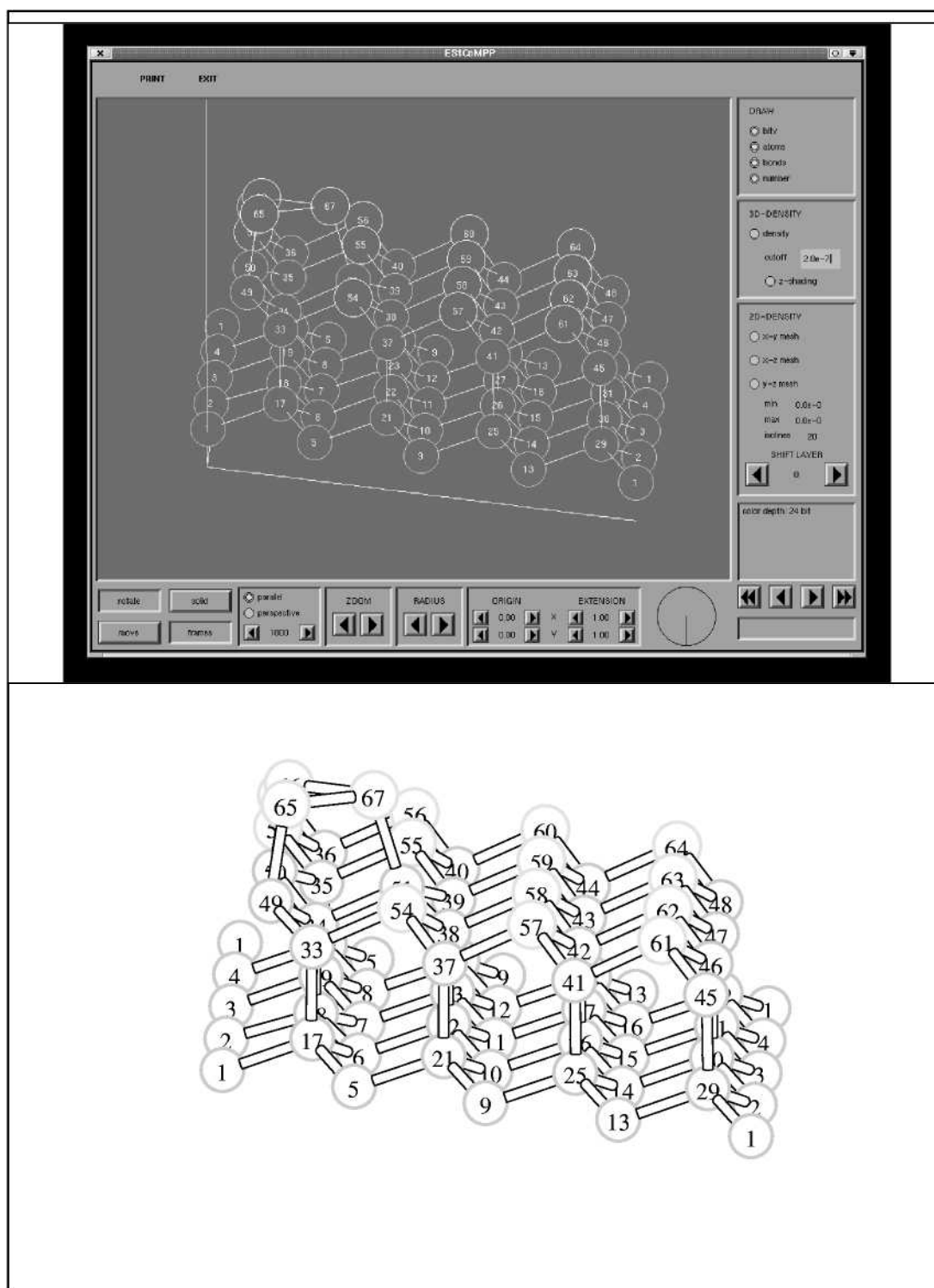


Figure 5.2: Atoms and bonds in **frames**-mode and the generated postscript output.

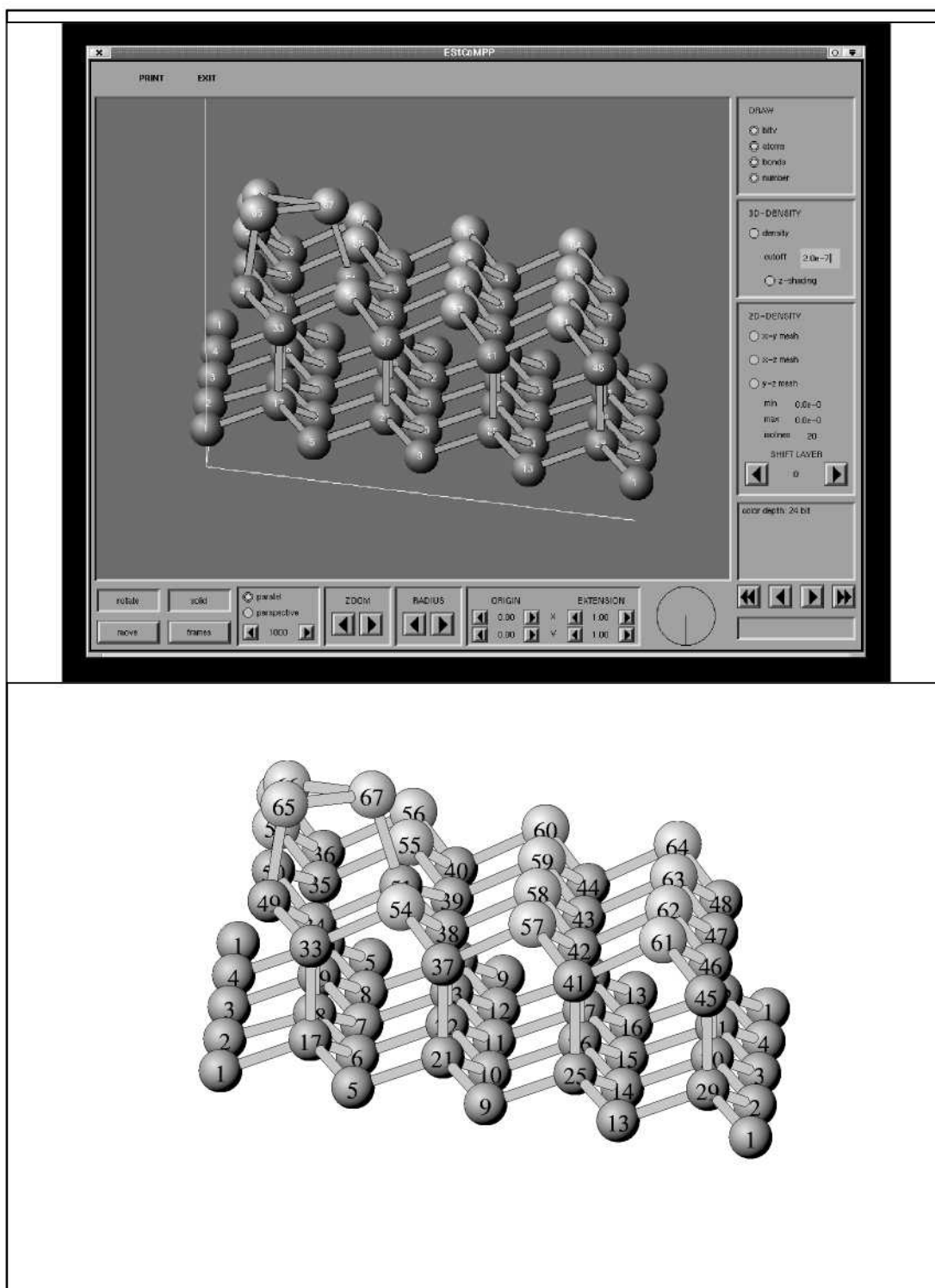


Figure 5.3: Atoms and bonds in solid-mode and the generated postscript output.

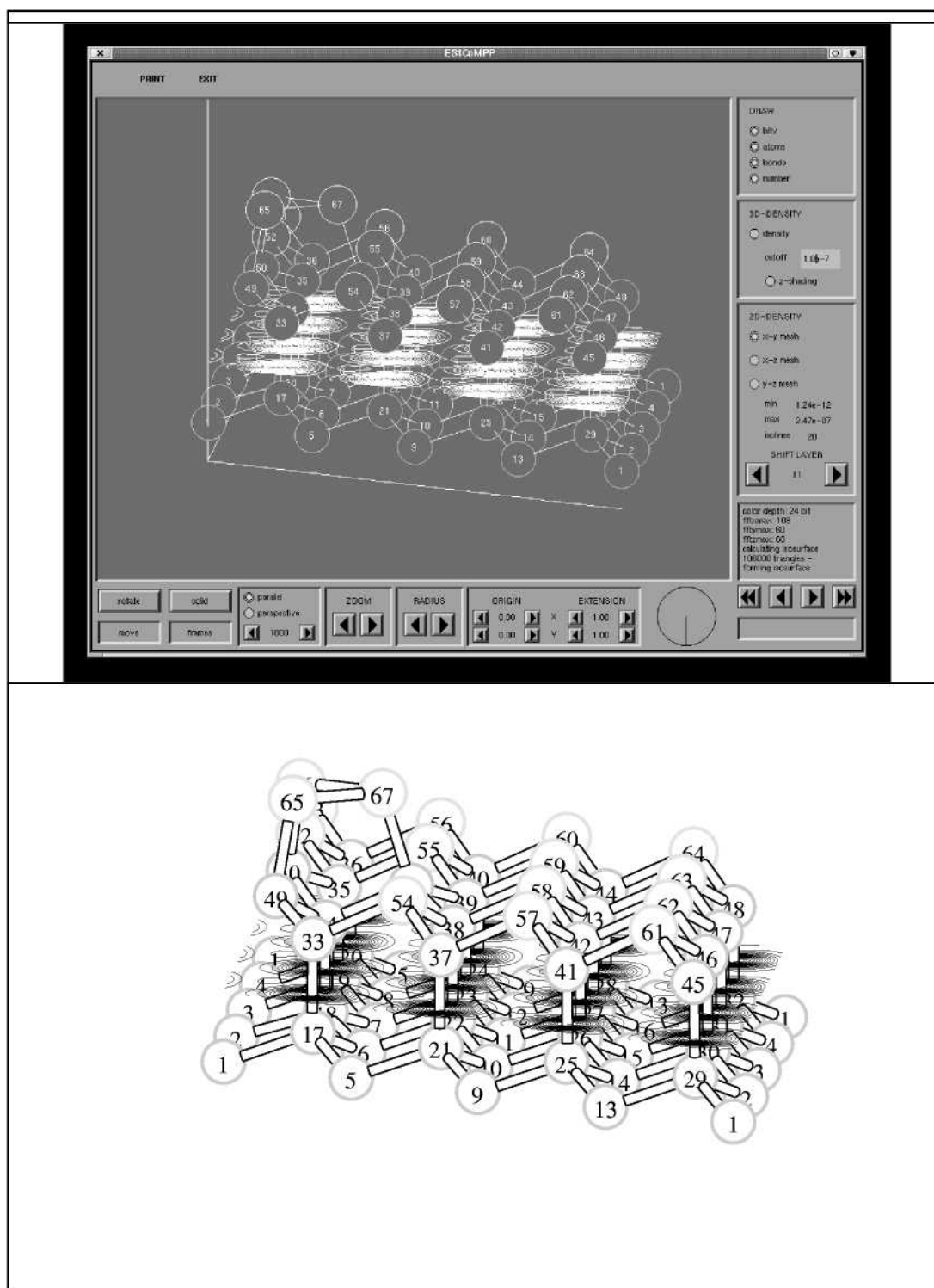


Figure 5.4: Atoms and bonds in **frames-mode** with 2D x-y planar density and the generated postscript output.

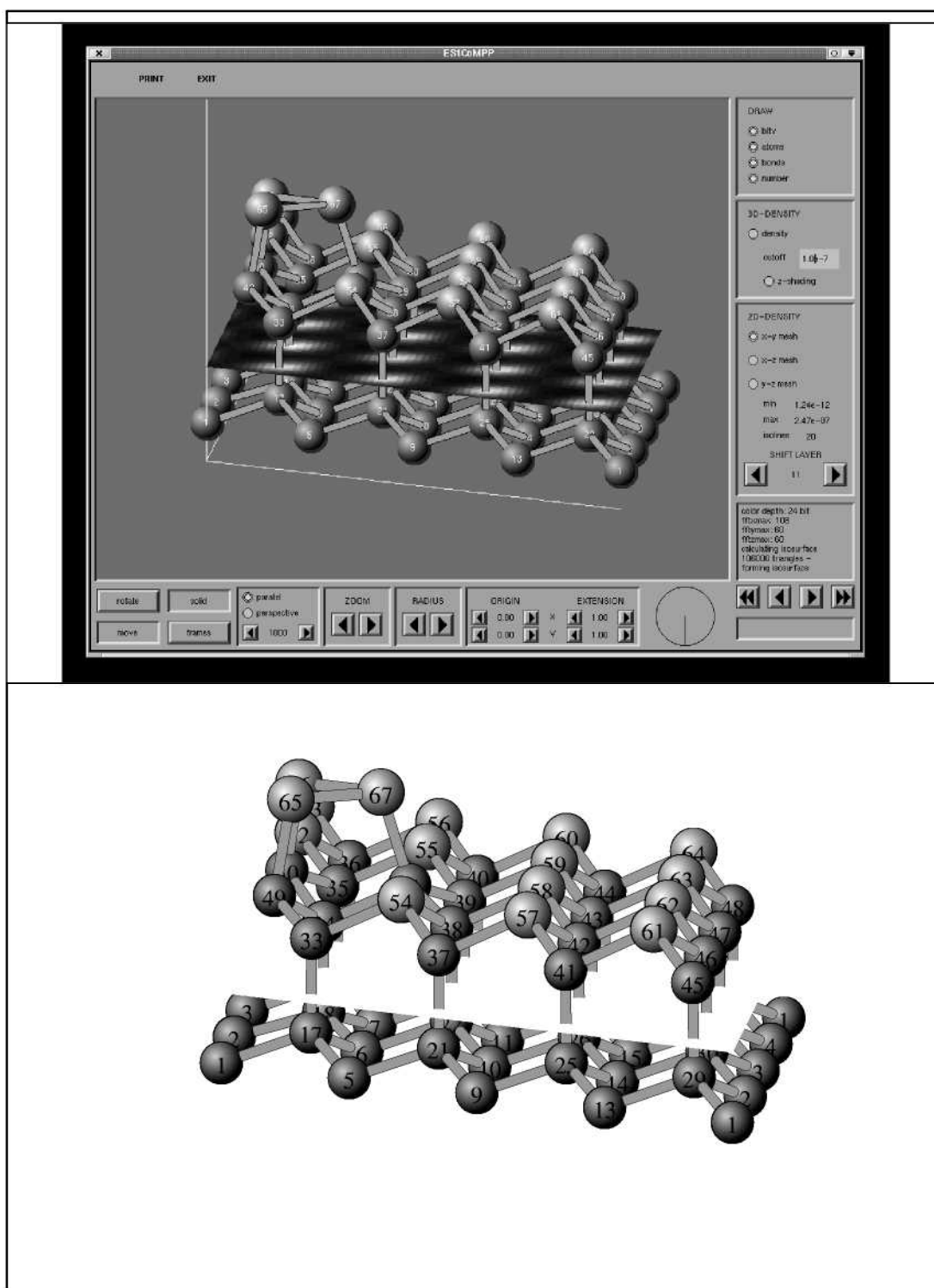


Figure 5.5: Atoms and bonds in solid-mode with 2D x-y planar density and the generated postscript output.

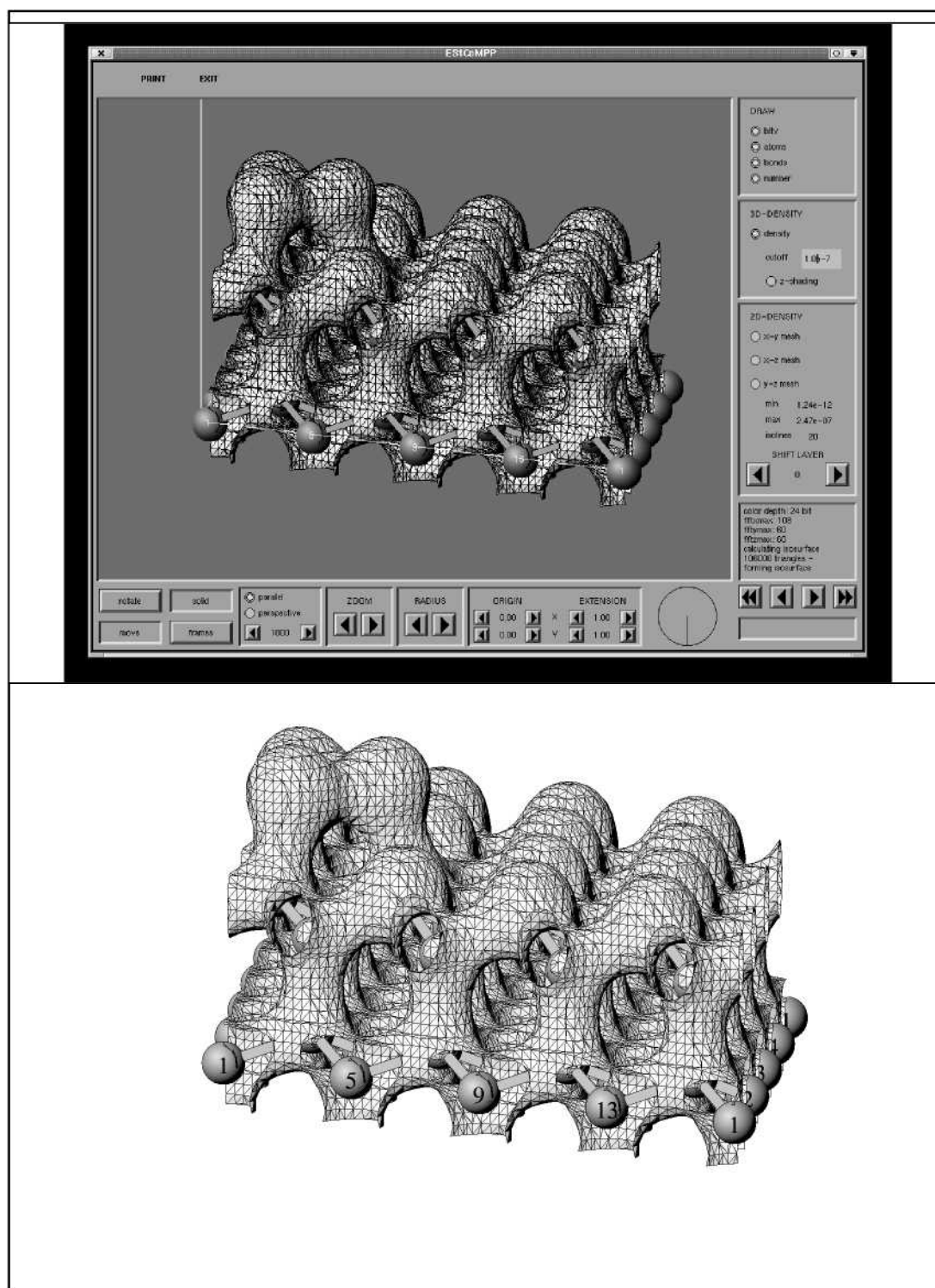


Figure 5.6: Atoms and bonds in solid-mode with 3D iso-electron density surface and the generated postscript output.

5.1 Startup Information Files

When the **ESStCoMPP-VT** is started, it reads some startup information files which can be changed by the user. The two startup information files are the **predefined_colors.dat** and the **bondlength.dat** file. The **ESStCoMPP-VT** can handle up to 7 different kinds of atoms. The colors in which these atoms are drawn on the screen and in the postscript output is defined in the **predefined_colors.dat** file, e.g.

```
1 0.8 0.8 0.8 1.0
2 1.0 1.0 1.0 1.1
3 0.6 0.6 0.6 1.1
4 0.8 0.8 0.8 1.1
5 0.0 0.0 0.0 1.2
6 0.3 0.3 0.3 1.25
7 1.0 0.0 1.0 1.3
```

The first column contains the number n of the kind of atom. In the second to fourth column the Red-Green-Blue (RGB) part of the color is defined. The fifth column is a scaling factor for the radius of the atoms of atom kind n .

In the **ESStCoMPP-VT** the bonds are determined by calculating the distance between two atoms. If the distance is smaller than a certain cutoff-distance a bond is drawn. The information about these cutoff-distances is contained in a (7×7) -matrix in the **bondlength.dat** file for different atom kinds, e.g.

```
6.30 6.30 6.30 6.30 6.30 6.30 6.30
6.30 6.30 6.30 6.30 6.30 6.30 6.30
6.30 6.30 6.30 6.30 6.30 6.30 6.30
6.30 6.30 6.30 6.30 6.30 6.30 6.30
6.30 6.30 6.30 6.30 6.30 6.30 6.30
6.30 6.30 6.30 6.30 6.30 6.30 6.30
6.30 6.30 6.30 6.30 6.30 6.30 6.30
```

The columns and rows are the different kind of atoms respectively.

5.2 Data-File Preparation

Two different data-files are used by the **ESStCoMPP-VT**. One file contains the information about the coordinate-system and the atom position and the other one is the density-file where the information for the electron-density is stored on a grid. Both files have to be specified when starting the **ESStCoMPP-VT**, e.g.:

```
estcomp_vt coord.dat density.dat
```

The structure of **coord.dat** file is explained in the following example:

67

```

0.0000000 0.0000000 53.2545480
25.1044350 -14.4940520 0.0000000
0.0000000 28.9881040 0.0000000
1
0.0416667 0.0000000 0.0000000 1 1
0.0416667 0.0000000 0.2500000 1 2
0.0416667 0.0000000 0.5000000 2 3
.
.
```

In first row the number of atoms in the supercell and in the second to fourth row the unit vectors ($\mathbf{a}_1, \mathbf{a}_2, \mathbf{a}_3$) of the supercell are defined. The periodic extension mentioned in the definition of the buttons can only be done in directions \mathbf{a}_2 and \mathbf{a}_3 .

For better performance of the fast-fourier-transformation the coordinate-axes are permuted by the EStCoMPP-program in such a way that the longest axis (axis perpendicular to the surface for surface calculations) is always first. The fifth row gives the number of sets of different atom positions, e.g. along a diffusion path, which are included in this file. The atom positions (relative coordinates with respect to the previous defined unit vectors) for all atoms in the supercell start at row six. The order is the same as for the unit vectors. The next two numbers identify the atoms, first the kind of atom is specified and then a serial number to identify the atom of the same kind on the screen or the output.

An examples for the `density.dat` file is shown below.

```

nfftwk,nfftgp,nrgvfd,nrgvfl,nrgvfm,nrgvfn
2*388800, 2*108, 60, 60
38754.930395326519          voluni
rho:
0.222696E-06 0.213638E-06 0.176191E-06 0.109715E-06 0.553695E-07
0.545380E-07 0.921025E-07 0.116906E-06 0.102735E-06 0.668558E-07
0.362311E-07 0.192751E-07 0.117047E-07 0.887694E-08 0.856667E-08
0.971956E-08 0.114511E-07 0.129288E-07 0.135455E-07 0.130539E-07
0.116002E-07 0.963555E-08 0.762719E-08 0.581636E-08 0.424569E-08
0.292667E-08 0.189853E-08 0.118417E-08 0.756540E-09 0.529446E-09
```

It contains a header line first, where any comments can be included. The format of the second line has to be exactly like in the above. It has to contain four columns separated by commas. The first two columns are two times the total number of grid points and two times the number of grid points in z-direction and have to be written explicitly as 2*nnn. The third and fourth column are the number of grid points in x and y direction. The next two lines are ignored by the EStCoMPP-VT and can be used as comment lines, but must not be erased! The information of the electron-density which is stored on the grid points starts

at row five. The order in which the density, or any other information which is defined in space (e.g. $|\psi|^2$ in a certain energy range for STM-images), has to be stored is here also z, x, y. Thus the information is read out by three encapsulated loops where the innermost increases z, the middle x and the outermost the y.

While the `density.dat` file is given directly as `fort.97` by the **ESCoMPP**-program, the information for the `coord.dat` file has to be extracted from the main output. The perl-script, which generates the `coord.dat` file from the output is listed in the appendix.

5.3 Algorithms and Data-Structures

The **ESCoMPP-VT**-program was written in C. The **Forms Library**, which was developed by T.C. Zhao and M. Overmars [ZO97], was used to build up the interaction forms with buttons and input fields. Although the **Forms Library** is not public domain, the permission for non-commercial and not-for-profit use is granted by the authors. The **Forms Library** offers a 'canvas' on which the drawing is done.

In the following the drawing elements like atoms, bonds, lines, triangles etc. are referred to as elements. With the given transformation-matrix in the `coord.dat` the positions of the elements are calculated in a Cartesian frame. To give the impression of a three dimensional view, the elements closer to the camera have to be in front of the elements further to the back. Since a real hidden-surface-removing algorithms (e.g. scan-line algorithms) is much too slow for real-time application, a simple painters-algorithm was used. Thus, before each drawing a depth sorting algorithm (i.e. quicksort) is applied to the elements. The bonds are simply drawn as filled (**solid-mode**) or empty (**frames-mode**) polylines. In the **frames-mode** the atoms are drawn as circles, filled with the background color. In **solid-mode** the atoms are drawn to look like solid spheres. As mentioned before, the **ESCoMPP-VT** code can handle up to seven different atom kinds. Thus on a 256 color display, where 32 colors are reserved for the buttons and input fields of the **Forms Library**, there are 32 colors left for each of the seven different kinds of atoms. Obviously this is not enough for a convincing, realistic shading of the atoms. Thus a dithering algorithm had to be implemented. The best results were obtained by using an error diffusion algorithm. Starting from an realistic shaded atom, with an unlimited number of colors (i.e. 16777216 colors) the RGB-values from the original pixel is taken and replaced by the best matching RGB-value from the reduced color palette (256 colors). The difference (error) from the original to the approximated RGB-values is distributed to the nearby pixels in the original, realistic shaded atom. Starting with the upper left pixel and proceeding to the lower right this algorithm reduces the error at one pixel by changing the color of the neighbored pixels. The quality of the result depends mainly on the reduced color palette. If for example an

atom should be blue and there is no blue in the reduced color palette this error can not be overcome by the error-diffusion algorithm. Finding the optimal colors for the reduced color-palette is an np-complete problem and thus in principle not solvable. A good approximation is to determine the basic-color in which the atom should be drawn (e.g. red) and then set the 32 corresponding entries in the color-palette to $n \times \text{basic-color}$, where n goes from totally black to maximum brightness in equidistant steps. Since it is not possible to calculate the shading of an atom each time it is drawn with such a computationally demanding procedure, the shading is calculated for each atom kind ones and the results are stored in a pixmap. For the actual drawing of the atoms a fast XCopyArea command is used in combination with a pixmask. Only if the radius of the atoms is changed either directly or by zooming in or out, the pixmaps have to be re-calculated.

For the investigation of the electron density, or any other physical property which is defined on a grid in space, iso-line and iso-surface algorithms are implemented in the **ES**tCoMPP-**VT** code. To construct 2-D contour lines on a given grid (i.e. a plane out of the three dimensional grid on which the electron-density is defined) a fixed value, the iso-value or contour value, has to be defined. Four next

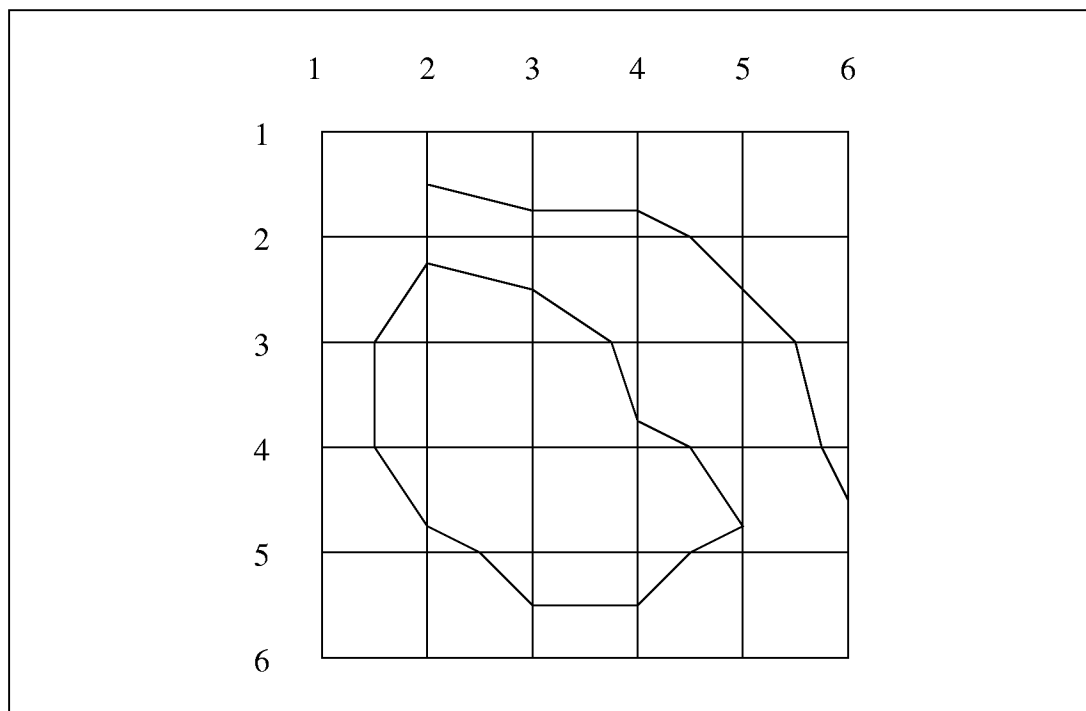


Figure 5.7: Schematic view of isolines on a 5×5 grid

neighbored grid-points form a cell (Fig.5.7). These cells either contain pieces of the contour or are empty. If the value at all corner-points of the cell are either above or below the iso-value, the cell contains no piece of the contour. If the corner points have values both above and below the iso-value, the points x_i at

which the isolines meet the borders of the cell are calculated by linear interpolation. Since the cell has eight corners and two states (either above or below the iso-value) there are $2^4 = 16$ cases how the isolines can be arranged in the cell. The contour line is drawn by connecting the points x_i of adjacent borders in each cell. This technique is called the "marching-square" algorithm.

The determination of an iso-surface on a three dimensional grid is in principle an extension of the marching square technique to three dimensions. For 3-D surface contours this is called the "marching-cubes" algorithm in analogy to the marching-square algorithm. As can be seen in Fig.5.8, the contours consists of

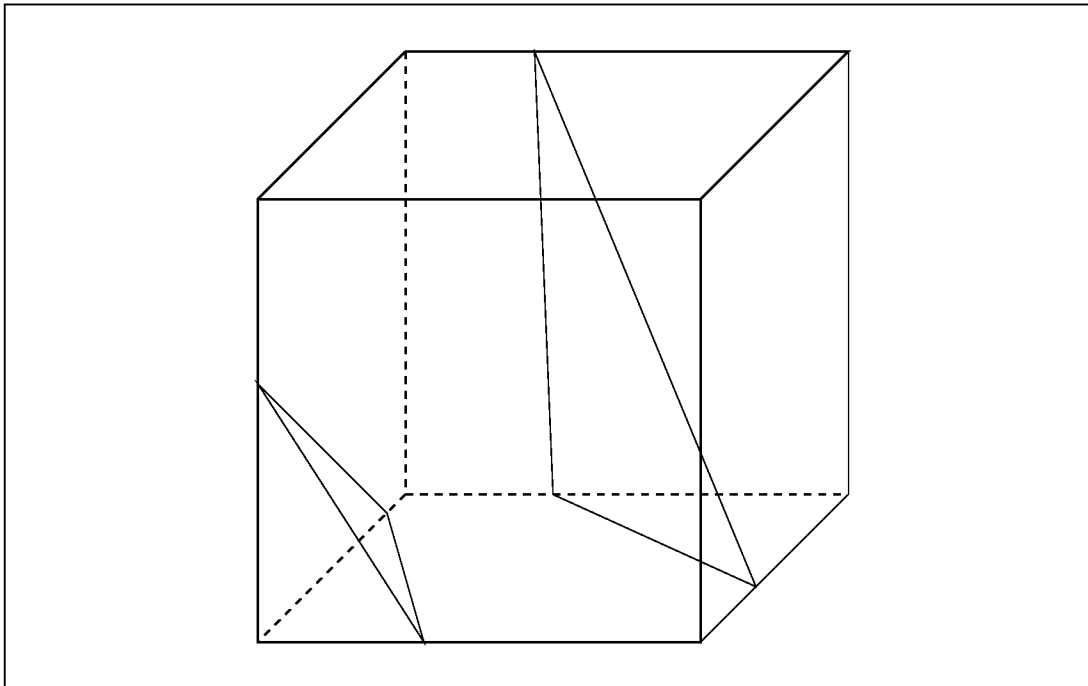


Figure 5.8: Schematic view of isosurfaces in a cube.

triangles in the cubes, formed by eight next neighbored points of the three dimensional grid. Each cube has eight vertices and two states (either above or below the iso-value), so the number of cases in which the triangles can be arranged in the cubes is $2^8 = 256$. As in the marching-square algorithm, the points x_i at which the isolines meet the edges of the cube are calculated by linear interpolation. The edges of the iso-triangles, which are the smallest elements of the iso-surface are defined by the points x_i of adjacent edges. The fast marching-cubes algorithm, which is based on the look-up tables from Cory Gene Bloyd, was taken from Paul Bourke (<http://astronomy.swin.edu.au/pbourke/modelling/polygonise/>). For the shading of the iso-surface the normal vectors of each triangle in direction to the imaginary light source are calculated. Following Lambert's Rule the brightness of a surface is given by $B = I \cdot \cos(\omega)$ where I is the intensity of the light source and ω the angle between the surface normal and the direction of the

incoming light.

5.4 Generating High Quality Output

High quality output, which can be used for articles, posters etc. cannot be delivered by simple screen-shots. Thus, natural postscript routines were developed to achieve high quality, scalable output. The principle of two of the postscript subroutines will be explained in more detail. The first is the subroutine which draws the shaded atoms. Since most postscript printers are very slow when interpreting the postscript commands a fast algorithm is required. Thus, dithering algorithms as for the *ES*tCoMPP-*VT* are not favorable. Also, when scaling the graphics, e.g. for posters etc., the quality should remain as good as possible. Since postscript offers natural routines for drawing filled circles, an algorithm was developed which draws concentric circles on top of each other where the radius becomes smaller and smaller. If the color of this filled circles are changed accordingly to the radius and Lambert's Rule, and the result is clipped outside a circle which is centered off-center of the other circles, a convincing realistically shaded sphere results, as is shown in Fig. 5.9.

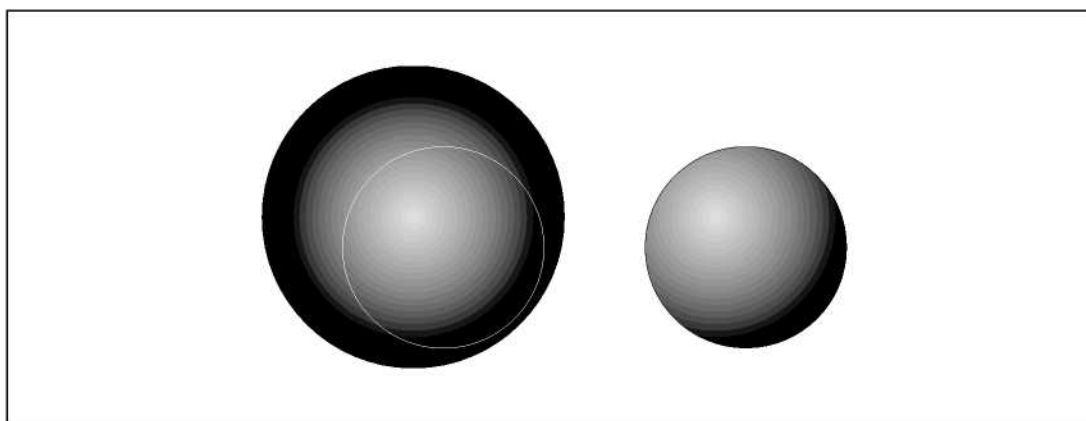


Figure 5.9: Schematic view of the construction of shaded spheres with a reduced number of circles (i.e. 16 shades of grey). The clipping circle is drawn in white.

For a high quality output of continuous data on a two dimensional grid (e.g. 2D electron density plot), an interpolation between the data on the grid points is necessary. Most programs for creating graphics are capable of interpolating values on regular, rectangular grids. But the interpolation of data on non-rectangular grids are rarely offered. Thus the output of most graphics packages look like Fig.5.10. Instead of a smooth interpolation as can be seen on the right side, blocks with the colors of the according points are drawn to fill the space between the grid points. After a simple triangulation of the two dimensional grid and a

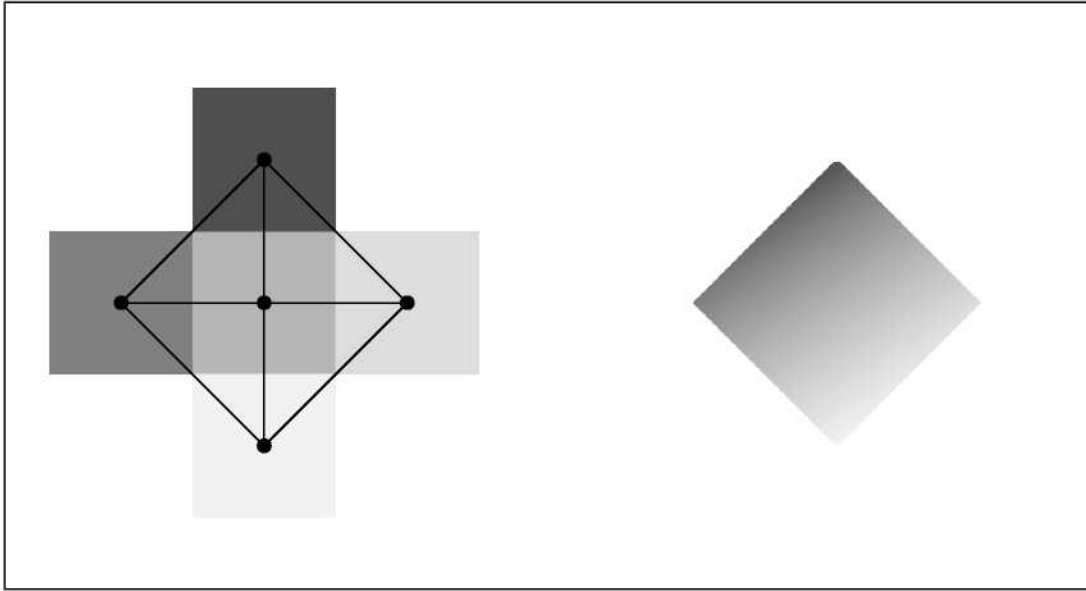


Figure 5.10: Comparison of a non-interpolated block fill on the left side and the linear interpolation on the right of a five point grid.

renormalization of the data to a range between 0 and 1, the interpolation can be done by a postscript routine. The input for this subroutine are the coordinates of the three corners and the corresponding color-value. A fast, linear interpolation is done by:

$$\begin{aligned}
 I_a &= I_1 \frac{y_s - y_2}{y_1 - y_2} + I_2 \frac{y_1 - y_s}{y_1 - y_2} \\
 I_b &= I_1 \frac{y_s - y_3}{y_1 - y_3} + I_3 \frac{y_1 - y_s}{y_1 - y_3} \\
 I &= I_a \frac{x_b - x_p}{x_b - x_a} + I_b \frac{x - x_a}{x_b - x_a}
 \end{aligned} \tag{5.1}$$

The meaning of the variables in the above formulas can be seen in Fig.5.11

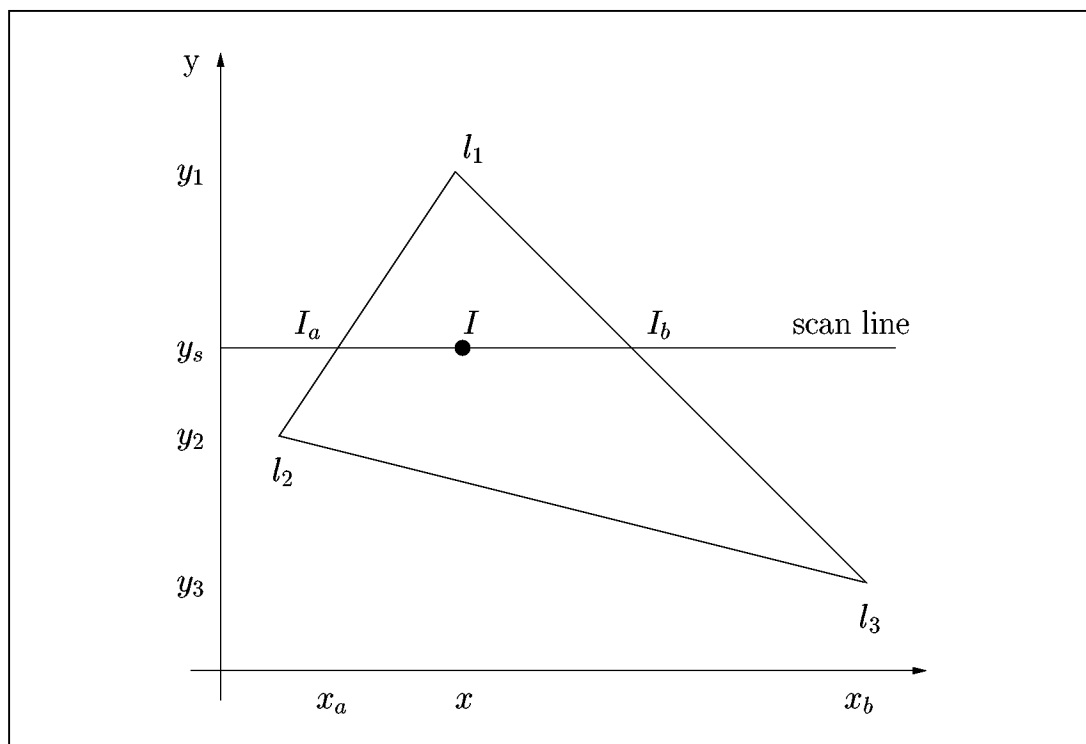


Figure 5.11:

Chapter 6

Atomistic Processes at Surfaces

The growth of crystals depends on many external parameters as well as materials properties. The main processes responsible for nucleation and growth (within the first deposited layer on the substrate) on a low indexed flat surface are sketched schematically in Fig. 6.1. Nucleation and growth of crystals have been discussed in terms of rate equations for a long time [VSH84]. Many of the atomistic processes (adsorption, diffusion, nucleation etc.) can be incorporated into these rate equations if the energy of the states and the energy-barriers for the processes are known. Also for other methods with different time- and length-scales like Monte-Carlo simulations or molecular dynamics calculations with empirical potentials, the energies of the atomistic processes are decisive ingredients. Since these energies are hardly accessible by experiments, they have to be calculated by reliable *ab-initio* methods.

6.1 Adsorption and Desorption

A qualitative distinction is usually made between chemisorption and physisorption. In chemisorption a strong chemical bond is formed between the adsorbate and the substrate. In this case, the adsorption energy E_a of the ad-atom is likely to be a good fraction of the sublimation energy of the substrate of the order of a few eV. Physisorption is weaker and the energy of interaction is largely due to the van der Waals force. Physisorption energies are of order 50 – 500 meV per atom. Adsorption of molecules often proceeds in two stages. A first precursor stage has all the characteristics of physisorption, but this state is metastable. In further steps molecules can transform into a chemisorbed state, usually resulting in splitting the molecule and adsorbing the individual atoms (dissociative chemisorption).

The adsorption rate R is the most important parameter governing the growth rate. It is given by the flux of particles to the unit surface area (measured in $\text{cm}^{-2}\text{s}^{-2}$ and can be varied by gas pressure and temperature over many orders

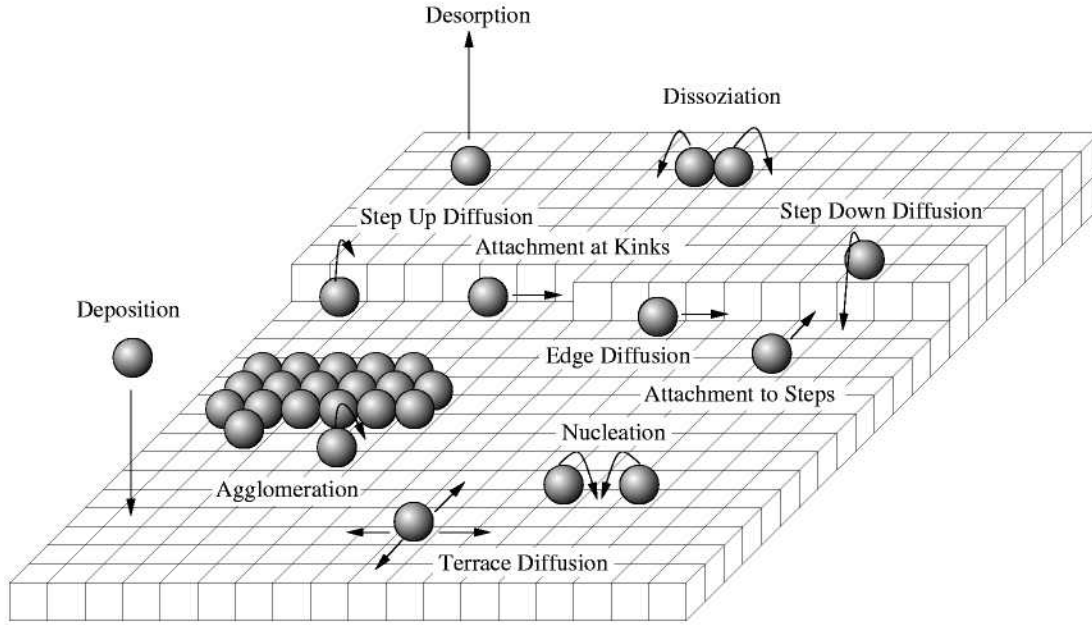


Figure 6.1: Elemental atomistic processes at surfaces.

of magnitude. In most cases, epitaxy is performed for a large supersaturation of ad-atoms, which means high particle flux and a negligible desorption rate. The desorption rate R_{des} depends linearly on the number of absorbed atoms and exponentially on the ratio of the binding energy E_a and the substrate temperature T_S . Thus the desorption rate is time dependent as long as the ad-atom density $n_1(t)$ is changing:

$$R_{des}(t) = n_1(t) \nu_a \exp(-E_a/k_B T_S) = n_1(t)/\tau_a \quad (6.1)$$

τ_a is the mean residence time of the ad-atoms on the surface before it desorbs at a given temperature T_S . The pre-factor ν_a is determined by the curvature of the binding energy surface of an ad-atom as a function of vertical distance calculated at the equilibrium adsorption distance. The ratio of the adsorption and desorption rates defines the "sticking coefficient" β

$$\beta = 1 - R_{des}(t)/R = 1 - n_1(t)/(R\tau_a). \quad (6.2)$$

The adsorption-desorption equilibrium is reached when as many ad-atoms desorb as are deposited, i.e. $\beta = 0$:

$$\frac{dn_1(t)}{dt} = R - \frac{n_1}{\tau_a} = 0, \quad \text{i.e.} \quad n_1 = R\tau_a : \beta \rightarrow 0. \quad (6.3)$$

For epitaxial growth conditions desorption is prevented to a large extent because the ad-atoms undergo reactions into states of higher binding energy, e.g. nucleation of clusters, agglomeration to islands, or attachment to steps. Thus the adsorption-desorption equilibrium is usually not reached.

6.2 Diffusion Reactions

Real surfaces may be far from perfect, they usually contain sections of ideal terraces, steps, kinks, dislocations and point defects. These imperfections can influence the binding of single ad-atoms and small clusters to the substrate and thus change the adsorption, diffusion and nucleation behavior. Ad-atoms or Clusters, which initially form at defect sites or on the terrace, are not necessarily in their most stable state. To reach the lowest-energy positions, re-arrangement processes like dissociation, step-up, and step-down diffusion are necessary. In the early stages of growth the ad-atoms have to move across the surface in order to meet other ad-atoms or existing defects. Thus the most important process is the terrace diffusion. The terrace diffusion can be described as a random walk by thermally excited jumps to any of the nearest neighbor sites with a rate

$$\Gamma_D = \nu_D \exp(E_D/k_B T_S), \quad (6.4)$$

where ν_D is the attempt frequency and E_D the activation energy for a diffusion jump. The mean square displacement on an ad-atom depends linearly on time:

$$\langle r^2(t) \rangle = \langle x^2(t) \rangle + \langle y^2(t) \rangle = 4Dt, \quad (6.5)$$

where D is the diffusion constant which depends on the underlying lattice. The important quantity which governs the probability of reactions is the mean distance an ad-atom travels on the surface before it is desorbed, i.e. in the time interval τ_a :

$$x_a = (4D\tau_a)^{1/2} = 2a(\nu_d/\nu_a)^{1/2} \exp\left(\frac{E_a - E_d}{2kT_S}\right). \quad (6.6)$$

If $x_a \geq d_{sink}$, the mean distance between sinks, then ad-atom reactions take place and a new adsorption equilibrium is reached.

A first reaction possibility is the attachment to steps and kinks, which is important for vicinal surfaces when the diffusion distance is larger than the terrace width: $x_a > L_T$. The binding energies E_{step} and E_{kink} determine the stability of the attached configurations. If this is the most probable reaction, growth proceeds via step flow.

Another possibility is nucleation and growth of clusters (islands) on the flat terraces. For this reaction the density n_1 of single ad-atoms (called monomers in the following) has to be large, which will be the case for relatively low substrate temperatures T_S and large deposition rates R . The mean distance between monomers x_M can be estimated by $n_1 \pi x_M^2 = 1$, which means that one assigns a circle with radius x_M to each of the existing monomers which on the average contains no other monomer. If this distance is the smallest, i.e. $x_M < (L_T, x_a)$, agglomeration of ad-atoms into clusters (islands) of increasing size ($i \geq 2$) takes place. The binding energies E_i depend on the island size i , and for large islands they tend towards the binding energy E_{step} .

6.3 Growth Kinetics

In order to understand the time evolution of the growing crystal under a constant flux of deposited atoms one has to calculate the developing coverage of every newly created crystal plane due to agglomeration of the deposited atoms to islands and at terrace steps. In the following only growth by agglomeration of ad-atoms to islands on the terrace is considered. Thus, the time dependence of island densities and sizes have to be described by kinetic equations.

6.3.1 Kinetic Equations

For the case of homogeneous deposition and homogeneous nucleation, only the time dependence of spatially averaged densities of monomers $n_1(t)$ and clusters $n_j(t)$, $j > 1$ have to be considered. The derivation holds for 2-dim and 3-dim islands. More details can be found in the review paper of Venables,[VSH84].

Under the assumption that the monomers are the only diffusing species with diffusion coefficient D , only diffusion reactions of mobile monomers with existing clusters of any size and the decay of clusters by emitting monomers have to be considered.

The diffusion reactions are bimolecular reactions of the general form:

$$U_j = D \sigma_j n_1 n_j, \quad (6.7)$$

where σ_j is a reaction cross-section determined by the strength and distance dependence of the interaction of a j -cluster with a monomer.

The decay reactions are mono-molecular reactions of the form:

$$K_j n_j = \exp\left(-\frac{E_j - E_{j-1}}{kT_s}\right) n_j, \quad (6.8)$$

where the difference of the binding energies $E_j - E_{j-1}$ of two consecutive cluster sizes (binding energy of the detached ad-atom) determines the reactions rate.

The time dependence of the densities is then governed by the following equations:

$$\frac{dn_1(t)}{dt} = R - \frac{n_1(t)}{\tau_a} - 2U_1 - \sum_{j \geq 2} U_j + \sum_{j \geq 2} K_j n_j \quad (6.9)$$

$$\frac{dn_j(t)}{dt} = U_{j-1} - U_j - K_j n_j + K_{j+1} n_{j+1} \quad (j > 1). \quad (6.10)$$

These equations have to be solved subject to the initial condition that all densities are zero at $t = 0$. For a (numerical) solution one has to know all activation energies (binding energies and diffusion barrier) and specify the deposition rate R .

6.3.2 Growth of Stable Islands

Under the assumption that there exist stable clusters of the size i it is reasonable to coarse grain the size distribution with the following arguments:

1. At long times the intermediate clusters with sizes $2 \leq j \leq i$ will reach a stationary density, the so-called Walton relation [Wal62] obtained by considering detailed balance of agglomeration and decay:

$$K_j n_j = D \sigma_{j-1} n_1 n_{j-1}, \quad (6.11)$$

$$\frac{n_j}{N_0} = \left(\frac{n_1}{N_0}\right)^j \exp\left(-\frac{E_j}{k T_S}\right). \quad (6.12)$$

Here N_0 is the planar density of atom sites.

2. The details of the time development of clusters with sizes $j > i + 1$ has to be calculated, under the reasonable assumption that such clusters do not decay anymore but rather absorb the attached ad-atoms and thus grow. The clusters with $j \geq i + 1$ are collected to one density n_x . Of course, the average size w_x of the stable x -clusters will also depend on time. The total number of atoms contained in these stable clusters then is $w_x n_x$.
3. The total coverage Z for 2-dim clusters can be expressed by

$$Z(t) = F_{at} \sum_j j n_j(t). \quad (6.13)$$

Since with the first assumption only the stable clusters grow, the time dependence of the coverage is entirely due to the change of the number of atoms in stable clusters:

$$\frac{dZ}{dt} = F_{at} \sum_{j \geq i+1} j \frac{dn_j}{dt} = F_{at} \frac{d(n_x w_x)}{dt}. \quad (6.14)$$

4. For larger coverage the direct deposition of atoms to stable clusters and the coalescence of clusters has to be taken into account.

With these assumptions the problem can be cast into the following kinetic equations:

$$\frac{dn_1(t)}{dt} = R - \frac{n_1(t)}{\tau_a} - \frac{d(w_x n_x)}{dt}; \quad \text{monomers} \quad (6.15)$$

$$\frac{dn_j(t)}{dt} = U_{j-1} - K_j n_j - U_j + K_{j+1} n_{j+1} = 0 \quad (2 \leq j \leq i)$$

$$\frac{dn_x(t)}{dt} = \sigma_x D n_1 n_x - 2 n_x \frac{dZ}{dt}; \quad \text{stable islands} \quad (6.16)$$

nucleation and coalescence

$$\frac{d(w_x n_x)}{dt} = (i+1) \sigma_i D n_1 n_i + \sigma_x D n_1 n_x + RZ; \text{ atoms in islands} \quad (6.17)$$

$$\frac{dZ}{dt} = F_{at} \frac{d(w_x n_x)}{dt}; \quad \text{coverage for 2-dim. islands} \quad (6.18)$$

Two limiting cases can easily be distinguished[VSH84] (see Fig.6.2):

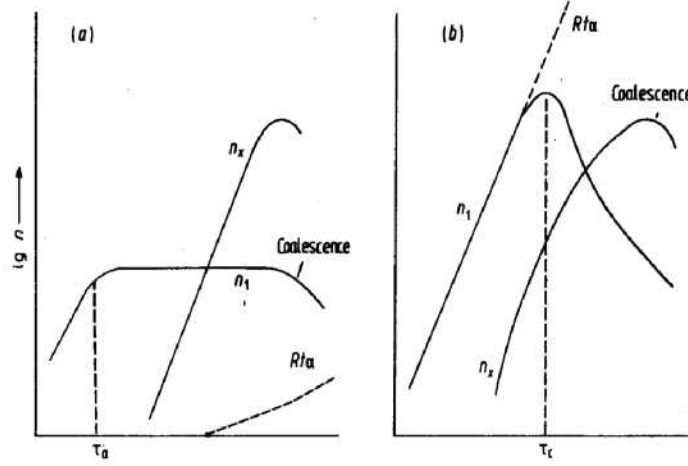


Figure 6.2: Time dependence of monomer concentration, $n_1(t)$, of growing islands, $n_x(t)$, and total number of atoms condensed, $Rt\alpha$, for the two extreme cases: (a) incomplete condensation (T_S high, $1/\tau_a \gg \sigma_x D n_x$. Then desorption is important, the monomer density is limited and growth of stable islands is slow. (b) complete condensation (T_S low, $1/\tau_a \ll \sigma_x D n_x$). Then the monomer density reaches a maximum at $\tau_x = 1/(\sigma_x D n_x)$. The density of stable islands and the total number of deposited atoms increase quickly.

1. Incomplete condensation when substrate temperature is high. Then most deposited atoms desorb again because $1/\tau_a \gg \sigma_x D n_x$. The monomer density saturates and the stable clusters and the coverage increase very slowly (Fig.6.2a).
2. Complete condensation when substrate temperature is low. Then all deposited atoms stick to the surface and the coverage increases linear in time. For large times all deposited atoms end up in stable clusters, because $1/\tau_a \ll \sigma_x D n_x$. This case is depicted in Fig.6.2b.

The general behavior of the maximal density of stable clusters n_x can be written as

$$n_x \propto R^p \exp\left(\frac{E}{kT_S}\right), \quad (6.19)$$

where the exponent p and the apparent activation energy E depend on the dimension of the islands, the substrate temperature T_S (i.e. on the relative importance of the desorption reaction), the size of the critical islands i and on the diffusion barrier E_d as well as the binding energy of atoms to the critical island E_i . The following table summarizes the important cases, the cases discussed above are underlined. More details can be found in the review paper by Venables.[VSH84]

Table 6.1: Parameters determining the maximal island density

Regime	3-dim. islands	2-dim. islands
high T_S (with desorpt.)	$p = 2i/3$ $E = \frac{2}{3} [E_i + (i+1)E_a - E_d]$	$\underline{p = i}$ $\underline{E = E_i + (i+1)E_a - E_d}$
low T_S (no desorpt.)	$p = i/(i+2.5)$ $E = [E_i + iE_d]/(i+2.5)$	$\underline{p = i/(i+2)}$ $\underline{E = [E_i + iE_d]/(i+2)}$

Chapter 7

Si Ad-Atoms on Si(111)(7 × 7)

Epitaxial growth of silicon on silicon surfaces is of interest both from the technological and the scientific point of view. Atomic diffusion is the key process that controls growth, motion of interfaces and microstructure evolution. In the most direct experimental measurements of ad-atom diffusion on surfaces, scanning tunneling microscopy (STM) and field ion emission techniques have been able to image diffusing atoms at successive stable or metastable positions, thus revealing a wealth of information on the microscopic atomic motion. Despite this progress, it is impossible to capture a diffusing ad-atom at the saddle-point configuration, and therefore the exact diffusion path is typically assumed to be a simple interpolation between initial and final configurations. For complicated structures this can yield misleading results. The diffusion of ad-atoms can only be investigated beyond the experimental limits by using reliable computational methods, i.e. *ab-initio* calculations. Studying diffusion on complicated, reconstructed surfaces as the Si(111) surface is still a computational challenge due to the large supercells and costly computational methods for the examination of the diffusion path.

7.1 Si(111)(7 × 7)

The (111) oriented Si/Ge surface has only one dangling bond per surface unit cell and therefore, even in comparison with other low index surfaces as the (100) and (110) surfaces, the smallest number of broken bonds per surface unit area. At room temperature a Si(111) surface created by cutting a bulk crystal shows a metastable (2×1) reconstruction. Heating the surface above 380°C transforms the surface reconstruction irreversibly to a (7×7) structure. The (7×7) reconstruction (Fig.7.1) is the most stable of a family of $((2n + 1) \times (2n + 1))$ reconstructions which are observed experimentally. There are a number of characteristic features in these reconstructions which are listed in table 7.1. The (7 × 7) reconstruction

conf.	dimer	ad-atom	stacking fault	rest atom	corner hole
3×3	3	2	1/2	0	1
5×5	6	6	1/2	2	1
7×7	9	12	1/2	6	1

Table 7.1: Number of characteristic features in the family of $(2n + 1) \times (2n + 1)$ reconstructions. 1/2 means a stacking fault in one-half of the unit cell.

of the Si(111) surface is perhaps the most complex and widely studied surface of solids. The *Dimer-Adatom-Stacking Fault* (DAS) Model proposed by Takayanagi *et al.* [TTTT85] contains 103 atoms in the surface unit cell and is shown in Fig. 7.1. The DAS structure extends over several layers and shows five characteristic features which are revealed in the (7 × 7) as well as in the (5 × 5) reconstruction: (i) The ad-atoms in the top-layer sit on T4 sites (above the empty hexagons) with respect to the next double-layer. (ii) Due to the arrangement of these ad-atoms, rest-atoms on T1 sites occur on symmetric positions between three of the ad-atoms. Each of these rest-atoms has one dangling bond. (iii) One half of the (7 × 7) unit cell shows a stacking fault in the second layer (with respect to the deeper bulk structure). The regular sequence of the layers in (111) direction is AABBC... Starting from layer 6 and going up instead of the expected, regular sequence AABBC, a sequenz AABBA is found (Fig.7.2). The triangular part of the (7 × 7) unit cell with the stacking fault is shaded darker in Fig.7.1. (iv) At the boundary between the faulted and unfaulted triangles the atoms of the third layer form dimers. In total 9 dimers are found in the (7 × 7) unit cell. (v) At the corner of the triangles atoms are missing (corner holes). The entire reconstruction leads to a reduction of dangling bonds. Instead of 49 per (7 × 7) surface area in the unreconstructed (1 × 1) surface only 19 dangling bonds are

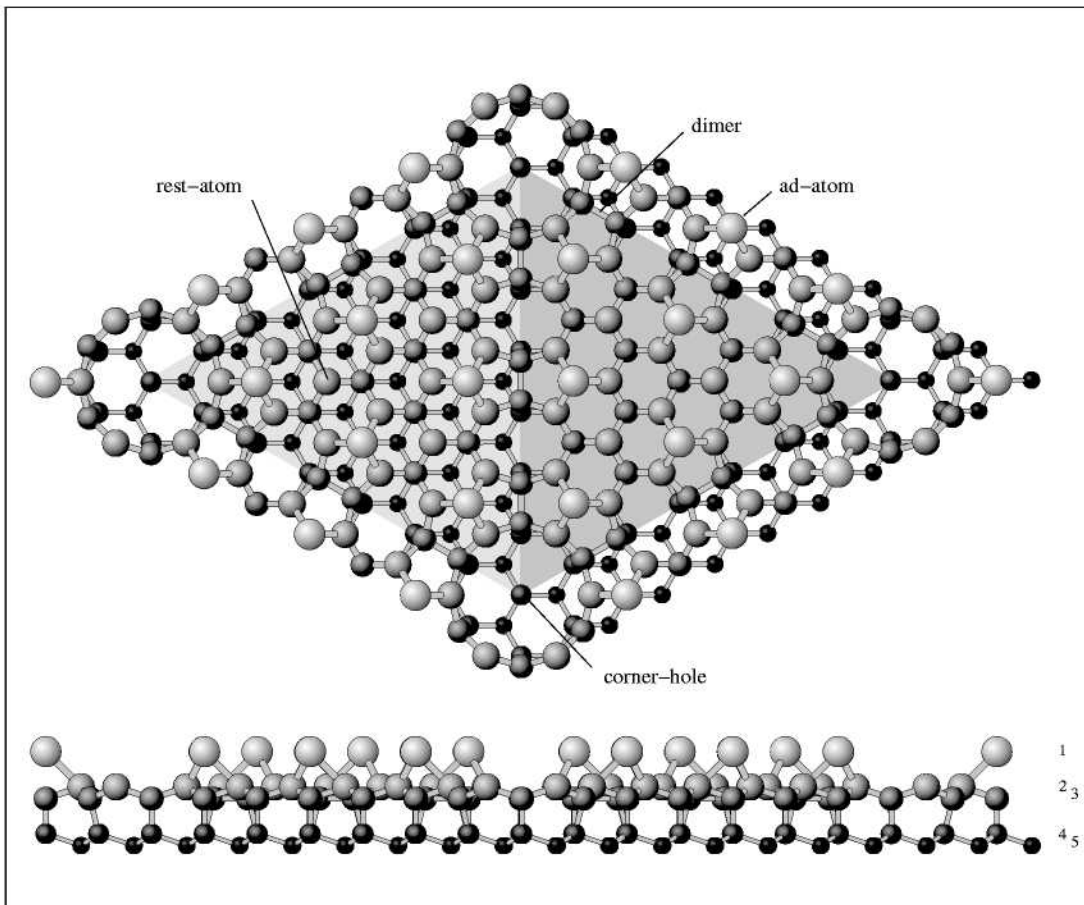


Figure 7.1: Top- and side view of the (7×7) reconstruction of the pure $\text{Si}(111)$ surface. The atoms size and the brightness increases from lower to upper atom-positions. The two shaded triangles mark the periodic (7×7) arrangement. The darker shaded triangle marks the area of stacking faults in the second layer.

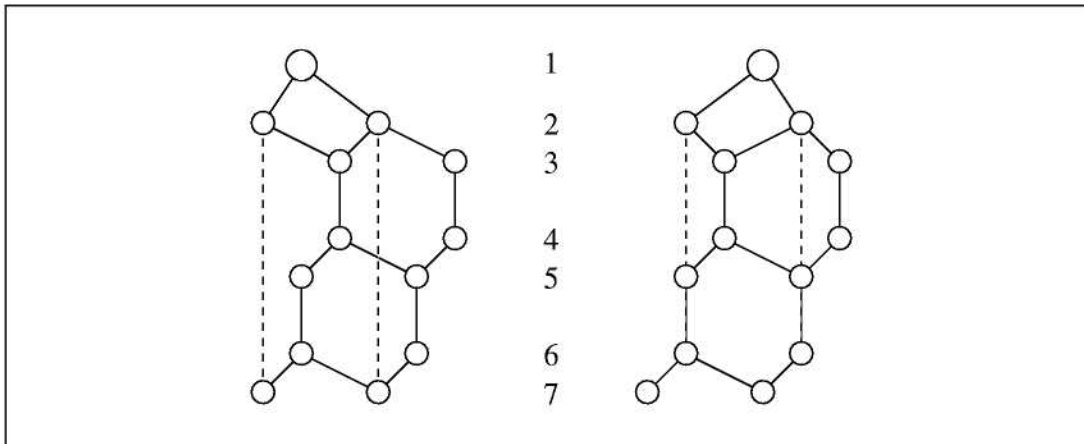


Figure 7.2: Schematic Side-view of Si with (right) and without (left) a stacking-fault in the second-layer.

found in the DAS-structure. This compensates the energy cost for creating the stacking fault and the elastic strain energy.

7.2 Si(111)(3 × 3)

The (3 × 3) reconstruction has only two ad-atoms in the unit cell. Thus there is no rest-atom, which would be located on a symmetric position between three ad-atoms in each half of the unit cell. The (3 × 3)-reconstruction is shown in Fig.7.3 in top- and side-view.

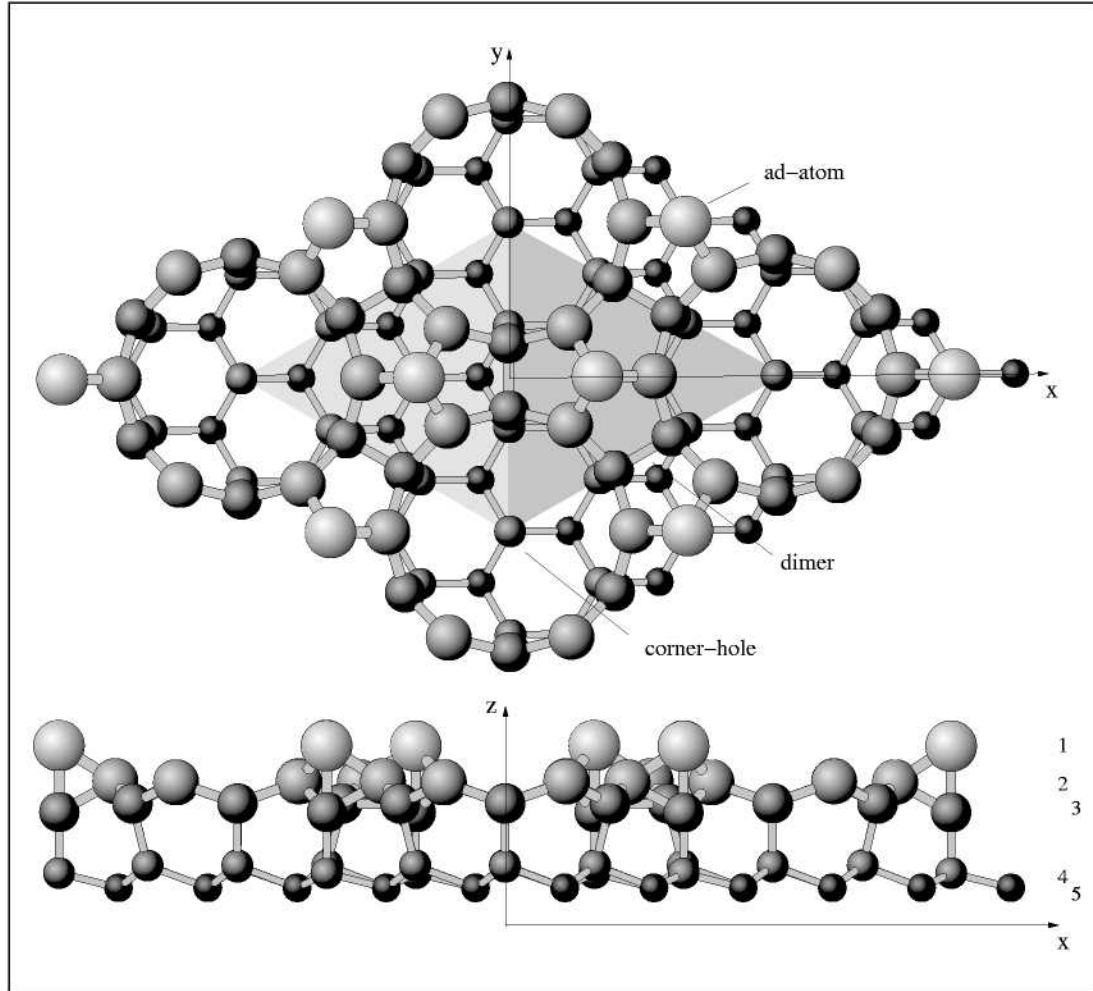


Figure 7.3: Top- and side view of the (3 × 3) reconstruction of the pure Si(111) surface. The atoms size and the brightness increases from lower to upper atom-positions. The two shaded triangles mark the periodic (3 × 3) arrangement. The darker shaded triangle marks the area of stacking faults in the second layer.

Ab-initio calculations have been performed to compare the total energy of

the $((2n+1) \times (2n+1))$ -reconstructions [Pay87, SPKSL92]. They show that the (7×7) DAS-structure has the lowest surface energy and the (5×5) and (3×3) are decreasingly stable, which is explained by structural trends across the series which can be correlated with the degree of charge transfer between the dangling bonds on the ad-atoms and rest-atoms.

7.3 Single Ad-Atom Kinetics on Si(111) (3 × 3)

Since the term "ad-atom" is reserved for the intrinsic ad-atoms in the DAS-structure the additional ad-atoms are in the following referred to as extra ad-atoms. Due to the large supercell it is almost impossible, even with modern supercomputers, to study the diffusion of extra ad-atoms on the (7 × 7)-reconstruction. Cho and Kaxiras argued that the most attractive sites for extra ad-atoms would be the rest-atoms with their dangling-bond [CK97, CK98], and they studied the diffusion of an extra ad-atom in an ideal periodic arrangement of ad-atoms and rest-atoms, omitting all other features of the (7 × 7)-reconstruction like stacking-fault; corner holes and dimers. They characterized the diffusion path by a *basin of attraction* around the rest-atom in which the extra ad-atom is localized until an intermittent jump to a nearby basin of attraction occurs. Their calculated positions are shown in Fig.7.4. They found the most stable position to be the B_2 -position (number 3 in Fig.7.4). The suggested path to the neighboring *basin of attraction* goes from B_2 via T_4 , B'_2 , H'_3 and B'_2 , T_4 to B_2 . The authors found the barrier $E(B'_2) - E(B_2) = 1.12\text{eV}$ at the saddle point B'_2 (number 5 in Fig.7.4).

To complete the picture the diffusion path of an extra ad-atom on the Si(111) surface, one has to study diffusion between the unit cells, including the stacking-fault, corner holes and dimers. Since the (5 × 5)-reconstruction, which includes all characteristic features of the DAS-reconstruction requires a supercell too large for dynamical calculations, we have investigated diffusion on the (3 × 3)-reconstruction which means that the already known diffusion in the basin of attraction around the rest-atoms is omitted. The common feature which is shared by the calculations of Cho and Kaxiras and our calculations of extra ad-atoms on the (3 × 3)-reconstructed surface are the ad-atoms on the reconstructed surface. The position which turns out to be the most stable position of an extra ad-atom in our calculations is marked by a "?" in Fig.7.4. From Chos and Kaxiras papers it is not clear if they have calculated an extra ad-atom at this position. Thus, the linkage between their and our results is not possible. Sato *et al.* [SKI00] have studied the initial adsorption processes on Si(111)(7 × 7) with (scanning tunneling microscopy) STM and the diffusion with STM tracking techniques recently and have found a higher residence time of the extra ad-atoms at the position favored by our calculations.

The calculations were done in an inversion-symmetric (3 × 3)-supercell with 68 atoms at the theoretical lattice-constant of $\approx 5.425\text{\AA}$. We used 2 k-points in the irreducible part of the Brillouin-zone and a cut-off energy 3.0Ry. A perspective view of the upper half of the unit-cell is shown in Fig.7.5. The positions of each atom in the relaxed (3 × 3)-structure can be found in appendix A.1.1. They are given with respect to a Cartesian coordinate system which is shown in Fig.7.3. The z-coordinate of the origin is located half a bondlength below the first layer.

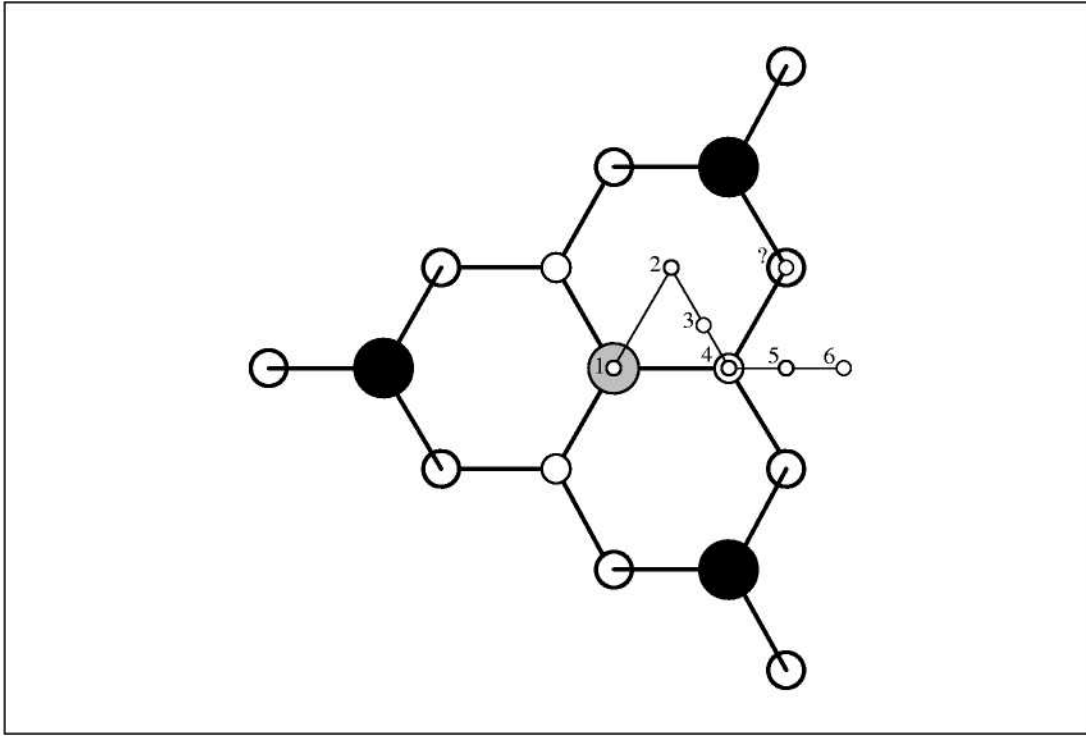


Figure 7.4: Schematic top-view representation of a portion of the Si(111) reconstruction containing three Si ad-atoms (large, filled black circles) and one rest atom (grey, filled circle) as well as the substrate atoms directly bonded to those (smaller open circles). The sites where the adsorbate atoms were placed by Cho and Kaxiras are indicated by the numbers 1-6, which refer to T_1 , H_3 , B_2 , T_4 , B'_2 and H'_3 -sites. From their papers it is not clear if they have placed an ad-atom at the position marked by "?".

The bondlength is given in atomic units (a.u.). The diffusion path of an extra ad-atom was calculated by mapping the total energy $E(x, y) = \min_z E(x, y, z)$ on a mesh by fixing the lateral positions of the extra ad-atom and minimizing the total energy with respect to the z -coordinate of the ad-atom. All other atoms, except the two innermost layers, i.e. the lowest layer in Fig.7.5, were allowed to relax freely. The two innermost layers were kept fixed to simulate bulk-crystal termination. We used a mesh of 10×10 -points, which is sufficiently dense to yield a good approximation of the diffusion path. Since the x - z -plane is a mirror-plane of the supercell the number of points which had to be calculated were reduced to 50. The results of the calculation are presented in Fig.7.6 and Fig.7.7. In both figures the total energy $E(x, y) = \min_z E(x, y, z)$ is shown. Dark areas indicate higher total energies, light areas lower total energies. Thus dark areas are regions of low binding energies and light areas indicate high binding energies of the extra ad-atom. The exact minima positions were calculated by a free relaxation of all atoms (except the two innermost layers), including the extra ad-

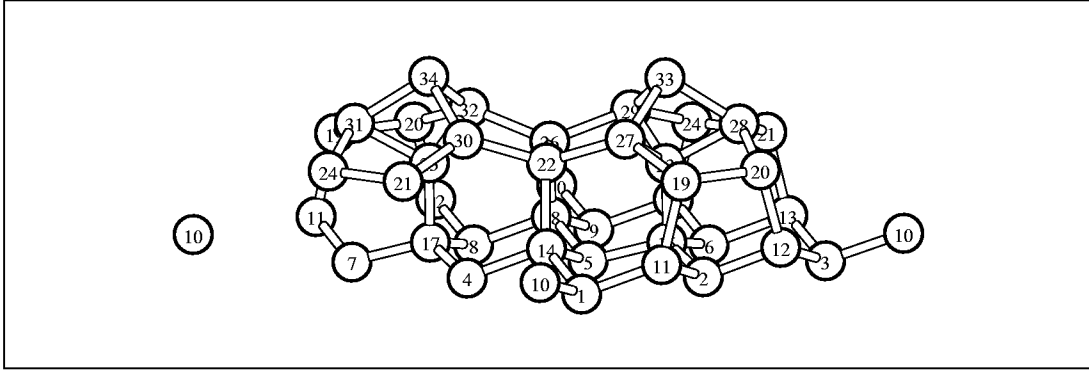


Figure 7.5: Perspective view of the upper half of the inversion-symmetric (3×3) -reconstructed supercell.

atom, starting from the favorite positions of the extra ad-atoms. The adsorption energy was found to be $\approx 4.5\text{eV}$ which is of the same order as the maximum adsorption energy of 3.94eV found by Cho and Kaxiras for the B_2 -position. The diffusion path is shown in Fig.7.7. The configurations and energies along the path (positions 2,3,4) are taken from the nearest grid points. The numbered circles indicate the calculated positions along the path. The most stable positions in the faulted and un-faulted half of the unit cell are number 1 and 5, respectively. The saddle-point (number 3) is located on the border of the faulted and un-faulted half. The energies relative to the adsorption energy at the most stable position are summarized in Table 7.2. The energy along the diffusion path and in addition

Position	1	2	3	4	5
adsorption energy	0.00 eV	0.27 eV	0.44 eV	0.34 eV	0.02 eV

Table 7.2: Energy along the diffusion path. The adsorption energy at the most stable position is set to 0.

a perspective view of the configurations of the extra ad-atom is shown in Fig.7.8. At the most stable positions the extra ad-atom sits at a bridge position between the ad-atom and one atom of the second layer. Moving towards the saddle-point it stretches the bonds to the ad-atom and second-layer atom. At the saddle point the bond between the ad-atom and second layer atom is re-established and the extra ad-atom does not show a covalent bonding to the surface. The barrier for diffusion beyond the boundary between the half-unit cells of $\approx 0.4\text{eV}$ found by our calculations is much lower than the activation energy of 1.14eV measured by [SKI00]. Thus, there must be a more stable extra ad-atom position on the Si(111)(7 × 7) than on the Si(111)(3 × 3) surface which might be the H_3 -position found by Cho and Kaxiras.

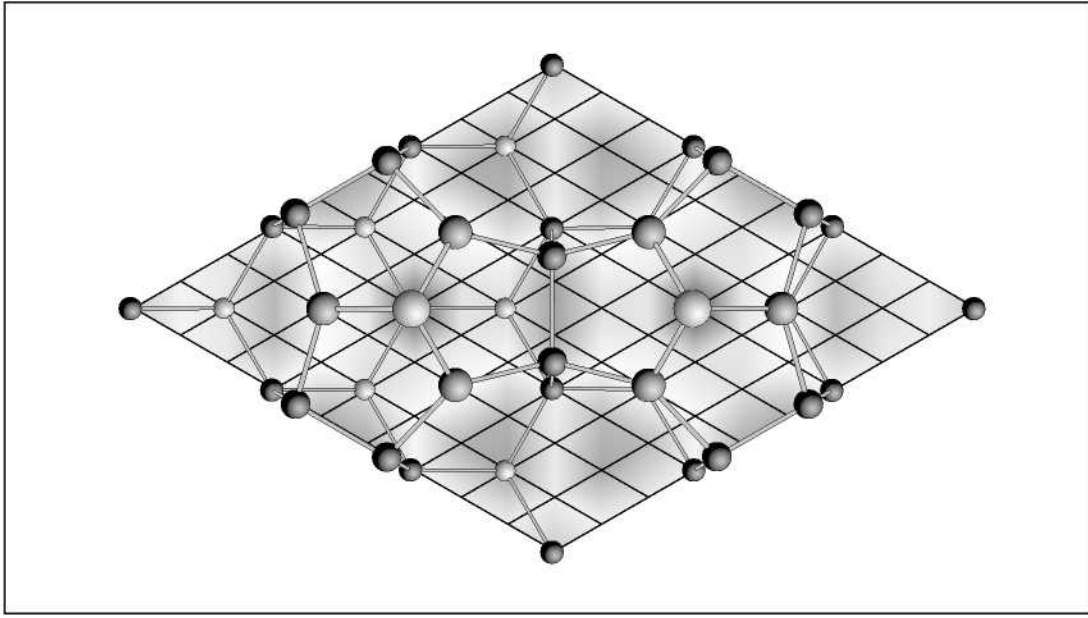


Figure 7.6: Total energy $E(x, y) = \min_z E(x, y, z)$ of an extra ad-atom on the (3×3) -reconstructed Si surface. Extra ad-atoms show a stronger binding in the light than in the dark areas. The grid-lines indicate the mesh on which the lateral coordinates of the extra ad-atoms were kept fixed.

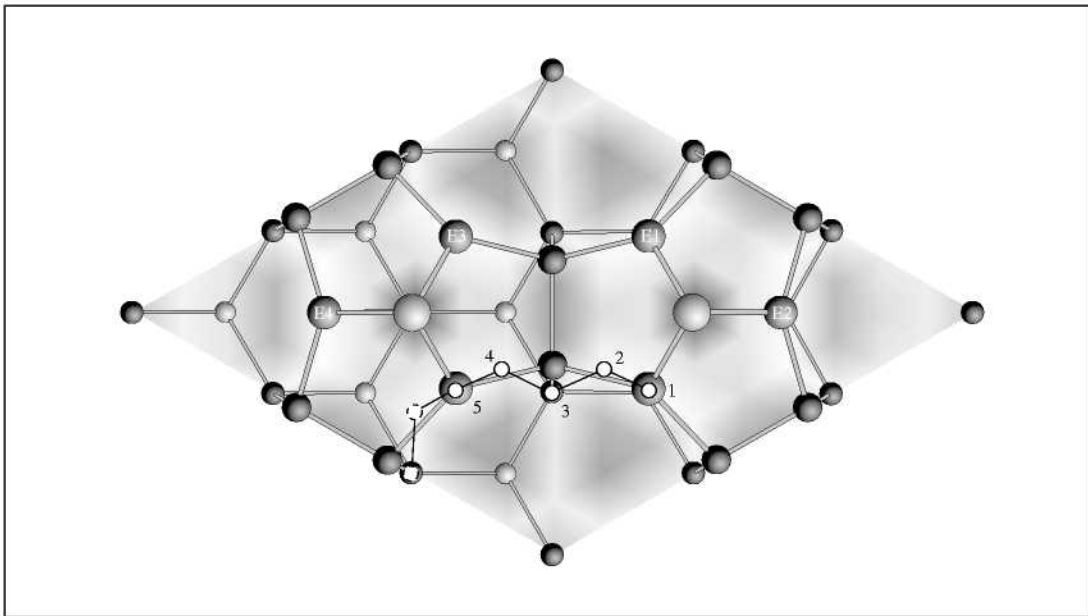


Figure 7.7: Top-view of the diffusion path. The circles indicate the calculated positions.

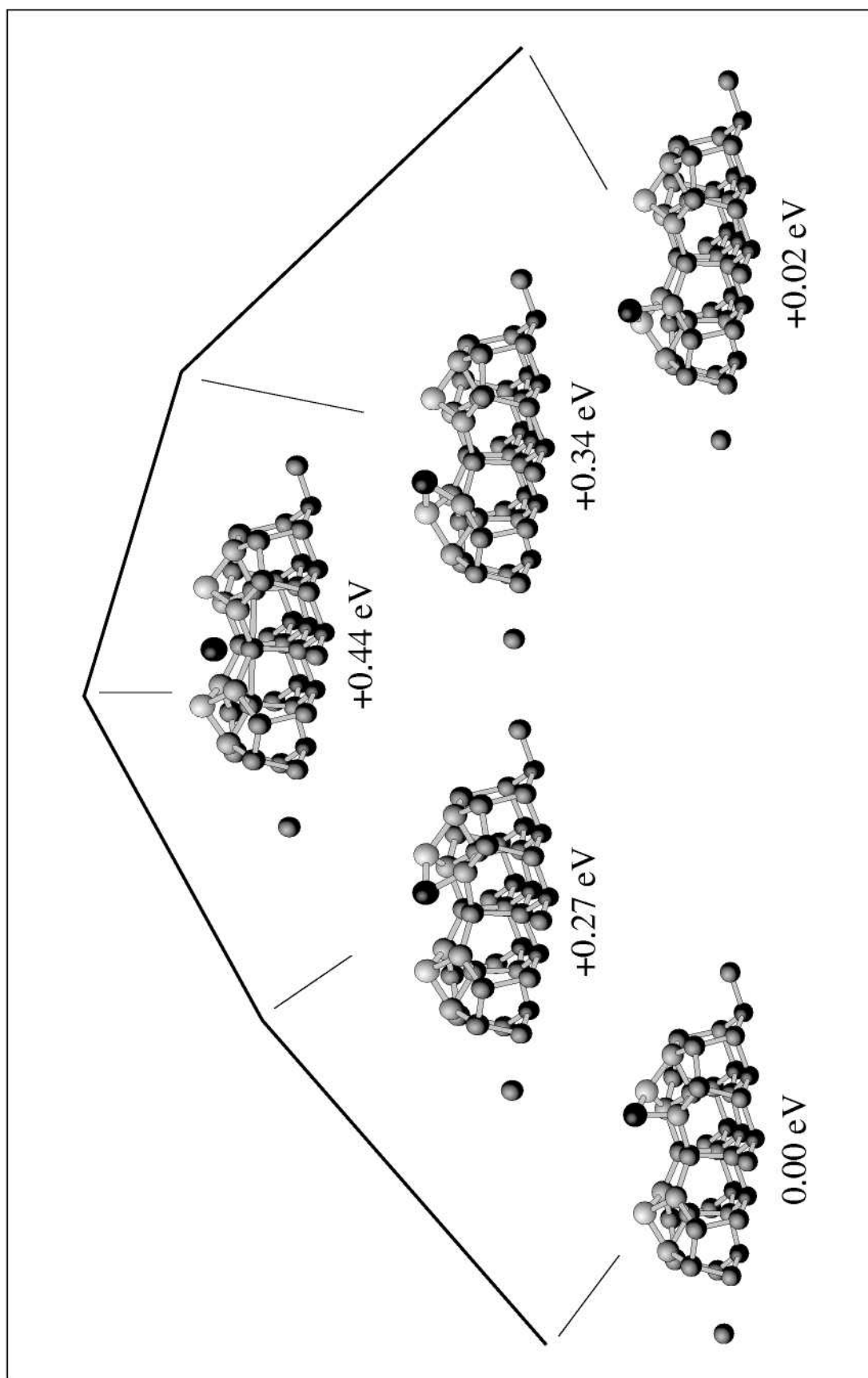


Figure 7.8: Energy along the diffusion path. The path proceeds from position 1 on the left to position 5 on the right. The energies are not symmetric in the faulted and unfaulted half.

7.4 Small Clusters on Si(111) (3×3)

Understanding growth on Si(111)(7×7) is a complicated task. During growth the stacking fault in one half of the unit cell has to be converted to a normal bulk-structure, the dimers have to be broken and the corner holes have to be filled with Si atoms. Depending on the growth temperature the consecutive (7×7)-reconstruction is formed in the next layer simultaneously or in an annealing step afterwards. One first step towards the understanding of growth on Si(111)(7×7) is to identify the stable positions of Si ad-atoms. To get a first impression how Si ad-atoms are arranged on the (7×7) surface, the structure of small clusters with n atoms, $n \leq 5$, were studied. All calculation were carried out in a (3×3)-supercell, as for the investigation of the diffusion path. All structures were relaxed until the forces were below 1 mRy.

To allow a comparison of the different structures the mean adsorption energies for the n -clusters were calculated

$$E_{mean}^n = \frac{E_{tot}^n - n \cdot E_{Si}^{Vac}}{n}, \quad (7.1)$$

where E_{tot}^n is the total energy of the supercell after relaxation and E_{Si}^{Vac} is the energy of a Si atom in the vacuum (taken from an pseudo atom calculation).

The change in energy by increasing the size from a $(n-1)$ -cluster to a n -cluster by adding a Si atom out of the vacuum is defined as:

$$E_{cl}^{diff} = E_{cl}^n - (E_{cl}^{n-1} + E_{Si}^{Vac}). \quad (7.2)$$

The initial positions of the additional Si ad-atoms are shown in Fig.7.9. The relaxed configurations of the atoms in the upper half of the inversion symmetric supercell can be found in Appendix A.1.1.

In configuration (a) the extra Si ad-atom (1) sits on top of one Si atom of the second layer where the ad-atom binds to. This position is equivalent to all other extra ad-atom positions on top of a second-layer atom (around the ad-atom) due symmetry. The extra ad-atom breaks the bond between the second-layer atom and the ad-atom, and binds itself to the second layer atom and the neighboring ad-atom. The mean adsorption energy at this position is -4.20eV

The same configuration has been calculated for an extra ad-atom (2) in the unfaulted half of the unit cell (b). The adsorption energy is practically identical to the one of configuration (a).

In the next configurations (c) and (d) two extra Si ad-atoms (1,3 and 2,4) where positioned on top of a second layer atom close to the ad-atom. The extra ad-atoms and the original ad-atom form a triangle, where one of the corner atoms is positioned below the other Si atoms. A perspective view of the relaxed structures can be found in Appendix A.1.1. Comparing the energies in the faulted and unfaulted half shows that the difference in the mean adsorption energy is very

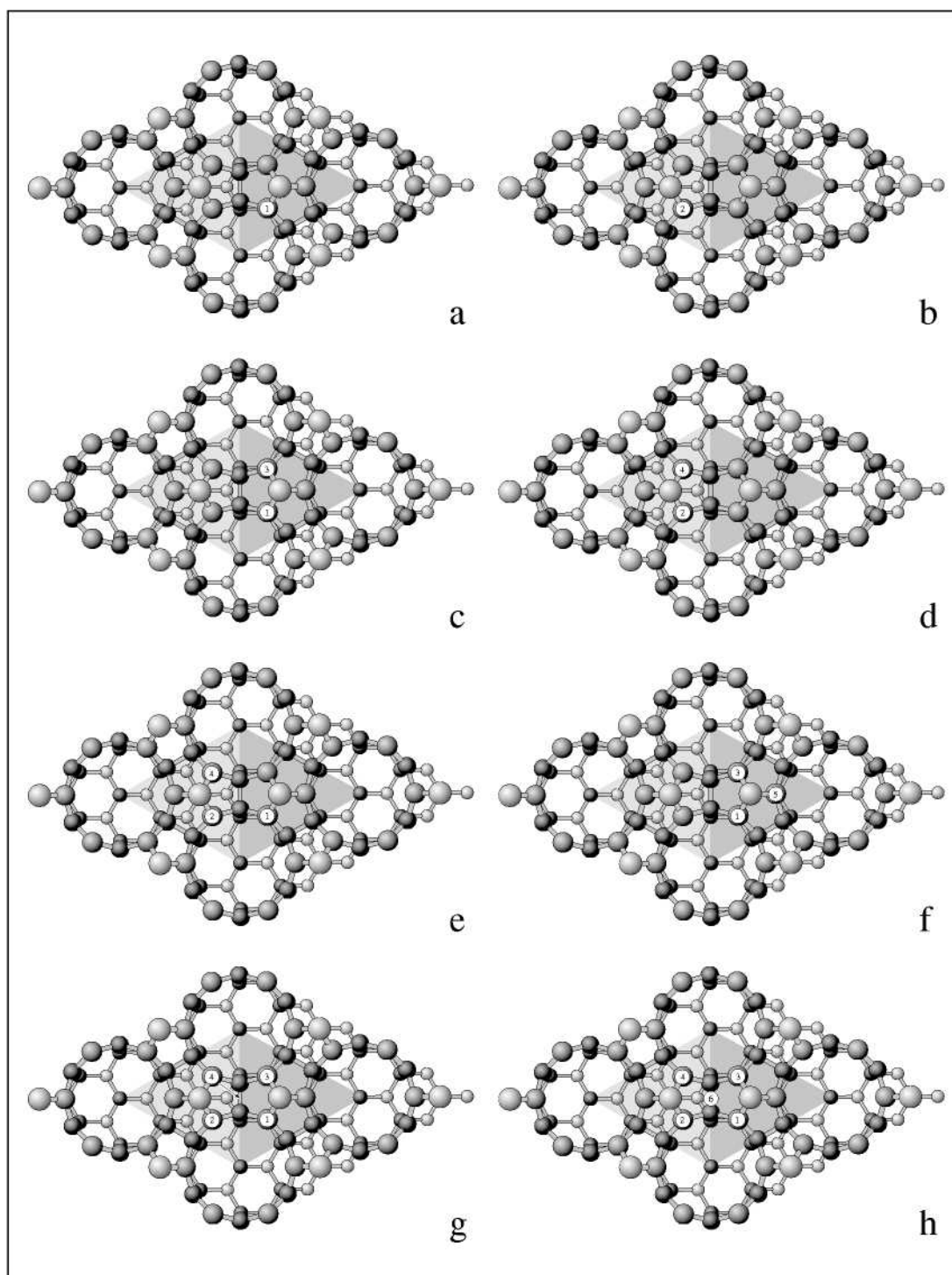


Figure 7.9: The initial positions of Si extra ad-atoms on Si(111)(3 × 3) are indicated by white circles.

small, -4.64eV for configuration (c) and -4.66eV for configuration (d). Since only a small cut-off energy of 3.0Ry was used and the forces were not relaxed below 0.1mRy , this difference is not significant. Thus, in the following calculations the configurations on the faulted and unfaulted half were not calculated separately. Another possible arrangement for two extra ad-atoms would be to put one extra ad-atom in each half of the unit cell. In our calculations a significant interaction between extra ad-atoms in different halves of the unit cell could not be observed due to the large distance between the extra ad-atoms. This will change drastically in configuration (g).

There are two different configurations (e) and (f) for three extra ad-atoms on the surface. In (e) two of them (2,4) are positioned in one half of the unit cell, above two second layer atoms, parallel to the dimer in the third layer. The third atom is put above a second layer atom in the other half of the unit cell. The energy of this configuration was estimated to be a combination of (b) and (d). Thus, the mean adsorption energy is -4.50eV . In configuration (f) all three extra ad-atoms sit on top of second layer atoms, forming a trimer. The ad-atom is lifted to a position above this trimer. The mean adsorption energy for this structure is -4.71eV .

The most interesting configuration is (g). In the initial arrangement the extra ad-atoms are placed above the second layer atoms parallel to the dimer in the third layer. Relaxation leads to a configuration where the extra ad-atoms and the ad-atom in each half of the unit cell form a trimer where the extra ad-atoms are above the ad-atom like in the relaxed configurations (c) or (d). In this partly relaxed positions, where the extra ad-atoms are raised to a higher position compared to single extra ad-atoms, they start to interact and move towards each other. Further relaxation breaks the symmetry of the extra ad-atoms. One extra ad-atom (4) moves downwards to the center of the unit cell, above the dimer. This structure show the largest mean adsorption energy of -4.97eV .

Starting with the positions of the atoms in configurations (g), a symmetric arrangement of 5 extra ad-atoms on the Si(111)(3×3) surface was calculated last. In the final configuration the atoms 1, 2, 3, and 4 are in a position above the ad-atoms and atom 6. The mean adsorption energy, -4.90eV , is close to the mean adsorption energy of structure (g).

The energies for the different arrangements of extra Si ad-atom on Si(111)(3×3) are summarized in Table 7.3.

Comparing the mean adsorption energies we can show that for clusters consisting of less than 4 Si atoms, an arrangement of the extra Si ad-atoms in one half of the unit cell is energetically favorable compared to the distribution of the extra ad-atoms on both half of the unit cell. A significant difference between the faulted and unfaulted could not be discovered. For clusters consisting of more than three Si atoms the formation of clusters above the center of the unit cell is preferred, where the extra ad-atoms can be found in both halves of the unit cell.

Recently Sato *et al.* [SKI00] have studied the initial adsorption process of Si

Table 7.3: Energetic evolution of the cluster formation of extra Si ad-atoms on Si(111)(3 × 3). The mean adsorption energy E_{mean}^n is given in the first row. The second row lists the change in energy E_{cl}^n by increasing the size from a $(n - 1)$ -cluster to a n -cluster by adding a Si from the vacuum.

Conf.	a	b	c	d	e	f	g	h
n	1	1	2	2	3	3	4	5
E_{mean}^n	-4.20	-4.20	-4.64	-4.66	-4.50	-4.71	-4.97	-4.90
E_{cl}^{diff}	-4.20	-4.20	-5.08	-5.12	-4.20	-4.82	-5.73	-4.61

atoms on Si(111)(7 × 7) by scanning tunneling microscopy. They found cross-shaped bright dots, exactly at the center of the unit cell, which do not exist on the clean (7 × 7) structure. They assume that they have found a Si-tetramer as shown in Fig.7.10. In their suggested structure the tetramer is not formed by four additional ad-atoms but by two extra ad-atoms and two ad-atoms which leave their tetraeder positions and move towards the center of the unit cell. In our calculations we have found no evidence that the extra ad-atoms interact before at least two extra ad-atoms are located in each half of the unit cell. Nevertheless, we have found the structure given by Sato *et al.* to be locally stable with a mean adsorption energy $E_{mean}^n = -4.55\text{eV}$. This is 0.11eV higher in energy than the preferred structure (d) of two extra Si ad-atom located around the ad-atom in the unfaulted half of the Si(111)(3 × 3) unit cell. Sato *et al.* stated explicitly that the bright spots are only found above the dimer at the center of the (7 × 7) unit cell, and not above a dimer close to the cornerholes. Exactly this dimer position cannot be modeled by a (3 × 3) nor a (5 × 5) unit-cell. Thus, this structure might be preferred on the (7 × 7) reconstructed surface.

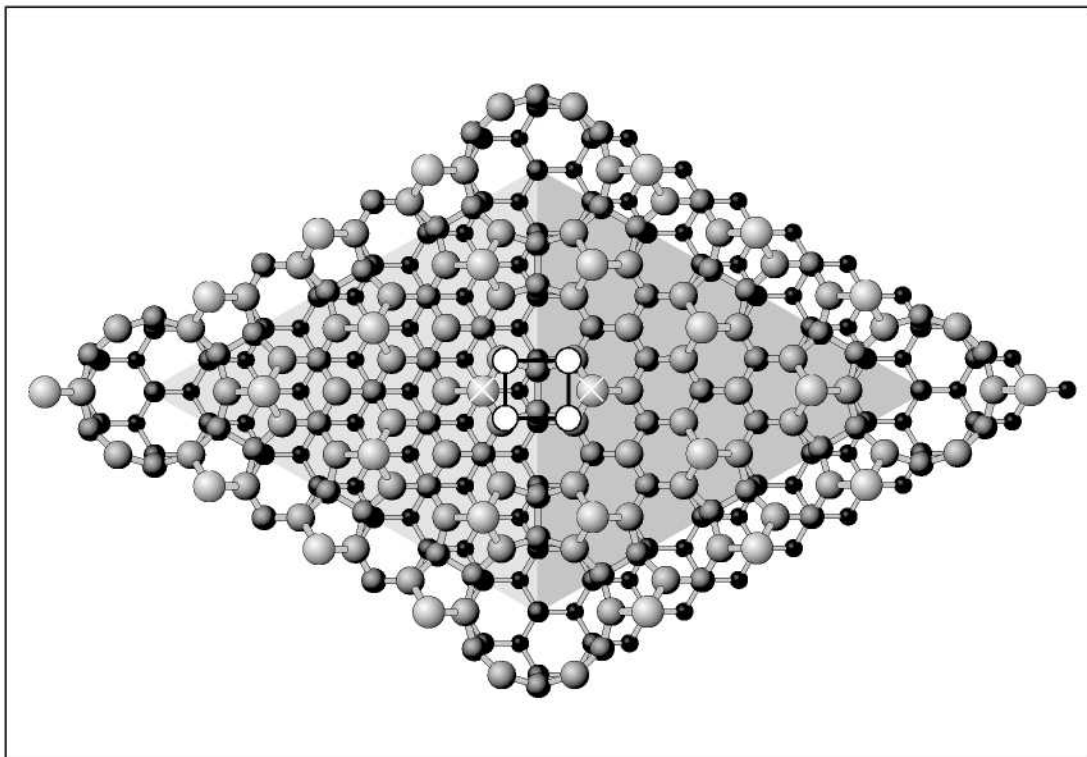


Figure 7.10: The initial positions of Si extra ad-atoms on Si(111)(7×7) are indicated by white circles.

Chapter 8

Surfactant modified Growth

8.1 Introduction

Epitaxial growth is a central problem in surface and materials physics. In particular, the advances in electronic materials have resulted in the use of multicomponent films with increasing requirements of controlling growth to obtain smooth abrupt interfaces. Depending on materials combinations growth of epitaxial films cannot be achieved easily. Instead growth often proceeds (i) with the formation of isolated three-dimensional islands either right from the very beginning of the deposition (island or Volmer-Weber growth), or (ii) after the deposition of several monolayers in a layer-by-layer mode (Stranski-Krastanov growth mode). The reason for island formation in the first case is the incomplete wetting of the substrate by the film material. This happens when the following interrelations of the surface free energies of the substrate, σ_s , over-growth material, σ , and the interface, σ_i , respectively, is met:

$$\sigma_s < \sigma + \sigma_i \quad (8.1)$$

Then it is favorable to keep a large area of the original surface uncovered. In the second case islanding is caused by the nonzero lattice mismatch of both materials although the condition for complete wetting is fulfilled:

$$\sigma_s > \sigma + \sigma_i \quad (8.2)$$

By manipulating the kinetics of deposited atoms one may be able to grow a continuous film B on substrate A, even if this is thermodynamically unfavorable. However, growth at low temperatures and/or high growth rate may result in poor crystal quality.

A deliberate pre-treatment of substrates with small amounts of foreign species can have a significant effect on the subsequent growth of thin films. Among such foreign species those known as surfactants are of special interest. The classic definition of surfactant is “surface-active agent, also called surfactant, substance

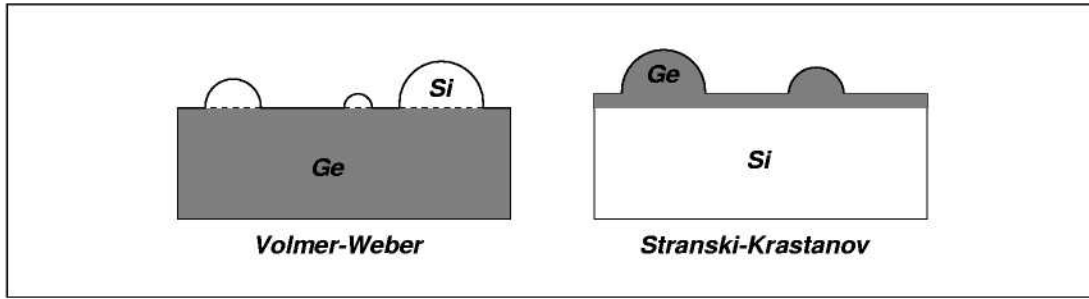


Figure 8.1: Under equilibrium conditions Si does not wet a Ge surface due to the difference in surface free energy. Si immediately forms three dimensional islands. Ge wets a Si surface and forms a Stranski-Krastanov layer of 3 monolayer thickness before it forms three-dimensional islands. Now the reason is accumulation of strain energy due to the lattice mismatch of $\Delta a = (a_{Ge} - a_{Si})/a_{Si} \approx 4\%$.

such as a detergent that, when added to a liquid, reduces its surface tension, thereby increasing its spreading and wetting properties” [Bri]. In solid state physics the term “surfactant” refers to a monolayer or a submonolayer of foreign atoms on the surface which exhibit two key properties: First, surfactants tend to change the growth mode of films from three-dimensional island growth to layer-by-layer growth. Second, surfactants tend to flow on top of the growing film as deposition proceeds. Ideally, surfactants are not incorporated as a contaminant in the growing film.

This behavior has been demonstrated for metal systems (Ag on Ag(111) by van der Vegt *et al.* [VPL⁺92]). The presence of Sb can induce layer-by-layer homoepitaxial growth at conditions typical for island growth in the pure system. The same has been shown for semiconductor systems: Si on Si homoepitaxy by Voigtländer *et al.* [VZWB95] with As as surfactant and Ge on Si heteroepitaxy by von Hoegen *et al.* [Hoe94, HCT⁺94] with Sb as surfactant.

8.2 Surfactant Mechanisms

The early observations of the surfactant effect were attributed to a modification of thermodynamic functions such as the surface energy of the films and substrates. The use of the term surfactant emphasizes the presumed thermodynamic origin of the effect. From a thermodynamic point of view a good surfactant has to satisfy the following inequality of the binding strength E_i :

$$(E_{A-A}, E_{A-B}) > (E_{A-S}, E_{B-S}) \gg E_{S-S} \quad (8.3)$$

as was originally shown for metal-on-metal homoepitaxial growth by Zhang *et al.* [ZL94]. Here A denotes the substrate atoms, B the adsorbed atoms and S the surfactant atoms. Otherwise the adsorbed atoms would either grow on top of the

surfactant atoms ($E_{B-S} > E_{A-B}$), or the surfactant atoms would tend to form clusters on the surface ($E_{S-S} > E_{A-A}$).

However, most thin films are grown far from equilibrium such that thermodynamic factors are not likely to be very important. Growth on a crystal surface is usually initiated by nucleation: the deposited adatoms diffuse on the surface until they meet and form nuclei. After a short period, a saturation density of nuclei is reached and further deposited atoms condense at the existing nuclei which grow into two-dimensional islands. The adatoms deposited on top of these islands determine how the film growth proceeds. Three-dimensional growth results when these adatoms form stable nuclei on top of the existing islands before the islands themselves grow to coalescence. A way to depress second-layer nucleation is to deplete the population of adatoms on top of the islands by increasing the probability that these atoms move down to lower layers of the film surface. This process is known as interlayer mass transport.

There are several ways how surfactants can alter the kinetics of interlayer mass transport. Zhang *et al.* [ZL94] have introduced a measure F which determines the probability that an atom will hop down from an island to a lower level terrace:

$$F \sim \frac{t_1}{t_0} \cdot \frac{N_p}{N_{tot}} \cdot \exp\left(-\frac{E}{k_B T}\right) \quad (8.4)$$

where t_1 is the average time interval between the deposition of two consecutive adatoms on a given island, t_0 is the average residence time of an adatom on the island, N_p is the number of sites along the perimeter of the island, N_{tot} is the total number of sites on the island, E the activation barrier for an adatom to step down from a site N_p , and $k_B T$ the thermal energy. The first ratio t_1/t_0 in Eq.(8.4) gives the fraction of time the first atom which landed on top of the island remains isolated before being joined by a second atom. The second ratio gives the hop attempts to step down. Assuming that a dimer will form an immobile nucleation center, F measures the probability that an adatom will hop off to a lower layer before a second adatom arrives on the same island, and thus is a measure of the interlayer mass transport. As can be seen in Eq. (8.4) modifying either the deposition rate or the island perimeter to island size ratio, or the activation barrier for stepping down will change the probability for an adatom to hop off to a lower layer. The latter two parameters can be altered by surfactant atoms which thus influence the interlayer mass transport.

8.2.1 Surfactant enhanced Island Density

It has been shown by Tersoff *et al.* [MVV⁺95b] that, as monolayer islands grow, there is a critical island radius R_c at which a second layer starts nucleating on top of the islands. If R_c is small compared to the island separation, islands will nucleate in a second layer before coalescence, yielding three-dimensional island growth. One possible mechanism to reduce both the island size and the spacing

between these islands is to enhance the island density. The importance of increasing the island density is that the mean island size becomes smaller. This in turn means that adatoms visit the rim of these island more often, so the frequency factor of the step-down rate is increased.

Surfactants are thought to enhance the island density by reducing the mobility of adatoms on the surface. This increases the probability that stable nuclei will be formed on the substrate, and hence increases the number of islands in the first layer of the film. For this mechanism to work, it seems that the surfactant must not affect the mobility of adatoms that are deposited on top of the islands. But Meyer *et al.* [MVV⁺95a] pointed out that only the difference between the hopping barriers on the terrace and at the step edges determines the amount of interlayer mass transport. Thus, if the barrier for diffusion on top of the surface is increased by the surfactant atoms and the barrier for stepping down is not affected, interlayer mass transport is enhanced.

Another possibility to enhance the frequency factor is to change the island shape. If the island shape is essentially compact, but the edge is rough, then the shape of the edge gives the adatoms more chance to escape, purely by geometry. A rougher edge also can result from reducing the mobility of the adatoms at the step edge.

Not only the mobility of adatoms influences the process of nucleation. Markov [Mar96] shows that surfactants affect the energetics of islands in two competing ways: The edge energy is decreased due to the saturation of dangling bonds with surfactant atoms at the rim of the islands. Thus less energy and a smaller number of atoms are required to form a critical nucleus. On the other hand the decoration of island edges with surfactant atoms leads to a larger circumference of the nuclei and to a larger work of nucleus formation and a larger number of atoms in the critical nuclei. Thus the presence or absence of surfactant atoms may result in different numbers of atoms in the critical nucleus at one and the same supersaturation.

For homoepitaxy on Si(111) modified by As/Sb as surfactant an increased island density was found by Voigtländer *et al.* [VZWB95]. It was shown by ab-initio calculation of the diffusion barriers by Schroeder *et al.* [SER98], that the increased island density was indeed caused by a reduced effective adatom mobility on the terrace compared to pure Si(111).

8.2.2 Surfactant modified Step-Edge Barrier

A second possible mechanism to increase the interlayer mass transport is a direct modification of the activation energy for climbing down across a step edge due to the step edge decoration with surfactant atoms. As has been shown by Markov [Mar94] for a system with a Schwoebel barrier, surfactant atoms can reverse the asymmetry of incorporating atoms at ascending or descending steps under the following assumptions: (i) the surfactant atoms occupy the kink sites on the

crystal surface, and (ii) the deposited atoms should displace them in order to join the crystal lattice. This gives rise to an additional kinetic barrier E_{Exch} the atoms have to overcome when joining an ascending step. One can speculate that the additional barrier depends on the number of bonds n which have to be broken between substrate and surfactant atoms:

$$E_{Exch} \approx n \cdot E_{surf-subst} \quad (8.5)$$

On the other hand, one could expect that for descending atoms the Schwoebel barrier is reduced due to the different strength of substrate-substrate and substrate-surfactant bonds:

$$E_{S_{red}} \approx E_S - n \cdot (E_{subst-subst} - E_{surf-subst}) \quad (8.6)$$

assuming that ad-atoms join a descending step from above by a replacing mechanism with and without surfactants.

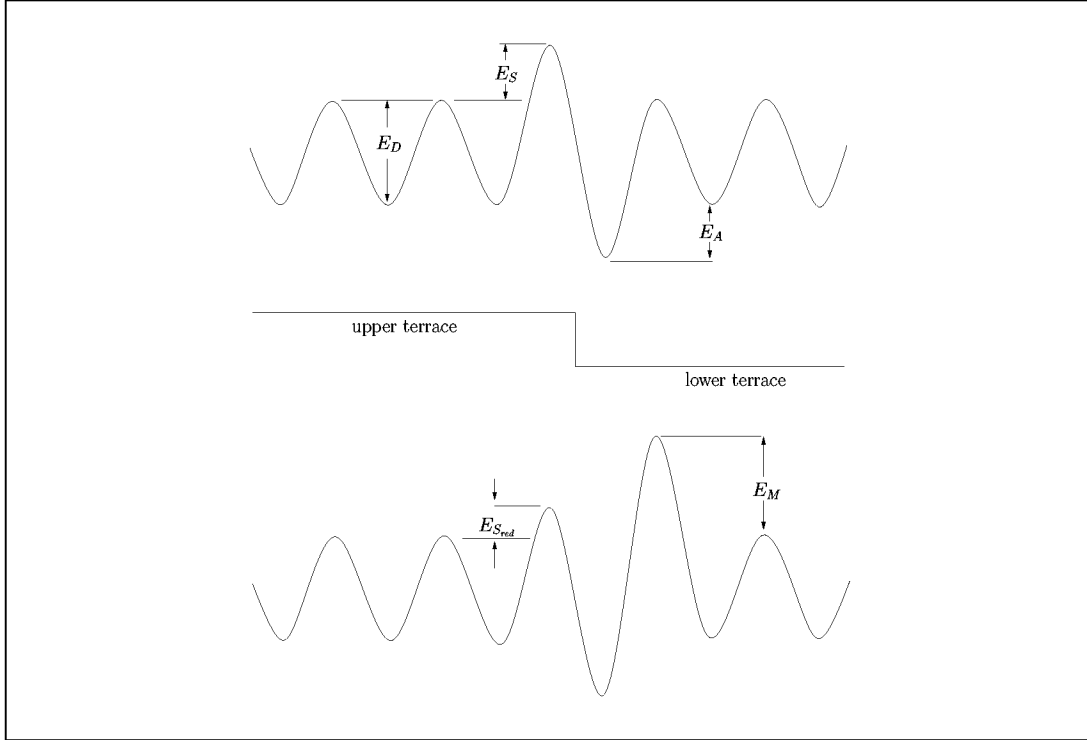


Figure 8.2: Schematic potential diagrams for atoms moving towards ascending and descending steps. E_D is the diffusion barrier, E_S and $E_{S_{red}}$ are Schwoebel barriers without and with surfactant respectively. E_A is the energy gained when joining a step, and E_{Exch} and additional barrier when joining an ascending step due to the necessary exchange with a surfactant atom.

Chapter 9

Homoepitaxial Growth on Si(111):As/Sb

In the preceding chapter the general surfactant mechanisms were discussed without taking into account the microscopic structure of the different systems. In the next section I will discuss the important structural features which allow group-V atoms to play the role of surfactants on group-IV substrates.

9.1 Surface Structures

The (7×7) surface reconstruction of pure Si(111), as described in section 7.2, changes drastically, if the Si substrate is covered with group-V atoms. Group-V atoms on the surface prefer three bonds, either to the substrate or to other group-V atoms. The remaining two electrons form a doubly occupied lone pair state, which lowers the surface free energy compared to Si dangling bonds. In (111) direction the Si/Ge bulk consists of a periodic arrangement of six layers. Pairs of Si/Ge layers, in which each atom has three bonds to the respective other one are significantly closer together. In the following such a pair will be called "double-layer". Surfactant atoms always replace Si/Ge atoms in the upper or lower part of this doublelayer, i.e. they are either incorporated into a doublelayer or sit on top of a full group-IV doublelayer. Depending on the substrate, e.g. Si or Ge, and the surfactant species, As or Sb, three different reconstructions are experimentally observed for a monolayer coverage: (i) The (1×1) reconstruction is achieved by simply replacing Si atoms in the upper part of a doublelayer with surfactant atoms, as is shown in the left side of Fig.9.1. Without any rearrangement of the surfactant atoms the surface is bulk-like terminated. The (1×1) reconstruction is realized for Arsenic on Silicon, Si(111):As. In this system the As-Si bondlength is close to its equilibrium value but the bond angles are too small. Thus tensile stress is exerted on the substrate as was shown by Meade and Vanderbilt [MV89]. (ii) In the (2×1) reconstruction the surfactant atoms sit on top of a full double-

layer. Thus there is only one surfactant-substrate bond. To saturate the other two bonds, every group-V atom is bonded to two other group-V atoms forming zigzag-rows on the surface as is shown in the middle of Fig.9.1. Antimony on Germanium, Ge(111):Sb shows this type of reconstruction. (iii) Instead of forming a zigzag-row it is also possible that surfactant atoms form trimers on top of a full Si/Ge doublelayer. In principle these trimers can be centered around two inequivalent positions on top of the surface, above a hollow site in the second Si/Ge layer, H3-centered, or directly above a second-layer atom, T4-centered, as is shown in Fig.(9.1) on the right side. The $(\sqrt{3} \times \sqrt{3})$ reconstruction with T4-centered trimers is the equilibrium structure for Antimony on Silicon, Si(111):Sb. Both, the (2×1) and the $(\sqrt{3} \times \sqrt{3})$ reconstructions, exert compressive stress on the substrate. The equilibrium structures of group-V surfactants on Si/Ge substrates and their implications for surfactant modified growth are discussed in a series of papers by Kaxiras *et al.* [Kax93, Kax95, KK95, Kax96]

9.2 Experimental Results

The Si on Si(111) homoepitaxy was studied experimentally in great detail by Voigtländer *et al.* [VZ93, VZWB95]. In their experiments, the Si(111) (7×7) substrates were prepared by an in situ thermal treatment. To prepare the surfactant covered surfaces Sb was evaporated on the silicon surface at a sample temperature of 670°C. As was evaporated from an effusion cell at 700°C sample temperature. After the furnace was shut off the sample was cooled down to 500°C until the gas pressure was below 10^{-9} mbar. Then the sample was cooled to room temperature. Si was grown on pure Si(111), As terminated Si(111) and Sb terminated Si(111) using an electron beam evaporator at a rate of 0.2 ML/min at different temperatures. The STM measurements were performed in an ultrahigh vacuum chamber in the constant current mode at sample bias voltage between 2.7 and -2.7 V and a tunneling current between 0.1 and 1 nA. Using the results of pure Si homoepitaxy as a reference, the STM images of the surfactant covered surfaces were analyzed after the deposition of a submonolayer Si. As shown in Fig. 9.2, the island density is drastically increased if the surface is covered with a monolayer of arsenic or antimony atoms. At 530°C the island density is 100 times for Si homoepitaxy on pure Si(111).

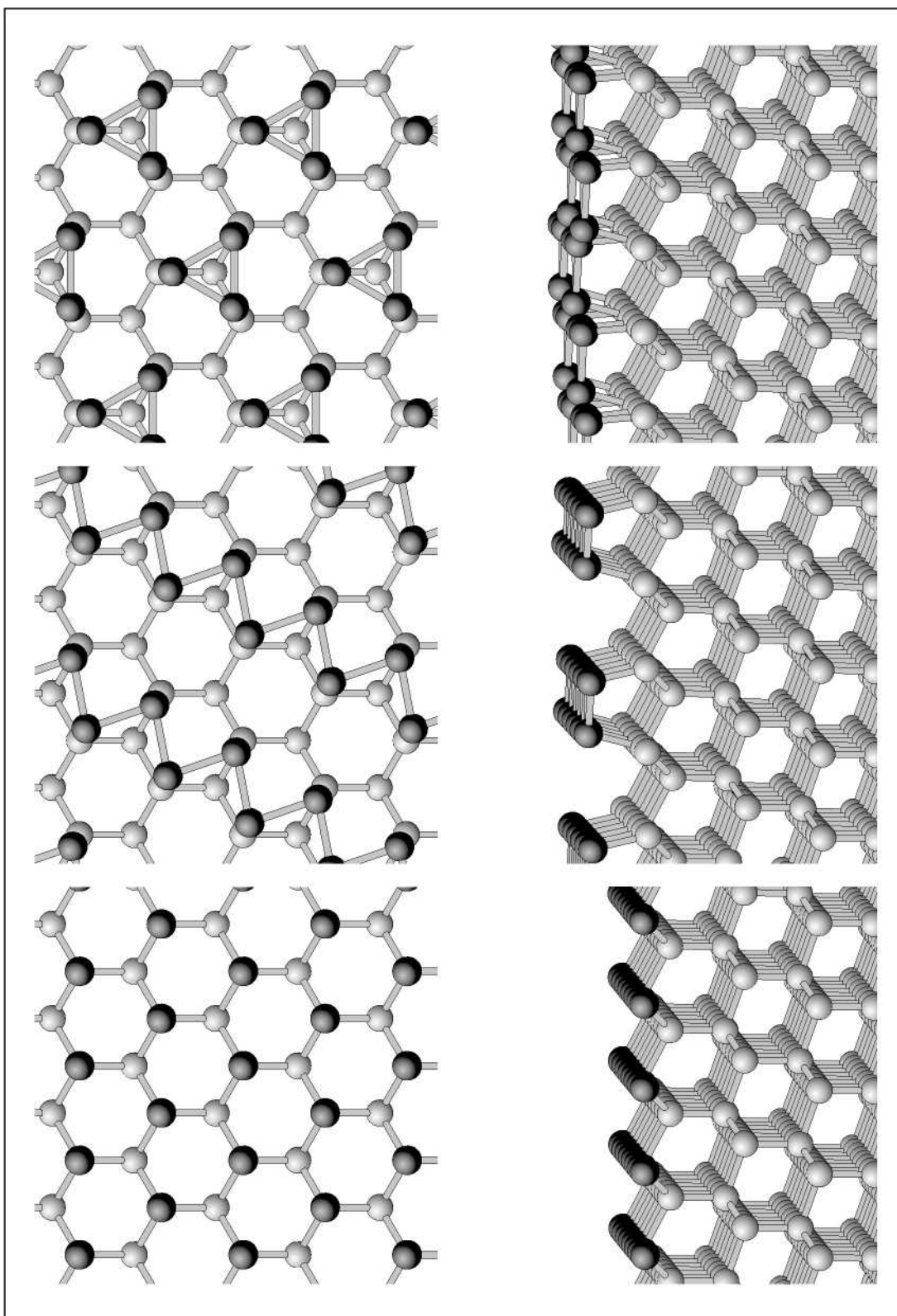


Figure 9.1: Top- and side view of the (1×1) , (2×2) and $(\sqrt{3} \times \sqrt{3})$ reconstructions (from left to right). Dark spheres refer to the surfactant-atoms light spheres to the substrate atoms. In top view only two Si-layers are shown to clarify the surfactant-atom positions relative to the substrate.

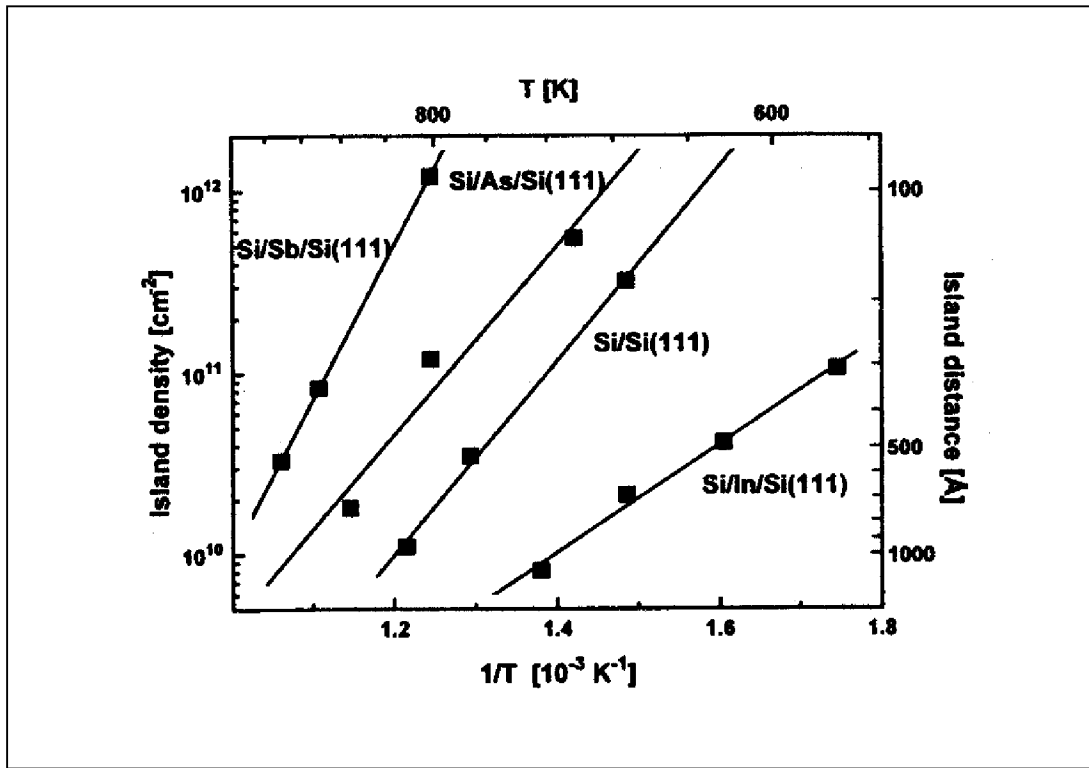


Figure 9.2: Island densities for submonolayer Si deposition shows Arrhenius behavior. Island densities for homoepitaxy on pure Si are found for surfactant covered (As,Sb) Si(111) which indicates small diffusion length.

The depleted zones at the step edges (Fig. 9.3) are also a measure for the diffusion length of Si adatoms. A more detailed analysis of the depleted zones at the step edge on the upper and lower terraces leads to the conclusion that there is no indication for a reflective potential barrier for the adatom motion in step-down direction, i.e. attachment at the step edges is as likely for adatoms coming from the lower or upper terrace.

The reduced diffusion length for surfactant-mediated Si homoepitaxy is also shown by other characteristic features of the growth morphology: The island shape and the form of the steps are irregular compared to the triangular island shape and the straight steps in pure Si/Si homoepitaxy. The STM images of As and Sb covered Si(111) show a surprising difference in the microstructure development of Si islands. Fig. 9.4 shows islands on the two surfaces after a deposition of less than 1 monolayer Si. For As-coverage (Fig. 9.4a), only islands bound by a meandering step with the height of a doublelayer are found. The surface on top of the islands as well as in between always shows the (1×1) terrace-equilibrium structure. On the other hand, for Sb (Fig. 9.4b) the experiments show an alternating sequence of terrace-equilibrium $(\sqrt{3} \times \sqrt{3})$ and (1×1) -structures. Compact islands with (1×1) -structure are growing on $(\sqrt{3} \times$

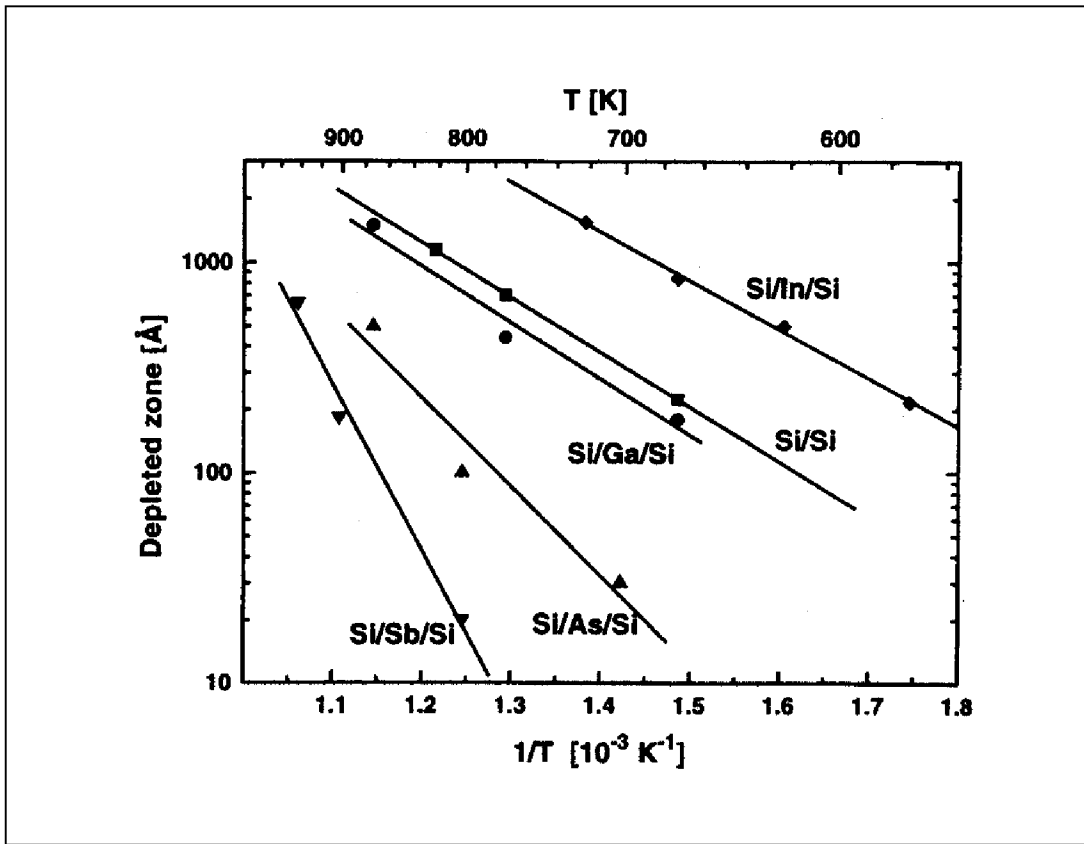


Figure 9.3: Depleted zones at the step edges as a function of temperature. The width of the depleted zone is a measure of the diffusion length for Si adatoms. The depleted zonewidth varies drastically in surfactant-mediated epitaxy.

$\sqrt{3}$) terraces which have the height of a single layer. In a second step T4-centered Sb-trimers are formed on top of the (1×1) -islands which grow into the $(\sqrt{3} \times \sqrt{3})$ terrace-equilibrium structure. The growth scenario for As- and Sb-mediated Si/Si homoepitaxy is drawn schematically on a non-atomic scale in Fig. 9.5. In this scheme a doublelayer consists of two elements with different height.

In Fig. 9.5a the As-mediated epitaxy is shown. The lower terrace is terminated by a short unit and thus shows the (1×1) -equilibrium structure. The island in the middle of the terrace consist of a doublelayer which is terminated by the (1×1) structure as well. Fig. 9.5b shows the Sb-mediated epitaxy. The lower terrace is terminated by the long unit and shows the $(\sqrt{3} \times \sqrt{3})$ terrace-structure of Sb terminated Si which is indicated by the fill pattern. On the terraces compact, monolayer high island form which consists of short units and show a (1×1) structure. On top of the (1×1) island, T4-centered trimers grow which coalescence to the $(\sqrt{3} \times \sqrt{3})$ structure. The structure of step edges in As- and Sb-mediated Si/Si homoepitaxy is discussed in more detail in section 10.

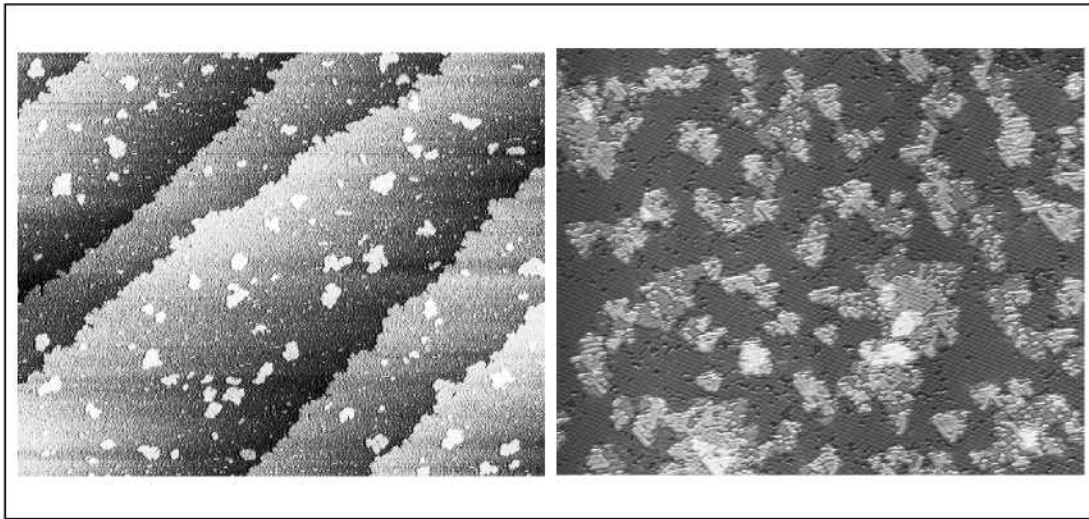


Figure 9.4: STM images of Si islands on surfactant-covered Si(111): (a) with As coverage, doublelayer height islands are formed which show the (1×1) -structure of the terraces: (b) with Sb-coverage, compact islands with (1×1) -structure are found on top of which smaller islands with the $(\sqrt{3} \times \sqrt{3})$ equilibrium structure of the terraces form.

9.3 Single Adatom Kinetics

The structure and kinetics of single ad-atoms on surfactant covered surfaces have been thoroughly investigated in our group [SER98, SAB⁺00, SABB00]. All calculations have been carried out with the **ES**tCoMPP-program, which was also used in this work. The surfactant covered surface was simulated by a repeated slab model consisting of 6 atomic Si(111) layers for the (1×1) surface structures in an inversion symmetric arrangement (and 8 layers for the $(\sqrt{3} \times \sqrt{3})$ structures), 1 monolayer (ML) surfactant on each Si surface, and in addition one ad-atom on each surfactant layer. The surfaces were separated by a vacuum equivalent to at least 6 atomic Si layers ($> 10\text{\AA}$). In lateral directions a (3×3) periodic cell was used. Four \mathbf{k}_{\parallel} -points in the surface Brillouin-zone and a 13.69 Ry cutoff energy in the plane wave basis set were necessary to obtain well converged results. To establish minimum energy configurations the forces were converged to less than 0.1 mRy/a.u.

The kinetics of ad-atoms is characterized by the competition of diffusion on top of the surfactant layer and the incorporation into the surfactant layer. Thus, the equilibrium positions of single Si ad-atoms on top of the surfactant layers as well as the equilibrium substitutional positions after exchange for all structures discussed in the preceding section were calculated. To determine the equilibrium structures a symmetry-unrestricted geometry optimization was carried out where all atoms except the two innermost layers could move freely. The diffusion and exchange barriers were determined for the Si(111):As system by restricted re-

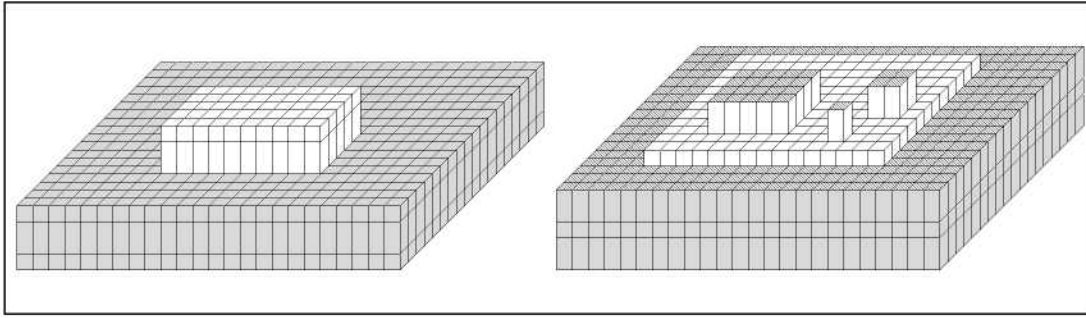


Figure 9.5: Schematic growth scenario: (a) with As coverage double layer height islands are formed which show the (1×1) -structure of the terraces: (b) with Sb-coverage compact islands with (1×1) -structure are found on top of which smaller islands with the $(\sqrt{3} \times \sqrt{3})$ equilibrium structure of the terraces form, which is indicated by the fill-pattern.

laxations similar to the "hyper-plane adaptive constraint (HAC)" method, i.e. by minimizing the energy subject to additional constraints. The results are summarized for single Si ad-atoms on As-covered Si(111)(1×1) and on the two relevant structures of Sb-covered Si(111) surfaces in Table 9.1.

9.3.1 Si Ad-Atoms on Si(111):As

The microscopic diffusion path on top of the As-layer is the same for all group-IV atoms (Fig. 9.6): The H3 position (on top of the hexagonal hole in the surface

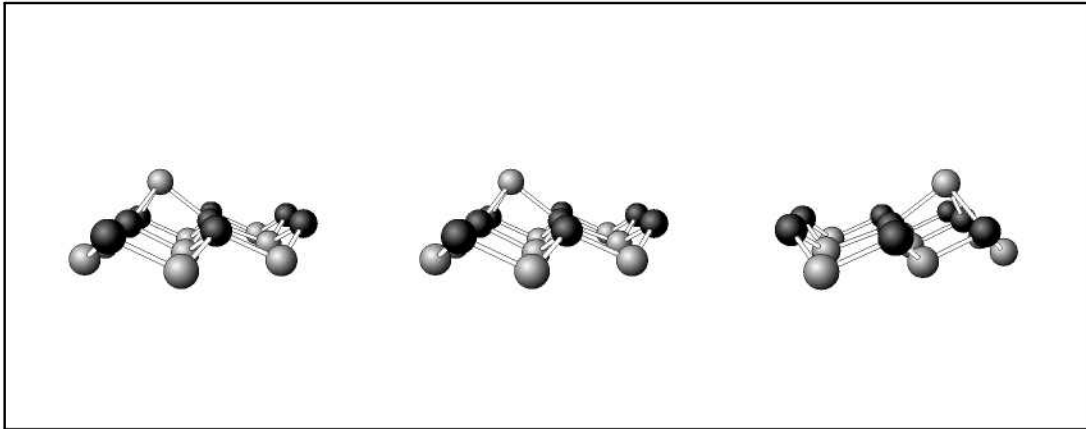


Figure 9.6: Diffusion path of Si ad-atoms on Si(111):As in perspective view: from the equilibrium configuration H3 on the left to the saddle point configuration T4 in the middle to a neighboring equilibrium configuration H3 on the right.

double-layer) is the equilibrium configuration of the ad-atoms, T4 (on top of the second layer Si) is the saddle-point. The height of the diffusion barrier is $E_D \approx 0.25\text{eV}$.

The exchange path from Si ad-atom to substitutional Si is rather complicated with several minima and saddle-points. The exchange path is shown in perspective view with one intermediate saddle-point configuration in Fig.9.7. The

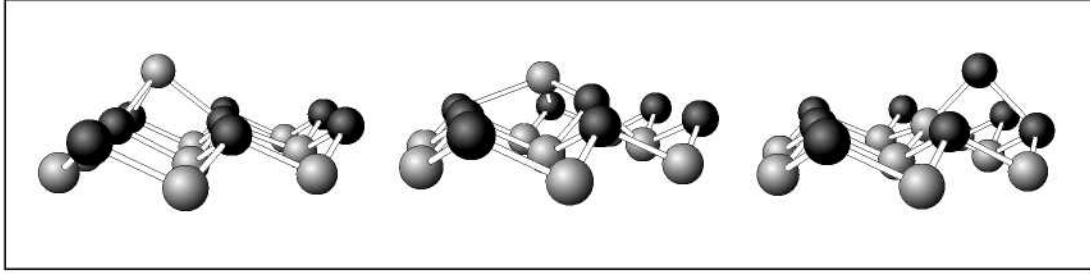


Figure 9.7: Exchange path of Si ad-atoms on Si(111):As in perspective view: from the equilibrium configuration H3 on the left to a saddle-point configuration (Si-As-pair before full re-bonding has taken place) in the middle to the equilibrium substitutional-site on the right.

exchanging Si-As pair performs an concerted motion which avoids to a large extend the simultaneous breaking of bond. A top-view of the exchange path, which gives an impression of the complicated motion, is shown in Fig. 9.8. First, the Si ad-atom moves partially towards the diffusion saddle-point breaking the bond to only one of the three As neighbors. Then it dips down towards the Si-layer, while one of the As atoms moves out of its substitutional position. There is a first local minimum position SM1 where both exchanging partners bind to atoms in the layer below. Then the path proceeds to a dimer configuration where the Si and As atoms form a dimer molecule lying parallel to the surface with the center nearly vertically above the original substitutional As position. The final section brings the Si atom to the substitutional position with the formation of tetrahedral bonds while the As atom moves upwards and finally ends up as an As ad-atom at a bridge position between the Si atom and a second As atom. The fact that the bonds are broken one at a time is the reason for the unexpected low activation barrier of $E_{Ex} \approx 0.27\text{eV}$. The reexchange barrier is the $E_{Reex} = E_{Ex} + E_B \approx 1.06\text{eV}$. The energy along the diffusion path and along the exchange path is shown in Fig. 9.9. The atomic configurations for important minima are shown as insets: *H3*: ad-atom equilibrium; *SM1*: asymmetric dimer; *Si_{sub}*: substitutional Si and As ad-atom. As can be seen, the barrier for diffusion (from H3 over T4 to another H3 position to the left) is as high as the exchange barrier (from H3 over SM1-, dimer-configuration to the substitutional position on the right).

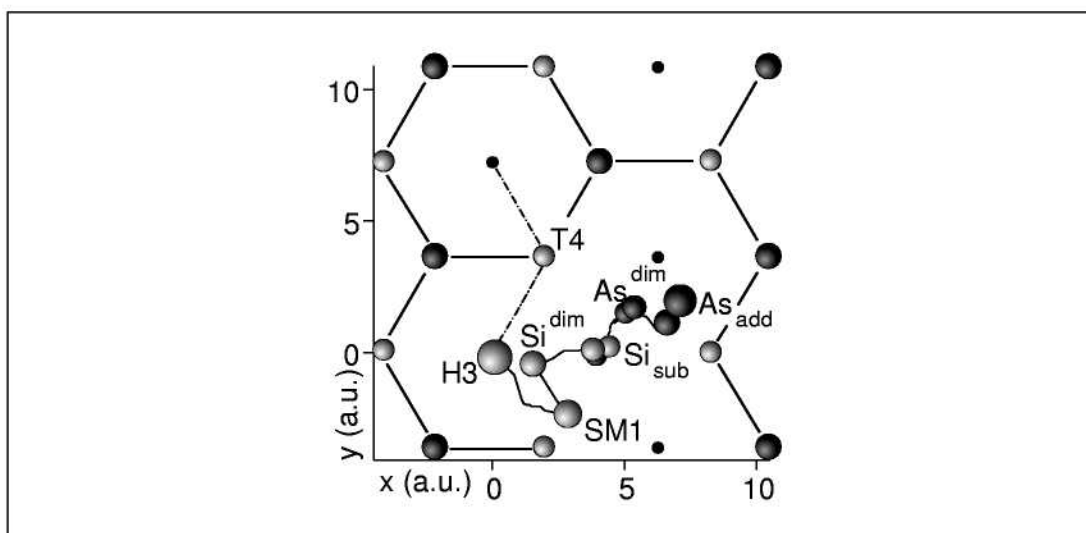


Figure 9.8: Top view of the exchange path of Si on Si(111):As. The exchange process involves the concerted motion of the two exchanging partners and the relaxation of the neighboring atoms. The path consists of several sections between local equilibrium sites (SM1, dimer). The Si atoms are indicated by lighter – the As atoms by darker spheres. The size of the spheres indicates the height of the atoms.

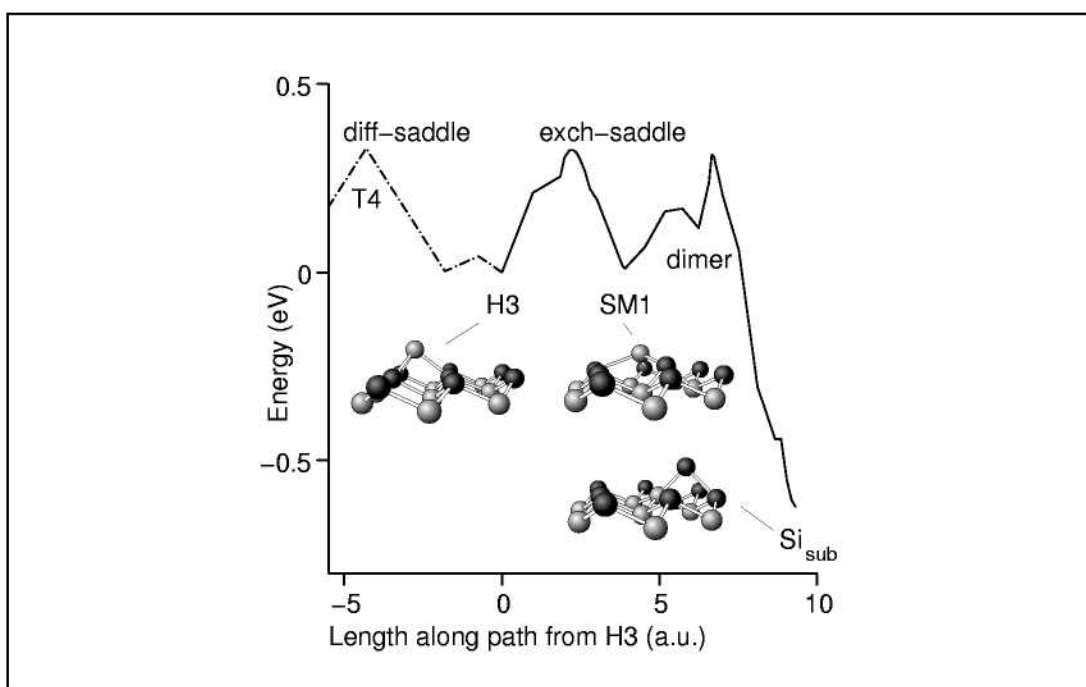


Figure 9.9: Energy versus path.

9.3.2 Si Ad-Atoms on Si(111):Sb

For the Sb-covered surface one has to consider two different surface structures. The calculations show that the geometry of single Si ad-atoms on Si(111):Sb(1×1) is identical to Si on Si(111):As(1×1). The diffusion path is the same ($H3$ equilibrium, $T4$ saddle-point), and the diffusion barrier is of the same height ($E_D \approx 0.2eV$). But, both the exchange barrier ($E_{Ex} \approx 0.6eV$) and the energy gained by the substitutional Si atom ($E_B \approx 1.5eV$) are much larger than on As-covered Si(111). Thus the re-exchange energy ($E_{Re-Ex} \approx 2.1eV$) is also very much larger than on Si(111):As.

Si ad-atoms on Si(111):($\sqrt{3} \times \sqrt{3}$) have a very different geometry. The $T4$ -trimer structure is much more open than the (1×1) structure, there are more possible inequivalent sites for the ad-atoms. The ($\sqrt{3} \times \sqrt{3}$) structure shows $T4$ sites occupied by Sb-trimers as well as empty $T4$ and $H3$ sites. The diffusion path is shown in Fig. 9.10. The Si atom moves from an equilibrium $H3$ -position

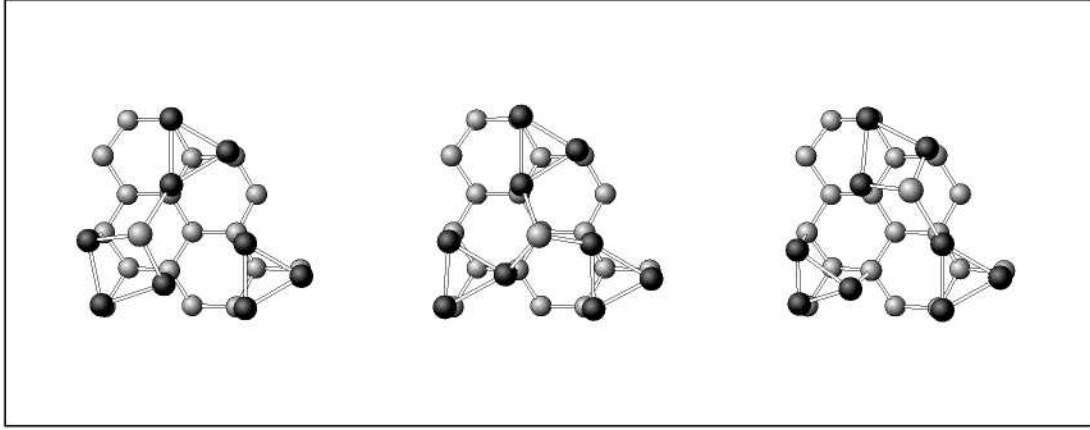


Figure 9.10: Diffusion path of Si ad-atoms on Si(111):As($\sqrt{3} \times \sqrt{3}$) in top-view: from the equilibrium configuration ($H3$) on the left to the saddle point configuration (empty $T4$ -site) in the middle to a neighboring equilibrium configuration ($H3$) on the right.

over the empty $T4$ -site saddle-point to neighbored $H3$ -position. The diffusion barrier on the ($\sqrt{3} \times \sqrt{3}$) is $E_D \approx 0.55eV$. The third configuration mentioned above, the Si ad-atom on the occupied $T4$ site (on top of the Sb-trimer) has a much higher energy and is avoided by the diffusing Si ad-atom. The exchange of the Si ad-atom with one of the Sb-atoms in the $T4$ -trimer is shown in Fig. 9.11. The exchange has an extremely low barrier ($E_{Ex} \approx 0.2eV$). The energy gain is $E_B \approx 0.8eV$. The configuration of the exchanged Si-Sb pair is very close to the geometry of the atoms in the (1×1) structure: The Si atom sits at a position in the lower half of an additional double-layer, the Sb atom in the upper layer, at an $H3$ -site with respect to the full Si double-layer. The reexchange energy is $E_{Reex} = E_{Ex} + E_B \approx 1.0eV$ which is similar to the one for Si on As-covered

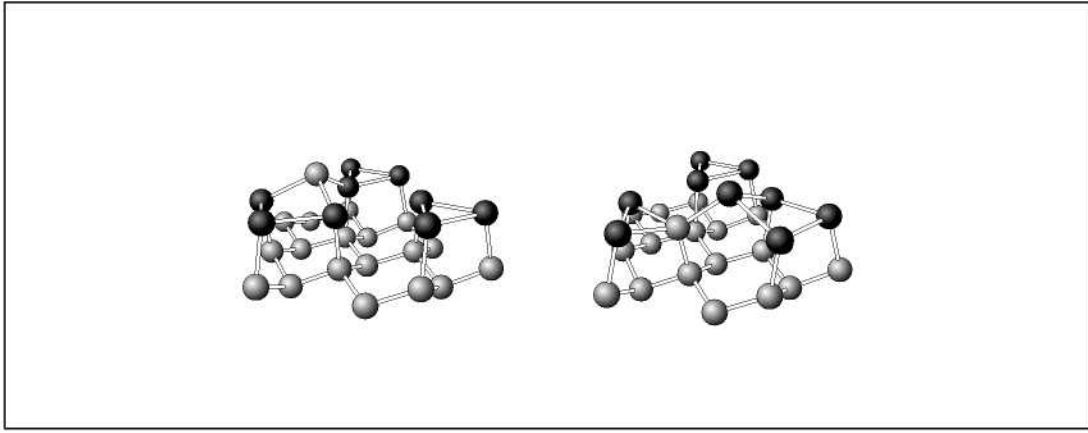


Figure 9.11: Exchange path of Si ad-atom on Si(111):As($\sqrt{3} \times \sqrt{3}$) in perspective-view: The equilibrium ad-atom configuration (H3) is shown on the left, the substitutional equilibrium position on the right site.

Si(111). The geometry in Fig. 9.11 shows that this reexchange can directly lead to a displacement of the Si ad-atom to a neighboring $H3$ -site different from the original one before an exchange, which is equivalent to a diffusion jump.

9.3.3 Preliminary Conclusions for the growth mechanisms

The quantitative results for the binding energies and barriers are summarized in Table 9.1.

Conf	Si(111):As (1×1)	Si(111):Sb (1×1)	Si(111):Sb ($\sqrt{3} \times \sqrt{3}$)
E_D	0.25 eV	0.21 eV	0.55 eV
E_{Ex}	0.27 eV	0.60 eV	0.20 eV
E_B	-0.80 eV	-1.50 eV	-0.80 eV
E_{Re-Ex}	1.06 eV	2.10 eV	1.00 eV
$E_{D,eff}$	1.06 eV	0.21 eV	1.00 eV

Table 9.1: Binding energies and activation energies of Si ad-atoms on Si(111):As and Si(111):Sb

For Si ad-atoms on Si(111):As(1×1) the activation energy for exchange is not larger than the diffusion barrier across the surfactant covered terrace ($E_{Ex} \approx E_D \approx 0.25\text{eV}$). Thus, Si ad-atoms on Si(111):As (1×1) are very effectively

incorporated into the As-layer. After the exchange the Si atom is tightly bound at the substitutional site ($E_B \approx 0.8eV$). In order to perform a long-range diffusion the Si atom has to be reactivated to the surface by overcoming the re-exchange barrier ($E_{Re-Ex} = E_{Ex} + E_B \approx 1.1eV$). This is larger than the estimated diffusion barrier of 0.6 eV on clean Si(111) and thus the diffusion length of Si ad-atoms on Si(111):As (1×1) is expected to be reduced, which leads to an increase of the island density due to the As coverage, in full agreement with the experiments.

The experiments show always the (1×1) reconstruction on the terrace as well as on the islands. Thus, growth proceeds as double-layer growth. The open question is at what island size the double layer islands are manifested.

On Si(111):Sb(1×1) the diffusion barrier for Si ad-atoms has the same value as on Si(111):As(1×1) ($E_D = 0.2eV$). But, both the exchange barrier ($E_{Ex} \approx 0.6eV$) and the energy gained by the substitutional Si atom ($E_B \approx 1.5eV$) are much larger than on Si(111):As(1×1). Thus, the long-range diffusion behavior is governed by the normal on-top diffusion process.

Although the on-top diffusion is very fast, the experiments do not show large, compact islands on the Si(111):Sb(1×1) surface. A possible explanation, which has to be proved, is that the trimers which are growing on the Si(111):Sb(1×1), do not act as sinks for diffusing Si ad-atoms.

On Si(111):Sb($\sqrt{3} \times \sqrt{3}$) the diffusion barrier ($E_D \approx 0.55eV$) is larger than the exchange barrier ($E_{Ex} \approx 0.2eV$), which means that newly deposited Si ad-atoms will be incorporated immediately. The energy gain is $E_B \approx 0.8eV$. Thus, for the long-range diffusion the Si ad-atoms have to be reactivated to the surface by overcoming the re-exchange barrier ($E_{Re-Ex} = E_{Ex} + E_B \approx 1.0eV$) as in the case of Si on Si(111):As(1×1).

The experiments show large, compact, (1×1)-reconstructed islands with trimers on top. The reasonable assumption that the (1×1)-reconstructed islands acts as sinks for diffusing ad-atoms was recently proved by calculations in our group.

9.4 Island Evolution

The structures and energies of small clusters ($n \leq 4$) on a (1×1) reconstructed surface were studied in an inversion-symmetric (4×4) supercell, containing 96 Si atoms covered by 32 As (Sb) surfactant atoms plus the additional Si ad-atoms. Of the 8 layers in the supercell (6 Si layers plus 1 As(Sb) layer on each side), 6 were allowed to relax freely. The two innermost layers were kept fixed to simulate bulk-crystal termination. The ideal (1×1) reconstructed surfaces were separated by a vacuum equivalent to 10 atomic Si layers. For a fast comparison of the structures an energy cut-off of 9Ry and 1 k-point in the irreducible part of the Brillouin-zone was used. For Si(111):As the important structures were recalculated with an increased cut-off of 13.69Ry and 2 k-points in the irreducible part of the Brillouin-zone. The energetic order of the cluster was the same for both basis sets. All structures were relaxed until all forces were below 0.1mRy.

To allow a comparison of the different structures one has to define a quantitative measure which characterizes the clusters. This measure is the binding energy of the cluster respectively the change in energy by increasing the size of the cluster due to the incorporation of ad-atoms.

The energy of a n-cluster on the (1×1) reconstructed Si(111):As surface is defined as:

$$E^n = E_{tot}^n - E_{ref}, \quad (9.1)$$

where E_{tot}^n is the total energy of a surface with n Si atoms forming a cluster and E_{ref} is the total energy of a (1×1) reconstructed Si(111):As surface without any additional ad-atoms. With the definitions above $E^1 = E_{tot}^1 - E_{ref}$ is the energy of one exchanged Si atom (forming a 1-cluster) and $E_{SiH3}^1 = E_{tot,SiH3}^1 - E_{ref}$ is the energy of one Si ad-atom at the H3 position of the As layer. We define the binding energy of a single, incorporated Si atom relative to a Si ad-atom at the H3 position by

$$E_B^1 = E^1 - 1 \cdot E_{SiH3}^1, \quad (9.2)$$

Thus the mean binding energy of a n-cluster, compared to n separated Si ad-atoms, is given by

$$E_{Bmean}^n = \frac{E^n - n \cdot E_{SiH3}^1}{n}. \quad (9.3)$$

The change in energy by increasing the size of the cluster instead of creating a new cluster by a single exchange process somewhere on the surface is

$$E_{cl}^n = E_B^n - (E_B^{n-1} + E_B^1). \quad (9.4)$$

Considering the large energy gain ($E_B = 0.8\text{eV}$, see section 9.3.3) by incorporating a Si ad-atom into the As layer, the formation of clusters is expected to begin with by a series of exchange processes on the terrace. Nevertheless, after the first exchange an additional Si ad-atom might prefer a position on top of the surfactant layer close to the already exchanged Si atom. Thus, calculations with possible positions of a second Si ad-atom close to the exchanged Si atom were performed. The configurations are shown in Fig.9.12.

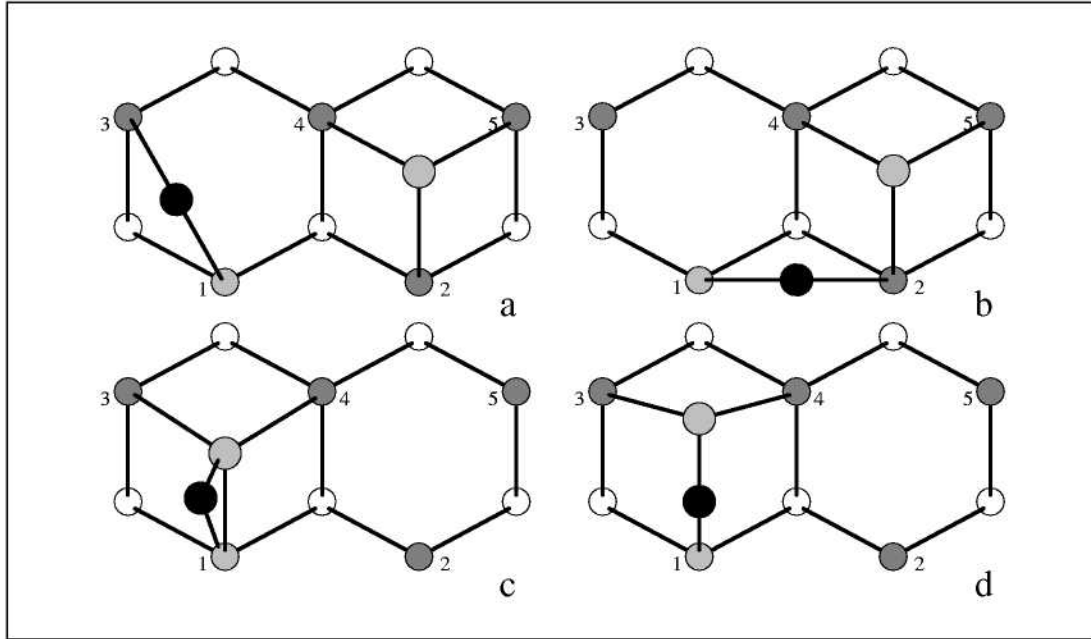


Figure 9.12: Schematic pictures of four of the calculated structures for one additional Si ad-atom and one exchanged Si atom. The white circles indicate the Si substrate atoms, the light shaded circles the two Si atoms, the darker shaded circles the As/Sb surfactant atoms and the black circles the As/Sb surfactant atoms which have been pushed out of their substitutional position by the incorporated Si atoms.

In the least stable configuration (a) the additional Si ad-atom is sitting on the surface at a large distance such that the two Si atoms do not interact. All other configurations are energetically compared to this structure.

The next configuration (b) where the Si atom on top shares a surfactant atom (2) with the As that was replaced by the exchanged Si atom is more stable by 0.52eV . The energy gain can be made plausible by the following arguments. Surfactant atoms in the ideal positions on top of the surface have always three bonds and one doubly occupied lone pair. In configuration (b) the exchanged As atom binds to the incorporated Si atom (position 1) and As atom (2). Thus, the lone pair is broken on As (2) and an additional Si ad-atom can saturate the bonds of As (2) again.

In configuration (c) the additional Si ad-atom sits on an $H3$ position binding to two As (3 and 4) and the exchanged Si (1) atom. The replaced As sits on top of the Si ad-atom and bends over to the exchanged Si atom position. The bending is limited since the Si ad-atom prefers a bond direction perpendicular to the surface. This configuration is already 1.97eV lower in energy than configuration (a) due to the saturation of the dangling bond of the Si ad-atom.

The most stable configuration (d) shows a similar arrangement of the atoms but the Si-Si distance is larger and the As atom is located between the exchanged Si atom and the Si atom on top of the surface. One can speculate that the As-Si dimer forms a double-bond. Then both Si atom would have four bonds and the As atom three bonds as on the ideal positions on the surface, which would explain the low energy of 2.00eV in this configuration.

Compared to the energy of two Si atom exchanged separately on the surface, configuration (a) is 0.35eV higher in energy. But the configurations (b)-(d) are 0.17eV, 1.62eV and 1.65eV lower in energy which means that one exchanged Si atom already acts as a sink for Si ad-atoms.

Table 9.2: Energy of different Si ad-atom and exchanged Si atom arrangements, see Fig.9.12. The energies in the first row (E_a) are given relative to the configuration with the highest energy (a). The energies in the second row (E_b) compare the configurations with two isolated-exchanged Si atoms. The third row gives the mean binding energy $E_{B_{mean}}^2$ per Si atom compared to two single Si ad-atoms on top of the surface.

Conf.	a	b	c	d
E_a	0.00eV	-0.52eV	-1.97eV	-2.00eV
E_b	+0.35eV	-0.17eV	-1.62eV	-1.65eV
$E_{B_{mean}}^2$	0.17eV	0.43eV	1.16eV	1.17eV

Starting with the configuration of a single incorporated Si atom, a series of calculation for possible arrangements of As atoms which were replaced by two neighboring exchanged Si atoms were carried out next. Six of the structures are shown in Fig.9.13.

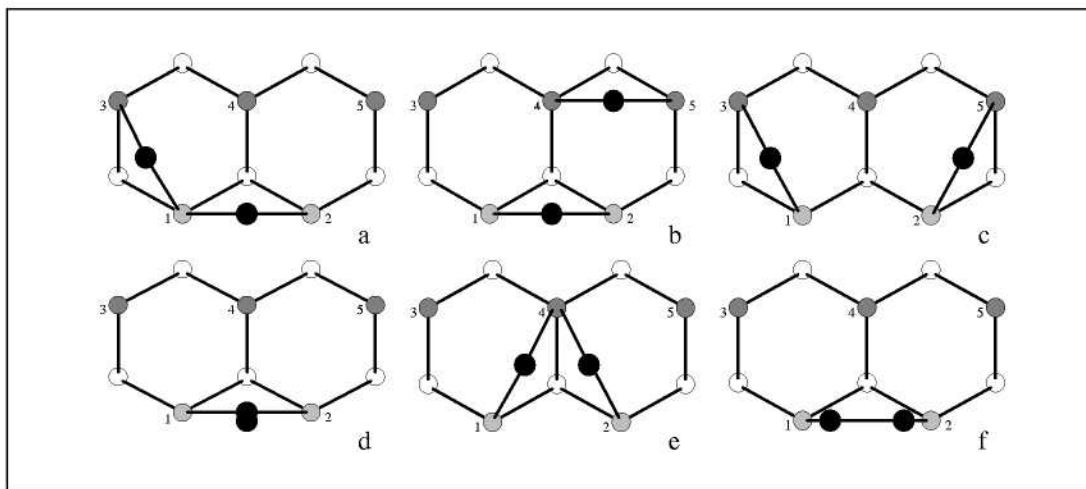


Figure 9.13: Schematic pictures of six of the calculated structures for two exchanged Si atoms. The white circles indicate the Si substrate atoms, the light shaded circles the two exchanged Si atoms, the darker shaded circles the As/Sb surfactant atoms and the black circles the As/Sb surfactant atoms which have been pushed out of their substitutional position by the incorporated Si atoms.

Configurations where the As atoms do not bind to either one or both of the Si atoms turned out to have very high energies due to the remaining Si dangling bonds and are not shown in Fig.9.13.

Configuration (a), where two As atoms bond to the same Si is the least favorable of the structures shown, since the As atoms share one Si bond. All energies will be given with respect to this structure.

Comparing configurations (b) and (c) one expects very similar energies for these structures since the numbers of As-Si and As-As bonds are identical. Indeed, configuration (b) is 1.04eV lower in energy, and configuration (c) is 1.06eV lower in energy than configuration (a).

The fourth configuration (d), with one As atom on top of the other, is already 1.45eV lower in energy.

Configuration (e) is 2.47eV lower in energy than (a). The two As atoms bind to one As atom in the surface and thus, the As atom at position (4) has saturated all five bonds (three to Si in the next layer and two As-As bonds). Although all atoms have saturated bonds it is not the most stable structure probably due the tilting of the As-Si bonds which prefer to be perpendicular to the surface.

The most stable structure is configuration (f), where two As atoms form a dimer on top of the exchanged Si atoms. It is 3.5eV lower in energy than

configuration (a). One can assume that the As-dimer atoms form a double-bond like in As_2 and thus all Si bonds are saturated and the As atoms have three bonds and one double occupied dangling bond each, as in the ideal positions on the surface.

Table 9.3: Energy of different surfactant atom configurations for two exchanged Si atoms. The energies in the first row (E_a) are listed relative to the least stable configuration (a). The mean binding energy ($E_{B_{mean}}^2$) per Si atom compared to two single Si ad-atoms is given in the second row.

Configuration	a	b	c	d	e	f
E_a	0.00eV	-1.04eV	-1.06eV	-1.45eV	-2.47eV	-3.50eV
$E_{B_{mean}}^2$	-0.17eV	0.35eV	0.36eV	0.55eV	1.04eV	1.58eV

Comparing the mean binding energies of the configurations of one exchanged atom plus one additional Si ad-atom and the energies for two next neighbored exchanged Si atoms, we find that the most stable configuration of two Si atoms on $\text{Si}(111):\text{As}$ consists of two next neighbored exchanged Si atoms where the replaced As atoms are arranged as shown Fig.9.13 (f).

From our calculations we can conclude that all configurations where the bonds of the incorporated Si atoms are not saturated by a nearby As atom (having a Si dangling bond) are energetically unfavorable and can be excluded when forming larger clusters. We proceed to form clusters of three neighboring incorporated Si atoms. Starting from the most stable arrangement of two exchanged Si atoms (Fig.9.13 (f)) the third Si atom can be incorporated at position 5 (or equivalent 3) or in a triangular arrangement at position 4 (see Fig.9.14).

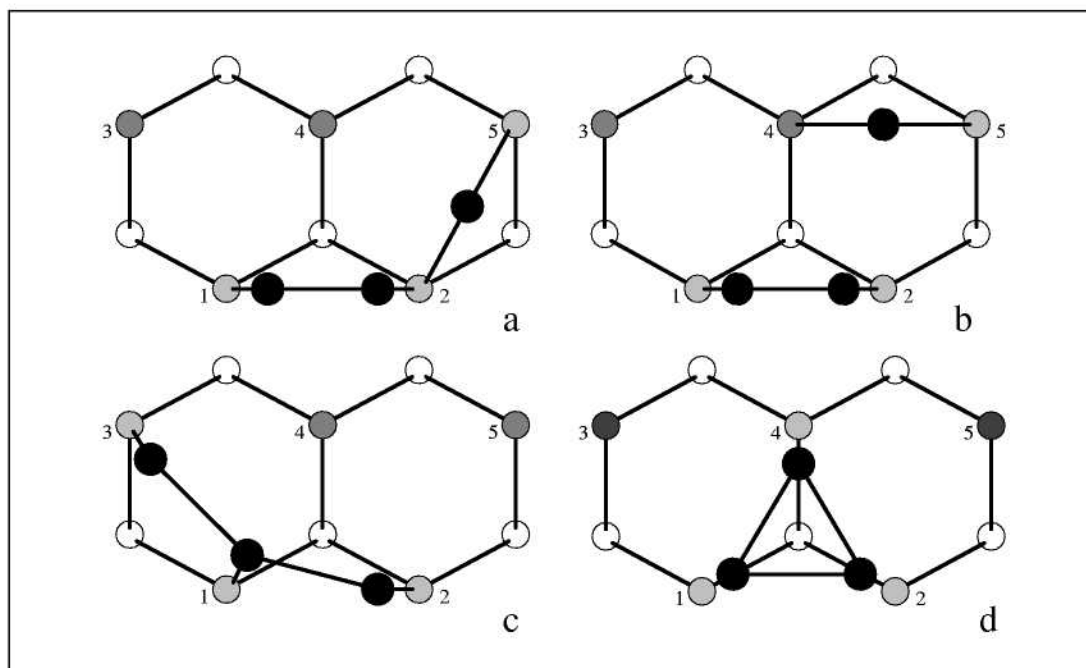


Figure 9.14: Schematic pictures of four possible arrangements of three exchanged Si atoms. The white circles indicate the Si substrate atoms, the light shaded circles the two exchanged Si atoms, the darker shaded circles the As/Sb surfactant atoms and the black circles the As/Sb surfactant atoms which have been pushed out of their substitutional position by the incorporated Si atoms..

Fig.9.14(a) shows the As atom placed between the new exchanged Si atom (on position 5) and an the exchanged Si atom (2). Thus, two As atoms share one Si bonds which has already been proved to be an unfavorable configuration (Fig.9.13 (a)).

The next configuration (b) is an exchange at the next neighbor position (5), where the As atom binds to a As atom in the surface. The energy of this configuration can be estimated to be the energy of configuration (f) in Fig.9.13 plus the energy of a separately exchanged Si atom. This energy is taken as the reference energy for the following structures.

It is also possible to construct a small chain (c). This structure is 1.09eV lower in energy than configuration (b), but if this would be the most stable arrangement

for three Si atoms on the Si(111):As surface, then it would also be favorable to form longer chains. Because the open ends of a chain-structure are the most unfavorable position, the mean binding energy would increase with increasing chain length. Experimentally there is no evidence for chain-structures on the Si(111):As surface during growth.

The most stable position is a trimer of three As atoms on top of three Si atoms (d). In this configuration all Si bonds are saturated and all As atoms have three bonds like in the ideal position on the surface. This structure is 2.71eV lower in energy than configuration (a). According to Kaxiras [Kax93, Kax95] and our calculations a full coverage of a Si(111) double layer with As trimers is the second most stable configuration, and it is the equilibrium structure of Sb on Si(111).

Table 9.4: Energy of different surfactant atom configurations for three exchanged Si atoms. Configuration (a) is ignored and the energies in the first row (E_a) are listed relative to configuration (b). The mean binding energy (E_{Bmean}^2) per Si atom compared to three single Si ad-atoms is given in the second row.

Configuration	b	c	d
E_a	0.00eV	-1.09eV	-2.71eV
E_{Bmean}^2	1.17eV	1.53eV	2.07eV

Starting from the trimer configuration, a fourth Si atom is added to the cluster. Instead of the exchange on the terrace, now the Si atom can also replace one of the As atoms which form the trimer. Instead of exchanging atoms on the ter-

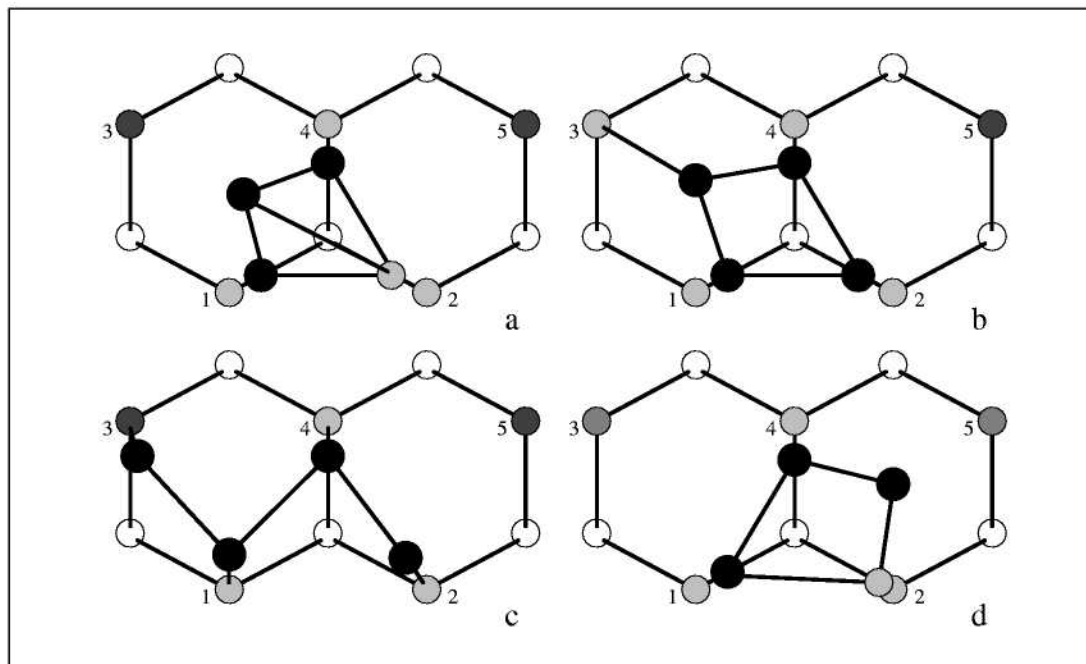


Figure 9.15: Schematic pictures of four possible arrangements of three exchanged Si atoms. The white circles indicate the Si substrate atoms, the light shaded circles the two exchanged Si atoms, the darker shaded circles the As/Sb surfactant atoms and the black circles the As/Sb surfactant atoms which have been pushed out of their substitutional position by the incorporated Si atoms..

race we can put the Si atom at various positions close to the trimer, i.e. in front of the trimer as ad-atom or on top of the trimer which results in structures with unfavorable high energies. Far lower energies were obtained by replacing one of the As trimer atoms with Si and varying the position of the replaced As atom. One stable structure is shown in (a). Starting from a position of the As atom centered on the trimer, the As relaxes to a position between the remaining two As trimer atoms, almost centered above the neighboring hexagon. All energies will be given with respect to this configuration.

Exchanging atoms on the lower terrace we can exclude a lot of possible configurations. From the previous calculation we know that the As atom, which is pushed out of its substitutional position by the Si atom, will not bind to one of the other Si atoms, since these bonds are already occupied by the As trimer atoms. If it binds to another As atom on the surface then we can estimate the energy approximately from the configurations we have determined before. One new structure is shown in (b), where the fourth As atom binds to other As atoms of

the trimer. This configuration is only 0.04eV lower in energy than configuration (a).

The third structure is formed by breaking up the trimer and forming a short chain (c). From the calculations of the 3-cluster we know, that the chain is not a favorable structure, and is only 0.09eV lower in energy than (a).

In the most stable structure (d) which is favored by 0.57eV compared to (a), the As atom sits at a bridge position between an As trimer atom and the Si corner atom. The As atom is also pushed slightly upwards and is close to a (1×1) -equilibrium structure in the second layer. By replacing one As trimer atom with Si an energy of 0.55eV is gained compared to a single Si exchange on the terrace. Thus the most stable arrangement of four Si atoms on the Si(111)(1×1) surface is the structure Fig.9.15 (d). This structure establishes the nucleus of double-layer island growth in homoepitaxy on Si(111):As.

Table 9.5: Energy of different surfactant atom configurations for four exchanged Si atoms. The energies in the first row (E_a) are listed relative to configuration (x). The mean binding energy ($E_{B_{mean}}^2$) per Si atom compared to four single Si ad-atoms is given in the second row.

Conf.	a	b	c	d
E_a	0.00eV	-0.04eV	-0.09eV	-0.57eV
$E_{B_{mean}}^2$	1.64eV	1.65eV	1.66eV	1.78eV

From the energetics of the different configurations of the small clusters one can make an educated guess how the growth of the cluster proceeds:

The two other As atoms in the trimer can also be replaced by Si atoms, yielding the structure of a 6-cluster of Si atoms shown in Fig.9.16 on the left side. The next exchange will then take place on the terrace, pushing one As atom up which will bind to one As atom in the upper layer as is shown in Fig.9.16 on the right side. Repeating this sequence of incorporating Si atoms in the upper new layer and on the terrace further growth of the cluster can be imagined as well.

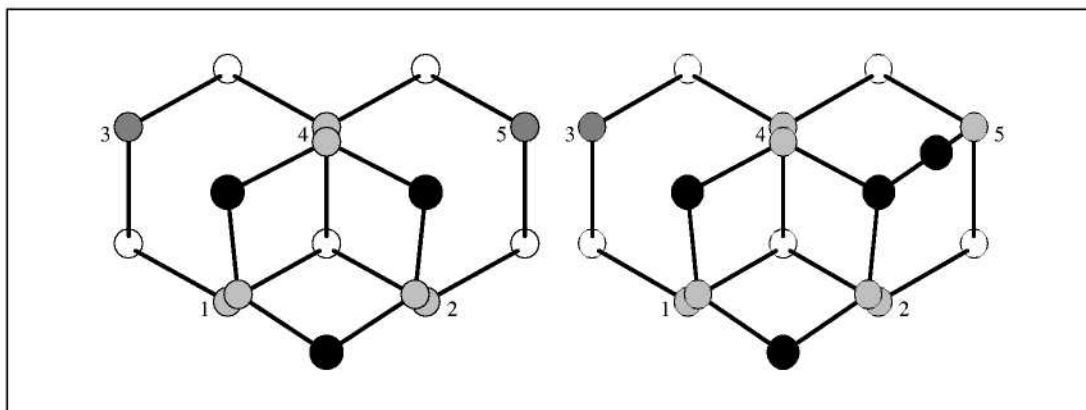


Figure 9.16: Further evolution of the cluster.

Combining the most stable configurations of Si atoms on the Si(111):As surface, cluster formation proceeds most probably in the sequence shown in Fig.9.17:

(i) One Si ad-atom is incorporated into the As layer. (ii) A second Si ad-atom is captured by the already exchanged Si atom while diffusing on the surface. The Si ad-atom exchanges at a neighboring position and the two As atoms form a dimer on top of the Si atoms. (iii) The third Si atom exchanges at neighboring sites to the Si cluster, constituting a triangle which locally completes a double layer, and the three replaced As-atoms form a T4-centered trimer on top of the Si atoms. (iv) The fourth Si atom attaches to the As trimer. It replaces one of the As atoms of the trimer and lifts it to a nearly ideal H3-position in the upper layer of the next double layer while itself sits in the lower layer. This attachment is energetically favorable compared to the individual exchange on the As covered terrace. Thus, this cluster of four exchanged Si atoms (decorated with four As atoms) is the nucleus for the double layer islands observed in experiments. (v) The growth of the tetramer then proceeds by attachment of additional Si atoms lifting the other two As atoms also to the next layer. Our proposal is that the neighboring As atoms which form the terrace are replaced by Si atoms establishing on each side of the triangle a structure similar to an As decorated step edge of $(\bar{1}\bar{1}2)$ orientation. Further growth proceeds very similar to the motion of steps.

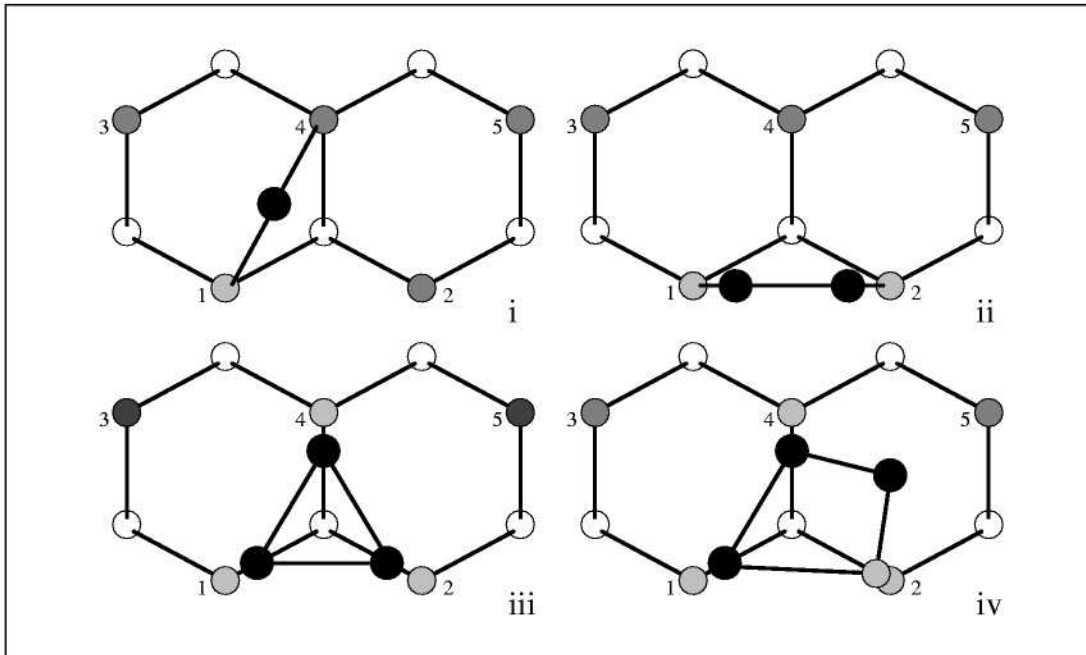


Figure 9.17: Schematic pictures of the most stable configurations for increasing numbers of Si atoms.

The energetic evolution of the cluster formation of Si on Si(111):As(1×1) is summarized in Table 9.6:

Table 9.6: Energetic evolution of the cluster formation of Si on Si(111):As. In the first row the change in energy E_{cl}^n by increasing the cluster size instead of building up an new cluster by a single exchange process is listed. The mean binding energy ($E_{B_{mean}}^2$) per Si atom is given in the second row. The last two rows are the re-calculated energies for the higher cutoff of 13.69Ry and 2 k-points in the irreducible part of the Brillouin-zone.

Conf.	i	ii	iii	iv
E_{cl}^n	-0.35eV	-2.45eV	-2.70eV	-0.55eV
$E_{B_{mean}}^2$	0.35eV	1.58eV	2.07eV	1.78eV
E_{cl}^n	-0.84eV	-2.72eV	-2.80eV	-0.63eV
$E_{B_{mean}}^2$	0.84eV	2.20eV	2.68eV	2.38eV

The growth of small clusters was also studied for Sb mediated Si homoepitaxie. The cluster formation on Si(111):Sb(1×1) follows the same sequence as for As coverage up to $n = 3$. But the fourth Si atom is more favorably exchanged on the Sb-covered terrace rather than built into the existing Sb trimer. It serves as a nucleation center for a new Sb-trimer on top of a full Si double layer. Thus, for Sb-coverage individual T4-centered Sb trimers are formed on Si(111):Sb(1×1) which can grow to the coherent ($\sqrt{3} \times \sqrt{3}$) structure found in equilibrium for Si(111):Sb. The energies for the different clusters on Sb-covered Si(111) are summarized in Table 9.7.

Table 9.7: Energetic evolution of the cluster formation of Si on Si(111):Sb. In the first row the change in energy E_{cl}^n by increasing the cluster size instead of building up an new cluster by a single exchange process is listed. The mean binding energy ($E_{B_{mean}}^2$) per Si atom is given in the second row.

Conf.	i	ii	iii	iv
E_{cl}^n	-1.56eV	-1.99eV	-2.55eV	+0.28eV
$E_{B_{mean}}^2$	1.56eV	2.55eV	3.07eV	2.62eV

In summary, our findings are in full agreement with the experimental observations. The different growth behavior of As- and Sb-covered Si(111) can be understood on the basis of these calculations. The results are summarized in Fig.9.18. The positions and bond angles of the most stable configurations are listed in Appendix A.2. To complete the picture of Si homoepitaxy, we are currently calculating the formation and growth of clusters on the Si(111):Sb ($\sqrt{3} \times \sqrt{3}$) reconstructed surface. To establish a full kinetic picture, also the barriers for the qualitatively different attachment steps at clusters have to be calculated: from single substitutional Si atoms to Si dimers, Si trimers and to tetramers, and also at straight double steps of various orientations.

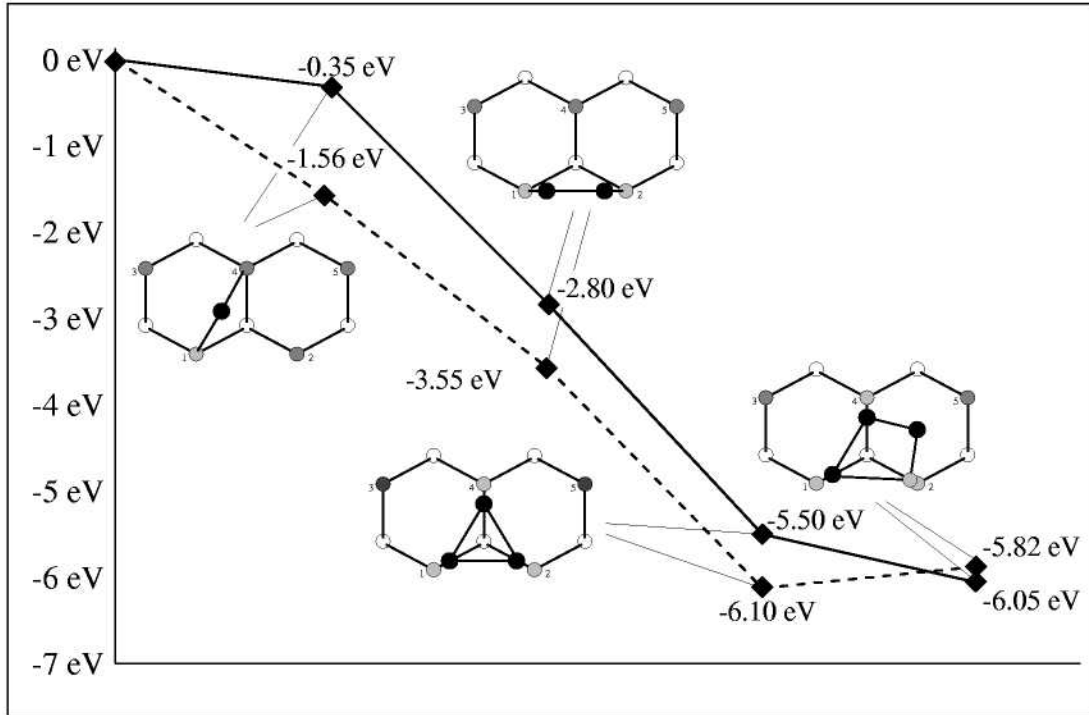


Figure 9.18: Development of small clusters on surfactant covered Si(111) during homoepitaxy. (a) As: The full line indicates the energy $E_{cl} - nE_B^1$ which is gained by a n-cluster compared to n isolated exchanged atoms. The relative energies between two configurations show the energy difference $E_{cl}^n - E_{cl}^{n-1} - E_B^1$ between a cluster with n Si atoms and a (n-1) cluster plus an isolated exchanged Si atom. (b) Sb: The dashed line shows that an Si atom added to a Sb trimer leads to an increasing energy, leading to a ($\sqrt{3} \times \sqrt{3}$) trimer structure on top of the (1×1) terrace as is experimentally observed.

Chapter 10

Steps on Si(111):As

Scanning Tunneling Microscopy (STM) has proven to be a very important tool to observe structural properties at surfaces. This method also was applied to monitor island growth and the structure of steps (rims of islands) on As-covered Si(111) [Voi]. In order to interpret the STM-images correctly it is necessary to correlate the measured electronic density of states of the surface to the underlying atomic structure. This can be done by *ab initio* calculations. First, we will shortly repeat the basis for STM-imaging, then give an account of the experimental results and finally present our *ab initio* STM simulations of steppedges.

10.1 Tersoff-Hamann-Approximation

If the interaction between the tip and the surface which should be investigated is not too large, an approximation for the tunnel current can be made by a first-order perturbation-theory [Bar61]. The potential $U(\mathbf{r})$ can be separated in two contributions which arise from the surface and the tip

$$U(\mathbf{r}) = U_S(\mathbf{r}) + U_T(\mathbf{r}), \quad U_S(\mathbf{r}) \cdot U_T(\mathbf{r}) = 0, \quad (10.1)$$

where surface and tip have the eigenvalues and eigenfunctions:

$$(T + U_S)\Psi_\mu^S = E_\mu^S \Psi_\mu^S \quad (10.2)$$

$$(T + U_T)\Psi_\nu^T = E_\nu^T \Psi_\nu^T \quad (10.3)$$

The system is in the eigenstate Ψ_μ^S of the surface for $t < 0$, if the potential of the tip is zero for $t < 0$. The time-dependent wave-function $\Psi(\mathbf{r}, t)$ can be expanded in the eigenstates of the tip $(T + U_T)\Psi_\nu^T$ if the potential of the tip U_T increases adiabatically for $t > 0$ as

$$\Psi(\mathbf{r}, t) = \Psi_\mu^S e^{-\frac{i}{\hbar} E_\mu^S t} + \sum_\nu c_\nu(t) \Psi_\nu^T e^{-\frac{i}{\hbar} E_\nu^T t}. \quad (10.4)$$

Solving the Schrödinger-equation yields the following differential equation for the expansion coefficients c_ν :

$$i\hbar \frac{d}{dt} c_\nu(t) = \langle \Psi_\nu^T | U_T | \Psi_\mu^S \rangle e^{-\frac{i}{\hbar}(E_\mu^S - E_\nu^T)t} + \sum_\lambda c_\lambda(t) \langle \Psi_\nu^T | U_S | \Psi_\lambda^T \rangle e^{-\frac{i}{\hbar}(E_\lambda^T - E_\nu^T)t} \quad (10.5)$$

This differential equation can be solved in first-order perturbation-theory:

$$c_\nu(t) = \frac{1}{i} \int_0^t dt' e^{-\frac{i}{\hbar}(E_\mu^S - E_\nu^T)t'} \langle \Psi_\nu^T | U_T | \Psi_\mu^S \rangle \quad (10.6)$$

$$|c_\nu(t)|^2 = 2\pi \frac{t}{\hbar} \delta(E_\nu^T - E_\mu^S) |\langle \Psi_\nu^T | U_T | \Psi_\mu^S \rangle|^2 \quad (10.7)$$

$$w_{\mu\nu} = \frac{|c_\nu(t)|^2}{t} = \frac{2\pi}{\hbar} \delta(E_\nu^T - E_\mu^S) |\langle \Psi_\nu^T | U_T | \Psi_\mu^S \rangle|^2 \quad (10.8)$$

$$(10.9)$$

The probability to find an electron at a time t in the state Ψ_ν^T , if it was in the state Ψ_μ^S at $t = 0$ is given by $|c_\nu(t)|^2$ with the transition rate $w_{\mu\nu}$. The transition-matrix element $M_{\mu\nu} = \langle \Psi_\nu^T | U_T | \Psi_\mu^S \rangle$ can be expressed as an integral over a separating surface Σ between the surface S and the tip T

$$M_{\mu\nu} = -\frac{\hbar}{2m} \int_\Sigma d\vec{S} \cdot (\Psi_\nu^{T*} \Delta \Psi_\mu^S - \Psi_\mu^{S*} \Delta \Psi_\nu^T), \quad (10.10)$$

where m is the electron mass

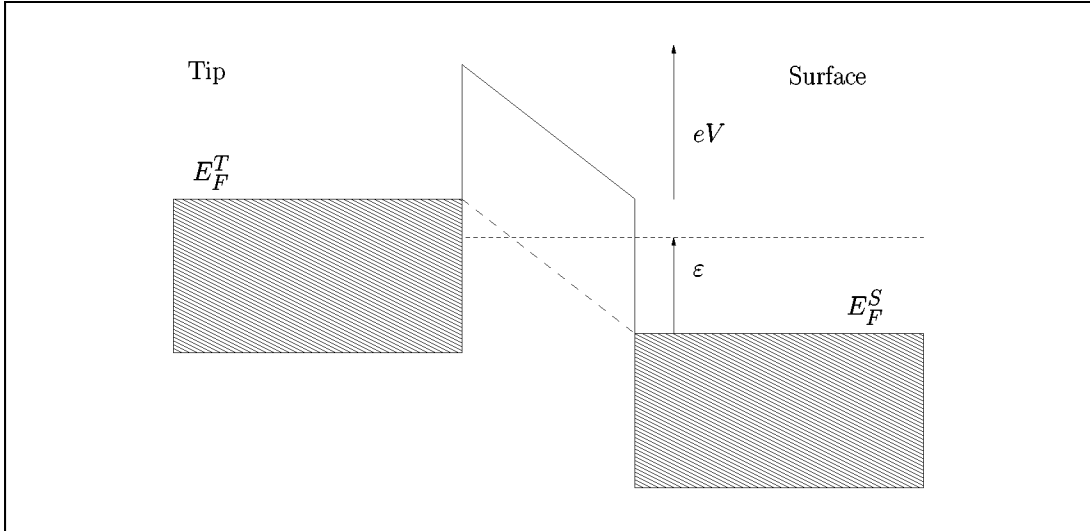


Figure 10.1: Schematic description of the tunnel-current. At a positive voltage V the electrons tunnel from the occupied states of the tip to the unoccupied states of the surface.

Obviously an electron can only tunnel from Ψ_μ^S to Ψ_ν^T , if Ψ_μ^S is occupied and Ψ_ν^T is un-occupied. The summation over all transition-rates, taking into account the occupancy of the states Ψ_μ^S and Ψ_ν^T , yields an expression for the tunnel current:

$$I = \frac{4\pi e}{\hbar} \sum_{\nu\mu} [f(E_\mu^S - E_F^S) - f(E_\nu^T - E_F^T)] |M_{\mu\nu}|^2 \delta(E_\nu^T - E_\mu^S), \quad (10.11)$$

where $f(E)$ is the Fermi-distribution. If a voltage V is applied the equation is generalized to:

$$I = o \frac{4\pi e}{\hbar} \sum_{\nu\mu} [f(E_\mu^S - E_F^S) - f(E_\nu^T - E_F^T)] |M_{\mu\nu}|^2 \delta(E_\nu^T - E_\mu^S - eV) \quad (10.12)$$

If the sum is replaced by an integral

$$\sum_\mu \rightarrow \int dE_\mu^S \rho^S(E_\mu^S), \quad \sum_\nu \rightarrow \int dE_\nu^T \rho^T(E_\nu^T), \quad (10.13)$$

where ρ^S and ρ^T are the density of state (DOS) at the surface and the tip respectively, one can perform an energy integration. This yields:

$$I = \frac{4\pi e}{\hbar} \int d\varepsilon [f(E_F^T - eV + \varepsilon) - f(E_F^S + \varepsilon)] \times \rho^T(E_F^T - eV + \varepsilon) \rho^S(E_F^S + \varepsilon) |M(E_F^S + \varepsilon, E_F^T - eV + \varepsilon)|^2 \quad (10.14)$$

For $T \rightarrow 0$ this equation is reduced to:

$$I = \frac{4\pi e}{\hbar} \int_0^{eV} d\varepsilon \rho^T(E_F^T - eV + \varepsilon) \rho^S(E_F^S + \varepsilon) |M|^2 \quad (10.15)$$

For further calculations one needs information about the wave function of the tip that contribute to the tunnel current. The simplest approximation was introduced by Tersoff and Hamann [TH85] who assumed s character for the tip wave-functions:

$$\Psi_s^T(\mathbf{r}) = C \frac{1}{\kappa r} e^{-\kappa r}, \quad r = |\mathbf{r} - \mathbf{R}|, \quad (10.16)$$

with the decay constant κ and a normalization constant C . The explicit expression for the square of the transition-matrix element then contains the occupation probability of the surface wave functions $\Psi_\mu^S(\mathbf{R})$ at the position \mathbf{R} of the tip:

$$|M_{\mu s}|^2 = \left(\frac{2\pi C \hbar}{\kappa m} \right)^2 |\Psi_\mu^S(\mathbf{R})|^2. \quad (10.17)$$

If, in addition, one assumes a smooth (nearly energy independent) DOS of the tip in the important energy interval around the Fermi energy ($\rho^T = \text{const.}$) the

tunnel current can be expressed by the local density of states (LDOS) $\rho_{loc}^S(\mathbf{R}, \varepsilon)$ of the crystal surface evaluated at the position \mathbf{R} of the tip:

$$I(\mathbf{R}, V) = \frac{16\pi^3 C^2 \hbar^3 e}{\kappa^2 m^2} \rho^T \int_0^{eV} d\varepsilon \rho_{loc}^S(\mathbf{R}, E_F^S + \varepsilon) \quad (10.18)$$

$$\frac{dI}{dV} = \frac{16\pi^3 C^2 \hbar^3 e}{\kappa^2 m^2} \rho^T \rho_{loc}^S(\mathbf{R}, E_F^S + eV) \quad (10.19)$$

Thus, the derivative of the tunnel-current with respect to the voltage (V) is proportional to the local density of states ($\rho_{loc}^S(\mathbf{R})$) at the location (\mathbf{R}) of the tip. Based on this relation we can calculate the STM-images for discrete wave-functions as

$$I(\mathbf{R}, V) \sim \sum_{E_\mu=E_F}^{E_F+eV} |\Psi_\mu(\mathbf{R})|^2, \quad (10.20)$$

where Ψ_μ are the discrete, self-consistent calculated states of the surface-supercell. All wave-functions contribute which have a finite occupancy probability at the site of the tip and an eigenvalue in the range $(E_F, E_F + eV)$.

10.2 Step Structures and Experimental Results

On the fcc Si(111):As surface only two different kinds of step-orientations appear. The structure of these step-edges were investigated by *ab initio* calculations by R.Berger [Ber01] in our group. The lowest energy structures are the As passivated steps shown in Fig.10.2. The exposed second layer Si atoms at the step edges are replaced by As atoms. At the $(11\bar{2})$ step this leads to a stable configuration since the As atoms are in a naturally threefold coordinated position, i.e. the As atoms at the step edge are in equivalent positions as on the (111) oriented terraces. At the $(\bar{1}\bar{1}2)$ step, in the unrelaxed positions the As atoms are only twofold coordinated. Thus, they form dimers to saturate their bonds. For the $(\bar{1}\bar{1}2)$ step there exists an alternative structure where the As atoms at the edge of the upper terrace bind directly to Si atoms on the lower terrace. Which of this structures will occur in nature depends also on the details of kinetic effects, and cannot be settled at this stage purely by *ab initio* calculations. In order to relate our calculations to experiment, we concentrate on the $(11\bar{2})$ step-edge in further *ab initio* STM-image calculations.

Voigtländer has investigated the step-edges on Si(111):As using scanning tunneling microscopy (STM). The STM-images (Fig.10.3) were taken at a bias voltage of +1.9V at the surface. The height of the tip when moving across the step edges from the lower to the upper terrace was also analyzed by Voigtländer. The linescans are shown in Fig.10.4. From the experiment it is unclear which of the

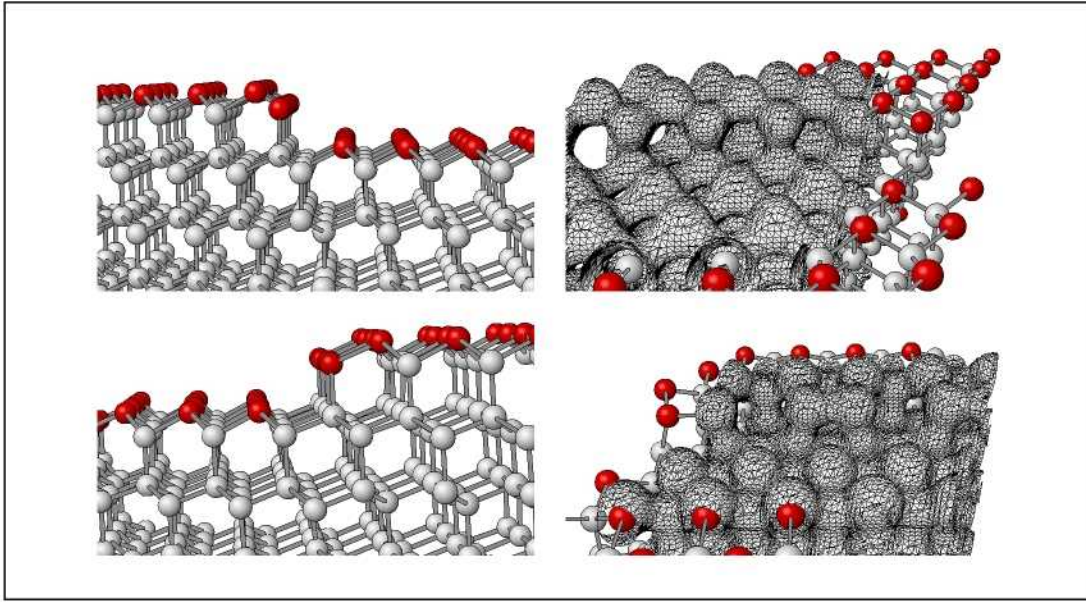


Figure 10.2: Sideview (left panels) and frontview (right panels) of the two step-edges on Si(111):As. The upper images show the $(11\bar{2})$ and the lower pictures the $(\bar{1}\bar{1}2)$ step-edge. In the frontview on the right side the contour of the constant valence electron density is also drawn, showing, the dimers at the $(\bar{1}\bar{1}2)$ step-edge.

triangular shaped islands shows preferably $(11\bar{2})$ or $(\bar{1}\bar{1}2)$ step-edges. To discriminate between the two steps orientations, there has to be a (7×7) reconstructed area which was not present in the experiment, due to the As-coverage. On the other hand Voigtländer observed the islands with two different step-edges with different frequency. In combination with our results for the energetics of step-edges [Ber01] we assume that the island shown in (Fig.10.3) is the $(11\bar{2})$ oriented one.

The STM-image as well as the linescans show an increased height of the atom at the rim of the islands. This can be an electronic and/or a structural effect. Since in the structures favored by our calculations only one kind of atoms, i.e. As atoms, are present at the step-edges, a naive interpretation would suggest a position of the As atoms at the step-edge above the atoms on the upper terrace. Since in the estimated step-edge structures in Fig.10.2 the As atoms at the step-edge are at the same height as the As atoms at the upper terrace, we conclude either we did not find the preferred step-edge configuration in our calculations, or it is an electronic effect. To investigate this point further we present the first theoretical STM calculation of a semiconductor step-edge in the next section.

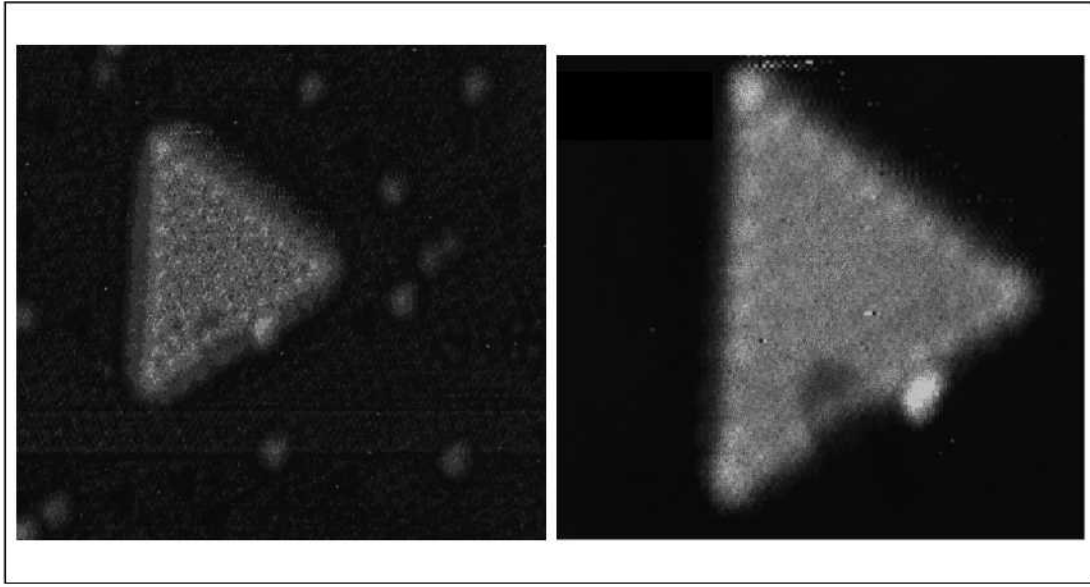


Figure 10.3: STM-images of a triangular island with steps of one kind of step orientation only. The right image shows an enlarged sector of the left picture, where the contrast is adapted to show more details of rim of the island. Image is taken at room temperature and at a STM voltage of +1.9V.

10.3 Calculated STM-images

The electronic structure calculations were carried out in an inversion-symmetric supercell with a width of the step-edge of 2 and a terrace length of 4 As atoms. The energy cutoff was 13.69Ry. The relaxed positions of the atoms were taken from the calculations of Berger [Ber01]. To avoid interaction between the two surfaces, six atomic layers of Si bulk were added to the supercell used by Berger for the structural relaxations. The vacuum was also increased by a distance equivalent to six atomic Si layers. Thus, the supercell consists of 20 Si layers (168 Si atoms), one layer of As on each side of the inversion-symmetric surfaces (20 As atoms) and a vacuum region equivalent to 8 atomic Si layer or 12.54Å.

To simulate the constant-current STM-images we determined the local density of states in the vacuum region using 6 \mathbf{k} -points in the irreducible part of the Brillouin-zone, which refer to 64 equidistant \mathbf{k} -points in the two-dimensional (1×1) surface unit cell. Since the corrugation of the local density of states (LDOS) is sensitive to the \mathbf{k} -point distribution, we used \mathbf{k} -points including the high symmetry points and the boundary of the Brillouin-zone.

Due to the large height difference between the upper and lower terrace the surface LDOS cannot be calculated at a fixed distance above the surface, as it is usually done for flat terraces. Instead the `ESTCoMPP-VT` was used to calculate the surface of constant LDOS, integrated over all states in an energy interval, at a height of around $z_0 = 3.8\text{\AA}$ above the terrace. The value of the integrated LDOS

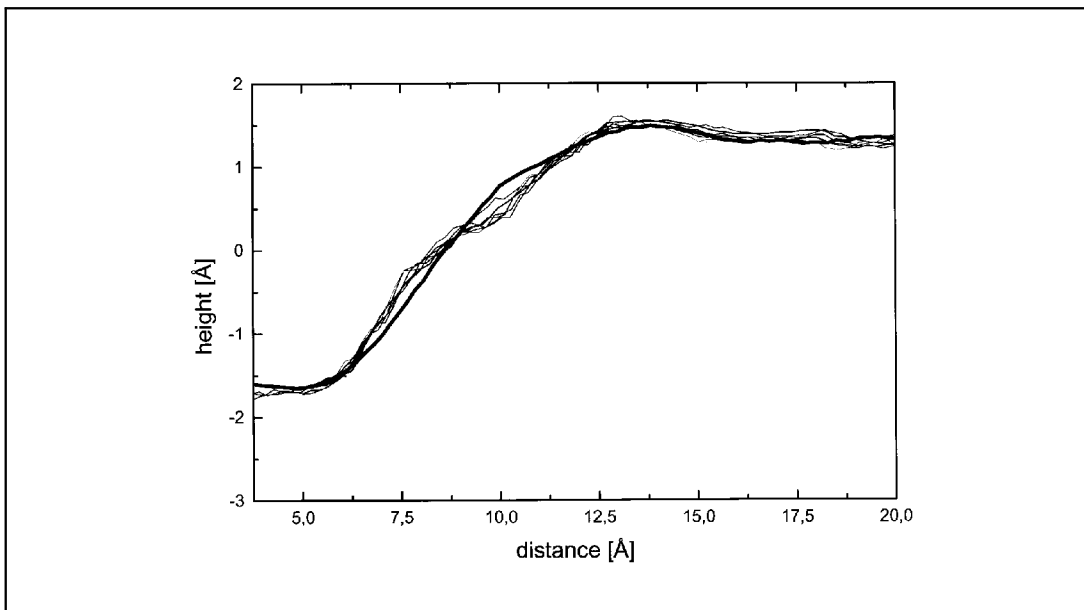


Figure 10.4: Linescans over the edge of the island shown in Fig.10.3. Voigtländer suggest that the bunch of thin lines show linescans for the $(11\bar{2})$ step-edge, and the thick line is a linescan for the $(\bar{1}\bar{1}2)$ step-edge. The linescans were made at room temperature and at a STM voltage of +1.9V.

(ILDOS) was chosen to be as small as possible, i.e. such that the iso-surface was still an continuous area. The height difference between the lowest and highest point of the surface was mapped onto a grey-scale as in the experiments, using the **z-shading** option of the **EStCoMPP-VT**. Thus, the topview of the surface of constant ILDOS corresponds to the experimental STM images, while the sideview can be interpreted as a series of linescans.

The calculated STM-images of the occupied states are presented in Fig.10.5. Shown are the STM images at different bias voltage: $[-2.0,0.0]$, $[-1.5,0.0]$, and $[-1.0,0.0]$. The best resolution is achieved at a voltage range of $[-1.0,0.0]$. The details vanish if larger voltages are applied. The calculated STM-images of the empty states are presented in Fig.10.6. The STM images at different voltage: $[0.0,1.0]$, $[0.0,1.5]$, and $[0.0,2.0]$ are presented. The best resolution is achieved at a voltage range of $[0.0,1.0]$. Compared to the STM images calculated at negative voltages, the As atoms between the lower and upper step-edge are not resolved. The STM images show far less details than the STM images of the occupied states. In agreement with the experiment the linescans, on the left side, show an increased height of the surface at constant ILDOS above the step-edge which makes the As rim atom appear larger or higher. The height decreases with increasing voltage.

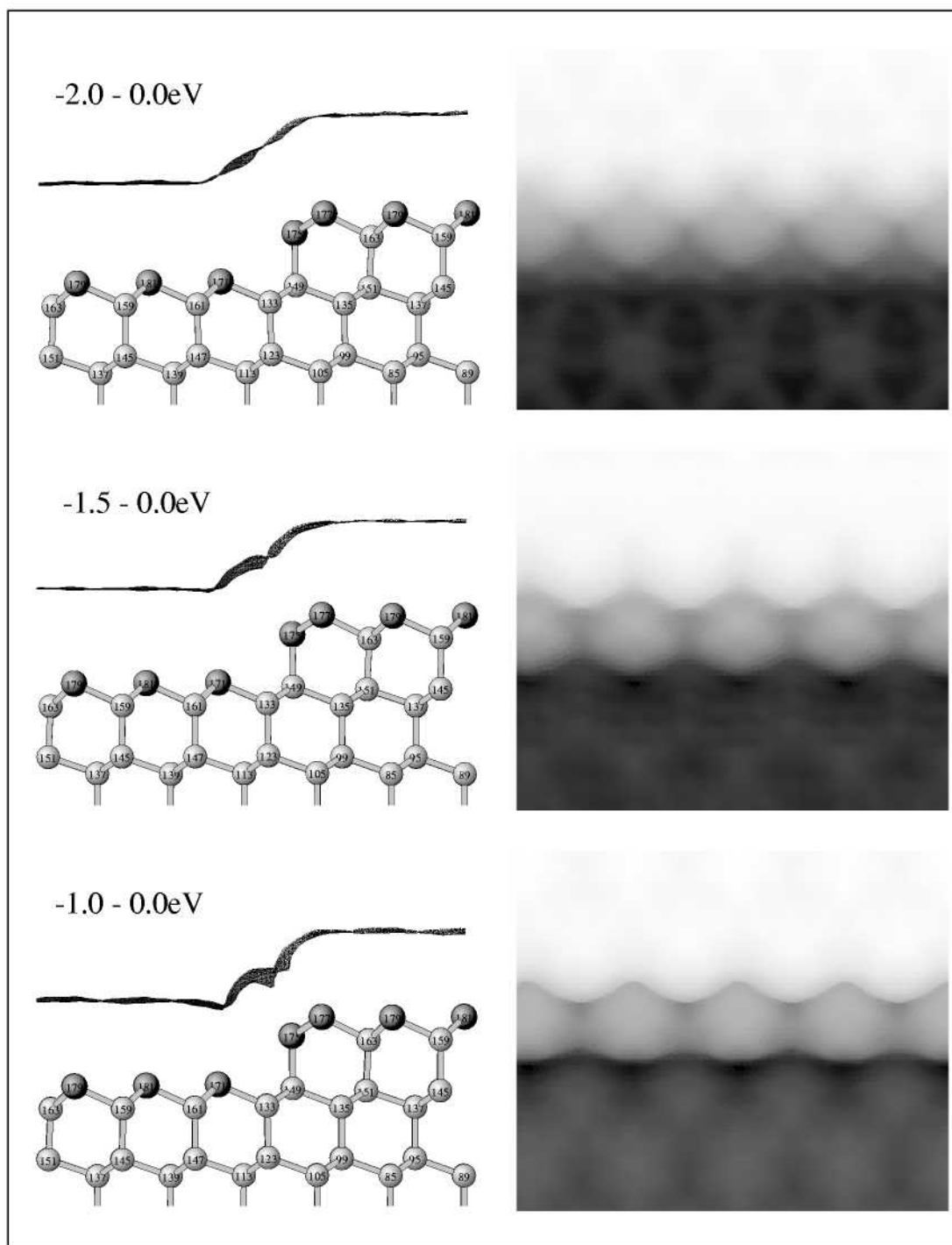


Figure 10.5: Theoretical constant current STM images of the $(11\bar{1})$ step-edge at different negative bias voltages. On the left a sideview of the surface of constant ILDOS is presented which can be interpreted as a superposition of linescans. The respective topview (the STM image) is shown on the right.

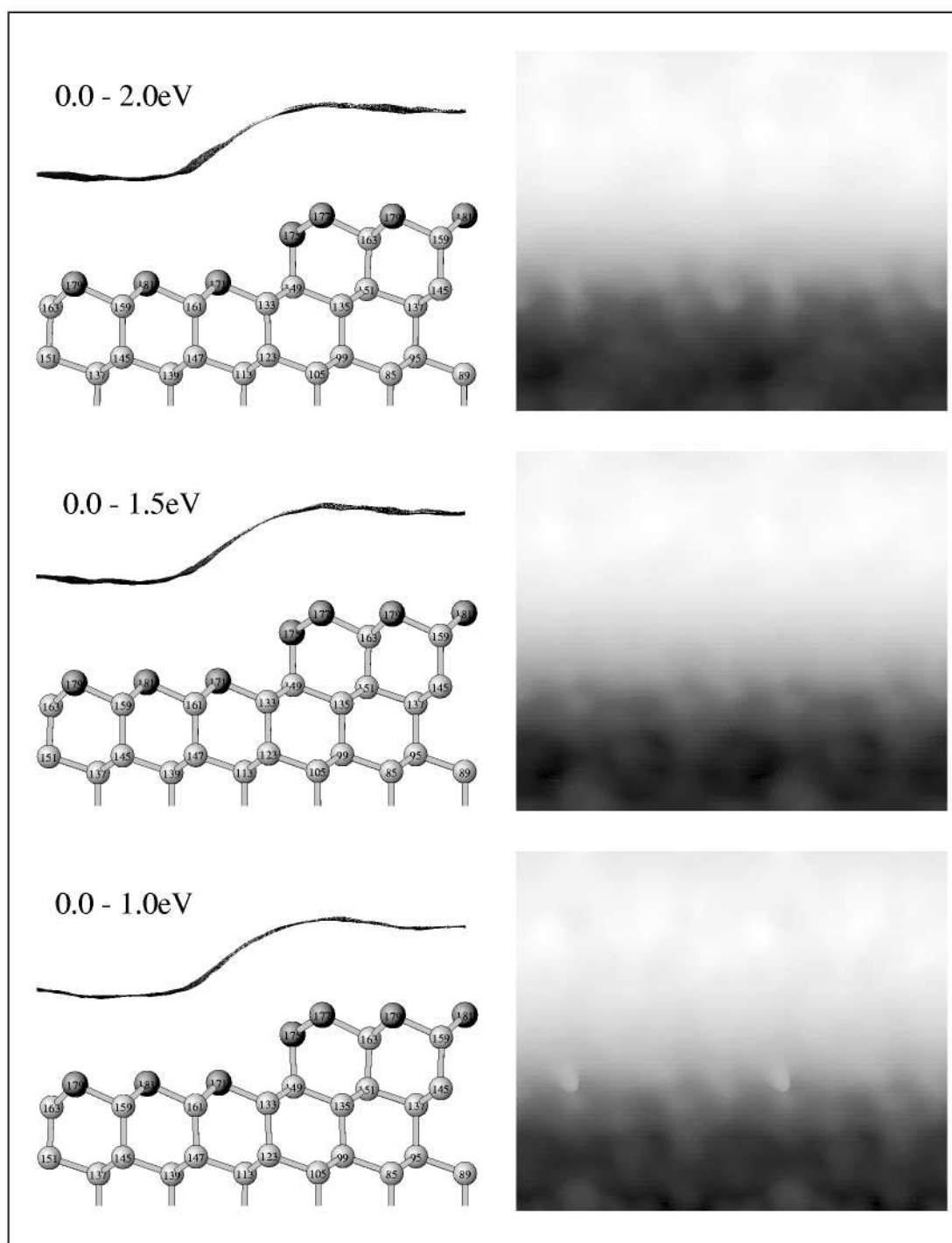


Figure 10.6: Theoretical constant current STM images of the $(11\bar{2})$ step-edge at different positive bias voltages. On the left a sideview of the surface of constant ILDOS is presented which can be interpreted as a superposition of linescans. The respective topview (the STM image) is shown on the right.

To get a better understanding which states contribute to the STM-image, the energy interval over which the tunneling states are summarized are in steps of 0.5eV from -2.0 to $+2.0$ eV. The results are shown in Fig.10.7 and Fig.10.8. As can be seen only the LDOS in the negative energy range $[-1.0, -0.5]$ reproduces the atomic structure of the surface.

To understand why the resolution gets worse by applying larger voltages, the LDOS has been calculated in the energy ranges $[-1.0, 0.0]$, $[-2.0, 0.0]$, and $[0.0, 1.0]$. The contour-plot, in a plane perpendicular to the vector along the step-edge, are shown in Fig.10.9. The plane was positioned such that the As atoms between the lower and upper terrace (175) is cut by the plane. In the left pictures in Fig.10.9 the contour close to the atoms are shown. The p-bond of the atom between the lower and upper terrace, which points into the vacuum, can be identified as well as the backbond to the underlying Si atom (149). The bond to the As atom (177) above atom (175) is out of plane. In the energy range $[-1.0, 0.0]$ the p-states at the atom (175) are fairly localized. States in the energy interval $[-2.0, -1.0]$ seem less localized, put weight into the vacuum and smear out the charge density distribution in the vacuum. For the LDOS in the vacuum region (Fig.10.9 on the left side), this leads to a drastic change of the spatial resolution. The outermost contour-line was chosen to be identical to the surface at constant ILDOS in the previous figures. In the energy range $[-1.0, 0.0]$ the isolines in the vacuum still reveals the atomic structure of the surface. For higher voltages the outermost isolines became smooth and only a fuzzy image of the step-edges structure is resolved. Applying positive voltages lead to unstructured contour-plots even close to the atoms. In the vacuum region only the increased height of the contour-lines above the step edge appears.

For As atoms at different sites the PLDOS was analyzed. The wave-functions were projected to angular momentum quantum numbers and integrated in a sphere around the atoms, where the radius was half the nearest-neighbor distance. This analysis was performed for As atoms on the lower terrace (171), the upper terrace (179), at the step edge (177), and between the lower and upper terrace (175). The results are presented in Fig.10.10. The main difference between the As atoms on the terrace and at the step edges are marked by an arrow. Compared to the As atoms on the terrace, in the positive voltage range $[0.0, 1.6]$ the As atoms at the step-edge show an increased DOS, most pronounced for the p-channel. The As atoms on the terrace have only bonds to Si atoms in the layer beneath. The As atoms at the step edges have 1 Si-As bond and two As-As bonds. Thus, the increased PLDOS is most likely due to the As-As bonds. This increased PLDOS at the As step-edge atoms is most likely the electronic origin of larger size appearance of As rim atoms in the STM-image.

Summarizing our results we could show that the best resolution of STM-images can be resolved at a voltage of -1.0 V. Since in atomic semiconductors the conductivity is largely determined by the occupied states, the tip induces a

band bending at the surface due to the effective charging of the surface layer. Thus, the optimal voltage which has to be applied to the surface will probably be larger in the experiment. The increased height of the tip above the step-edge was found in our calculated STM-images for positive voltage in full agreement with the experiment. Thus the structure of the step-edges, as predicted by the calculations of Berger, is most likely as shown in Fig.10.2.

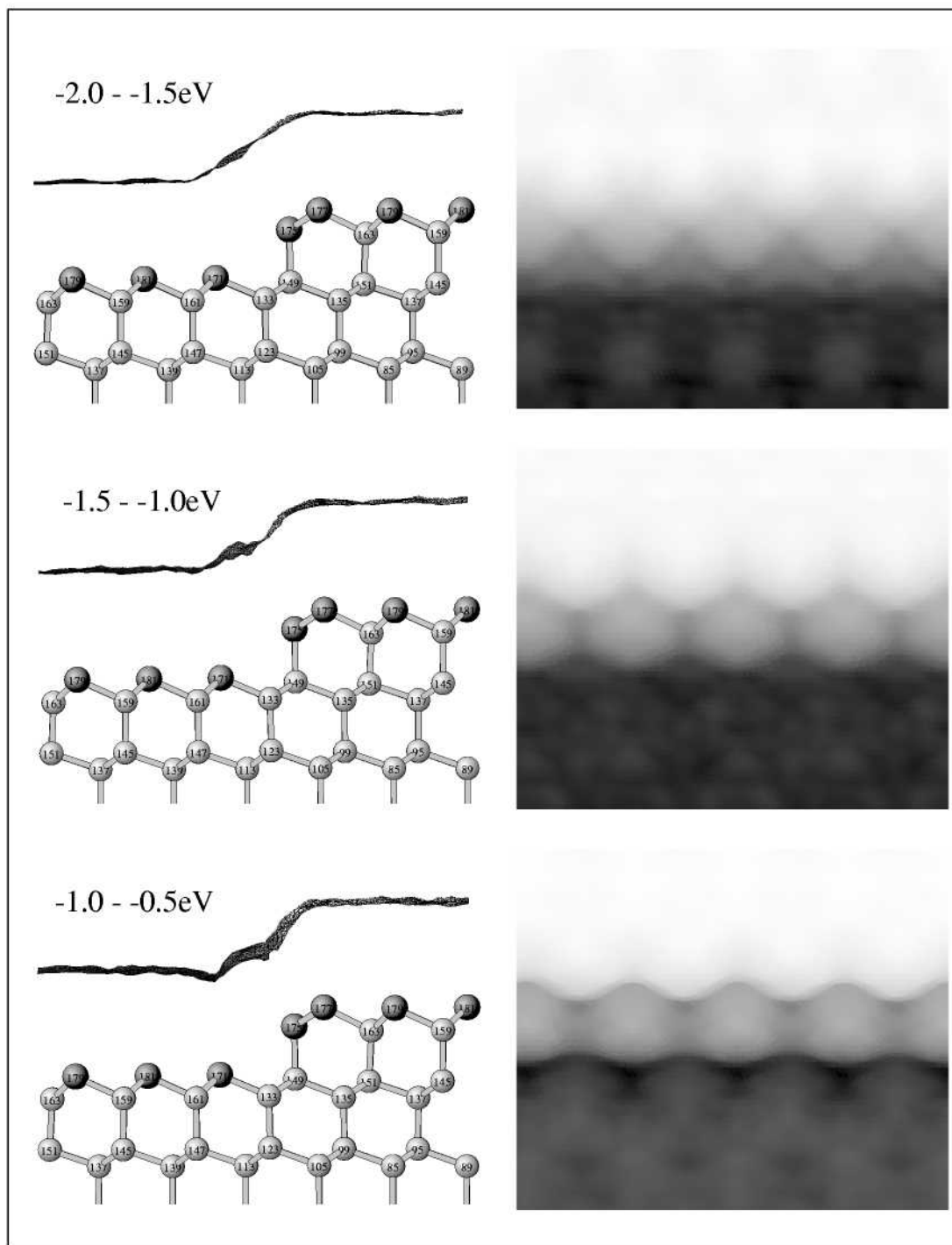


Figure 10.7: Theoretical STM images of the $(11\bar{2})$ step-edge at negative voltages. A fixed energy range of 0.5V was shifted in steps of 0.5V.

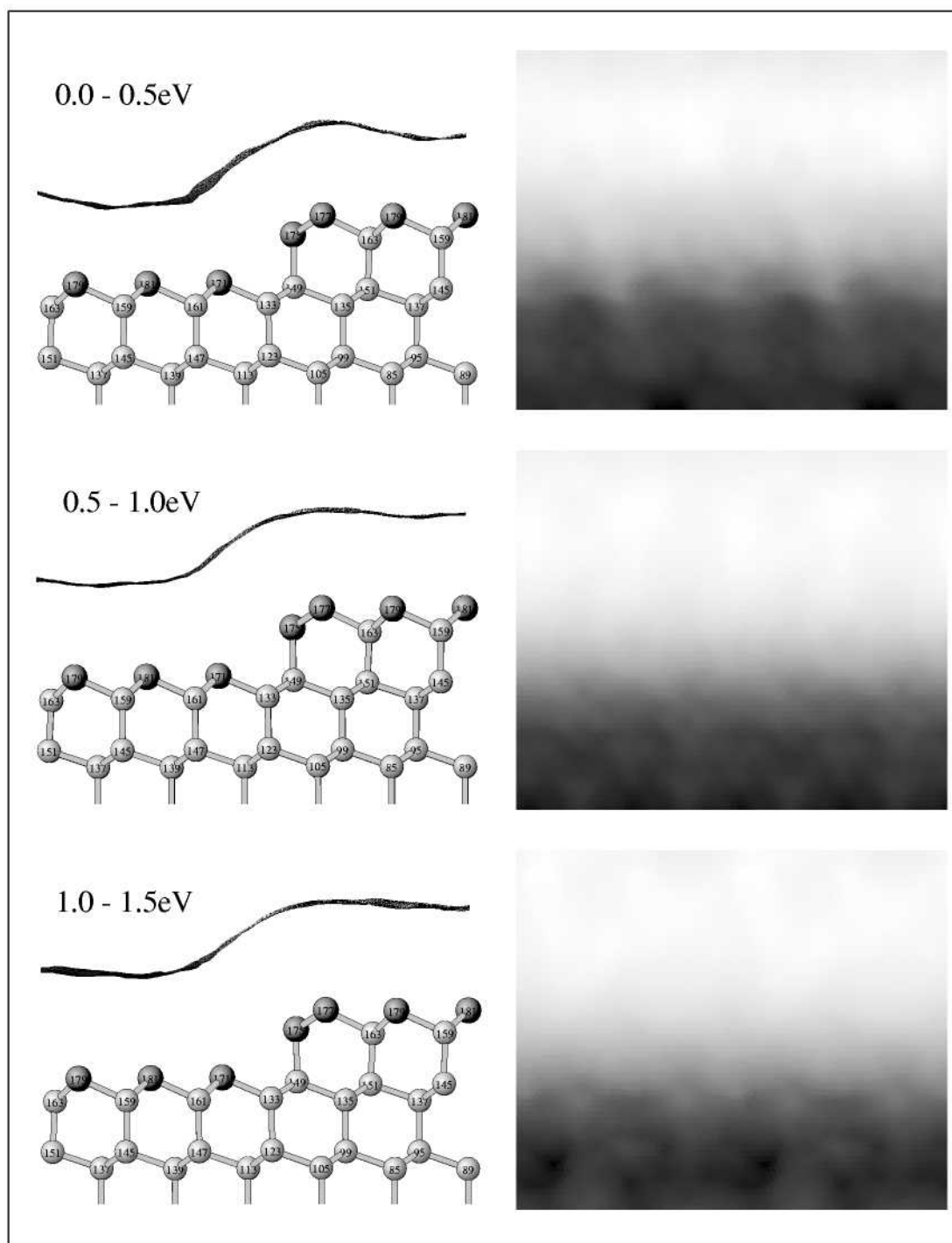


Figure 10.8: Theoretical STM images of the $(11\bar{2})$ step-edge at positive voltages. A fixed energy range of 0.5V was shifted in steps of 0.5V.

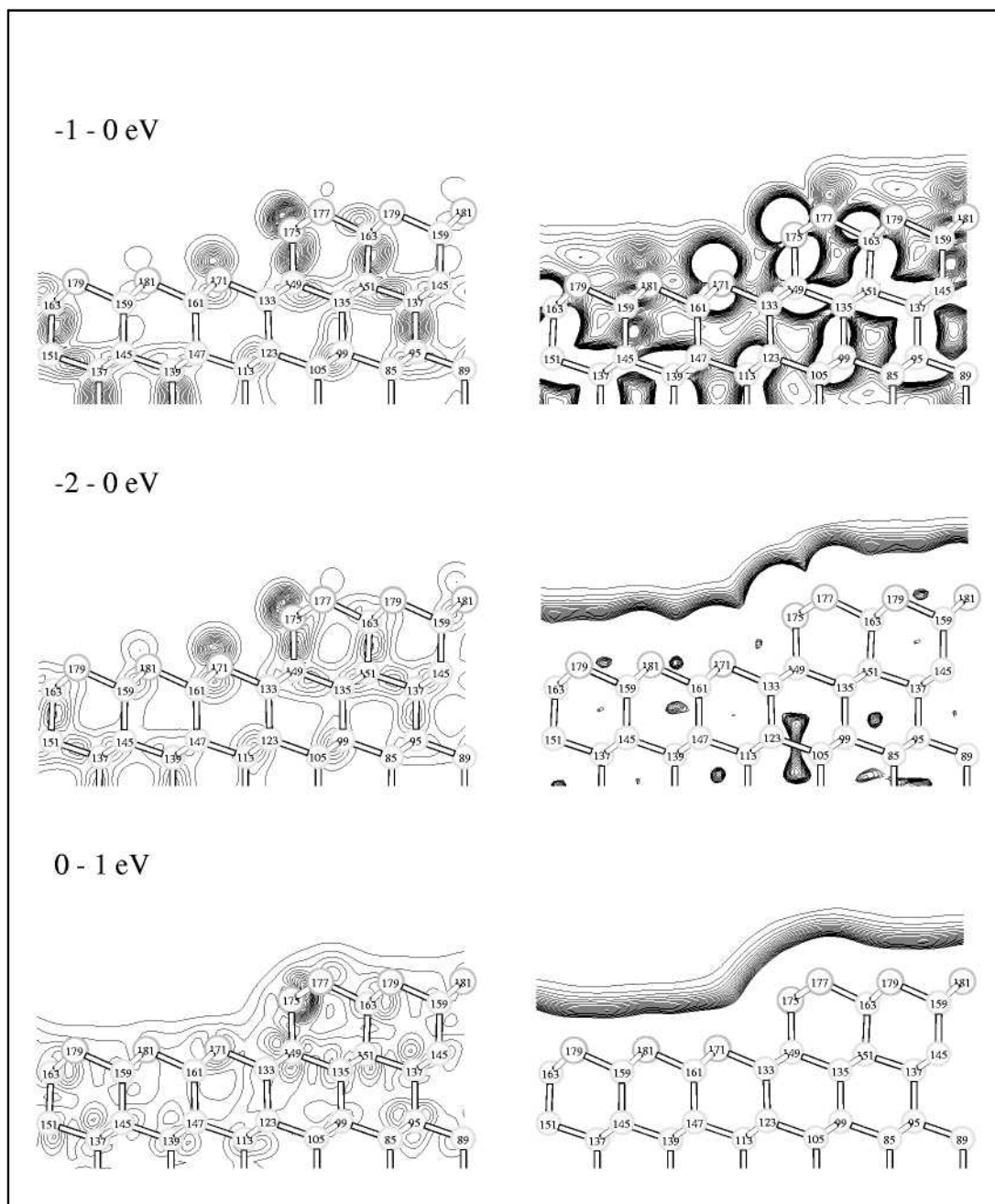


Figure 10.9: Contour-plot of the integrated LDOS at the $(11\bar{2})$ step-edge at different voltages. The plane at which the contour-plot is synthesized cuts through the As atom between the upper and lower step-edge. On the left the ILDOS close to the atoms is shown. On the right the contour-plots are drawn such that the outermost line is identical to the surface of constant ILDOS in the previous figures.

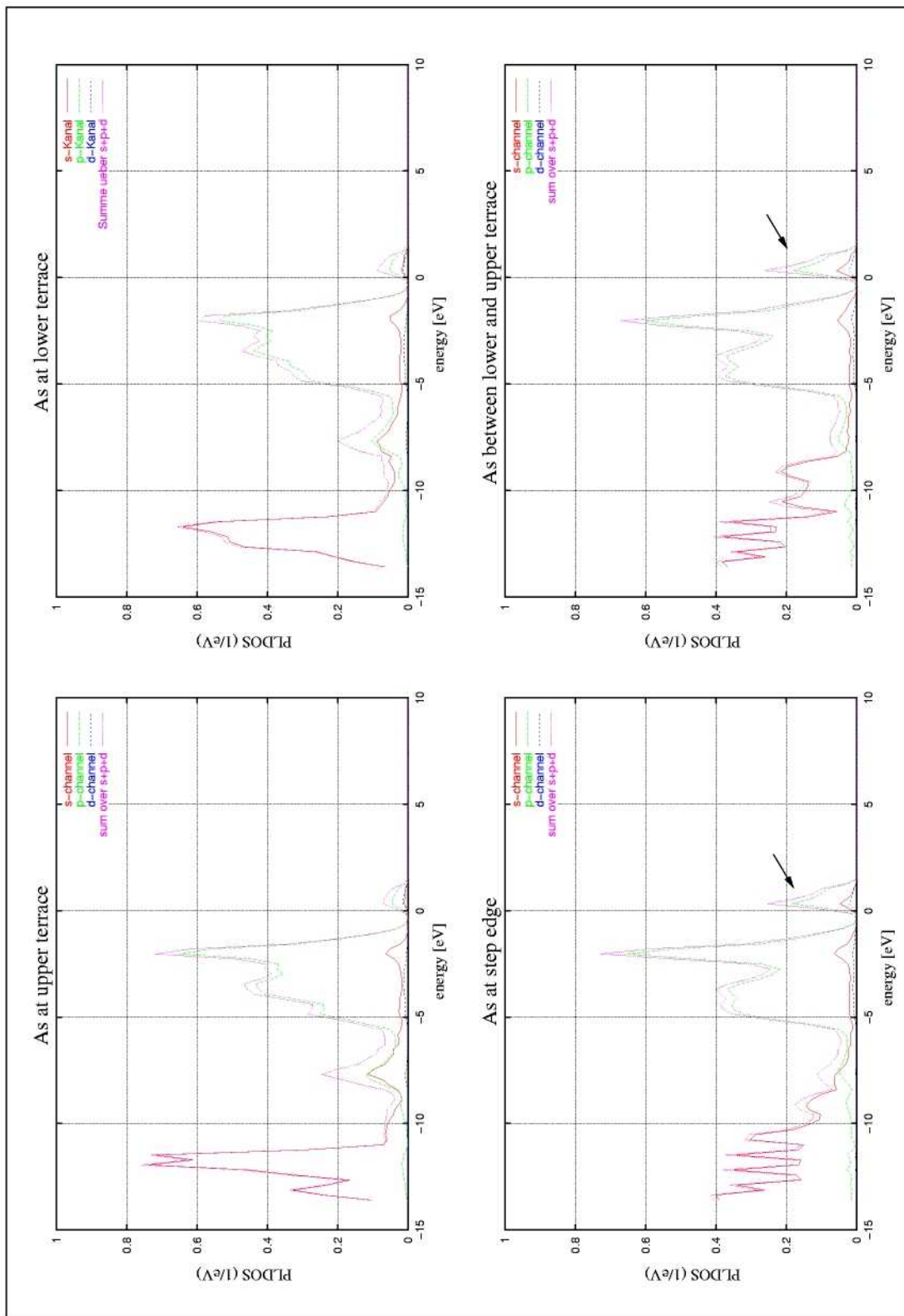


Figure 10.10: PLDOS integrated in a sphere around the atoms.

Chapter 11

Growth of Ge films on Si(111):Sb

In the preceding chapter the homoepitaxial growth of Si on Si(111) terminated with As or Sb was discussed. Each time a double-layer is deposited in homoepitaxial growth (and the system is tempered), the system is in the same state as it was before, i.e. the surface shows the same type of reconstruction, and only the growth front has moved. For heteroepitaxy, i.e. Ge on Si(111):Sb, this is vastly different due to the stress which is brought into the system by the lattice mismatch between Si and Ge.

11.1 Experimental Results

N. Theuerkauf has studied the heteroepitaxial growth of Ge on Si(111):Sb in great detail by scanning tunneling microscopy [The00]. The starting point for his experiments was the Sb terminated Si(111) surface, which shows the $(\sqrt{3} \times \sqrt{3})$ -reconstruction (Fig.11.1).

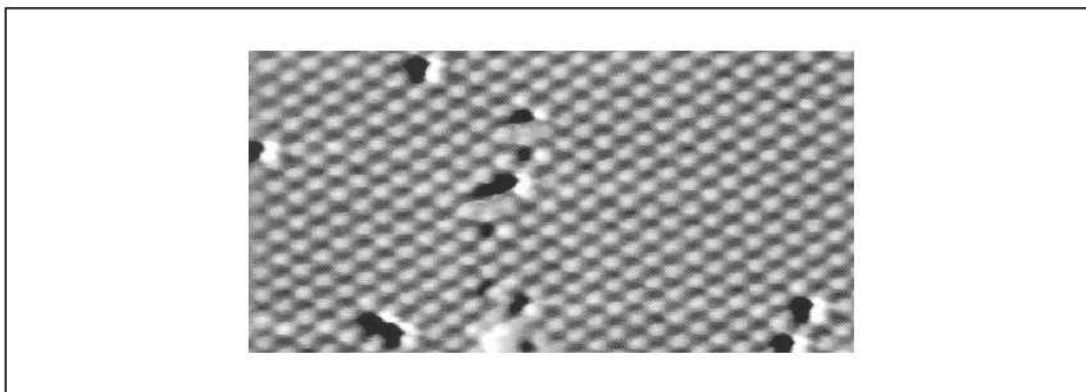


Figure 11.1: STM image of the $(\sqrt{3} \times \sqrt{3})$ -reconstruction of Sb on Si(111).

On this surface he deposited three monolayer (ML) Ge at a deposition rate of 0.5ML/min, and at a substrate-temperature of 670°C. After the deposition the

surface shows a $(6\sqrt{3} \times 6\sqrt{3})$ -reconstruction consisting of a patchwork of hexagonal structures as is shown in Fig.11.2. The surface shows no three-dimensional

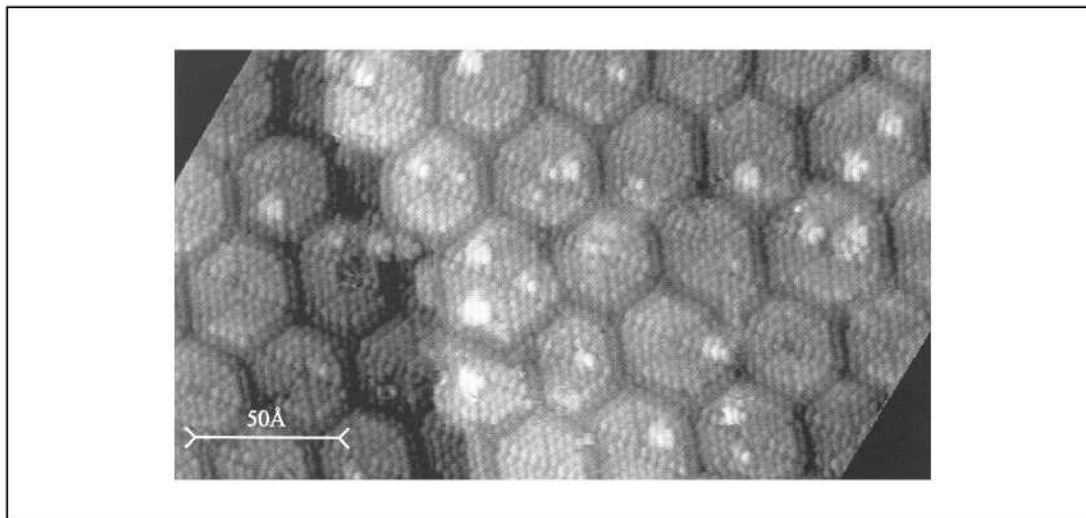


Figure 11.2: STM-image of the hexagonal-reconstruction of Sb on Si(111)/Ge after the deposition of three monolayer Ge.

islands and is atomically flat over a large area. Voigtländer and Zinner [VZ96] introduced a detailed model (Fig.11.3) for the structure of the hexagonal patches. The Sb atoms form triangles with an edge-length of four Sb atoms. Inside these triangles a (1×1) -reconstruction is found. Six triangles form a hexagon with a hole in the center. Two neighbored triangles share two Ge-dimers at the boundary. The hexagons are separated by deep trenches where Ge atoms of the third layer appear. Whereas Voigtländer assumes that Sb atoms only sit in the top surface layer we suggest from our calculations of the structure of step-edges of As- or Sb-covered Si(111) [Ber01] that the Ge atoms of the second layer at the rim of the hexagons are removed and that the Sb atoms move down and bond directly to Ge atoms of the third layer. Voigtländer compared the suggested model with the STM-images and found a 5-8% larger distance between the Sb atoms in the experiment than in the ideal model structure.

Further deposition leads to a rough surface with a roughness of up to 5 layers. At higher coverage above 14 monolayers and in the temperature range between 580°C and 630°C the Sb-covered Ge-film on Si(111) forms a smooth surface again. Theuerkauf attributed this to the formation of a dislocation network at the Si/Ge-interface. Due to the dislocation network the Ge atoms at the surface can relax and the Ge bondlength is close to its equilibrium value. Thus, Ge films on Si(111):Sb thicker than 14 monolayers show the same (2×1) surface reconstruction as on pure Ge(111):Sb (Fig.11.4). The same growth scenario has been found by Horn-von Hoegen [Hoe94] using SPA-LEED (Spot Profile Analyzing Low-Energy Diffraction).

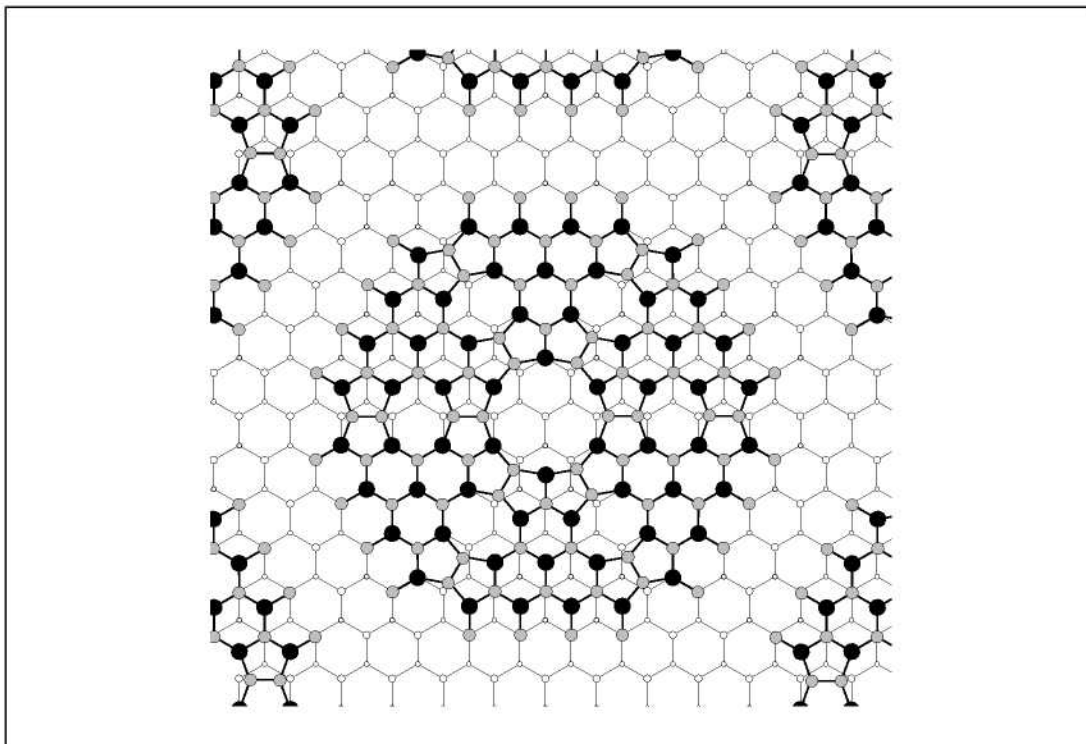


Figure 11.3: Model of the hexagonal reconstruction as suggested by Theuerkauf. The Sb atoms (the large filled circles) are the upper layer of an (111) doublelayer. The Ge atoms of the third layer are filled in grey. The Ge atoms of the second and first layer are circles with decreasing sizes.

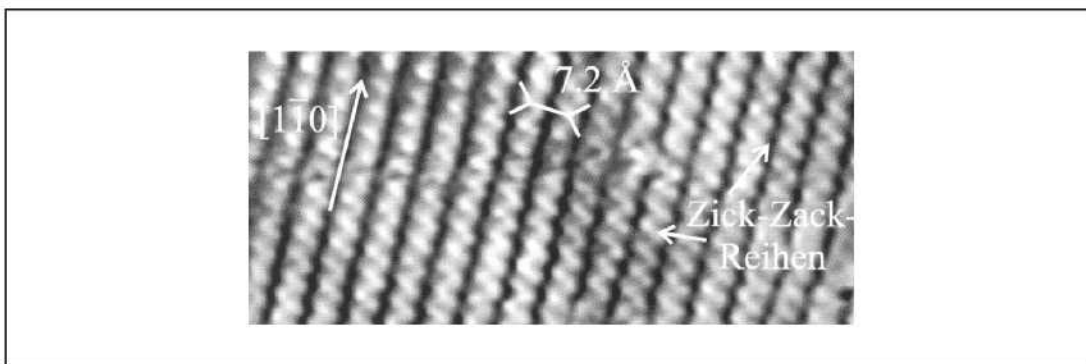


Figure 11.4: STM-image of the $(\sqrt{3} \times \sqrt{3})$ equilibrium hexagonal-reconstruction of Sb covered Ge(111).

11.2 Surface Reconstructions and Stress (Ge(111):Sb)

In order to understand the structures of the growing and relaxing Ge film deposited on the Sb-covered Si(111) substrate one has to investigate the dependence of the energies for the various geometries as a function of lateral lattice constant. Kaxiras [Kax93, Kax95] has investigated the Sb-covered Ge doublelayer deposited on the Si(111) substrate at the Si lattice constant, and Sb-covered Ge(111) substrate at the equilibrium lattice constant of Ge. The latter represents the case where a large amount of Ge has been deposited onto the Si(111) substrate and the film has relaxed.

According to these calculations, for Sb/Ge(DL)/Si(111) the lowest energy geometry becomes the (2×1) chain structure, with the T_4 -trimer structure having slightly higher energy, and for Sb/Ge(111) the lowest energy geometry is the substitutional one. However, in the experiments only the chain geometry has been observed on the Ge(111) substrate [The00].

We have investigated the stability of four different structures of Ge:(111):Sb as a function of the lateral lattice constant. (In the following the term "lattice constant" always refers to the lateral lattice constant). All structures are shown in Fig.9.1, except the H_3 -centered trimer. This structure shows the same Sb-trimers on top of the surface as the T_4 -trimer structure, but they are centered above the empty hexagons in Fig.9.1.

The surfaces are modeled by slabs which are periodically repeated in the direction perpendicular to the surface. The slabs consist of 10 atomic Ge(111) layers for substitutional geometry and 8 for chain and trimer geometries in an inversion symmetric arrangement, and 2 Sb layers covering the two sides of the slab. Each layer is separated by so large vacuum regions that the interaction between different layers can be neglected. We used a cutoff energy of 13.69 Ry in the plane wave basis, which yields well converged results. Furthermore, for reliable energy comparisons of structures with different periodicity, a comparable well-converged sampling of the k-points in the surface Brillouin zone is essential. We choose a set of 2×2 k-points in the surface Brillouin zone for the 3×3 unit cell used for the H_3 and T_4 trimer structures, and correspondingly larger sets for the structures with smaller periodicity (3×6 k-points for the (2×1) periodic cell for the chain structure and 6×6 k-points for the (1×1) substitutional structure). All k-point sets correspond to a set of 6×6 k-points in the surface Brillouin zone for the (1×1) unit cell. To establish minimum energy configurations the forces acting on the atoms are required to be less than 0.1mRy/a.u..

The calculated surface energies E_s with varying lattice constants for different structures are shown in Fig.11.5. We find that the surface energy of the chain geometry is lower than the other three geometries at the theoretical and experimental equilibrium lattice constants of bulk Ge, indicating that the chain

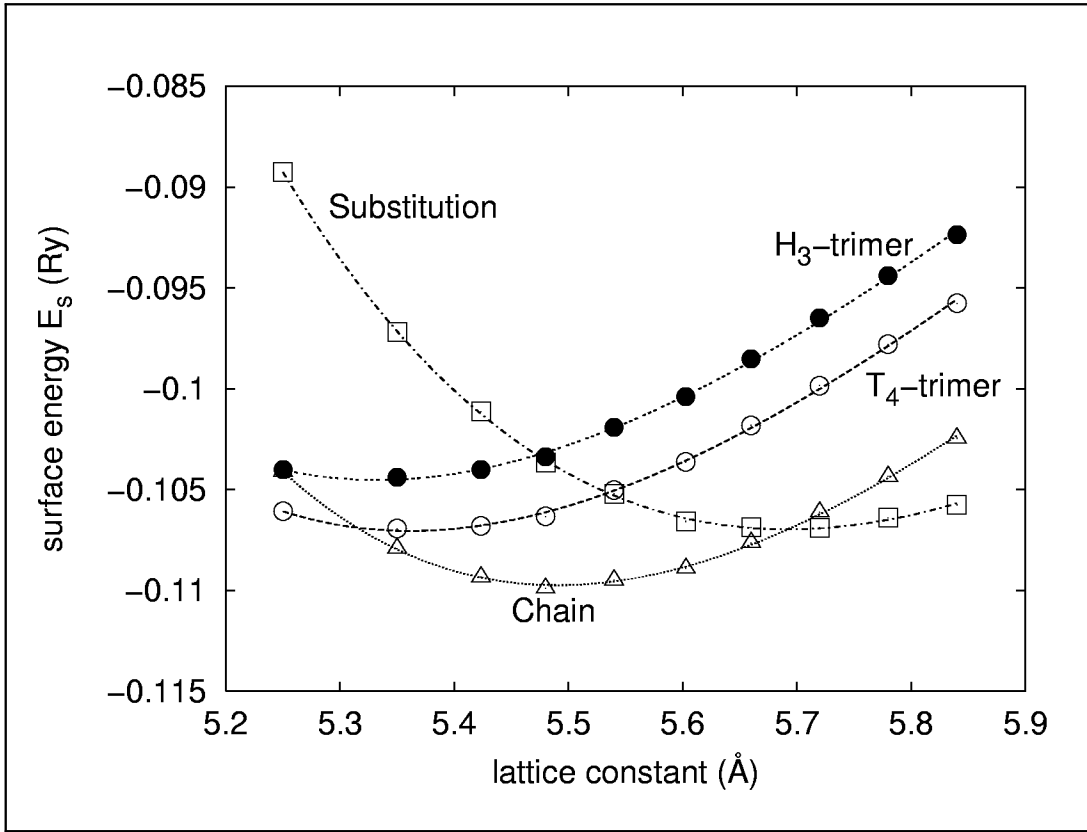


Figure 11.5: Surface energies E_s per Sb atom plotted against lateral lattice constant a for different structures. The filled circles, empty circles, triangles, and squares represent the H_3 -trimer, T_4 -trimer, chain, and substitutional geometries, respectively.

geometry is the most stable structure. The theoretical equilibrium lattice constant $a_{th}=5.632\text{\AA}$ is obtained from the universal binding energy relation [BS88] of bulk Ge based on our calculations under the same conditions as the above and the experimental value $a_{exp}=5.657\text{\AA}$ is from Ref.[Roh00].

This is in agreement with experimental observations [The00], but different from Kaxiras's proposal [Kax93, Kax95]. The substitutional geometry is slightly higher in energy than the chain at a_{th} (22 meV higher) or a_{exp} (12 meV higher). One can also find in Fig.11.5 that the H_3 -trimer configuration is the highest-energy structure compared with the other structures at a_{th} or a_{exp} , partially consistent with Kaxiras's results [Kax93].

We also present the surface energies for different structures against the deviation of lateral lattice constant Δa from the theoretical-equilibrium lattice constant of bulk Ge a_{th} (Δa is defined as $\Delta a = \frac{a - a_{th}}{a_{th}} \times 100\%$) in Fig.11.6. We find that the (2×1) -reconstruction of Ge(111):Sb experimentally found to be stable at the equilibrium lattice constant of Ge is also the stable structure for slightly

dilated Ge films ($<1\%$). For larger dilatation the (1×1) -structure becomes stable. For compressed Ge films the $(\sqrt{3}\times\sqrt{3})T_4$ -structure (found experimentally on Si(111):Sb) becomes competitive. It is stable for lattice constants compressed larger than 5%. It is worth analyzing these results in some detail. Which one

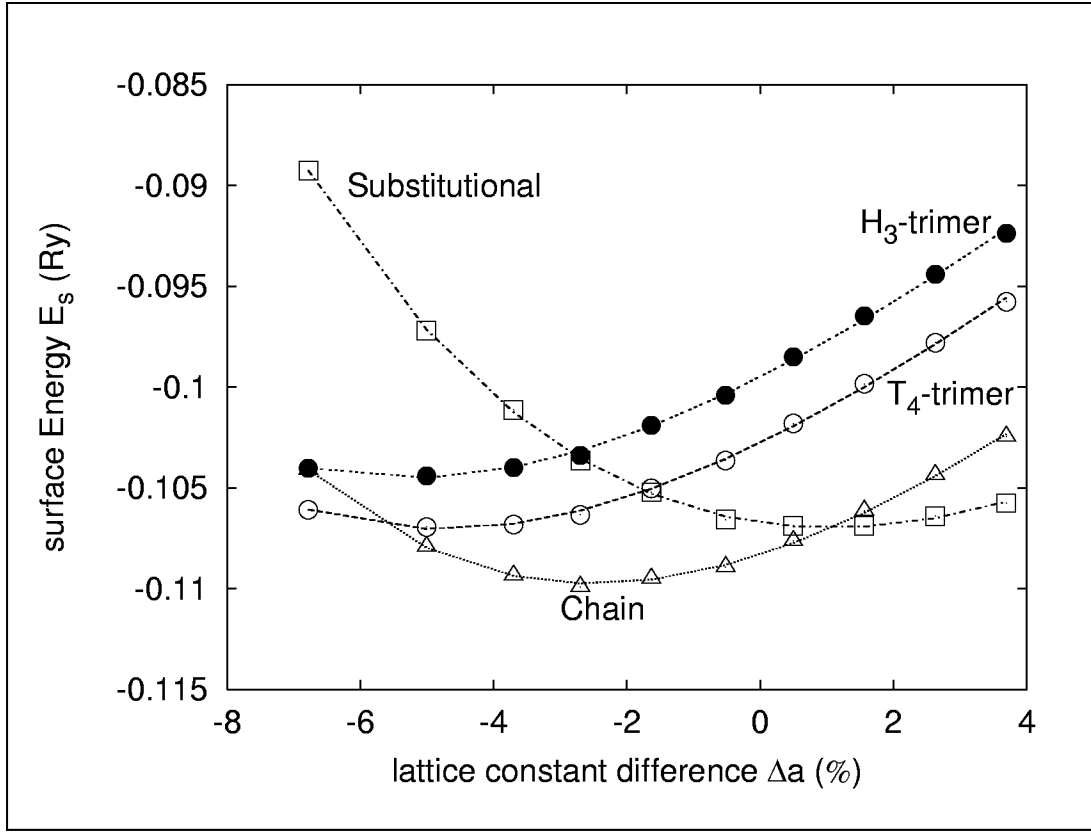


Figure 11.6: Surface energies E_s per Sb atom plotted against the deviation of lateral lattice constant Δa from the theoretical-equilibrium lattice constant of bulk Ge for different structures. The filled circles, empty circles, triangles, and squares represent the H_3 -trimer, T_4 -trimer, chain, and substitutional geometries, respectively.

is stable at certain lattice constant among the above four different structures depends on two parameters: (i) the matching of bond length distances between adsorbate Sb atoms and (ii) the relative strength of Sb-Ge chemical bond compared to Sb-Sb bond at this lattice constant. The Sb-Sb bond does not exist in the substitutional geometry, but it exists in all the other three structures. This leads to a completely different gross feature of the curve of surface energy for substitutional geometry from the other three geometries in the Fig.11.5 and Fig.11.6: The surface energy of substitutional geometry decreases with increasing the lateral lattice constant till its minimum at the dilated Ge film. The surface energies of all the other three geometries decrease with decreasing the lateral

lattice constant till their minima at the compressed film.

The bond lengths of trimer and chain are determined by the balance of chemical interactions of Sb atoms with one another and with the substrate Ge atoms. This balance leads to two distinctly different trends for the bond length distances between Sb atoms in the trimer and chain geometries, when approaching to their minimum energies with compressed Ge films (see Fig.11.7): The bond length distance between Sb atoms in the chain geometry decreases with decreasing the lateral lattice constant, and at $a_{min}=5.491$ Å approximately equals that of ground-state Sb_4 cluster. The bond length of ground-state Sb_4 molecule is 2.82Å, obtained from our calculations based on the same calculation conditions as the above. For that we have also relaxed a free double chain (Fig.11.8) of Sb

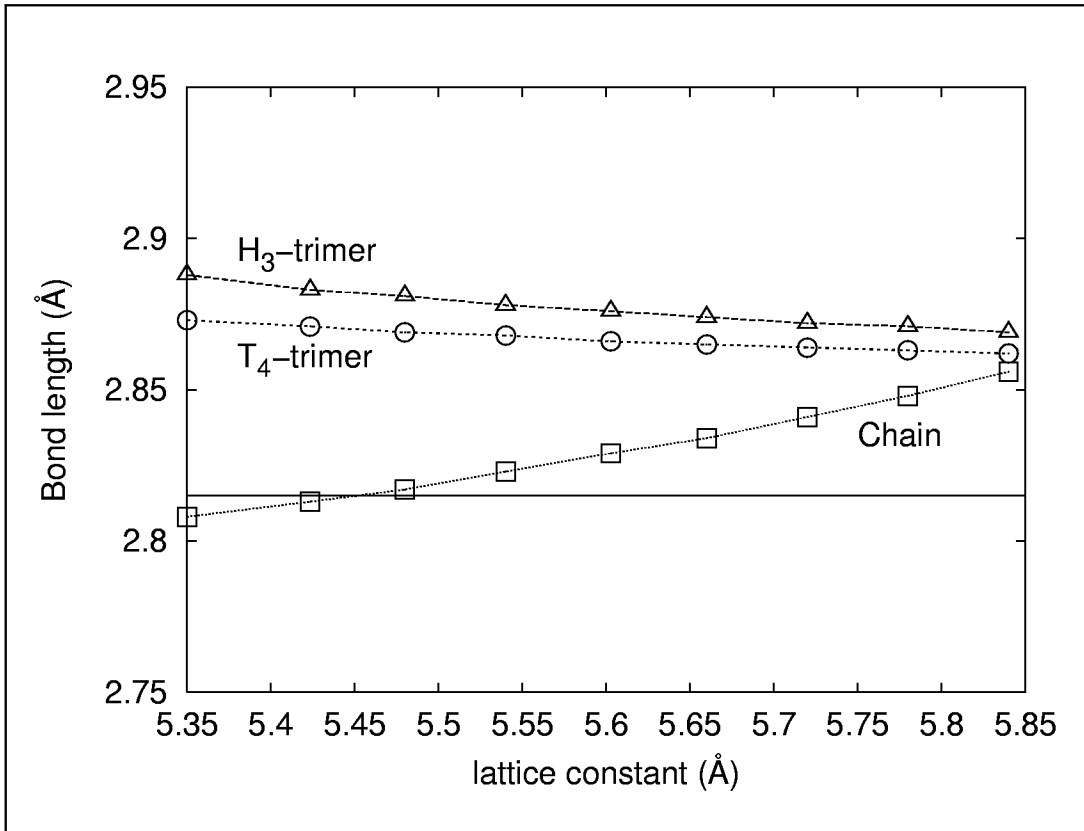


Figure 11.7: Bond length distances between adsorbate Sb atoms plotted against lateral lattice constant a in the H_3 -trimer, T_4 -trimer and chain geometries on Ge(111) substrate. The triangles, empty circles and squares represent the H_3 -trimer, T_4 -trimer and chain geometries, respectively. The line corresponds to the calculated bond length of ground-state Sb_4 -cluster.

based on the same conditions. We find that the obtained bond length ($=2.82$ Å) is the same as that of Sb chain on the Ge(111) substrate at the equilibrium-lateral lattice constant $a_{min}=5.491$ Å. The fact that the bond length distance between Sb

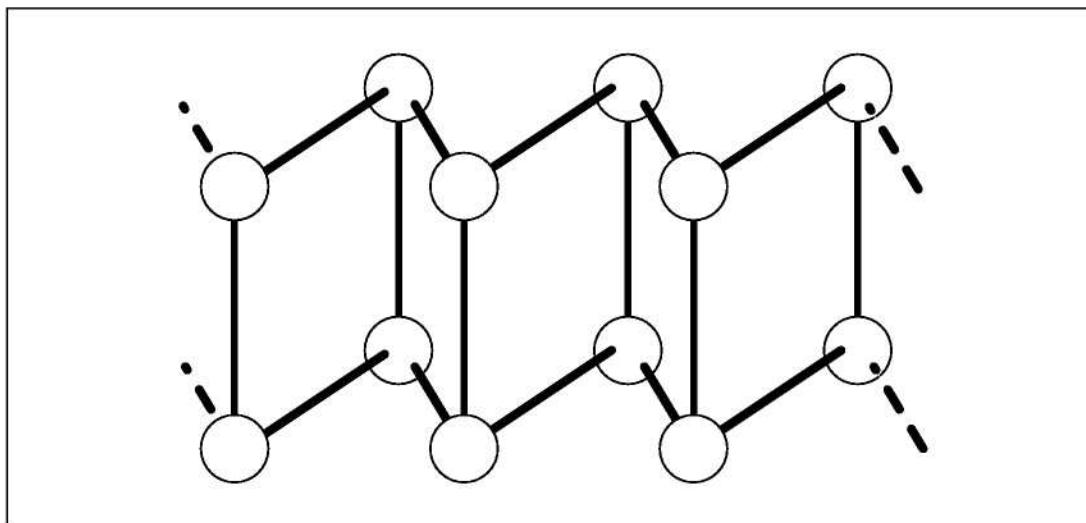


Figure 11.8: Schematic picture of the free double chain.

atoms in the chains decreases with decreasing the lattice constant and approaches to the free chain at the equilibrium lattice constant indicates that the chemical interactions between Sb atoms in neighboring chains can be neglected. However, in both H_3 and T_4 trimers, the bond length distances between Sb atoms slightly increase with the decrease of lattice constant. This indicates that the chemical interactions between Sb atoms in different trimers become more and more important with decreased lattice constant, and the system is more and more metallic. To see this, we have also presented the electronic density distribution for T_4 -trimer at two different lattice constants $a=5.84\text{\AA}$ and 5.35\AA in Fig.11.9. We find

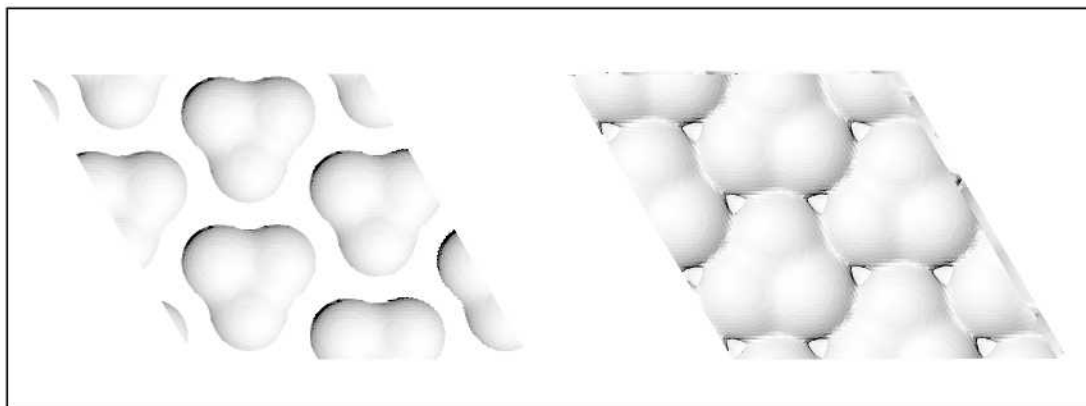


Figure 11.9: The electronic density distribution for T_4 -trimer at two different lateral lattice constants $a=5.84\text{\AA}$ and $a=5.35\text{\AA}$, respectively. The left panel is the electronic density distribution at $a=5.84\text{\AA}$ and the right panel shows the electronic density distribution at $a=5.35\text{\AA}$.

that, at the large lattice constant, different trimers are separated from each other,

but at the small lateral lattice constant, different trimers begin to interact with each other. It is the interactions between Sb atoms in different trimers that lead to the slight increase of the bond length distances between adsorbate Sb atoms in the trimer. To prove this further, we have relaxed an isolated T_4 -trimer on the Ge(111) substrate at two different lattice constants $a=5.84\text{\AA}$ and 5.35\AA , respectively. For isolated trimers the trend is reversed, and the obtained bond length distances between Sb atoms in the trimer ($=2.850\text{\AA}$ at $a=5.84\text{\AA}$, and 2.847\AA at $a=5.35\text{\AA}$) slightly decrease with decreasing the lateral lattice constant.

Comparing our results with the experiments, we find at the initial Si(111):Sb surface the expected $(\sqrt{3} \times \sqrt{3})$ -reconstruction for small lattice constants to be energetically favored. After the deposition of three monolayers Ge, Theuerkauf observed a $(6\sqrt{3} \times 6\sqrt{3})$ hexagonal reconstruction, where the (1×1) reconstructed is found on top of the hexagons. This is an unexpected result, since according to our calculations the (1×1) reconstruction is only preferable above the other reconstructions for large lattice constants. In our model for the hexagonal-reconstruction, we assume that the Sb atoms at the edge of the hexagons are bound directly to Ge atoms on the lower terrace. Since a calculation of the large $(6\sqrt{3} \times 6\sqrt{3})$ is not feasible, we have calculated a step edge, where the two innermost layers are Si atoms, covered with three layers of Ge and Sb on top. At the step edge, the Sb atom was in the same position as we have predicted for the hexagonal-reconstruction. The step-edge is shown in Fig.11.10. All atoms, except the two innermost Si-layers, which were kept fixed on their bulk positions, are relaxed below 0.1mRy/a.u. . Compared to the distance between the Si atoms in the bulk (d_1), the distance between the Sb atoms (d_2) on top of the surface was enlarged by 8%, in full agreement with the experimental observations. Since the lattice mismatch between the Si-bulk and the Ge-film is only $\approx 4\%$, one can conclude that the large relaxation of the Sb atoms on top is induced by the Sb atoms. The calculation of Berger [Ber01] for different step-edge structures of As-covered Si(111) show that the Sb atom at the step-edge induces this over-relaxation. Comparing this dilated lattice constant with our calculation for the energies of the four different structures, we find that for the 5.84\AA (Si lattice constant plus the 8% relaxation), the (1×1) structure is favorable, in full agreement with the experiment. For more than 15 monolayers of Ge, close to the Ge equilibrium lattice constant, we find the (2×1) structure to be energetically preferred. Thus, all observed reconstructions on growing Ge-films on Si(111):Sb, can be understood by the dependence of the energies for the different reconstructions as a function of the lateral lattice constant.

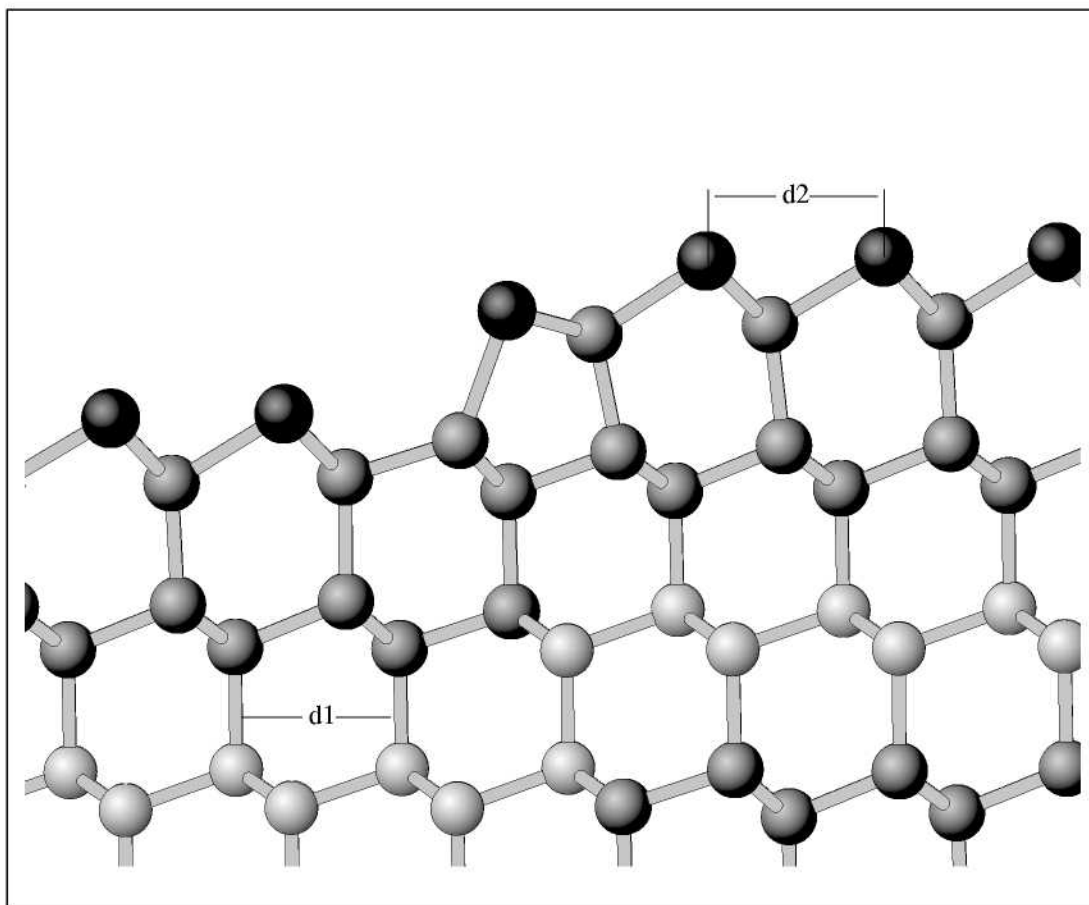


Figure 11.10: Sideview of the Si/Ge(111):Sb step-edge, used to simulate the rim of the hexagonal $(6\sqrt{3} \times 6\sqrt{3})$ -reconstruction.

Chapter 12

Summary

We have shown in this thesis that it is possible to contribute to the understanding of surfactant mediated growth by means of first-principles calculations. Using the self-developed program package **EStCoMPP** which is based on density functional theory combined with pseudopotentials we have investigated four different problems:

1. The paths and energy barriers for diffusion of single Si ad-atoms on the clean (3×3) -reconstructed Si(111) surface were calculated. We also investigated the structure of small Si-clusters on this surface (see chapter 7).
2. The structure and development of small Si-clusters on surfactant terminated (1 monolayer of As or Sb) Si(111) was calculated. The investigated cluster sizes range from single ad-atoms to 4 atoms. With the results we are able to explain experimentally determined features of the initial stages of homoepitaxial growth characteristic for the different surfactants (see chapter 9).
3. The atomic and electronic structure of two different step-edges of the As terminated Si(111) double-step is presented and connected to STM experiments (see chapter 10).
4. The influence of lattice strain on the structure of Sb-covered Ge films grown on Si(111) with increasing thickness was investigated and compared to experimental results. (see chapter 11).

This work provides the basis for the calculation of the relevant kinetic parameters during surfactant mediated growth, for cluster development, or for attachment at steps. All important configurations, which are either the initial or final configurations of kinetic processes have been determined. After the energy barriers will be worked out for these atomistic processes, a full kinetic picture of the surfactant mediated growth of Si or Ge on Si(111):As/Sb can be given.

All calculations presented in this thesis were carried out with the *ab initio* molecular dynamics program **EStCoMPP** developed in our group, which is based on norm-conserving pseudopotentials and a plane wave basis-set set. The results are analyzed with the recently developed visualization tool **EStCoMPP-VT**. The results presented here are at the cutting edge of supercomputing and have been realized by extensive use of the Cray T3E massively parallelized supercomputing system.

In detail we find the following results:

For clean Si surfaces we have determined the diffusion path of single Si ad-atoms on the (3×3) reconstructed Si surface by mapping the total energy $E(x, y) = \min_z E(x, y, z)$ of Si ad-atoms. We find a rather low activation energy for diffusion of ≈ 0.4 eV when the ad-atom crosses the boundary between the faulted and unfaulted half of the (3×3) unit cell. – Starting from the equilibrium Si ad-atom positions we added successively more Si ad-atoms at various positions on the surface. For clusters containing up to three Si atoms, the separate formation of clusters in one triangular half of the unit cell (with or without stacking fault) is preferred. By adding a fourth Si atom, the clusters in both halves interact, and for larger sizes clusters located at the center of the unit cell become stable.

We have determined many possible structures of small Si clusters on surfactant-covered (1×1) reconstructed Si(111) surfaces containing up to 4 Si atoms. From our calculations we conclude that the cluster evolution is identical for Si(111):As and Si(111):Sb up to a cluster-size of 3 Si atoms:

(i) One Si ad-atom exchanges on the surface, moving to a substitutional position and shifting the replaced As/Sb atom to a bridge site between the Si atom and a As/Sb atom on the surface. (ii) The second Si atom exchanges at a neighboring position and the As/Sb atoms form a dimer on top of the Si atoms. (iii) The third Si atom exchanges at a position neighboring both of the previously exchanged Si atoms, and the replaced As/Sb atoms form a T4-centered trimer on top of the incorporated Si atoms.

On the Sb-covered surface, the fourth Si atom is not added to the cluster. Instead, it is energetically favorable for the Si atom to exchange on the terrace, and act as nucleus for a new Sb-trimer. Thus, the $(\sqrt{3} \times \sqrt{3})$ structure grows on top of the (1×1) reconstruction as observed in the experiment.

On the As-covered surface, the fourth Si atom replaces one of the As trimer atoms, shifting the As atom upwards to a position close to a (1×1) equilibrium position in the next layer. Thus, for Si on Si(111):As double-layer growth starts with the fourth Si atom.

We summarize this part of the investigation by concluding that the microstructure evolution of clusters consisting of up to 4 Si atoms has been de-

terminated in full agreement with the experiment.

Our calculations for the barriers of the competing processes on Si(111):As, i.e. Ge diffusion on top of the As-covered surface and Ge–As exchange, show that Ge ad-atoms can diffuse far across the surface and may reach existing step edges. To decide if growth occurs by step flow mode, one has to know the attachment barrier for Ge ad-atoms at islands which is decisively influenced by the details of the step structure. We have calculated STM-images for the previously determined As-covered steps using the Tersoff-Hamann approximation. Our theoretical images coincide remarkably well with the experimental STM-images recently determined by B. Voigtländer. This proves that we have found the correct step-edge structure by total energy calculations.

Ge heteroepitaxy on Si(111):Sb shows a variety of surface reconstructions during growth. We have investigated the stability of different structures of Ge(111):Sb as a function of lateral lattice constant. We find that the (2×1) -reconstruction of Ge(111):Sb experimentally found to be stable at the equilibrium lattice constant is also the stable structure for slightly dilated films ($<1\%$), for larger dilatation the (1×1) structure becomes more stable. For compressed films the $(\sqrt{3} \times \sqrt{3})$ T_4 -structure (found experimentally on Si(111):Sb) becomes competitive. It is stable for lattice constants compressed by more than 5%. Applying the results to the growth of Ge films on Si(111):As, we can explain all the experimentally observed surface reconstructions during growth as a function of strain.

Appendix A

Tables of Positions and Angles

A.1 Clusters on Si(111)(3 × 3)

A.1.1 Si(111)(3 × 3) without extra ad-atoms

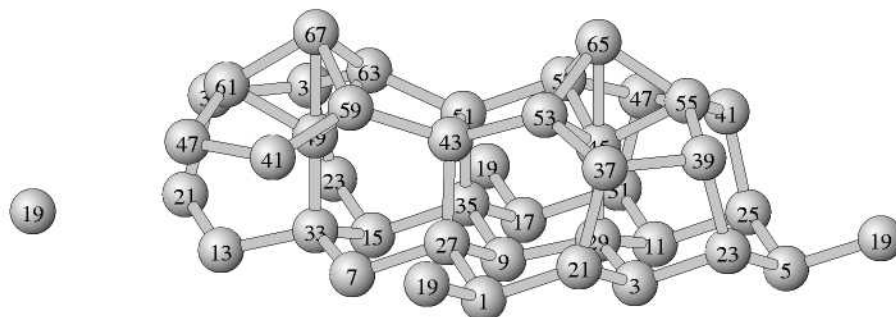


Figure A.1: Perspective view of the upper half of the inversion symmetric (3 × 3)-supercell.

Nr.	coordinates [a.u.]				bondlength [a.u]				bondangles							
	x	y	z	1-19	1-21	1-27	1-0	19-1-21	19-1-27	21-1-27	0-0-0	0-0-0	0-0-0	0-0-0	0-0-0	0-0-0
1	2.093	-7.249	2.220	4.429	4.521	4.516	0.000	109.37	109.29	107.77	0.00	0.00	0.00	0.00	0.00	0.00
3	8.371	-3.625	2.220	3-21	3-23	3-29	3-0	21-3-23	21-3-29	23-3-29	0-0-0	0-0-0	0-0-0	0-0-0	0-0-0	0-0-0
				4.417	4.435	4.313	0.000	107.28	111.95	111.77	0.00	0.00	0.00	0.00	0.00	0.00
5	14.648	-0.000	2.220	5-19	5-23	5-25	5-0	19-5-23	19-5-25	23-5-25	0-0-0	0-0-0	0-0-0	0-0-0	0-0-0	0-0-0
				4.445	4.526	4.515	0.000	109.28	109.10	107.71	0.00	0.00	0.00	0.00	0.00	0.00
7	-4.185	-3.625	2.220	7-27	7-33	7-0	7-0	27-7-33	0-0-0	0-0-0	0-0-0	0-0-0	0-0-0	0-0-0	0-0-0	0-0-0
				4.478	4.313	0.000	0.000	110.96	0.00	0.00	0.00	0.00	0.00	0.00	0.00	0.00
9	2.093	0.000	2.220	9-27	9-29	9-35	9-0	27-9-29	27-9-35	29-9-35	0-0-0	0-0-0	0-0-0	0-0-0	0-0-0	0-0-0
				4.422	4.315	4.431	0.000	111.89	107.43	111.73	0.00	0.00	0.00	0.00	0.00	0.00
11	8.371	3.625	2.220	11-25	11-29	11-31	11-0	25-11-29	25-11-31	29-11-31	0-0-0	0-0-0	0-0-0	0-0-0	0-0-0	0-0-0
				4.431	4.308	4.425	0.000	111.78	107.47	111.80	0.00	0.00	0.00	0.00	0.00	0.00
13	-10.463	0.000	2.220	13-21	13-33	13-0	13-0	21-13-33	0-0-0	0-0-0	0-0-0	0-0-0	0-0-0	0-0-0	0-0-0	0-0-0
				4.476	4.316	0.000	0.000	110.92	0.00	0.00	0.00	0.00	0.00	0.00	0.00	0.00
15	-4.185	3.625	2.220	15-23	15-33	15-35	15-0	23-15-33	23-15-35	33-15-35	0-0-0	0-0-0	0-0-0	0-0-0	0-0-0	0-0-0
				4.479	4.311	4.484	0.000	110.90	109.27	110.90	0.00	0.00	0.00	0.00	0.00	0.00
17	2.093	7.249	2.220	17-19	17-31	17-35	17-0	19-17-31	19-17-35	31-17-35	0-0-0	0-0-0	0-0-0	0-0-0	0-0-0	0-0-0
				4.449	4.517	4.521	0.000	109.20	109.34	107.61	0.00	0.00	0.00	0.00	0.00	0.00
19	18.838	0.012	3.705	19-5	19-0	19-0	19-0	0-0-0	0-0-0	0-0-0	0-0-0	0-0-0	0-0-0	0-0-0	0-0-0	0-0-0
				4.445	0.000	0.000	0.000	0.00	0.00	0.00	0.00	0.00	0.00	0.00	0.00	0.00
19	0.005	-10.861	3.705	19-1	19-0	19-0	19-0	0-0-0	0-0-0	0-0-0	0-0-0	0-0-0	0-0-0	0-0-0	0-0-0	0-0-0
				4.429	0.000	0.000	0.000	0.00	0.00	0.00	0.00	0.00	0.00	0.00	0.00	0.00
19	0.005	10.886	3.705	19-17	19-0	19-0	19-0	0-0-0	0-0-0	0-0-0	0-0-0	0-0-0	0-0-0	0-0-0	0-0-0	0-0-0
				4.449	0.000	0.000	0.000	0.00	0.00	0.00	0.00	0.00	0.00	0.00	0.00	0.00
19	-18.829	0.012	3.705	19-0	19-0	19-0	19-0	0-0-0	0-0-0	0-0-0	0-0-0	0-0-0	0-0-0	0-0-0	0-0-0	0-0-0
				0.000	0.000	0.000	0.000	0.00	0.00	0.00	0.00	0.00	0.00	0.00	0.00	0.00
21	6.331	-7.213	3.793	21-1	21-3	21-37	21-0	1-21-3	1-21-37	3-21-37	0-0-0	0-0-0	0-0-0	0-0-0	0-0-0	0-0-0
				4.521	4.417	4.547	0.000	108.38	123.59	97.41	0.00	0.00	0.00	0.00	0.00	0.00
21	-12.503	3.661	3.793	21-13	21-37	21-0	21-0	13-21-37	0-0-0	0-0-0	0-0-0	0-0-0	0-0-0	0-0-0	0-0-0	0-0-0
				4.476	4.547	0.000	0.000	110.00	0.00	0.00	0.00	0.00	0.00	0.00	0.00	0.00
23	12.508	-3.654	3.817	23-3	23-5	23-39	23-0	3-23-5	3-23-39	5-23-39	0-0-0	0-0-0	0-0-0	0-0-0	0-0-0	0-0-0
				4.435	4.526	4.525	0.000	107.99	97.75	123.80	0.00	0.00	0.00	0.00	0.00	0.00
23	-6.326	7.220	3.817	23-15	23-39	23-0	23-0	15-23-39	0-0-0	0-0-0	0-0-0	0-0-0	0-0-0	0-0-0	0-0-0	0-0-0
				4.479	4.525	0.000	0.000	110.23	0.00	0.00	0.00	0.00	0.00	0.00	0.00	0.00
25	12.508	3.647	3.803	25-5	25-11	25-41	25-0	5-25-11	5-25-41	11-25-41	0-0-0	0-0-0	0-0-0	0-0-0	0-0-0	0-0-0
				4.515	4.431	4.534	0.000	108.25	123.94	97.40	0.00	0.00	0.00	0.00	0.00	0.00
27	0.006	-3.567	3.794	27-1	27-7	27-9	27-43	1-27-7	1-27-9	1-27-43	7-27-9	7-27-43	9-27-43	7-27-43	9-27-43	9-27-43
				4.516	4.478	4.422	4.549	107.42	108.41	123.51	109.08	110.03	97.45	110.03	97.45	97.45
29	6.281	0.003	3.257	29-3	29-9	29-11	29-45	3-29-9	3-29-11	3-29-45	9-29-11	9-29-45	11-29-45	104.01	104.14	104.14
				4.313	4.315	4.308	4.279	114.32	114.47	103.64	114.41	104.01	104.14	104.01	104.14	104.14

Nr.	coordinates [a.u.]			bondlength [a.u]					bondangles				
	x	y	z	31-11	31-17	31-47	31-0	11-31-17	11-31-47	17-31-47	0-0-0	0-0-0	0-0-0
31	6.323	7.214	3.802	4.425	4.517	4.536	0.000	108.32	97.56	123.94	0.00	0.00	0-0-0
33	-6.275	0.001	3.263	33-7	33-13	33-15	33-49	7-33-13	7-33-15	7-33-49	13-33-15	13-33-49	15-33-49
35	0.006	3.569	3.813	35-9	35-15	35-17	35-51	9-35-15	9-35-17	9-35-51	15-35-17	15-35-51	17-35-51
37	-11.452	4.264	8.176	4.431	4.484	4.521	4.524	108.81	108.15	97.80	107.22	110.12	123.75
37	7.382	-6.610	8.176	37-21	37-39	37-61	37-0	21-37-39	21-37-61	39-37-61	0-0-0	0-0-0	0-0-0
39	11.473	-4.259	8.180	4.547	4.719	4.706	0.000	105.50	105.30	103.04	0.00	0.00	0.00
39	-7.361	6.615	8.180	37-21	37-39	37-53	37-0	21-37-39	21-37-53	39-37-53	0-0-0	0-0-0	0-0-0
41	-7.375	-6.605	8.170	4.547	4.719	4.683	0.000	105.50	104.56	103.09	0.00	0.00	0.00
41	11.459	4.269	8.170	39-23	39-37	39-55	39-0	23-39-37	23-39-55	37-39-55	0-0-0	0-0-0	0-0-0
43	0.007	-2.362	8.180	4.525	4.719	4.690	0.000	105.32	104.37	102.85	0.00	0.00	0.00
45	6.288	-0.018	7.536	39-23	39-37	39-63	39-0	23-39-37	23-39-63	37-39-63	0-0-0	0-0-0	0-0-0
47	7.387	6.630	8.173	4.525	4.719	4.691	0.000	105.32	105.32	102.96	0.00	0.00	0.00
47	-11.446	-4.244	8.173	41-47	41-59	41-0	41-0	47-41-59	0-0-0	0-0-0	0-0-0	0-0-0	0-0-0
49	-6.295	0.001	7.578	41-25	41-47	41-55	41-0	25-41-47	25-41-55	47-41-55	0-0-0	0-0-0	0-0-0
51	-0.004	2.376	8.177	4.534	4.707	4.690	0.000	105.64	104.28	103.19	0.00	0.00	0.00
53	4.318	-3.409	9.691	43-27	43-51	43-53	43-59	27-43-51	27-43-53	27-43-59	51-43-53	51-43-59	53-43-59
55	10.225	0.005	9.682	4.549	4.739	4.687	4.706	105.32	104.59	105.00	103.05	102.84	133.39
57	4.319	3.416	9.651	45-29	45-53	45-55	45-57	29-45-53	29-45-55	29-45-57	29-45-65	53-45-65	53-45-57
59	-4.309	-3.417	9.733	4.279	4.475	4.484	4.487	118.99	118.68	117.82	179.23	99.21	99.20
61	-10.229	0.003	9.758	47-31	47-41	47-57	47-0	31-47-41	31-47-57	41-47-57	0-0-0	0-0-0	0-0-0
				4.536	4.707	4.683	0.000	105.48	103.80	102.86	0.00	0.00	0.00
				47-41	47-61	47-0	47-0	41-47-61	0-0-0	0-0-0	0-0-0	0-0-0	0-0-0
				4.707	4.694	0.000	0.000	103.29	0.00	0.00	0.00	0.00	0.00
				49-33	49-59	49-61	49-63	33-49-59	33-49-61	33-49-63	33-49-67	59-49-61	59-49-63
				4.315	4.502	4.499	4.504	118.47	119.25	118.63	179.43	98.87	98.67
				51-35	51-43	51-57	51-63	35-51-43	35-51-57	35-51-63	43-51-57	43-51-63	57-51-63
				4.524	4.739	4.684	4.698	105.32	104.05	105.41	102.68	102.88	133.78
				53-37	53-43	53-45	53-65	37-53-43	37-53-45	37-53-65	43-53-45	43-53-65	45-53-65
				4.683	4.687	4.475	4.695	130.56	94.25	113.58	94.61	113.32	61.47
				55-39	55-41	55-45	55-65	39-55-41	39-55-45	39-55-65	41-55-45	41-55-65	45-55-65
				4.690	4.690	4.484	4.692	130.80	94.34	113.59	94.68	113.14	61.43
				57-45	57-47	57-51	57-65	45-57-47	45-57-51	45-57-65	47-57-51	47-57-65	51-57-65
				4.487	4.683	4.684	4.693	95.12	94.99	61.40	131.13	113.31	113.47
				59-41	59-43	59-49	59-67	41-59-43	41-59-49	41-59-67	43-59-49	43-59-67	49-59-67
				4.691	4.706	4.502	4.680	129.92	93.91	113.72	94.38	113.50	61.31
				61-37	61-47	61-49	61-67	37-61-47	37-61-49	37-61-67	47-61-49	47-61-67	49-61-67
				4.706	4.694	4.499	4.685	129.66	93.71	113.59	93.59	113.50	61.30

Nr.	coordinates [a.u.]			bondlength [a.u.]					bondangles				
	x	y	z	63-39	63-49	63-51	63-67	39-63-49	39-63-51	39-63-67	49-63-51	49-63-67	51-63-67
63	-4.309	3.415	9.745	4.691	4.504	4.698	4.674	94.00	129.47	113.93	94.35	61.34	113.73
65	6.283	0.020	12.226	65-45	65-53	65-55	65-57	45-65-53	45-65-55	45-65-57	53-65-55	53-65-57	55-65-57
				4.690	4.695	4.692	4.693	56.95	57.09	57.14	93.24	93.27	93.22
67	-6.269	-0.001	12.262	67-49	67-59	67-61	67-63	49-67-59	49-67-61	49-67-63	59-67-61	59-67-63	61-67-63
				4.684	4.680	4.685	4.674	57.47	57.39	57.54	93.78	93.83	93.77

A.1.2 One additional Si ad-atom (a)

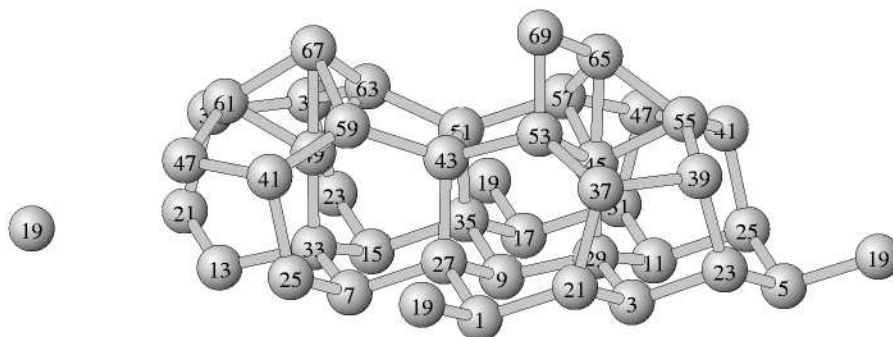


Figure A.2: Perspective view of the upper half of the inversion symmetric (3×3) -supercell with one extra ad-atom (69) on top.

Nr.	coordinates [a.u.]			bondlength [a.u.]				bondangles							
	x	y	z	1-19	1-21	1-27	1-0	19-1-21	19-1-27	21-1-27	0-0-0	0-0-0	0-0-0	0-0-0	0-0-0
1	2.093	-7.249	2.220	4.425	4.512	4.513	0.000	109.39	109.48	108.14	0.00	0.00	0.00	0.00	0.00
3	8.371	-3.625	2.220	4.414	4.444	4.318	0.000	21-3-23	21-3-29	23-3-29	0-0-0	0-0-0	0-0-0	0-0-0	0-0-0
5	14.648	-0.000	2.220	5-19	5-23	5-25	5-0	19-5-23	19-5-25	23-5-25	0-0-0	0-0-0	0-0-0	0-0-0	0-0-0
7	-4.185	-3.625	2.220	4.471	4.467	4.318	0.000	25-7-27	25-7-33	27-7-33	0-0-0	0-0-0	0-0-0	0-0-0	0-0-0
9	2.093	0.000	2.220	9-27	9-29	9-35	9-0	27-9-29	27-9-35	29-9-35	0-0-0	0-0-0	0-0-0	0-0-0	0-0-0
11	8.371	3.625	2.220	11-25	11-29	11-31	11-0	25-11-29	25-11-31	29-11-31	0-0-0	0-0-0	0-0-0	0-0-0	0-0-0
13	-10.463	0.000	2.220	13-21	13-33	13-0	13-0	21-13-33	0-0-0	0-0-0	0-0-0	0-0-0	0-0-0	0-0-0	0-0-0
15	-4.185	3.625	2.220	15-23	15-33	15-35	15-0	23-15-33	23-15-35	33-15-35	0-0-0	0-0-0	0-0-0	0-0-0	0-0-0
17	2.093	7.249	2.220	17-19	17-31	17-35	17-0	19-17-31	19-17-35	31-17-35	0-0-0	0-0-0	0-0-0	0-0-0	0-0-0
19	18.846	0.011	3.701	19-5	19-0	19-0	19-0	0-0-0	0-0-0	0-0-0	0-0-0	0-0-0	0-0-0	0-0-0	0-0-0
19	0.013	-10.863	3.701	19-1	19-0	19-0	19-0	0-0-0	0-0-0	0-0-0	0-0-0	0-0-0	0-0-0	0-0-0	0-0-0
19	0.013	10.884	3.701	19-17	19-0	19-0	19-0	0-0-0	0-0-0	0-0-0	0-0-0	0-0-0	0-0-0	0-0-0	0-0-0
19	-18.821	0.011	3.701	19-0	19-0	19-0	19-0	0-0-0	0-0-0	0-0-0	0-0-0	0-0-0	0-0-0	0-0-0	0-0-0
21	6.330	-7.219	3.769	21-1	21-3	21-37	21-0	1-21-3	1-21-37	3-21-37	0-0-0	0-0-0	0-0-0	0-0-0	0-0-0
21	-12.504	3.655	3.769	21-13	21-37	21-0	21-0	13-21-37	0-0-0	0-0-0	0-0-0	0-0-0	0-0-0	0-0-0	0-0-0
23	12.507	-3.643	3.843	23-3	23-5	23-39	23-0	3-23-5	3-23-39	5-23-39	0-0-0	0-0-0	0-0-0	0-0-0	0-0-0
23	-6.326	7.230	3.843	23-15	23-39	23-0	23-0	15-23-39	0-0-0	0-0-0	0-0-0	0-0-0	0-0-0	0-0-0	0-0-0
25	-6.318	-7.225	3.794	25-7	25-41	25-0	25-0	7-25-41	0-0-0	0-0-0	0-0-0	0-0-0	0-0-0	0-0-0	0-0-0
25	12.516	3.648	3.794	25-5	25-11	25-41	25-0	5-25-11	5-25-41	11-25-41	0-0-0	0-0-0	0-0-0	0-0-0	0-0-0
27	0.001	-3.564	3.775	27-1	27-7	27-9	27-43	1-27-7	1-27-9	1-27-43	7-27-9	7-27-43	109.40	97.68	97.68

Nr.	coordinates [a.u.]			bondlength [a.u.]				bondangles					
	x	y	z	29-3	29-9	29-11	29-45	3-29-9	3-29-11	3-29-45	9-29-11	9-29-45	11-29-45
29	6.274	-0.010	3.307	4.318	4.320	4.335	4.268	114.12	113.81	104.44	113.76	104.51	104.76
31	6.320	7.220	3.783	4.424	4.508	4.536	0.000	108.51	97.72	124.10	0.00	0.00	0.00
33	-6.272	0.002	3.285	4.318	4.324	4.314	4.322	7-33-13	7-33-15	7-33-49	13-33-15	13-33-49	15-33-49
35	0.010	3.570	3.841	4.440	4.498	4.527	4.554	9-35-15	9-35-17	9-35-51	15-35-17	15-35-51	17-35-51
37	-11.437	4.180	8.168	37-21	37-39	37-61	37-0	21-37-39	21-37-61	39-37-61	0-0-0	0-0-0	0-0-0
37	7.397	-6.693	8.168	37-21	37-39	37-53	37-0	21-37-39	21-37-53	39-37-53	0-0-0	0-0-0	0-0-0
39	11.472	-4.286	8.240	39-23	39-37	39-55	39-0	23-39-37	23-39-55	37-39-55	0-0-0	0-0-0	0-0-0
39	-7.362	6.588	8.240	39-23	39-37	39-63	39-0	23-39-37	23-39-63	37-39-63	0-0-0	0-0-0	0-0-0
41	-7.352	-6.544	8.166	41-25	41-47	41-59	41-0	25-41-47	25-41-59	47-41-59	0-0-0	0-0-0	0-0-0
41	11.482	4.329	8.166	41-25	41-47	41-55	41-0	25-41-47	25-41-55	47-41-55	0-0-0	0-0-0	0-0-0
43	-0.058	-2.364	8.177	43-27	43-51	43-53	43-59	27-43-51	27-43-53	27-43-59	51-43-53	51-43-59	53-43-59
45	6.268	-0.027	7.575	45-29	45-53	45-55	45-57	29-45-53	29-45-55	29-45-57	29-45-65	53-45-55	53-45-57
47	7.412	6.692	8.153	47-31	47-41	47-57	47-0	31-47-41	31-47-57	41-47-57	0-0-0	0-0-0	0-0-0
47	-11.422	-4.182	8.153	47-41	47-61	47-0	47-0	41-47-61	0-0-0	0-0-0	0-0-0	0-0-0	0-0-0
49	-6.290	0.010	7.607	49-33	49-59	49-61	49-63	33-49-59	33-49-61	33-49-63	33-49-67	59-49-61	59-49-63
51	-0.040	2.373	8.234	51-35	51-43	51-57	51-63	35-51-43	35-51-57	35-51-63	43-51-57	43-51-63	57-51-63
53	4.261	-3.503	9.719	53-37	53-43	53-45	53-69	37-53-43	37-53-45	37-53-69	43-53-45	43-53-69	45-53-69
55	10.234	0.075	9.662	55-39	55-41	55-45	55-65	39-55-41	39-55-45	39-55-65	41-55-45	41-55-65	45-55-65
57	4.350	3.490	9.623	57-45	57-47	57-51	57-65	45-57-47	45-57-51	45-57-65	47-57-51	47-57-65	51-57-65
59	-4.326	-3.389	9.760	59-41	59-43	59-49	59-67	41-59-43	41-59-49	41-59-67	43-59-49	43-59-67	49-59-67
				4.653	4.666	4.477	4.692	128.85	93.71	114.11	94.09	114.22	62.45

Nr.	coordinates [a.u.]			bondlength [a.u]				bondangles					
	x	y	z	61-37	61-47	61-49	61-67	37-61-47	37-61-49	37-61-67	47-61-49	47-61-67	49-61-67
61	-10.205	-0.001	9.804	61-39 4.656	63-49 4.657	63-51 4.489	63-67 4.689	39-63-49 127.78	39-63-51 93.24	39-63-67 114.50	49-63-51 93.24	49-63-67 114.28	51-63-67 62.39
63	-4.330	3.398	9.788	63-39 4.665	63-49 4.481	63-51 4.677	63-67 4.692	39-63-49 94.07	39-63-51 129.48	39-63-67 114.12	49-63-51 94.23	49-63-67 62.42	51-63-67 113.82
65	6.413	0.401	12.307	65-45 4.753	65-55 4.658	65-57 4.583	65-69 4.338	45-65-55 56.88	45-65-57 57.59	45-65-69 109.88	55-65-69 94.82	55-65-69 127.46	57-65-69 121.49
67	-6.276	-0.007	12.363	67-49 4.757	67-59 4.692	67-61 4.689	67-63 4.692	49-67-59 56.57	49-67-61 56.75	49-67-63 56.62	59-67-61 92.66	59-67-63 92.64	61-67-63 92.70
69	4.196	-2.840	14.150	69-53 4.480	69-65 4.338	69-0 0.000	69-0 0.000	53-69-65 71.52	0-0-0 0.00	0-0-0 0.00	0-0-0 0.00	0-0-0 0.00	0-0-0 0.00

A.1.3 One additional Si ad-atom (b)

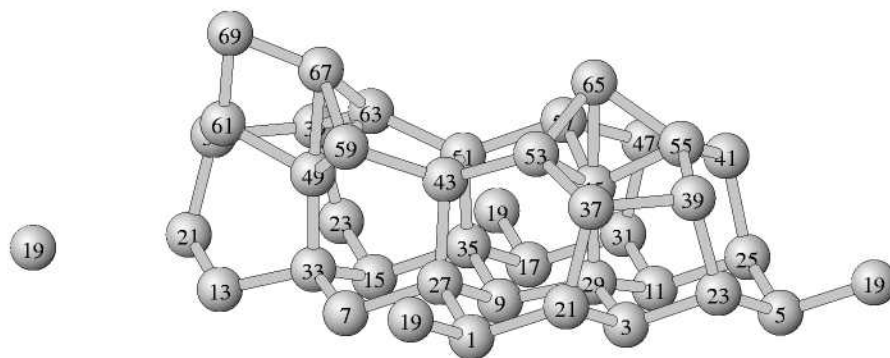


Figure A.3: Perspective view of the upper half of the inversion symmetric (3×3) -supercell with one extra ad-atom (69) on top.

Nr.	coordinates [a.u.]				bondlength [a.u.]				bondangles							
	x	y	z		1-19	1-21	1-27	1-0	19-1-21	19-1-27	21-1-27	0-0-0	0-0-0	0-0-0	0-0-0	0-0-0
1	2.093	-7.249	2.220		4.453	4.509	4.505	0.000	109.18	109.19	107.76	0-0-0	0-0-0	0-0-0	0-0-0	0-0-0
3	8.371	-3.625	2.220		3-21	3-29	3-29	3-0	21-3-23	21-3-29	23-3-29	0-0-0	0-0-0	0-0-0	0-0-0	0-0-0
					4.409	4.449	4.314	0.000	107.39	111.84	111.67	0-0-0	0-0-0	0-0-0	0-0-0	0-0-0
5	14.648	-0.000	2.220		5-19	5-23	5-25	5-0	19-5-23	19-5-25	23-5-25	0-0-0	0-0-0	0-0-0	0-0-0	0-0-0
					4.463	4.529	4.518	0.000	108.66	108.82	107.59	0-0-0	0-0-0	0-0-0	0-0-0	0-0-0
7	-4.185	-3.625	2.220		7-27	7-33	7-0	7-0	27-7-33	0-0-0	0-0-0	0-0-0	0-0-0	0-0-0	0-0-0	0-0-0
					4.482	4.332	0.000	0.000	110.84	0.00	0.00	0-0-0	0-0-0	0-0-0	0-0-0	0-0-0
9	2.093	0.000	2.220		9-27	9-29	9-35	9-0	27-9-29	27-9-35	29-9-35	0-0-0	0-0-0	0-0-0	0-0-0	0-0-0
					4.417	4.313	4.436	0.000	111.79	107.58	111.65	0-0-0	0-0-0	0-0-0	0-0-0	0-0-0
11	8.371	3.625	2.220		11-25	11-29	11-31	11-0	25-11-29	25-11-31	29-11-31	0-0-0	0-0-0	0-0-0	0-0-0	0-0-0
					4.437	4.312	4.416	0.000	111.74	107.56	111.77	0-0-0	0-0-0	0-0-0	0-0-0	0-0-0
13	-10.463	0.000	2.220		13-21	13-33	13-0	13-0	21-13-33	0-0-0	0-0-0	0-0-0	0-0-0	0-0-0	0-0-0	0-0-0
					4.480	4.320	0.000	0.000	110.69	0.00	0.00	0-0-0	0-0-0	0-0-0	0-0-0	0-0-0
15	-4.185	3.625	2.220		15-23	15-33	15-35	15-0	23-15-33	23-15-35	33-15-35	0-0-0	0-0-0	0-0-0	0-0-0	0-0-0
					4.484	4.325	4.487	0.000	110.45	108.97	110.70	0-0-0	0-0-0	0-0-0	0-0-0	0-0-0
17	2.093	7.249	2.220		17-19	17-31	17-35	17-0	19-17-31	19-17-35	31-17-35	0-0-0	0-0-0	0-0-0	0-0-0	0-0-0
					4.456	4.508	4.520	0.000	109.08	108.90	107.60	0-0-0	0-0-0	0-0-0	0-0-0	0-0-0
19	18.840	0.002	3.753		19-5	19-0	19-0	19-0	0-0-0	0-0-0	0-0-0	0-0-0	0-0-0	0-0-0	0-0-0	0-0-0
					4.463	0.000	0.000	0.000	0.00	0.00	0.00	0-0-0	0-0-0	0-0-0	0-0-0	0-0-0
19	0.006	-10.872	3.753		19-1	19-0	19-0	19-0	0-0-0	0-0-0	0-0-0	0-0-0	0-0-0	0-0-0	0-0-0	0-0-0
					4.453	0.000	0.000	0.000	0.00	0.00	0.00	0-0-0	0-0-0	0-0-0	0-0-0	0-0-0
19	0.006	10.875	3.753		19-17	19-0	19-0	19-0	0-0-0	0-0-0	0-0-0	0-0-0	0-0-0	0-0-0	0-0-0	0-0-0
					4.456	0.000	0.000	0.000	0.00	0.00	0.00	0-0-0	0-0-0	0-0-0	0-0-0	0-0-0
19	-18.827	0.002	3.753		19-0	19-0	19-0	19-0	0-0-0	0-0-0	0-0-0	0-0-0	0-0-0	0-0-0	0-0-0	0-0-0
					0.000	0.000	0.000	0.000	0.00	0.00	0.00	0-0-0	0-0-0	0-0-0	0-0-0	0-0-0
21	6.324	-7.206	3.778		21-1	21-3	21-37	21-0	1-21-3	1-21-37	3-21-37	0-0-0	0-0-0	0-0-0	0-0-0	0-0-0
					4.509	4.409	4.553	0.000	108.74	122.60	97.40	0-0-0	0-0-0	0-0-0	0-0-0	0-0-0
21	-12.510	3.668	3.778		21-13	21-37	21-0	21-0	13-21-37	0-0-0	0-0-0	0-0-0	0-0-0	0-0-0	0-0-0	0-0-0
					4.480	4.553	0.000	0.000	110.48	0.00	0.00	0-0-0	0-0-0	0-0-0	0-0-0	0-0-0
23	12.515	-3.653	3.837		23-3	23-5	23-39	23-0	3-23-5	3-23-39	5-23-39	0-0-0	0-0-0	0-0-0	0-0-0	0-0-0
					4.449	4.529	4.564	0.000	107.69	97.84	124.17	0-0-0	0-0-0	0-0-0	0-0-0	0-0-0
23	-6.319	7.221	3.837		23-15	23-39	23-0	23-0	15-23-39	0-0-0	0-0-0	0-0-0	0-0-0	0-0-0	0-0-0	0-0-0
					4.484	4.564	0.000	0.000	110.44	0.00	0.00	0-0-0	0-0-0	0-0-0	0-0-0	0-0-0
25	12.511	3.647	3.814		25-5	25-11	25-41	25-0	5-25-11	5-25-41	11-25-41	0-0-0	0-0-0	0-0-0	0-0-0	0-0-0
					4.518	4.437	4.565	0.000	108.08	123.74	97.57	0-0-0	0-0-0	0-0-0	0-0-0	0-0-0
27	0.015	-3.570	3.783		27-1	27-7	27-9	27-43	1-27-7	1-27-9	1-27-43	7-27-9	7-27-43	9-27-43	9-27-43	9-27-43
					4.505	4.482	4.417	4.545	107.53	108.67	123.27	109.10	110.19	110.19	97.12	97.12
29	6.278	0.001	3.262		29-3	29-9	29-11	29-45	3-29-9	3-29-11	3-29-45	9-29-11	9-29-45	11-29-45	11-29-45	11-29-45
					4.314	4.313	4.312	4.306	114.33	114.35	104.03	114.38	103.45	103.45	104.47	104.47

Nr.	coordinates [a.u.]			bondlength [a.u.]				bondangles							
	x	y	z	31-11	31-17	31-47	31-0	11-31-17	11-31-47	17-31-47	0-0-0	0-0-0	0-0-0	0-0-0	0-0-0
31	6.320	7.208	3.786	4.416	4.508	4.558	0.000	108.64	97.15	123.45	0.00	0.00	13-33-15	13-33-49	0.00
33	-6.284	0.004	3.312	33-7	33-13	33-15	33-49	7-33-13	7-33-15	7-33-49	13-33-15	13-33-49	104.46	104.96	15-35-51
35	0.006	3.573	3.820	35-9	35-15	35-17	35-51	9-35-15	9-35-17	9-35-51	15-35-17	15-35-51	107.18	123.88	17-35-51
37	7.312	-6.578	8.178	37-21	37-39	37-53	37-0	21-37-39	21-37-53	39-37-53	0-0-0	0-0-0	0-0-0	0-0-0	0-0-0
37	-11.522	4.296	8.178	4.553	4.750	4.652	0.000	105.57	106.12	103.35	0.00	0.00	0-0-0	0-0-0	0-0-0
39	11.462	-4.268	8.236	4.553	4.750	4.740	0.000	105.57	104.37	102.75	0.00	0-0-0	0-0-0	0-0-0	0-0-0
39	-7.371	6.605	8.236	39-23	39-37	39-63	39-0	23-39-37	23-39-63	37-39-63	0-0-0	0-0-0	0-0-0	0-0-0	0-0-0
41	11.457	4.247	8.215	41-25	41-47	41-55	41-0	25-41-47	25-41-55	47-41-55	0-0-0	0-0-0	0-0-0	0-0-0	0-0-0
43	0.042	-2.363	8.165	43-27	43-51	43-53	43-59	27-43-51	27-43-53	27-43-59	51-43-53	51-43-59	102.64	102.69	53-43-59
45	6.238	-0.017	7.567	45-29	45-53	45-55	45-57	29-45-53	29-45-55	29-45-57	53-45-55	53-45-57	118.86	118.86	99.07
47	7.366	6.586	8.178	47-31	47-41	47-57	47-0	31-47-41	31-47-57	41-47-57	0-0-0	0-0-0	0-0-0	0-0-0	0-0-0
49	-6.297	-0.016	7.621	49-33	49-59	49-61	49-63	33-49-59	33-49-61	33-49-63	59-49-61	59-49-63	103.04	100.98	98.26
51	0.000	2.369	8.202	51-35	51-43	51-57	51-63	35-51-43	35-51-57	35-51-63	43-51-57	43-51-63	175.11	102.77	133.57
53	4.293	-3.401	9.739	53-37	53-43	53-45	53-65	37-53-43	37-53-45	37-53-65	43-53-45	43-53-65	113.71	114.16	61.93
55	10.189	-0.009	9.673	55-39	55-41	55-45	55-65	39-55-41	39-55-45	39-55-65	41-55-45	41-55-65	93.69	113.31	61.88
57	4.317	3.403	9.725	57-45	57-47	57-51	57-65	45-57-47	45-57-51	45-57-65	51-57-65	51-57-65	113.65	113.59	113.87
59	-4.229	-3.438	9.708	59-43	59-49	59-67	59-0	43-59-49	43-59-67	49-59-67	0-0-0	0-0-0	130.01	113.59	113.87
61	-10.341	-0.018	9.745	61-37	61-49	61-69	61-0	37-61-49	37-61-69	49-61-69	0-0-0	0-0-0	63.82	0.00	0.00
63	-4.294	3.354	9.773	63-39	63-49	63-51	63-67	39-63-49	39-63-51	39-63-67	49-63-51	49-63-67	110.41	0.00	0.00
65	6.287	0.009	12.288	65-45	65-53	65-55	65-57	45-65-53	45-65-55	45-65-57	53-65-55	53-65-57	124.11	62.97	110.42
				4.721	4.701	4.697	4.687	56.59	56.77	56.83	92.74	92.90	95.22	55-65-57	92.72

Nr.	coordinates [a.u.]			bondlength [a.u]					bondangles				
	x	y	z	67-49	67-59	67-63	67-69		49-67-59	49-67-63	49-67-69	59-67-63	59-67-69
67	-5.927	-0.178	12.394	4.790	4.552	4.692	4.342		57.65	56.27	108.81	94.55	114.63
69	-9.833	-1.068	14.071	69-61	69-67	69-0	69-0		61-69-67	0-0-0	0-0-0	0-0-0	0-0-0
				4.480	4.342	0.000	0.000		71.41	0.00	0.00	0.00	0.00

A.1.4 Two additional Si ad-atoms (c)

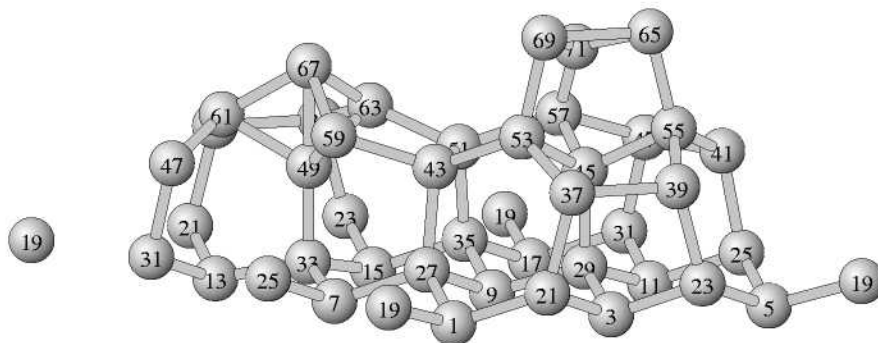


Figure A.4: Perspective view of the upper half of the inversion symmetric (3×3) -supercell with two extra ad-atoms (69,71) on top.

Nr.	coordinates [a.u.]			bondlength [a.u]				bondangles						
	x	y	z	1-19	1-21	1-27	1-0	19-1-21	19-1-27	21-1-27	0-0-0	0-0-0	0-0-0	0-0-0
1	2.093	-7.249	2.220	4.348	4.529	4.534	0.000	110.27	110.21	108.15	0.00	0.00	0.00	0.00
3	8.371	-3.625	2.220	4.428	4.452	4.404	0.000	106.99	110.22	109.93	0.00	0.00	0.00	0.00
5	14.648	-0.000	2.220	5-19	5-23	5-25	5-0	19-5-23	19-5-25	23-5-25	0-0-0	0-0-0	0-0-0	0-0-0
				4.401	4.531	4.527	0.000	110.42	109.93	107.94	0.00	0.00	0.00	0.00
7	-4.185	-3.625	2.220	7-25	7-27	7-33	7-0	25-7-27	25-7-33	27-7-33	0-0-0	0-0-0	0-0-0	0-0-0
				4.469	4.462	4.300	0.000	109.42	111.39	111.14	0.00	0.00	0.00	0.00
9	2.093	0.000	2.220	9-27	9-29	9-35	9-0	27-9-29	27-9-35	29-9-35	0-0-0	0-0-0	0-0-0	0-0-0
				4.430	4.394	4.440	0.000	110.18	106.98	109.98	0.00	0.00	0.00	0.00
11	8.371	3.625	2.220	11-25	11-29	11-31	11-0	25-11-29	25-11-31	29-11-31	0-0-0	0-0-0	0-0-0	0-0-0
				4.434	4.389	4.430	0.000	110.02	107.14	110.02	0.00	0.00	0.00	0.00
13	-10.463	0.000	2.220	13-21	13-31	13-33	13-0	21-13-31	21-13-33	31-13-33	0-0-0	0-0-0	0-0-0	0-0-0
				4.456	4.460	4.304	0.000	109.57	111.26	111.40	0.00	0.00	0.00	0.00
15	-4.185	3.625	2.220	15-23	15-33	15-35	15-0	23-15-33	23-15-35	33-15-35	0-0-0	0-0-0	0-0-0	0-0-0
				4.466	4.291	4.459	0.000	111.31	109.07	111.27	0.00	0.00	0.00	0.00
17	2.093	7.249	2.220	17-19	17-31	17-35	17-0	19-17-31	19-17-35	31-17-35	0-0-0	0-0-0	0-0-0	0-0-0
				4.403	4.526	4.530	0.000	110.00	110.57	108.17	0.00	0.00	0.00	0.00
19	18.851	0.033	3.525	19-5	19-0	19-0	19-0	0-0-0	0-0-0	0-0-0	0-0-0	0-0-0	0-0-0	0-0-0
				4.401	0.000	0.000	0.000	0.00	0.00	0.00	0.00	0.00	0.00	0.00
19	-18.816	0.033	3.525	19-0	19-0	19-0	19-0	0-0-0	0-0-0	0-0-0	0-0-0	0-0-0	0-0-0	0-0-0
				0.000	0.000	0.000	0.000	0.00	0.00	0.00	0.00	0.00	0.00	0.00
19	0.018	10.907	3.525	19-17	19-0	19-0	19-0	0-0-0	0-0-0	0-0-0	0-0-0	0-0-0	0-0-0	0-0-0
				4.403	0.000	0.000	0.000	0.00	0.00	0.00	0.00	0.00	0.00	0.00
19	0.018	-10.841	3.525	19-1	19-0	19-0	19-0	0-0-0	0-0-0	0-0-0	0-0-0	0-0-0	0-0-0	0-0-0
				4.348	0.000	0.000	0.000	0.00	0.00	0.00	0.00	0.00	0.00	0.00
21	-12.494	3.641	3.792	21-13	21-37	21-0	21-0	13-21-37	0-0-0	0-0-0	0-0-0	0-0-0	0-0-0	0-0-0
				4.456	4.570	0.000	0.000	110.89	0.00	0.00	0.00	0.00	0.00	0.00
21	6.340	-7.232	3.792	21-1	21-3	21-37	21-0	1-21-3	1-21-37	3-21-37	0-0-0	0-0-0	0-0-0	0-0-0
				4.529	4.428	4.570	0.000	108.05	122.36	97.74	0.00	0.00	0.00	0.00
23	12.523	-3.665	3.826	23-3	23-5	23-39	23-0	3-23-5	3-23-39	5-23-39	0-0-0	0-0-0	0-0-0	0-0-0
				4.452	4.531	4.556	0.000	107.59	97.96	122.80	0.00	0.00	0.00	0.00
23	-6.311	7.208	3.826	23-15	23-39	23-0	23-0	15-23-39	0-0-0	0-0-0	0-0-0	0-0-0	0-0-0	0-0-0
				4.466	4.556	0.000	0.000	111.34	0.00	0.00	0.00	0.00	0.00	0.00
25	-6.323	-7.213	3.809	25-7	25-0	25-0	25-0	0-0-0	0-0-0	0-0-0	0-0-0	0-0-0	0-0-0	0-0-0
				4.469	0.000	0.000	0.000	0.00	0.00	0.00	0.00	0.00	0.00	0.00
25	12.510	3.660	3.809	25-5	25-11	25-41	25-0	5-25-11	5-25-41	11-25-41	0-0-0	0-0-0	0-0-0	0-0-0
				4.527	4.434	4.556	0.000	107.97	122.48	98.14	0.00	0.00	0.00	0.00
27	-0.014	-3.560	3.804	27-1	27-7	27-9	27-43	1-27-7	1-27-9	1-27-43	7-27-9	7-27-43	9-27-43	97.97
				4.534	4.462	4.430	4.569	107.37	107.94	121.95	109.22	111.53	111.53	97.97

Nr.	coordinates [a.u.]			bondlength [a.u.]				bondangles						
	x	y	z	29-3	29-9	29-11	29-45	3-29-9	3-29-11	3-29-45	9-29-11	9-29-45	11-29-45	
29	6.276	0.009	3.565	4.404	4.394	4.389	4.370	110.95	111.04	106.97	111.24	108.14	108.33	
31	-12.498	-3.643	3.795	4.460	4.542	0.000	0.000	109.84	0.00	0.00	0.00	0.00	0.00	
31	6.336	7.231	3.795	4.430	4.526	4.542	0.000	108.06	97.36	123.81	0.00	0.00	0.00	
33	-6.272	0.005	3.198	4.300	4.304	4.291	4.292	114.82	115.10	103.03	115.00	103.61	102.84	
35	-0.019	3.569	3.807	4.440	4.459	4.530	4.545	109.10	107.82	97.37	107.51	110.59	123.44	
37	7.309	-6.607	8.214	4.570	4.830	4.704	0.000	104.82	108.51	103.01	0.00	0.00	0.00	
37	-11.524	4.267	8.214	4.570	4.830	4.674	0.000	104.82	103.08	102.06	0.00	0.00	0.00	
39	-7.344	6.687	8.232	4.556	4.830	4.680	0.000	104.47	103.02	102.58	0.00	0.00	0.00	
39	11.490	-4.187	8.232	4.556	4.830	4.708	0.000	104.47	108.25	103.39	0.00	0.00	0.00	
41	11.503	4.182	8.221	4.566	4.777	4.671	0.000	103.77	108.60	104.00	0.00	0.00	0.00	
43	0.081	-2.435	8.231	4.569	4.797	4.658	4.683	103.71	109.12	102.35	104.02	101.68	132.68	
45	6.301	-0.048	7.934	4.370	4.485	4.496	4.529	117.64	117.33	111.79	102.01	103.41	102.70	
47	7.405	6.638	8.169	4.542	4.777	4.654	0.000	106.23	103.68	104.13	0.00	0.00	0.00	
47	-11.428	-4.236	8.169	4.542	4.654	0.000	0.000	104.06	0.00	0.00	0.00	0.00	0.00	
49	-6.237	0.014	7.490	4.292	4.503	4.495	4.493	118.27	117.79	119.13	179.19	99.16	99.71	
51	0.007	2.361	8.188	5.135	5.143	5.157	5.163	35.5143	35.5157	35.5163	43.5157	43.5163	57.5163	
53	4.269	-3.482	9.981	4.704	4.658	4.485	4.503	126.10	92.54	110.23	93.65	119.86	103.97	
55	10.305	0.023	9.977	4.708	4.671	4.496	4.500	126.31	92.39	109.84	94.10	119.80	104.27	
57	4.231	3.585	9.674	4.529	4.654	4.643	4.369	95.18	94.67	76.09	133.62	113.14	113.23	
59	-4.279	-3.439	9.614	4.683	4.503	4.609	0.000	95.81	113.03	59.30	0.00	0.00	0.00	

Nr.	coordinates [a.u.]			bondlength [a.u]						bondangles					
	x	y	z	61-37	61-47	61-49	61-67	37-61-47	37-61-49	37-61-67	47-61-49	47-61-67	49-61-67	49-61-67	49-61-67
61	-10.196	0.012	9.618	4.674	4.654	4.495	4.612	131.47	96.18	113.88	94.95	112.40	59.33	59.33	59.33
63	-4.291	3.437	9.654	4.680	4.493	4.666	4.612	95.75	131.71	113.48	94.12	59.34	112.17	112.17	112.17
65	9.325	-0.359	14.353	4.500	4.869	4.310	0.000	103.34	83.95	55.68	0.00	0.00	0.00	0.00	0.00
67	-6.246	-0.020	11.998	4.508	4.609	4.612	4.612	59.18	59.05	59.01	59.67-61	59.67-63	96.45	61-67-63	95.49
69	5.108	-2.794	14.351	4.503	4.869	4.315	0.000	103.78	84.43	55.58	0.00	0.00	0.00	0.00	0.00
71	5.539	1.339	13.186	4.369	4.310	4.315	0.000	133.10	132.81	68.74	0.00	0.00	0.00	0.00	0.00

A.1.5 Two additional Si ad-atoms (d)

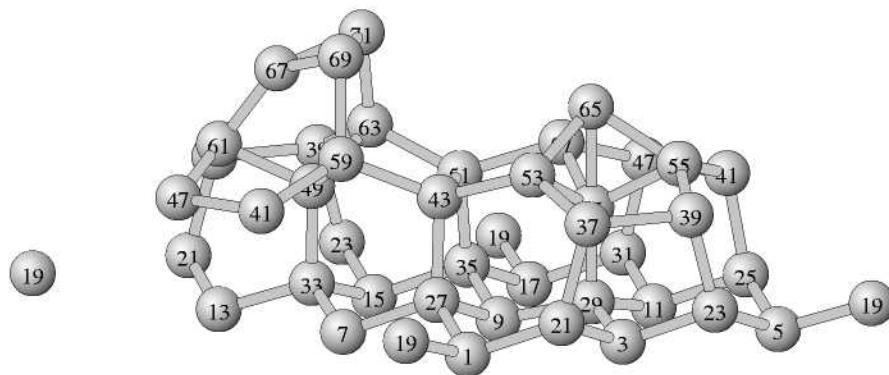


Figure A.5: Perspective view of the upper half of the inversion symmetric (3×3) -supercell with two extra ad-atoms (69,71) on top.

Nr.	coordinates [a.u.]			bondlength [a.u.]					bondangles				
	x	y	z	1-19	1-21	1-27	1-0	19-1-21	19-1-27	21-1-27	0-0-0	0-0-0	0-0-0
1	2.093	-7.249	2.220	4.351	4.505	4.508	0.000	110.31	110.21	107.97	0.00	0.00	0.00
3	8.371	-3.625	2.220	4.426	4.450	4.291	0.000	21-3-23	21-3-29	23-3-29	0-0-0	0-0-0	0-0-0
5	14.648	-0.000	2.220	5-19	5-23	5-25	5-0	19-5-23	19-5-25	23-5-25	0-0-0	0-0-0	0-0-0
7	-4.185	-3.625	2.220	7-27	7-33	7-0	7-0	27-7-33	0-0-0	0-0-0	0-0-0	0-0-0	0-0-0
9	2.093	0.000	2.220	9-27	9-29	9-35	9-0	27-9-29	27-9-35	29-9-35	0-0-0	0-0-0	0-0-0
11	8.371	3.625	2.220	11-25	11-29	11-31	11-0	25-11-29	25-11-31	29-11-31	0-0-0	0-0-0	0-0-0
13	-10.463	0.000	2.220	13-21	13-33	13-0	13-0	21-13-33	0-0-0	0-0-0	0-0-0	0-0-0	0-0-0
15	-4.185	3.625	2.220	15-23	15-33	15-35	15-0	23-15-33	23-15-35	33-15-35	0-0-0	0-0-0	0-0-0
17	2.093	7.249	2.220	17-19	17-31	17-35	17-0	19-17-31	19-17-35	31-17-35	0-0-0	0-0-0	0-0-0
19	18.853	0.033	3.536	19-5	19-0	19-0	19-0	0-0-0	0-0-0	0-0-0	0-0-0	0-0-0	0-0-0
19	0.019	-10.841	3.536	19-1	19-0	19-0	19-0	0-0-0	0-0-0	0-0-0	0-0-0	0-0-0	0-0-0
19	0.019	10.906	3.536	19-17	19-0	19-0	19-0	0-0-0	0-0-0	0-0-0	0-0-0	0-0-0	0-0-0
19	-18.814	0.033	3.536	19-0	19-0	19-0	19-0	0-0-0	0-0-0	0-0-0	0-0-0	0-0-0	0-0-0
21	6.320	-7.223	3.778	21-1	21-3	21-37	21-0	1-21-3	1-21-37	3-21-37	0-0-0	0-0-0	0-0-0
21	-12.514	3.650	3.778	21-13	21-37	21-0	21-0	13-21-37	0-0-0	0-0-0	0-0-0	0-0-0	0-0-0
23	12.524	-3.648	3.815	23-3	23-5	23-39	23-0	3-23-5	3-23-39	5-23-39	0-0-0	0-0-0	0-0-0
23	-6.309	7.226	3.815	23-15	23-39	23-0	23-0	15-23-39	0-0-0	0-0-0	0-0-0	0-0-0	0-0-0
25	12.515	3.641	3.808	25-5	25-11	25-41	25-0	5-25-11	5-25-41	11-25-41	0-0-0	0-0-0	0-0-0
27	0.006	-3.579	3.800	27-1	27-7	27-9	27-43	1-27-7	1-27-9	1-27-43	7-27-9	7-27-43	9-27-43
29	6.282	0.005	3.158	29-3	29-9	29-11	29-45	3-29-9	3-29-11	3-29-45	9-29-11	9-29-45	11-29-45

Nr.	coordinates [a.u.]			bondlength [a.u]					bondangles				
	x	y	z	31-11	31-17	31-47	31-0	11-31-17	11-31-47	17-31-47	0-0-0	0-0-0	0-0-0
31	6.313	7.217	3.792	4.429	4.504	4.542	0.000	108.49	97.22	124.13	0.00	0.00	0.00
33	-6.276	0.001	3.559	33-7	33-13	33-15	33-49	7-33-13	7-33-15	7-33-49	13-33-15	13-33-49	15-33-49
35	0.004	3.585	3.822	35-9	35-15	35-17	35-51	9-35-15	9-35-17	9-35-51	15-35-17	15-35-51	17-35-51
37	7.392	-6.615	8.150	4.448	4.486	4.511	4.544	108.48	108.02	98.54	107.36	109.46	123.97
37	-11.441	4.259	8.150	37-21	37-39	37-53	37-0	21-37-39	21-37-53	39-37-53	0-0-0	0-0-0	0-0-0
39	11.576	-4.280	8.215	4.542	4.792	4.667	0.000	106.53	103.14	103.71	0.00	0.00	0.00
39	-7.258	6.594	8.215	4.542	4.792	4.639	0.000	106.53	104.48	104.36	0.00	0.00	0.00
41	-7.256	-6.585	8.215	4.790	4.658	0.000	0.000	103.81	0.00	0.00	0.00	0.00	0.00
41	11.578	4.289	8.215	41-25	41-47	41-55	41-0	25-41-47	25-41-55	47-41-55	0-0-0	0-0-0	0-0-0
43	-0.054	-2.416	8.201	43-27	43-51	43-53	43-59	27-43-51	27-43-53	27-43-59	51-43-53	51-43-59	53-43-59
45	6.299	0.004	7.439	45-29	45-53	45-55	45-57	29-45-53	29-45-55	29-45-57	53-45-55	53-45-57	53-45-57
47	-11.433	-4.243	8.163	47-41	47-61	47-0	47-0	41-47-61	0-0-0	0-0-0	0-0-0	0-0-0	0-0-0
47	7.400	6.631	8.163	47-31	47-41	47-57	47-0	31-47-41	31-47-57	41-47-57	0-0-0	0-0-0	0-0-0
49	-6.231	-0.010	7.942	49-33	49-59	49-61	49-63	33-49-59	33-49-61	33-49-63	59-49-61	59-49-63	61-49-63
51	-0.065	2.419	8.213	51-35	51-43	51-57	51-63	35-51-43	35-51-57	35-51-63	43-51-57	43-51-63	57-51-63
53	4.312	-3.404	9.561	53-37	53-43	53-45	53-65	37-53-43	37-53-45	37-53-65	43-53-45	43-53-65	45-53-65
55	10.252	0.003	9.541	55-39	55-41	55-45	55-65	39-55-41	39-55-45	39-55-65	41-55-45	41-55-65	45-55-65
57	4.315	3.404	9.554	57-45	57-47	57-51	57-65	45-57-47	45-57-51	45-57-65	57-51-65	57-51-65	59-57-65
59	-4.266	-3.486	9.993	59-41	59-43	59-49	59-69	41-59-43	41-59-49	41-59-69	43-59-49	43-59-69	49-59-69
61	-10.411	0.008	9.694	61-37	61-47	61-49	61-67	37-61-47	37-61-49	37-61-67	47-61-49	47-61-67	49-61-67
				4.639	4.633	4.532	4.370	132.98	94.58	113.25	94.14	113.69	75.85

Nr.	coordinates [a.u.]			bondlength [a.u]					bondangles				
	x	y	z	63-39	63-49	63-51	63-71	39-63-49	39-63-51	39-63-71	49-63-51	49-63-71	51-63-71
63	-4.290	3.477	10.009	4.663	4.494	4.711	4.503	93.83	125.05	120.35	92.18	104.90	110.45
65	6.314	-0.008	11.974	4.535	4.622	4.629	4.636	45-65-53	45-65-55	45-65-57	53-65-55	53-65-57	55-65-57
67	-7.788	0.032	13.189	4.370	4.309	4.305	0.000	61-67-69	61-67-71	69-67-71	0-0-0	0-0-0	0-0-0
69	-4.452	-2.426	14.369	4.506	4.309	4.880	0.000	59-69-67	59-69-71	67-69-71	0-0-0	0-0-0	0-0-0
71	-4.438	2.454	14.391	4.503	4.305	4.880	0.000	63-71-67	63-71-69	67-71-69	0-0-0	0-0-0	0-0-0
								83.19	102.87	55.52	0.00	0.00	0.00

A.1.6 Three additional Si ad-atoms (f)

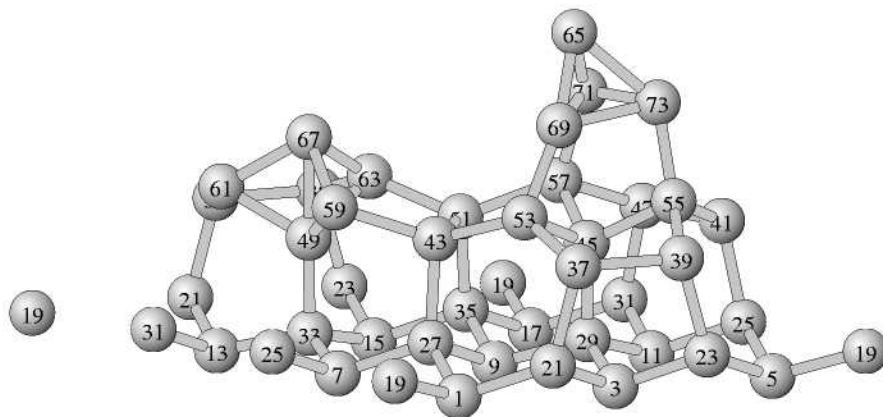


Figure A.6: Perspective view of the upper half of the inversion symmetric (3×3) -supercell with three extra ad-atoms (69,71,73) on top.

Nr.	coordinates [a.u.]			bondlength [a.u.]				bondangles							
	x	y	z	1-19	1-21	1-27	1-0	19-1-21	19-1-27	21-1-27	0-0-0	0-0-0	0-0-0	0-0-0	0-0-0
1	2.093	-7.249	2.220	4.350	4.533	4.533	0.000	110.28	110.23	108.32	0.00	0.00	0.00	0.00	0.00
3	8.371	-3.625	2.220	4.424	4.451	4.376	0.000	106.77	110.80	110.30	0.00	0.00	0.00	0.00	0.00
5	14.648	-0.000	2.220	5-19	5-23	5-25	5-0	19-5-23	19-5-25	23-5-25	0.00	0.00	0.00	0.00	0.00
				4.402	4.545	4.528	0.000	110.36	109.91	107.69	0.00	0.00	0.00	0.00	0.00
7	-4.185	-3.625	2.220	7-25	7-27	7-33	7-0	25-7-27	25-7-33	27-7-33	0.00	0.00	0.00	0.00	0.00
				4.482	4.455	4.302	0.000	109.42	111.40	111.15	0.00	0.00	0.00	0.00	0.00
9	2.093	0.000	2.220	9-27	9-29	9-35	9-0	27-9-29	27-9-35	29-9-35	0.00	0.00	0.00	0.00	0.00
				4.427	4.381	4.449	0.000	110.68	106.78	110.33	0.00	0.00	0.00	0.00	0.00
11	8.371	3.625	2.220	11-25	11-29	11-31	11-0	25-11-29	25-11-31	29-11-31	0.00	0.00	0.00	0.00	0.00
				4.436	4.369	4.435	0.000	110.18	107.05	110.28	0.00	0.00	0.00	0.00	0.00
13	-10.463	0.000	2.220	13-21	13-31	13-33	13-0	21-13-31	21-13-33	31-13-33	0.00	0.00	0.00	0.00	0.00
				4.449	4.480	4.305	0.000	109.51	111.19	111.37	0.00	0.00	0.00	0.00	0.00
15	-4.185	3.625	2.220	15-23	15-33	15-35	15-0	23-15-33	23-15-35	33-15-35	0.00	0.00	0.00	0.00	0.00
				4.467	4.286	4.469	0.000	111.12	108.91	111.11	0.00	0.00	0.00	0.00	0.00
17	2.093	7.249	2.220	17-19	17-31	17-35	17-0	19-17-31	19-17-35	31-17-35	0.00	0.00	0.00	0.00	0.00
				4.403	4.530	4.543	0.000	109.93	110.39	107.69	0.00	0.00	0.00	0.00	0.00
19	18.852	0.032	3.528	19-5	19-0	19-0	19-0	0-0-0	0-0-0	0-0-0	0.00	0.00	0.00	0.00	0.00
				4.402	0.000	0.000	0.000	0.00	0.00	0.00	0.00	0.00	0.00	0.00	0.00
19	-18.816	0.032	3.528	19-0	19-0	19-0	19-0	0-0-0	0-0-0	0-0-0	0.00	0.00	0.00	0.00	0.00
				0.000	0.000	0.000	0.000	0.00	0.00	0.00	0.00	0.00	0.00	0.00	0.00
19	0.018	10.906	3.528	19-17	19-0	19-0	19-0	0-0-0	0-0-0	0-0-0	0.00	0.00	0.00	0.00	0.00
				4.403	0.000	0.000	0.000	0.00	0.00	0.00	0.00	0.00	0.00	0.00	0.00
19	0.018	-10.842	3.528	19-1	19-0	19-0	19-0	0-0-0	0-0-0	0-0-0	0.00	0.00	0.00	0.00	0.00
				4.350	0.000	0.000	0.000	0.00	0.00	0.00	0.00	0.00	0.00	0.00	0.00
21	-12.487	3.640	3.785	21-13	21-37	21-0	21-0	13-21-37	0-0-0	0-0-0	0.00	0.00	0.00	0.00	0.00
				4.449	4.558	0.000	0.000	109.83	0.00	0.00	0.00	0.00	0.00	0.00	0.00
21	6.347	-7.234	3.785	21-1	21-3	21-37	21-0	1-21-3	1-21-37	3-21-37	0.00	0.00	0.00	0.00	0.00
				4.533	4.424	4.558	0.000	108.06	122.95	98.02	0.00	0.00	0.00	0.00	0.00
23	12.517	-3.673	3.839	23-3	23-5	23-39	23-0	3-23-5	3-23-39	5-23-39	0.00	0.00	0.00	0.00	0.00
				4.451	4.545	4.563	0.000	107.37	98.01	123.43	0.00	0.00	0.00	0.00	0.00
23	-6.317	7.201	3.839	23-15	23-39	23-0	23-0	15-23-39	0-0-0	0-0-0	0.00	0.00	0.00	0.00	0.00
				4.467	4.563	0.000	0.000	111.16	0.00	0.00	0.00	0.00	0.00	0.00	0.00
25	-6.327	-7.220	3.823	25-7	25-0	25-0	25-0	0-0-0	0-0-0	0-0-0	0.00	0.00	0.00	0.00	0.00
				4.482	0.000	0.000	0.000	0.00	0.00	0.00	0.00	0.00	0.00	0.00	0.00
25	12.506	3.653	3.823	25-5	25-11	25-41	25-0	5-25-11	5-25-41	11-25-41	0.00	0.00	0.00	0.00	0.00
				4.528	4.436	4.561	0.000	107.93	122.69	97.51	0.00	0.00	0.00	0.00	0.00
27	-0.018	-3.559	3.794	27-1	27-7	27-9	27-43	1-27-7	1-27-9	1-27-43	7-27-9	7-27-43	109.40	9-27-43	98.06
				4.533	4.455	4.427	4.564	107.50	107.99	123.21	109.40	109.84	109.40	98.06	98.06

Nr.	coordinates [a.u.]			bondlength [a.u.]				bondangles					
	x	y	z	29-3	29-9	29-11	29-45	3-29-9	3-29-11	3-29-45	9-29-11	9-29-45	11-29-45
29	6.284	0.004	3.496	4.376 31-13	4.381 31-0	4.369 31-0	4.351 31-0	111.73 0-0-0	111.97 0-0-0	106.97 0-0-0	111.87 0-0-0	106.65 0-0-0	107.28 0-0-0
31	-12.504	-3.653	3.821	4.480 31-11	0.000 31-17	0.000 31-47	0.000 31-0	0.00 11-31-17	0.00 11-31-47	0.00 17-31-47	0.00 0-0-0	0.00 0-0-0	0.00 0-0-0
31	6.330	7.221	3.821	4.435 33-7	4.530 33-13	4.554 33-15	0.000 33-49	107.92 7-33-13	97.64 7-33-15	122.72 7-33-49	0.00 13-33-15	0.00 13-33-49	0.00 15-33-49
33	-6.271	0.010	3.196	4.302 4.302	4.305 4.305	4.286 4.286	4.301 4.301	114.76 9-35-15	115.14 9-35-17	102.67 9-35-51	115.10 15-35-17	102.65 15-35-51	104.07 17-35-51
35	-0.020	3.566	3.837	4.449 37-21	4.469 37-39	4.543 37-53	4.562 37-0	108.75 21-37-39	107.43 21-37-53	98.13 39-37-53	107.09 0-0-0	111.04 0-0-0	123.38 0-0-0
37	7.364	-6.673	8.192	4.558 37-21	4.777 37-39	4.656 37-61	0.000 37-0	105.41 21-37-39	103.12 21-37-61	103.24 39-37-61	0.00 0-0-0	0.00 0-0-0	0.00 0-0-0
37	-11.469	4.201	8.192	4.558 39-23	4.777 39-37	4.669 39-63	0.000 39-0	105.41 23-39-37	104.25 23-39-63	103.83 37-39-63	0.00 0-0-0	0.00 0-0-0	0.00 0-0-0
39	-7.362	6.640	8.245	4.563 39-23	4.777 39-37	4.667 39-55	0.000 39-0	104.41 23-39-37	103.22 23-39-63	101.91 37-39-55	0.00 0-0-0	0.00 0-0-0	0.00 0-0-0
39	11.472	-4.234	8.245	4.563 41-25	4.777 41-47	4.660 41-55	0.000 41-0	104.41 25-41-47	107.32 25-41-55	102.96 47-41-55	0.00 0-0-0	0.00 0-0-0	0.00 0-0-0
41	11.434	4.144	8.228	4.561 43-27	4.791 43-51	4.706 43-53	0.000 43-59	104.84 27-43-51	108.09 27-43-53	102.92 27-43-59	0.00 51-43-53	0.00 51-43-59	0.00 53-43-59
43	-0.047	-2.386	8.205	4.564 45-29	4.776 45-53	4.649 45-55	4.676 45-57	105.36 29-45-53	102.85 29-45-55	104.22 29-45-57	103.41 53-45-55	103.99 53-45-57	134.30 55-45-57
45	6.261	-0.008	7.847	4.351 47-31	4.424 47-41	4.441 47-57	4.438 47-0	113.72 31-47-41	117.36 31-47-57	117.36 41-47-57	102.07 0-0-0	102.50 0-0-0	101.54 0-0-0
47	7.294	6.555	8.222	4.554 49-33	4.791 49-59	4.706 49-61	0.000 49-63	104.94 33-49-59	107.65 33-49-61	102.70 33-49-63	0.00 33-49-67	0.00 59-49-61	0.00 59-49-63
49	-6.305	-0.049	7.496	4.301 51-35	4.498 51-43	4.493 51-57	4.513 51-63	119.14 35-51-43	118.99 35-51-57	117.68 35-51-63	178.81 43-51-57	98.53 43-51-63	99.26 57-51-63
51	0.009	2.389	8.245	4.562 53-37	4.776 53-43	4.650 53-45	4.669 53-69	104.47 37-53-43	106.97 37-53-45	103.35 37-53-69	103.09 43-53-45	101.85 43-53-69	133.97 45-53-69
53	4.237	-3.527	9.606	4.656 55-39	4.649 55-41	4.424 55-45	4.355 55-73	133.87 39-55-41	96.27 39-55-45	109.38 39-55-73	96.13 41-55-45	115.63 41-55-73	86.32 45-55-73
55	10.195	-0.073	9.909	4.660 57-45	4.706 57-47	4.441 57-51	4.410 57-71	126.91 45-57-47	95.15 45-57-51	123.28 45-57-71	93.13 47-57-51	104.34 47-57-71	105.59 51-57-71
57	4.245	3.379	9.886	4.438 59-43	4.706 59-49	4.650 59-67	4.411 59-0	93.35 43-59-49	95.12 43-59-67	103.11 49-59-67	127.52 0-0-0	103.10 0-0-0	124.83 0-0-0
59	-4.356	-3.479	9.656	4.676 61-37	4.498 61-49	4.620 61-67	0.000 61-0	94.15 37-61-49	111.89 37-61-67	59.61 49-61-67	0.00 0-0-0	0.00 0-0-0	0.00 0-0-0
61	-10.252	-0.067	9.642	4.669 4.669	4.493 4.493	4.616 4.616	0.000 0.000	94.41 94.41	112.05 112.05	59.67 59.67	0.00 0.00	0.00 0.00	0.00 0.00

Nr.	coordinates [a.u.]			bondlength [a.u]				bondangles					
	x	y	z	63-39	63-49	63-51	63-67	39-63-49	39-63-51	39-63-67	49-63-51	49-63-67	51-63-67
63	-4.328	3.386	9.656	4.667	4.513	4.669	4.601	95.81	131.42	113.21	95.73	59.64	113.32
65	5.787	-0.446	17.393	65-69	65-71	65-73	65-0	69-65-71	69-65-73	71-65-73	0-0-0	0-0-0	0-0-0
				4.203	4.712	4.907	0.000	65.98	61.75	54.76	0.00	0.00	0.00
67	-6.301	-0.025	12.029	67-49	67-59	67-61	67-63	49-67-59	49-67-61	49-67-63	59-67-61	59-67-63	61-67-63
				4.533	4.620	4.616	4.601	58.85	58.81	59.22	95.04	96.24	96.14
69	5.440	-1.933	13.476	69-53	69-65	69-71	69-73	53-69-65	53-69-71	53-69-73	65-69-71	65-69-73	71-69-73
				4.355	4.203	4.873	4.714	168.58	118.56	123.97	62.03	66.49	54.98
71	5.493	2.902	14.090	71-57	71-65	71-69	71-73	57-71-65	57-71-69	57-71-73	65-71-69	65-71-73	69-71-73
				4.411	4.712	4.873	4.427	139.68	89.09	108.37	51.99	64.86	60.68
73	9.313	0.665	14.167	73-55	73-65	73-69	73-71	55-73-65	55-73-69	55-73-71	65-73-69	65-73-71	69-73-71
				4.410	4.907	4.714	4.427	137.78	86.03	103.91	51.76	60.37	64.34

A.1.7 Four additional Si ad-atoms (g)

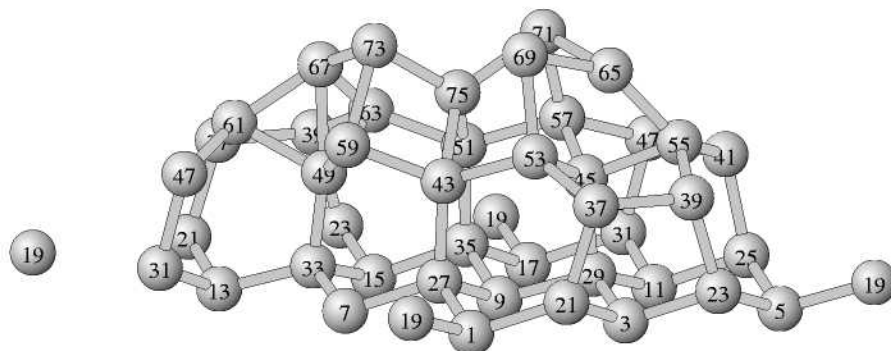


Figure A.7: Perspective view of the upper half of the inversion symmetric (3×3) -supercell with four extra ad-atoms (69,71,73,75) on top.

Nr.	coordinates [a.u.]			bondlength [a.u.]					bondangles				
	x	y	z	1-19	1-21	1-27	1-0	19-1-21	19-1-27	21-1-27	0-0-0	0-0-0	0-0-0
1	2.093	-7.249	2.220	4.357	4.530	4.473	0.000	110.12	110.80	109.00	0.00	0.00	0.00
3	8.371	-3.625	2.220	3-21	3-23	3-29	3-0	21-3-23	21-3-29	23-3-29	0-0-0	0-0-0	0-0-0
				4.421	4.407	4.359	0.000	108.13	111.21	110.67	0.00	0.00	0.00
5	14.648	-0.000	2.220	5-19	5-23	5-25	5-0	19-5-23	19-5-25	23-5-25	0-0-0	0-0-0	0-0-0
				4.413	4.462	4.502	0.000	111.09	110.12	108.29	0.00	0.00	0.00
7	-4.185	-3.625	2.220	7-27	7-33	7-0	7-0	27-7-33	0-0-0	0-0-0	0-0-0	0-0-0	0-0-0
				4.459	4.364	0.000	0.000	110.54	0.00	0.00	0.00	0.00	0.00
9	2.093	0.000	2.220	9-27	9-29	9-35	9-0	27-9-29	27-9-35	29-9-35	0-0-0	0-0-0	0-0-0
				4.398	4.389	4.479	0.000	110.50	107.42	110.79	0.00	0.00	0.00
11	8.371	3.625	2.220	11-25	11-29	11-31	11-0	25-11-29	25-11-31	29-11-31	0-0-0	0-0-0	0-0-0
				4.423	4.381	4.449	0.000	109.91	106.95	110.64	0.00	0.00	0.00
13	-10.463	0.000	2.220	13-21	13-31	13-33	13-0	21-13-31	21-13-33	31-13-33	0-0-0	0-0-0	0-0-0
				4.413	4.465	4.357	0.000	109.61	109.92	109.83	0.00	0.00	0.00
15	-4.185	3.625	2.220	15-23	15-33	15-35	15-0	23-15-33	23-15-35	33-15-35	0-0-0	0-0-0	0-0-0
				4.446	4.328	4.441	0.000	110.82	109.36	109.76	0.00	0.00	0.00
17	2.093	7.249	2.220	17-19	17-31	17-35	17-0	19-17-31	19-17-35	31-17-35	0-0-0	0-0-0	0-0-0
				4.403	4.564	4.559	0.000	109.45	109.82	108.08	0.00	0.00	0.00
19	0.023	-10.846	3.547	19-1	19-0	19-0	19-0	0-0-0	0-0-0	0-0-0	0-0-0	0-0-0	0-0-0
				4.357	0.000	0.000	0.000	0.00	0.00	0.00	0.00	0.00	0.00
19	-18.811	0.028	3.547	19-0	19-0	19-0	19-0	0-0-0	0-0-0	0-0-0	0-0-0	0-0-0	0-0-0
				0.000	0.000	0.000	0.000	0.00	0.00	0.00	0.00	0.00	0.00
19	18.856	0.028	3.547	19-5	19-0	19-0	19-0	0-0-0	0-0-0	0-0-0	0-0-0	0-0-0	0-0-0
				4.413	0.000	0.000	0.000	0.00	0.00	0.00	0.00	0.00	0.00
19	0.023	10.902	3.547	19-17	19-0	19-0	19-0	0-0-0	0-0-0	0-0-0	0-0-0	0-0-0	0-0-0
				4.403	0.000	0.000	0.000	0.00	0.00	0.00	0.00	0.00	0.00
21	6.359	-7.254	3.744	21-1	21-3	21-37	21-0	1-21-3	1-21-37	3-21-37	0-0-0	0-0-0	0-0-0
				4.530	4.421	4.509	0.000	108.16	125.66	97.42	0.00	0.00	0.00
21	-12.475	3.620	3.744	21-13	21-37	21-0	21-0	13-21-37	0-0-0	0-0-0	0-0-0	0-0-0	0-0-0
				4.413	4.509	0.000	0.000	106.17	0.00	0.00	0.00	0.00	0.00
23	-6.311	7.239	3.697	23-15	23-39	23-0	23-0	15-23-39	0-0-0	0-0-0	0-0-0	0-0-0	0-0-0
				4.446	4.468	0.000	0.000	109.59	0.00	0.00	0.00	0.00	0.00
23	12.522	-3.634	3.697	23-3	23-5	23-39	23-0	3-23-5	3-23-39	5-23-39	0-0-0	0-0-0	0-0-0
				4.407	4.462	4.468	0.000	109.63	95.03	122.67	0.00	0.00	0.00
25	12.503	3.631	3.796	25-5	25-11	25-41	25-0	5-25-11	5-25-41	11-25-41	0-0-0	0-0-0	0-0-0
				4.502	4.423	4.545	0.000	108.62	122.57	97.78	0.00	0.00	0.00
27	0.016	-3.578	3.712	27-1	27-7	27-9	27-43	1-27-7	1-27-9	1-27-43	7-27-9	7-27-43	9-27-43
				4.473	4.459	4.398	4.475	108.50	109.60	109.51	109.86	111.85	107.50
29	6.291	-0.013	3.498	29-3	29-9	29-11	29-45	3-29-9	3-29-11	3-29-45	9-29-11	9-29-45	11-29-45
				4.359	4.389	4.381	4.359	111.93	112.08	109.01	111.50	102.30	109.55

Nr.	coordinates [a.u.]			bondlength [a.u.]				bondangles						
	x	y	z	31-11	31-17	31-47	31-0	11-31-17	11-31-47	17-31-47	0-0-0	0-0-0	0-0-0	0-0-0
31	6.355	7.239	3.851	4.449	4.564	4.599	0.000	107.09	97.86	125.92	0.00	0.00	0.00	0.00
31	-12.479	-3.634	3.851	4.465	4.599	0.000	0.000	109.19	0.00	0.00	0.00	0.00	0.00	0.00
33	-6.271	0.022	3.404	33-7	33-13	33-15	33-49	7-33-13	7-33-15	7-33-49	13-33-15	13-33-49	15-33-49	15-33-49
				4.364	4.357	4.328	4.317	112.45	113.01	99.67	113.17	112.93	104.59	104.59
35	-0.055	3.575	3.852	35-9	35-15	35-17	35-51	9-35-15	9-35-17	9-35-51	15-35-17	15-35-51	17-35-51	17-35-51
				4.479	4.441	4.559	4.545	108.72	106.66	107.82	107.30	111.44	114.68	114.68
37	7.610	-6.844	8.057	37-21	37-39	37-53	37-0	21-37-39	21-37-53	39-37-53	0-0-0	0-0-0	0-0-0	0-0-0
				4.509	4.630	4.518	0.000	105.38	100.32	103.79	0.00	0.00	0.00	0.00
37	-11.224	4.029	8.057	37-21	37-39	37-61	37-0	21-37-39	21-37-61	39-37-61	0-0-0	0-0-0	0-0-0	0-0-0
				4.509	4.630	4.615	0.000	105.38	111.03	104.34	0.00	0.00	0.00	0.00
39	-7.424	6.673	7.988	39-23	39-37	39-63	39-0	23-39-37	23-39-63	37-39-63	0-0-0	0-0-0	0-0-0	0-0-0
				4.468	4.630	4.491	0.000	106.92	105.54	101.72	0.00	0.00	0.00	0.00
39	11.410	-4.200	7.988	39-23	39-37	39-55	39-0	23-39-37	23-39-55	37-39-55	0-0-0	0-0-0	0-0-0	0-0-0
				4.468	4.630	4.599	0.000	106.92	106.72	106.42	0.00	0.00	0.00	0.00
41	11.483	4.152	8.194	41-25	41-47	41-55	41-0	25-41-47	25-41-55	47-41-55	0-0-0	0-0-0	0-0-0	0-0-0
				4.545	4.679	4.645	0.000	105.29	104.44	104.47	0.00	0.00	0.00	0.00
43	0.196	-3.473	8.182	43-27	43-53	43-59	43-75	27-43-53	27-43-59	27-43-75	53-43-59	53-43-75	59-43-75	59-43-75
				4.475	4.457	4.532	4.654	110.26	107.95	136.66	139.05	81.93	80.42	80.42
45	5.938	-0.041	7.843	45-29	45-53	45-55	45-57	29-45-53	29-45-55	29-45-57	53-45-55	53-45-57	55-45-57	55-45-57
				4.359	4.643	4.559	4.545	113.82	107.80	115.30	99.19	116.64	101.36	101.36
47	7.555	6.694	8.257	47-31	47-41	47-57	47-0	31-47-41	31-47-57	41-47-57	0-0-0	0-0-0	0-0-0	0-0-0
				4.599	4.679	4.652	0.000	105.71	100.47	105.00	0.00	0.00	0.00	0.00
47	-11.278	-4.179	8.257	47-31	47-61	47-0	47-0	31-47-61	0-0-0	0-0-0	0-0-0	0-0-0	0-0-0	0-0-0
				4.599	4.676	0.000	0.000	106.53	0.00	0.00	0.00	0.00	0.00	0.00
49	-5.730	-0.191	7.681	49-33	49-59	49-61	49-63	33-49-59	33-49-61	33-49-63	33-49-67	59-49-61	59-49-63	59-49-63
				4.317	4.597	4.547	4.740	122.31	109.74	114.25	162.10	98.94	113.46	113.46
51	-0.065	3.240	8.385	51-35	51-57	51-63	51-75	35-51-57	35-51-63	35-51-75	57-51-63	57-51-75	63-51-75	63-51-75
				4.545	4.526	4.508	4.646	105.93	106.05	136.14	143.53	80.10	88.80	88.80
53	4.389	-4.062	9.573	53-37	53-43	53-45	53-69	37-53-43	37-53-45	37-53-69	43-53-45	43-53-69	45-53-69	45-53-69
				4.518	4.457	4.643	4.507	130.35	99.82	122.85	94.77	98.85	103.35	103.35
55	10.152	-0.075	9.584	55-39	55-41	55-45	55-65	39-55-41	39-55-45	39-55-65	41-55-45	41-55-65	45-55-65	45-55-65
				4.599	4.645	4.559	4.465	129.37	97.29	108.84	98.28	121.77	70.09	70.09
57	4.241	3.755	9.678	57-45	57-47	57-51	57-71	45-57-47	45-57-51	45-57-71	47-57-51	47-57-71	51-57-71	51-57-71
				4.545	4.652	4.526	4.530	97.95	98.33	96.67	131.49	126.77	96.09	96.09
59	-4.029	-3.922	9.760	59-43	59-49	59-73	59-0	43-59-49	43-59-73	49-59-73	0-0-0	0-0-0	0-0-0	0-0-0
				4.532	4.597	4.587	0.000	96.15	95.32	100.24	0.00	0.00	0.00	0.00
61	-9.775	-0.011	9.752	61-37	61-47	61-49	61-67	37-61-47	37-61-49	37-61-67	47-61-49	47-61-67	49-61-67	49-61-67
				4.615	4.676	4.547	4.596	124.19	98.44	108.60	96.04	125.83	62.77	62.77

Nr.	coordinates [a.u.]			bondlength [a.u]					bondangles				
	x	y	z	63-39	63-49	63-51	63-67	39-63-49	39-63-51	39-63-67	49-63-51	49-63-67	51-63-67
63	-4.338	3.879	9.673	4.491	4.740	4.508	4.466	100.07	129.23	113.48	92.10	62.21	115.76
65	7.155	-0.642	12.845	65-55 4.465	65-69 4.333	65-71 4.547	65-0 0.000	55-65-69 141.17	55-65-71 126.78	69-65-71 72.79	0-0-0 0.00	0-0-0 0.00	0-0-0 0.00
67	-6.052	0.735	12.341	67-49 4.762	67-61 4.596	67-63 4.466	67-73 4.436	49-67-61 58.12	49-67-63 61.73	49-67-73 99.97	61-67-63 95.09	61-67-73 128.90	63-67-73 115.02
69	3.802	-3.156	13.949	69-53 4.507	69-65 4.333	69-0 0.000	69-0 0.000	53-69-65 76.62	0-0-0 0.00	0-0-0 0.00	0-0-0 0.00	0-0-0 0.00	0-0-0 0.00
71	3.686	2.114	13.864	71-57 4.530	71-65 4.547	71-75 4.772	71-0 0.000	57-71-65 85.36	57-71-75 78.72	65-71-75 98.25	0-0-0 0.00	0-0-0 0.00	0-0-0 0.00
73	-3.117	-2.197	13.912	73-59 4.587	73-67 4.436	73-75 4.605	73-0 0.000	59-73-67 78.26	59-73-75 80.37	67-73-75 90.65	0-0-0 0.00	0-0-0 0.00	0-0-0 0.00
75	0.253	-0.200	11.491	75-43 4.654	75-51 4.646	75-71 4.772	75-73 4.605	43-75-51 92.56	43-75-71 134.70	43-75-73 93.42	51-75-71 91.29	51-75-73 128.49	71-75-73 118.39

A.1.8 Five additional Si ad-atoms (h)

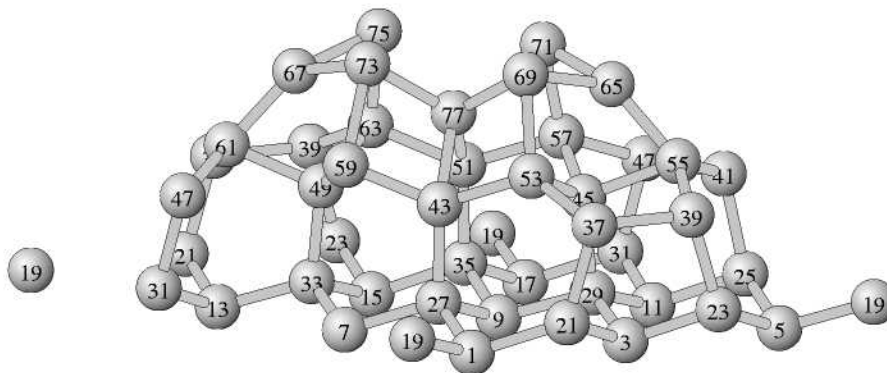


Figure A.8: Perspective view of the upper half of the inversion symmetric (3×3) -supercell with five extra ad-atoms (69,71,73,75,77) on top.

Nr.	coordinates [a.u.]			bondlength [a.u.]					bondangles				
	x	y	z	1-19	1-21	1-27	1-0	19-1-21	19-1-27	21-1-27	0-0-0	0-0-0	0-0-0
1	2.093	-7.249	2.220	4.351	4.512	4.435	0.000	110.35	110.69	109.77	0-0-0	0-0-0	0-0-0
3	8.371	-3.625	2.220	4.417	4.428	4.385	0.000	21-3-23	21-3-29	23-3-29	0-0-0	0-0-0	0-0-0
5	14.648	-0.000	2.220	5-19	5-23	5-25	5-0	19-5-23	19-5-25	23-5-25	0-0-0	0-0-0	0-0-0
7	-4.185	-3.625	2.220	7-27	7-33	7-0	7-0	27-7-33	0-0-0	0-0-0	0-0-0	0-0-0	0-0-0
9	2.093	0.000	2.220	9-27	9-29	9-35	9-0	27-9-29	27-9-35	29-9-35	0-0-0	0-0-0	0-0-0
11	8.371	3.625	2.220	11-25	11-29	11-31	11-0	25-11-29	25-11-31	29-11-31	0-0-0	0-0-0	0-0-0
13	-10.463	0.000	2.220	13-21	13-31	13-33	13-0	21-13-31	21-13-33	31-13-33	0-0-0	0-0-0	0-0-0
15	-4.185	3.625	2.220	15-23	15-33	15-35	15-0	23-15-33	23-15-35	33-15-35	0-0-0	0-0-0	0-0-0
17	2.093	7.249	2.220	17-19	17-31	17-35	17-0	19-17-31	19-17-35	31-17-35	0-0-0	0-0-0	0-0-0
19	0.020	-10.838	3.543	19-1	19-0	19-0	19-0	0-0-0	0-0-0	0-0-0	0-0-0	0-0-0	0-0-0
19	-18.814	0.036	3.543	19-0	19-0	19-0	19-0	0-0-0	0-0-0	0-0-0	0-0-0	0-0-0	0-0-0
19	18.853	0.036	3.543	19-5	19-0	19-0	19-0	0-0-0	0-0-0	0-0-0	0-0-0	0-0-0	0-0-0
19	0.020	10.909	3.543	19-17	19-0	19-0	19-0	0-0-0	0-0-0	0-0-0	0-0-0	0-0-0	0-0-0
21	6.342	-7.243	3.735	21-1	21-3	21-37	21-0	1-21-3	1-21-37	3-21-37	0-0-0	0-0-0	0-0-0
21	-12.492	3.630	3.735	21-13	21-37	21-0	21-0	13-21-37	0-0-0	0-0-0	0-0-0	0-0-0	0-0-0
23	-6.319	7.235	3.777	23-15	23-39	23-0	23-0	15-23-39	0-0-0	0-0-0	0-0-0	0-0-0	0-0-0
23	12.515	-3.639	3.777	23-3	23-5	23-39	23-0	3-23-5	3-23-39	5-23-39	0-0-0	0-0-0	0-0-0
25	12.516	3.637	3.775	25-5	25-11	25-41	25-0	5-25-11	5-25-41	11-25-41	0-0-0	0-0-0	0-0-0
27	-0.011	-3.612	3.638	27-1	27-7	27-9	27-43	1-27-7	1-27-9	1-27-43	7-27-9	7-27-43	9-27-43
29	6.285	0.014	3.498	29-3	29-9	29-11	29-45	3-29-9	3-29-11	3-29-45	9-29-11	9-29-45	11-29-45
				4.385	4.383	4.361	4.356	111.54	111.97	108.15	112.00	101.76	110.90

Nr.	coordinates [a.u.]			bondlength [a.u]				bondangles							
	x	y	z	31-11	31-17	31-47	31-0	11-31-17	11-31-47	17-31-47	0-0-0	0-0-0	0-0-0	0-0-0	0-0-0
31	6.337	7.239	3.781	4.432	4.523	4.545	0.000	108.10	96.29	124.82	0.00	0.00	0.00	0.00	0.00
31	-12.496	-3.634	3.781	4.448	4.545	0.000	0.000	13-31-47	0-0-0	0-0-0	0-0-0	0-0-0	0-0-0	0-0-0	0-0-0
33	-6.267	0.027	3.526	4.401	4.395	4.357	33-49	7-33-13	7-33-15	7-33-49	13-33-15	13-33-49	13-33-49	15-33-49	15-33-49
35	-0.030	3.552	3.828	35-9	35-15	35-17	35-51	9-35-15	9-35-17	9-35-51	15-35-17	15-35-51	15-35-51	17-35-51	17-35-51
37	7.471	-6.749	8.085	37-21	37-39	37-53	37-0	21-37-39	21-37-53	39-37-53	0-0-0	0-0-0	0-0-0	0-0-0	0-0-0
37	-11.362	4.125	8.085	37-21	37-39	37-61	37-0	21-37-39	21-37-61	39-37-61	0-0-0	0-0-0	0-0-0	0-0-0	0-0-0
39	-7.441	6.659	8.123	39-23	39-37	39-63	39-0	23-39-37	23-39-63	37-39-63	0-0-0	0-0-0	0-0-0	0-0-0	0-0-0
39	11.393	-4.214	8.123	39-23	39-37	39-55	39-0	23-39-37	23-39-55	37-39-55	0-0-0	0-0-0	0-0-0	0-0-0	0-0-0
41	11.457	4.168	8.153	41-25	41-47	41-55	41-0	25-41-47	25-41-55	47-41-55	0-0-0	0-0-0	0-0-0	0-0-0	0-0-0
43	0.036	-3.570	8.048	43-27	43-53	43-59	43-77	27-43-53	27-43-59	27-43-77	53-43-59	53-43-77	53-43-77	59-43-77	59-43-77
45	5.892	-0.100	7.835	45-29	45-53	45-55	45-57	29-45-53	29-45-55	29-45-57	53-45-55	53-45-57	53-45-57	55-45-57	55-45-57
47	7.500	6.625	8.132	47-31	47-41	47-57	47-0	31-47-41	31-47-57	41-47-57	0-0-0	0-0-0	0-0-0	0-0-0	0-0-0
47	-11.333	-4.249	8.132	47-31	47-61	47-0	47-0	31-47-61	0-0-0	0-0-0	0-0-0	0-0-0	0-0-0	0-0-0	0-0-0
49	-5.849	-0.087	7.881	49-33	49-59	49-61	49-63	33-49-59	33-49-61	33-49-63	59-49-61	59-49-63	59-49-63	61-49-63	61-49-63
51	-0.005	3.131	8.353	51-35	51-57	51-63	51-77	35-51-57	35-51-63	35-51-77	57-51-63	57-51-77	57-51-77	63-51-77	63-51-77
53	4.190	-3.932	9.553	53-37	53-43	53-45	53-69	37-53-43	37-53-45	37-53-69	43-53-45	43-53-69	43-53-69	45-53-69	45-53-69
55	10.091	-0.025	9.581	55-39	55-41	55-45	55-65	39-55-41	39-55-45	39-55-65	41-55-45	41-55-65	41-55-65	45-55-65	45-55-65
57	4.257	3.805	9.661	57-45	57-47	57-51	57-71	45-57-47	45-57-51	45-57-71	57-51-71	57-51-71	57-51-71	59-57-71	59-57-71
59	-4.123	-3.815	9.699	59-43	59-49	59-73	59-0	43-59-49	43-59-73	49-59-73	0-0-0	0-0-0	0-0-0	0-0-0	0-0-0
61	-10.059	-0.054	9.566	61-37	61-47	61-49	61-67	37-61-47	37-61-49	37-61-67	47-61-49	47-61-67	47-61-67	49-61-67	49-61-67
				4.621	4.613	4.535	4.449	130.15	98.59	102.94	97.72	126.91	126.91	70.67	70.67

Nr.	coordinates [a.u.]			bondlength [a.u]					bondangles				
	x	y	z	63-39	63-49	63-51	63-75	39-63-49	39-63-51	39-63-75	49-63-51	49-63-75	51-63-75
63	-4.272	3.849	9.803	4.557	4.655	4.564	4.587	97.69	129.05	123.67	93.02	106.13	51-63-75 100.19
65	7.060	0.428	12.850	4.481	4.566	4.336	0.000	55-65-69 125.98	55-65-71 142.15	69-65-71 72.47	0-0-0 0.00	0-0-0 0.00	0-0-0 0.00
67	-7.166	0.896	12.810	4.449	4.854	4.243	0.000	61-67-73 122.24	61-67-75 151.32	73-67-75 66.72	0-0-0 0.00	0-0-0 0.00	0-0-0 0.00
69	3.689	-2.498	13.807	4.517	4.566	4.790	0.000	53-69-65 85.64	53-69-77 76.38	65-69-77 99.10	0-0-0 0.00	0-0-0 0.00	0-0-0 0.00
71	3.593	2.762	14.005	4.516	4.336	0.000	71-0	57-71-65 75.56	0-0-0 0.00	0-0-0 0.00	0-0-0 0.00	0-0-0 0.00	0-0-0 0.00
73	-3.460	-2.037	13.915	4.623	4.854	4.661	0.000	59-73-67 85.14	59-73-77 76.72	67-73-77 104.23	0-0-0 0.00	0-0-0 0.00	0-0-0 0.00
75	-3.768	2.969	14.277	4.587	4.243	0.000	0.000	63-75-67 70.63	0-0-0 0.00	0-0-0 0.00	0-0-0 0.00	0-0-0 0.00	0-0-0 0.00
77	0.118	-0.335	11.460	4.702	4.656	4.790	4.661	43-77-51 91.58	43-77-69 93.32	43-77-73 96.75	51-77-69 133.07	51-77-73 127.09	69-77-73 98.58

A.2 Clusters on Si(111):As

A.2.1 One exchanged Si atom

In the following tables the positions of the atoms, the bondlength and the bondangles are summarized. The coordinates refer to a cartesian coordinate system which is shown in Fig.A.9. The center of the coordinate system is located in atom 1. The z-coordinate of the system is at the fourth layer as is shown in Fig.A.10.

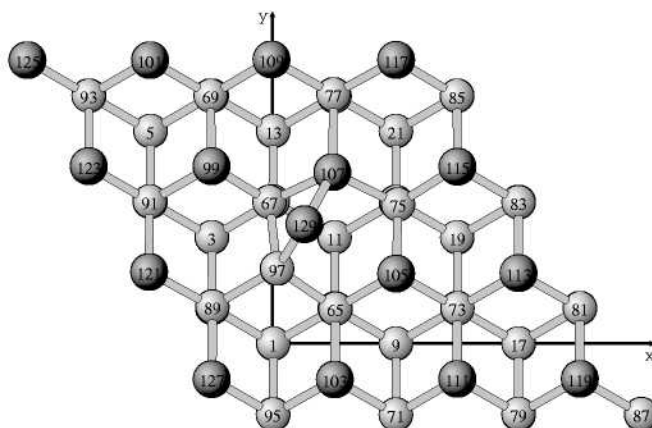


Figure A.9: Topview of a part of the (4×4) -supercell with one exchanged Si atom (97). The As atom (129) is shifted to a bridge position between the Si atom and a neighboring As atom (107).

Thus, the atoms with the numbers 33-64 are located directly beneath the atoms 65-95 in Fig.A.9.

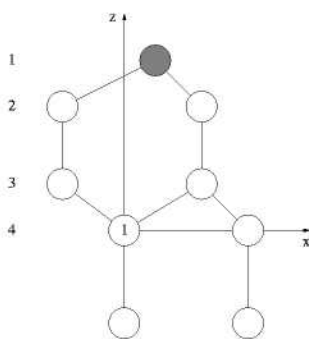


Figure A.10: Schematic sideview of the upper four layers of the inversion symmetric (4×4) -supercell.

Nr.	coordinates [a.u.]			bondlength [a.u.]					bondangles				
	x	y	z	33-65	33-0	33-0	33-0	33-0	0-0-0	0-0-0	0-0-0	0-0-0	0-0-0
33	3.622	2.067	1.462	4.386	0.000	0.000	0.000	0.000	0.00	0.00	0.00	0.00	0.00
35	-0.026	8.359	1.257	4.302	0.000	0.000	0.000	0.000	0.00	0.00	0.00	0.00	0.00
37	-3.612	14.584	1.451	4.376	0.000	0.000	0.000	0.000	0.00	0.00	0.00	0.00	0.00
39	7.211	-4.168	1.472	4.383	0.000	0.000	0.000	0.000	0.00	0.00	0.00	0.00	0.00
41	10.829	2.074	1.451	4.1-73	41-0	41-0	41-0	41-0	0.00	0.00	0.00	0.00	0.00
43	7.216	8.327	1.448	43-75	43-0	43-0	43-0	43-0	0.00	0.00	0.00	0.00	0.00
45	3.604	14.544	1.542	45-77	45-0	45-0	45-0	45-0	0.00	0.00	0.00	0.00	0.00
47	14.427	-4.167	1.464	47-79	47-0	47-0	47-0	47-0	0.00	0.00	0.00	0.00	0.00
49	18.037	2.080	1.469	49-81	49-0	49-0	49-0	49-0	0.00	0.00	0.00	0.00	0.00
51	14.428	8.336	1.479	51-83	51-0	51-0	51-0	51-0	0.00	0.00	0.00	0.00	0.00
53	10.820	14.579	1.463	53-85	53-0	53-0	53-0	53-0	0.00	0.00	0.00	0.00	0.00
55	21.644	-4.167	1.474	55-87	55-0	55-0	55-0	55-0	0.00	0.00	0.00	0.00	0.00
57	-3.583	2.096	1.592	57-89	57-0	57-0	57-0	57-0	0.00	0.00	0.00	0.00	0.00
59	-7.219	8.333	1.461	59-91	59-0	59-0	59-0	59-0	0.00	0.00	0.00	0.00	0.00
61	-10.823	14.581	1.453	61-93	61-0	61-0	61-0	61-0	0.00	0.00	0.00	0.00	0.00
63	0.000	-4.162	1.469	63-95	63-0	63-0	63-0	63-0	0.00	0.00	0.00	0.00	0.00
65	3.665	2.054	5.848	65-33	65-97	65-103	65-105	33-65-103	33-65-103	97-65-103	97-65-105	103-65-105	102.95
67	-0.214	8.338	5.555	67-35	67-97	67-99	67-107	35-67-99	35-67-107	97-67-99	97-67-107	99-67-107	103.26
69	-3.675	14.591	5.827	69-37	69-99	69-101	69-109	37-69-99	37-69-101	99-69-101	99-69-109	101-69-109	101.95
71	7.215	-4.169	5.855	71-39	71-103	71-111	71-0	39-71-103	39-71-111	103-71-111	103.26	0.00	0.00

Nr.	coordinates [a.u.]			bondlength [a.u.]					bondangles				
	x	y	z	73-41	73-105	73-111	73-113	41-73-105	41-73-111	41-73-113	105-73-111	105-73-113	111-73-113
73	10.828	2.089	5.838	4.388	4.606	4.598	4.590	116.41	115.02	115.57	102.04	102.96	111-73-113 102.87
75	7.338	8.189	5.834	4.390	4.561	4.597	4.589	118.39	108.64	116.04	105-75-107 100.82	105-75-115 104.75	107-75-115 106.62
77	3.548	14.664	6.003	4.464	4.814	4.570	4.592	106.22	115.19	114.03	107-77-109 106.91	107-77-117 107.79	109-77-117 106.28
79	14.426	-4.142	5.850	4.387	4.588	4.599	0.000	115.29	115.51	103.29	0.0-0	0.0-0	0.0-0
81	18.029	2.095	5.854	4.385	4.586	4.607	0.000	115.45	115.06	102.84	0.0-0	0.0-0	0.0-0
83	14.431	8.310	5.865	4.386	4.597	4.602	0.000	115.41	114.97	103.34	0.0-0	0.0-0	0.0-0
85	10.807	14.572	5.851	4.388	4.611	4.616	0.000	115.41	116.00	103.30	0.0-0	0.0-0	0.0-0
87	21.639	-4.145	5.867	4.393	4.598	0.000	0.000	115.32	0.00	0.00	0.0-0	0.0-0	0.0-0
89	-3.581	2.176	6.078	4.487	4.615	4.597	4.628	107.75	113.27	111.73	97-89-121 109.72	97-89-127 109.65	121-89-127 104.69
91	-7.264	8.354	5.845	4.384	4.607	4.601	4.584	114.31	115.69	116.02	99-91-121 103.13	99-91-123 103.53	121-91-123 102.39
93	-10.849	14.587	5.841	4.387	4.602	4.599	4.601	114.95	115.27	115.63	101-93-123 103.06	101-93-125 103.11	123-93-125 103.06
95	-0.012	-4.149	5.861	4.393	4.604	4.609	0.000	114.96	116.03	103.59	0.0-0	0.0-0	0.0-0
97	0.225	4.401	7.443	4.460	4.388	4.615	4.545	113.28	106.05	107.02	67-97-89 102.88	67-97-129 80.50	89-97-129 142.05
99	-3.628	10.428	7.769	4.575	4.594	4.607	0.000	102.53	100.44	69-99-91 102.91	0.0-0	0.0-0	0.0-0
101	-7.243	16.668	7.801	4.576	4.602	0.000	0.000	102.83	0.00	0.00	0.0-0	0.0-0	0.0-0
103	3.624	-2.104	7.808	4.597	4.580	4.604	0.000	102.64	103.21	103.81	0.0-0	0.0-0	0.0-0
105	7.230	4.115	7.880	4.592	4.606	4.561	0.000	102.29	102.76	100.12	0.0-0	0.0-0	0.0-0
107	3.480	10.079	7.471	4.511	4.597	4.814	4.802	112.16	104.46	76.56	75-107-77 105.73	75-107-129 105.72	77-107-129 145.29
109	-0.101	16.704	7.849	4.617	4.570	0.000	0.000	103.71	0.00	0.00	0.0-0	0.0-0	0.0-0
111	10.825	-2.071	7.798	4.605	4.598	4.588	0.000	103.47	103.33	103.12	0.0-0	0.0-0	0.0-0

Nr.	coordinates [a.u.]			bondlength [a.u.]					bondangles				
	x	y	z	113-73	113-81	113-83	113-0	73-113-81	73-113-83	81-113-83	0-0-0	0-0-0	0-0-0
113	14.425	4.146	7.813	4.590	4.586	4.597	0.000	103.40	103.00	102.89	0.00	0.00	0.00
115	10.831	10.404	7.823	4.589	4.602	4.611	115-0	75-115-83	75-115-85	83-115-85	0.00	0.00	0.00
117	7.229	16.679	7.867	4.592	4.616	117-0	117-0	77-117-85	0.00	0.00	0.00	0.00	0.00
119	18.030	-2.071	7.820	4.599	4.607	119-87	119-0	79-119-81	79-119-87	81-119-87	0.00	0.00	0.00
121	-7.294	4.217	7.860	4.597	4.601	121-91	121-0	89-121-91	0.00	0.00	0.00	0.00	0.00
123	-10.847	10.430	7.809	4.584	4.599	123-93	123-0	91-123-93	0.00	0.00	0.00	0.00	0.00
125	-14.451	16.667	7.807	4.601	4.600	125-93	125-0	0.00	0.00	0.00	0.00	0.00	0.00
127	-3.616	-2.091	7.867	4.628	4.609	127-95	127-0	89-127-95	0.00	0.00	0.00	0.00	0.00
129	1.839	7.020	10.788	4.545	4.802	129-107	129-0	97-129-107	0.00	0.00	0.00	0.00	0.00

A.2.2 Two exchanged Si atoms (As-dimer)

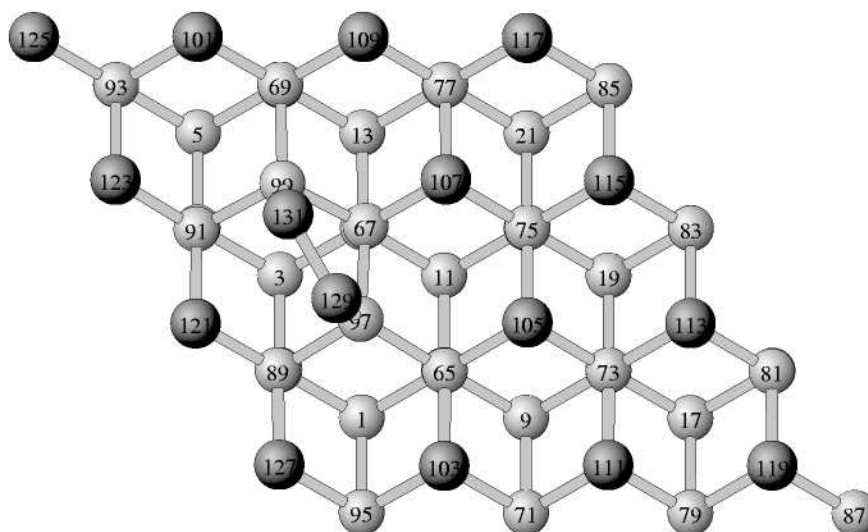


Figure A.11: Topview of a part of the (4×4) -supercell with two exchanged Si atoms (97,99). The As atoms (129,131) form a dimer on top of the Si atoms

Nr.	coordinates [a.u.]			bondlength [a.u.]					bondangles									
	x	y	z															
33	3.617	2.096	1.516	33-65 4.461	33-0 0.000	33-0 0.000	33-0 0.000	33-0 0.000	0-0-0 0.00	0-0-0 0.00	0-0-0 0.00	0-0-0 0.00	0-0-0 0.00	0-0-0 0.00	0-0-0 0.00	0-0-0 0.00	0-0-0 0.00	0-0-0 0.00
35	0.025	8.381	1.330	35-67 4.340	35-0 0.000	35-0 0.000	35-0 0.000	35-0 0.000	0-0-0 0.00	0-0-0 0.00	0-0-0 0.00	0-0-0 0.00	0-0-0 0.00	0-0-0 0.00	0-0-0 0.00	0-0-0 0.00	0-0-0 0.00	0-0-0 0.00
37	-3.622	14.634	1.517	37-69 4.461	37-0 0.000	37-0 0.000	37-0 0.000	37-0 0.000	0-0-0 0.00	0-0-0 0.00	0-0-0 0.00	0-0-0 0.00	0-0-0 0.00	0-0-0 0.00	0-0-0 0.00	0-0-0 0.00	0-0-0 0.00	0-0-0 0.00
39	7.246	-4.183	1.454	39-71 4.400	39-0 0.000	39-0 0.000	39-0 0.000	39-0 0.000	0-0-0 0.00	0-0-0 0.00	0-0-0 0.00	0-0-0 0.00	0-0-0 0.00	0-0-0 0.00	0-0-0 0.00	0-0-0 0.00	0-0-0 0.00	0-0-0 0.00
41	10.868	2.091	1.451	41-73 4.397	41-0 0.000	41-0 0.000	41-0 0.000	41-0 0.000	0-0-0 0.00	0-0-0 0.00	0-0-0 0.00	0-0-0 0.00	0-0-0 0.00	0-0-0 0.00	0-0-0 0.00	0-0-0 0.00	0-0-0 0.00	0-0-0 0.00
43	7.249	8.366	1.443	43-75 4.395	43-0 0.000	43-0 0.000	43-0 0.000	43-0 0.000	0-0-0 0.00	0-0-0 0.00	0-0-0 0.00	0-0-0 0.00	0-0-0 0.00	0-0-0 0.00	0-0-0 0.00	0-0-0 0.00	0-0-0 0.00	0-0-0 0.00
45	3.624	14.644	1.443	45-77 4.396	45-0 0.000	45-0 0.000	45-0 0.000	45-0 0.000	0-0-0 0.00	0-0-0 0.00	0-0-0 0.00	0-0-0 0.00	0-0-0 0.00	0-0-0 0.00	0-0-0 0.00	0-0-0 0.00	0-0-0 0.00	0-0-0 0.00
47	14.490	-4.183	1.451	47-79 4.397	47-0 0.000	47-0 0.000	47-0 0.000	47-0 0.000	0-0-0 0.00	0-0-0 0.00	0-0-0 0.00	0-0-0 0.00	0-0-0 0.00	0-0-0 0.00	0-0-0 0.00	0-0-0 0.00	0-0-0 0.00	0-0-0 0.00
49	18.108	2.088	1.437	49-81 4.393	49-0 0.000	49-0 0.000	49-0 0.000	49-0 0.000	0-0-0 0.00	0-0-0 0.00	0-0-0 0.00	0-0-0 0.00	0-0-0 0.00	0-0-0 0.00	0-0-0 0.00	0-0-0 0.00	0-0-0 0.00	0-0-0 0.00
51	14.492	8.370	1.454	51-83 4.393	51-0 0.000	51-0 0.000	51-0 0.000	51-0 0.000	0-0-0 0.00	0-0-0 0.00	0-0-0 0.00	0-0-0 0.00	0-0-0 0.00	0-0-0 0.00	0-0-0 0.00	0-0-0 0.00	0-0-0 0.00	0-0-0 0.00
53	10.870	14.642	1.435	53-85 4.396	53-0 0.000	53-0 0.000	53-0 0.000	53-0 0.000	0-0-0 0.00	0-0-0 0.00	0-0-0 0.00	0-0-0 0.00	0-0-0 0.00	0-0-0 0.00	0-0-0 0.00	0-0-0 0.00	0-0-0 0.00	0-0-0 0.00
55	21.740	-4.184	1.455	55-87 4.393	55-0 0.000	55-0 0.000	55-0 0.000	55-0 0.000	0-0-0 0.00	0-0-0 0.00	0-0-0 0.00	0-0-0 0.00	0-0-0 0.00	0-0-0 0.00	0-0-0 0.00	0-0-0 0.00	0-0-0 0.00	0-0-0 0.00
57	-3.636	2.088	1.445	57-89 4.406	57-0 0.000	57-0 0.000	57-0 0.000	57-0 0.000	0-0-0 0.00	0-0-0 0.00	0-0-0 0.00	0-0-0 0.00	0-0-0 0.00	0-0-0 0.00	0-0-0 0.00	0-0-0 0.00	0-0-0 0.00	0-0-0 0.00
59	-7.255	8.356	1.445	59-91 4.406	59-0 0.000	59-0 0.000	59-0 0.000	59-0 0.000	0-0-0 0.00	0-0-0 0.00	0-0-0 0.00	0-0-0 0.00	0-0-0 0.00	0-0-0 0.00	0-0-0 0.00	0-0-0 0.00	0-0-0 0.00	0-0-0 0.00
61	-10.867	14.640	1.448	61-93 4.401	61-0 0.000	61-0 0.000	61-0 0.000	61-0 0.000	0-0-0 0.00	0-0-0 0.00	0-0-0 0.00	0-0-0 0.00	0-0-0 0.00	0-0-0 0.00	0-0-0 0.00	0-0-0 0.00	0-0-0 0.00	0-0-0 0.00
63	-0.000	-4.182	1.448	63-95 4.400	63-0 0.000	63-0 0.000	63-0 0.000	63-0 0.000	0-0-0 0.00	0-0-0 0.00	0-0-0 0.00	0-0-0 0.00	0-0-0 0.00	0-0-0 0.00	0-0-0 0.00	0-0-0 0.00	0-0-0 0.00	0-0-0 0.00
65	3.661	2.072	5.977	65-33 4.461	65-97 4.553	65-103 4.578	65-105 4.589	65-107 4.592	33-65-97 106.27	33-65-103 113.63	33-65-105 113.50	33-65-107 113.50	33-65-109 109.80	33-65-111 109.80	33-65-113 109.80	33-65-115 109.80	33-65-117 109.80	33-65-119 109.80
67	0.154	8.454	5.668	67-35 4.340	67-97 4.434	67-107 4.434	67-117 4.434	67-127 4.434	35-67-97 110.55	35-67-107 110.54	35-67-117 110.54	35-67-127 110.54	35-67-137 110.54	35-67-147 110.54	35-67-157 110.54	35-67-167 110.54	35-67-177 110.54	35-67-187 110.54
69	-3.620	14.683	5.978	69-37 4.461	69-99 4.553	69-109 4.578	69-119 4.589	69-129 4.592	37-69-99 106.27	37-69-109 113.62	37-69-119 113.62	37-69-129 113.62	37-69-139 113.62	37-69-149 113.62	37-69-159 113.62	37-69-169 113.62	37-69-179 113.62	37-69-189 113.62
71	7.253	-4.179	5.854	71-39 4.400	71-103 4.579	71-113 4.595	71-123 4.595	71-133 4.595	39-71-103 114.96	39-71-113 114.56	39-71-123 114.56	39-71-133 114.56	39-71-143 114.56	39-71-153 114.56	39-71-163 114.56	39-71-173 114.56	39-71-183 114.56	39-71-193 114.56

Nr.	coordinates [a.u.]			bondlength [a.u.]					bondangles							
	x	y	z	73-41	73-105	73-111	73-113	41-73-105	41-73-111	41-73-113	105-73-111	105-73-113	105-73-113	105-73-113	105-73-113	111-73-113
73	10.880	2.093	5.848	4.397	4.580	4.596	4.579	114.86	114.51	114.63	104.04	103.37	103.37	103.37	103.37	104.03
75	7.292	8.381	5.838	4.395	4.610	4.578	4.576	114.75	113.86	115.16	104.36	103.67	103.67	103.67	103.67	103.68
77	3.659	14.672	5.839	4.396	4.578	4.610	4.577	113.85	114.74	115.15	104.37	103.69	103.69	103.69	103.69	103.68
79	14.498	-4.175	5.848	4.397	4.596	4.579	0.000	114.49	114.63	104.02	0.00	0.00	0.00	0.00	0.00	0.00
81	18.078	2.071	5.830	4.393	4.580	4.580	0.000	114.93	114.95	104.32	0.00	0.00	0.00	0.00	0.00	0.00
83	14.496	8.364	5.847	4.393	4.599	4.584	0.000	114.45	114.33	104.29	0.00	0.00	0.00	0.00	0.00	0.00
85	10.883	14.649	5.831	4.396	4.596	4.596	0.000	114.47	114.47	104.09	0.00	0.00	0.00	0.00	0.00	0.00
87	21.738	-4.178	5.848	4.393	4.599	0.000	0.000	114.44	0.00	0.00	0.00	0.00	0.00	0.00	0.00	0.00
89	-3.716	2.075	5.850	4.406	4.538	4.588	4.589	107.69	115.68	114.74	106.12	107.76	107.76	107.76	107.76	104.30
91	-7.306	8.293	5.850	4.406	4.538	4.588	4.589	107.68	115.69	114.73	106.11	107.78	107.78	107.78	107.78	104.30
93	-10.858	14.644	5.849	4.401	4.602	4.606	4.596	115.10	114.46	114.28	104.38	103.35	103.35	103.35	103.35	103.88
95	0.008	-4.176	5.849	4.400	4.602	4.606	0.000	115.10	114.46	104.38	0.00	0.00	0.00	0.00	0.00	0.00
97	-0.060	4.338	7.301	4.553	4.434	4.538	4.517	108.38	108.50	124.66	112.58	100.04	100.04	100.04	102.46	102.46
99	-3.518	10.327	7.301	4.434	4.553	4.538	4.517	108.40	112.59	100.02	108.49	124.66	124.66	124.66	102.45	102.45
101	-7.269	16.770	7.791	4.578	4.602	0.000	0.000	104.10	0.00	0.00	0.00	0.00	0.00	0.00	0.00	0.00
103	3.644	-2.131	7.791	4.578	4.579	4.602	0.000	103.90	104.11	104.20	0.00	0.00	0.00	0.00	0.00	0.00
105	7.303	4.201	7.782	4.589	4.580	4.610	0.000	103.89	104.64	103.96	0.00	0.00	0.00	0.00	0.00	0.00
107	3.693	10.497	7.717	4.572	4.578	4.578	0.000	102.58	102.58	105.01	0.00	0.00	0.00	0.00	0.00	0.00
109	0.045	16.772	7.784	4.589	4.610	0.000	0.000	104.64	0.00	0.00	0.00	0.00	0.00	0.00	0.00	0.00
111	10.875	-2.088	7.756	4.595	4.596	4.596	0.000	104.06	104.06	103.88	0.00	0.00	0.00	0.00	0.00	0.00

Nr.	coordinates [a.u.]			bondlength [a.u]					bondangles				
	x	y	z	113-73	113-81	113-83	113-0	73-113-81	73-113-83	81-113-83	0-0-0	0-0-0	0-0-0
113	14.490	4.175	7.745	4.579	4.580	4.599	0.000	103.62	104.14	104.18	0.00	0.00	0.00
115	10.891	10.470	7.741	4.576	4.584	4.596	115-0	75-115-83	75-115-85	83-115-85	0-0-0	0-0-0	0-0-0
117	7.268	16.746	7.743	4.577	4.596	0.000	0.000	103.92	103.93	104.31	0.00	0.00	0.00
119	18.107	-2.089	7.746	4.579	4.580	4.599	119-0	79-119-81	79-119-87	81-119-87	0-0-0	0-0-0	0-0-0
121	-7.335	4.130	7.779	4.588	4.588	0.000	121-0	89-121-91	0-0-0	0-0-0	0.00	0.00	0.00
123	-10.876	10.453	7.760	4.589	4.606	0.000	123-0	91-123-93	0-0-0	0-0-0	0.00	0.00	0.00
125	-14.484	16.736	7.745	4.596	0.000	0.000	125-0	0-0-0	0-0-0	0-0-0	0.00	0.00	0.00
127	-3.630	-2.096	7.760	4.589	4.606	0.000	127-0	89-127-95	0-0-0	0-0-0	0.00	0.00	0.00
129	-1.120	5.249	11.596	4.517	4.275	0.000	129-0	97-129-131	0-0-0	0-0-0	0.00	0.00	0.00
131	-3.258	8.952	11.596	4.517	4.275	0.000	131-0	99-131-129	0-0-0	0-0-0	0.00	0.00	0.00

A.2.3 Three exchanged Si atoms (As-trimer)

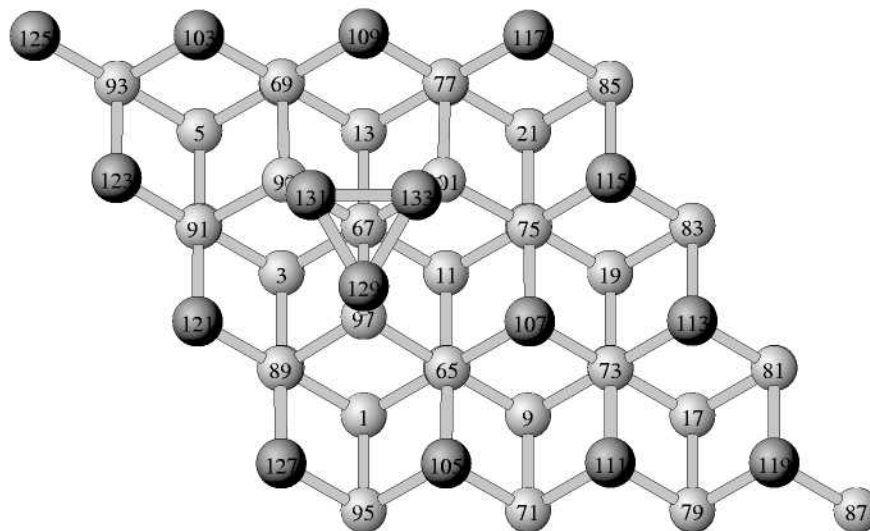


Figure A.12: Topview of a part of the (4×4) -supercell with three exchanged Si atoms (97,99,101). The As atoms (129,131,133) form a trimer on top of the Si atoms

Nr.	coordinates [a.u.]			bondlength [a.u.]				bondangles							
	x	y	z	33-65	33-0	33-0	33-0	0-0-0	0-0-0	0-0-0	0-0-0	0-0-0	0-0-0	0-0-0	0-0-0
33	3.625	2.092	1.487	4.439	0.000	0.000	0.000	0.00	0.00	0.00	0.00	0.00	0.00	0.00	0.00
35	-0.000	8.366	1.193	4.269	0.000	0.000	0.000	0.00	0.00	0.00	0.00	0.00	0.00	0.00	0.00
37	-3.621	14.644	1.487	4.439	0.000	0.000	0.000	0.00	0.00	0.00	0.00	0.00	0.00	0.00	0.00
39	7.241	-4.185	1.461	4.394	0.000	0.000	0.000	0.00	0.00	0.00	0.00	0.00	0.00	0.00	0.00
41	10.868	2.091	1.450	4.1-73	41-0	41-0	41-0	0.00	0.00	0.00	0.00	0.00	0.00	0.00	0.00
43	7.247	8.364	1.487	43-75	43-0	43-0	43-0	0.00	0.00	0.00	0.00	0.00	0.00	0.00	0.00
45	3.621	14.644	1.487	45-77	45-0	45-0	45-0	0.00	0.00	0.00	0.00	0.00	0.00	0.00	0.00
47	14.491	-4.182	1.450	47-79	47-0	47-0	47-0	0.00	0.00	0.00	0.00	0.00	0.00	0.00	0.00
49	18.113	2.091	1.449	49-81	49-0	49-0	49-0	0.00	0.00	0.00	0.00	0.00	0.00	0.00	0.00
51	14.491	8.371	1.461	51-83	51-0	51-0	51-0	0.00	0.00	0.00	0.00	0.00	0.00	0.00	0.00
53	10.868	14.641	1.443	53-85	53-0	53-0	53-0	0.00	0.00	0.00	0.00	0.00	0.00	0.00	0.00
55	21.740	-4.185	1.461	55-87	55-0	55-0	55-0	0.00	0.00	0.00	0.00	0.00	0.00	0.00	0.00
57	-3.626	2.092	1.487	57-89	57-0	57-0	57-0	0.00	0.00	0.00	0.00	0.00	0.00	0.00	0.00
59	-7.247	8.364	1.487	59-91	59-0	59-0	59-0	0.00	0.00	0.00	0.00	0.00	0.00	0.00	0.00
61	-10.868	14.641	1.443	61-93	61-0	61-0	61-0	0.00	0.00	0.00	0.00	0.00	0.00	0.00	0.00
63	-0.000	-4.183	1.443	63-95	63-0	63-0	63-0	0.00	0.00	0.00	0.00	0.00	0.00	0.00	0.00
65	3.688	2.072	5.926	65-33	65-97	65-105	65-107	33-65-97	33-65-105	33-65-107	97-65-105	97-65-107	105-65-107	104.83	104.83
67	-0.002	8.368	5.462	67-35	67-97	67-99	67-101	35-67-97	35-67-99	35-67-101	97-67-99	97-67-101	99-67-101	104.63	104.63
69	-3.610	14.712	5.926	69-37	69-99	69-103	69-109	37-69-99	37-69-103	37-69-109	99-69-103	99-69-109	103-69-109	104.82	104.82
71	7.247	-4.179	5.855	71-39	71-105	71-111	71-0	39-71-105	39-71-111	105-71-111	104.16	104.16	0.00	0.00	0.00

Nr.	coordinates [a.u.]			bondlength [a.u.]					bondangles				
	x	y	z	73-41	73-107	73-111	73-113	41-73-107	41-73-111	41-73-113	107-73-111	107-73-113	111-73-113
73	10.891	2.079	5.849	4.400	4.563	4.579	4.579	115.15	114.75	114.76	103.22	103.22	111-73-113 104.22
75	7.295	8.320	5.926	4.439	4.530	4.587	4.581	106.22	114.85	114.04	107.43	101-75-115 109.28	107-75-115 104.82
77	3.605	14.712	5.926	4.439	4.530	4.587	4.581	106.16	114.90	114.04	107.42	101-77-117 109.28	109-77-117 104.82
79	14.489	-4.153	5.850	4.400	4.579	4.579	0.000	114.80	114.75	104.22	0.00	0.00	0.00
81	18.087	2.079	5.849	4.400	4.579	4.579	0.000	114.79	114.75	104.22	0.00	0.00	0.00
83	14.489	8.363	5.855	4.394	4.599	4.581	0.000	114.50	114.72	104.16	0.00	0.00	0.00
85	10.865	14.642	5.843	4.400	4.603	4.604	0.000	114.78	114.83	104.32	0.00	0.00	0.00
87	21.730	-4.179	5.855	4.394	4.599	0.000	0.000	114.55	0.00	0.00	0.00	0.00	0.00
89	-3.692	2.072	5.926	4.440	4.530	4.587	4.581	106.19	114.89	114.02	107.42	97-89-127 109.29	121-89-127 104.82
91	-7.299	8.320	5.926	4.439	4.530	4.587	4.581	106.17	114.85	114.08	107.43	99-91-123 109.28	121-91-123 104.82
93	-10.870	14.642	5.843	4.400	4.603	4.603	4.596	114.78	114.78	114.46	103-93-123 104.32	103-93-125 103.54	123-93-125 103.55
95	-0.002	-4.181	5.843	4.400	4.603	4.604	0.000	114.79	114.83	104.31	0.00	0.00	0.00
97	-0.002	4.341	7.254	4.530	4.408	4.530	4.546	109.77	109.07	115.35	109.77	67-97-129 96.78	89-97-129 115.35
99	-3.491	10.382	7.253	4.408	4.530	4.530	4.545	109.78	109.78	96.79	69-99-91 109.10	69-99-131 115.30	91-99-131 115.34
101	3.486	10.382	7.253	4.408	4.530	4.530	4.545	109.78	109.79	96.79	75-101-133 109.09	75-101-133 115.34	77-101-133 115.31
103	-7.267	16.760	7.773	4.581	4.603	0.000	0.000	104.47	0.00	0.00	0.00	0.00	0.00
105	3.633	-2.120	7.773	105-65 4.581	105-71 4.581	105-95 4.603	105-0 0.000	65-105-71 103.49	65-105-95 104.48	71-105-95 104.25	0.00	0.00	0.00
107	7.323	4.139	7.812	107-65 4.587	107-73 4.563	107-75 4.587	107-0 0.000	65-107-73 103.85	65-107-75 103.70	73-107-75 103.85	0.00	0.00	0.00
109	-0.002	16.826	7.812	109-69 4.588	109-77 4.587	109-0 0.000	109-0 0.000	69-109-77 103.70	0.00	0.00	0.00	0.00	0.00
111	10.875	-2.085	7.755	111-71 4.599	111-73 4.579	111-79 4.579	111-0 0.000	71-111-73 104.17	71-111-79 104.18	73-111-79 103.58	0.00	0.00	0.00

Nr.	coordinates [a.u.]			bondlength [a.u.]				bondangles				
	x	y	z	113-73	113-81	113-83	113-0	73-113-81	73-113-83	81-113-83	0-0-0	0-0-0
113	14.489	4.175	7.755	4.579	4.579	4.599	0.000	103.59	104.18	104.17	0.00	0.00
115	10.898	10.463	7.773	4.581	4.581	4.603	0.000	75-115-83	75-115-85	83-115-85	0-0-0	0-0-0
117	7.263	16.760	7.774	4.581	4.604	0.000	0.000	77-117-85	0-0-0	0-0-0	0-0-0	0-0-0
119	18.103	-2.085	7.755	4.579	4.579	4.599	0.000	79-119-81	79-119-87	81-119-87	0-0-0	0-0-0
121	-7.327	4.139	7.812	4.587	4.587	0.000	0.000	89-121-91	0-0-0	0-0-0	0-0-0	0-0-0
123	-10.902	10.463	7.773	4.581	4.603	0.000	0.000	91-123-93	0-0-0	0-0-0	0-0-0	0-0-0
125	-14.493	16.734	7.744	4.596	4.604	0.000	0.000	0-0-0	0-0-0	0-0-0	0-0-0	0-0-0
127	-3.637	-2.120	7.774	4.581	4.604	0.000	0.000	89-127-95	0-0-0	0-0-0	0-0-0	0-0-0
129	-0.002	5.685	11.597	4.546	4.651	4.651	0.000	97-129-131	97-129-133	131-129-133	0-0-0	0-0-0
131	-2.327	9.713	11.595	4.545	4.651	4.651	0.000	99-131-129	99-131-133	129-131-133	0-0-0	0-0-0
133	2.323	9.713	11.595	4.545	4.651	4.651	0.000	101-133-129	101-133-131	129-133-131	0-0-0	0-0-0
								104.82	104.82	60.00	0.00	0.00

A.2.4 Four exchanged Si atoms (As/Si-trimer)

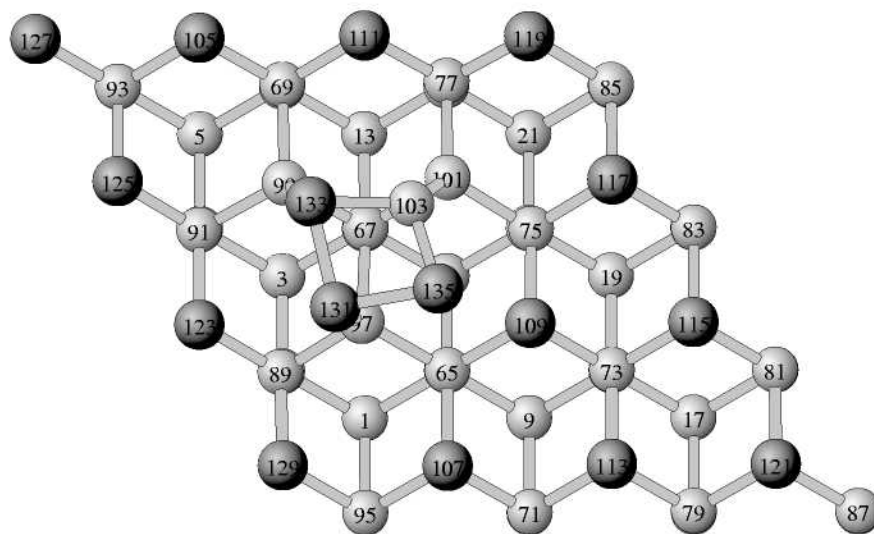


Figure A.13: Topview of a part of the (4×4) -supercell with four exchanged Si atoms. One of the As trimer atoms (135) has been replaced by Si (103). The As atom is shifted to a nearly ideal H3-position in the upper layer of the next double-layer.

Nr.	coordinates [a.u.]			bondlength [a.u]				bondangles							
	x	y	z												
33	3.619	2.099	1.535	33-65 4.478	33-0 0.000	33-0 0.000	33-0 0.000	0-0-0 0.00	0-0-0 0.00	0-0-0 0.00	0-0-0 0.00	0-0-0 0.00	0-0-0 0.00	0-0-0 0.00	0-0-0 0.00
35	0.016	8.357	1.284	35-67 4.328	35-0 0.000	35-0 0.000	35-0 0.000	0-0-0 0.00	0-0-0 0.00	0-0-0 0.00	0-0-0 0.00	0-0-0 0.00	0-0-0 0.00	0-0-0 0.00	0-0-0 0.00
37	-3.621	14.640	1.499	37-69 4.452	37-0 0.000	37-0 0.000	37-0 0.000	0-0-0 0.00	0-0-0 0.00	0-0-0 0.00	0-0-0 0.00	0-0-0 0.00	0-0-0 0.00	0-0-0 0.00	0-0-0 0.00
39	7.242	-4.182	1.457	39-71 4.397	39-0 0.000	39-0 0.000	39-0 0.000	0-0-0 0.00	0-0-0 0.00	0-0-0 0.00	0-0-0 0.00	0-0-0 0.00	0-0-0 0.00	0-0-0 0.00	0-0-0 0.00
41	10.873	2.088	1.454	41-73 4.389	41-0 0.000	41-0 0.000	41-0 0.000	0-0-0 0.00	0-0-0 0.00	0-0-0 0.00	0-0-0 0.00	0-0-0 0.00	0-0-0 0.00	0-0-0 0.00	0-0-0 0.00
43	7.249	8.359	1.491	43-75 4.450	43-0 0.000	43-0 0.000	43-0 0.000	0-0-0 0.00	0-0-0 0.00	0-0-0 0.00	0-0-0 0.00	0-0-0 0.00	0-0-0 0.00	0-0-0 0.00	0-0-0 0.00
45	3.624	14.663	1.441	45-77 4.412	45-0 0.000	45-0 0.000	45-0 0.000	0-0-0 0.00	0-0-0 0.00	0-0-0 0.00	0-0-0 0.00	0-0-0 0.00	0-0-0 0.00	0-0-0 0.00	0-0-0 0.00
47	14.491	-4.180	1.450	47-79 4.398	47-0 0.000	47-0 0.000	47-0 0.000	0-0-0 0.00	0-0-0 0.00	0-0-0 0.00	0-0-0 0.00	0-0-0 0.00	0-0-0 0.00	0-0-0 0.00	0-0-0 0.00
49	18.112	2.091	1.449	49-81 4.402	49-0 0.000	49-0 0.000	49-0 0.000	0-0-0 0.00	0-0-0 0.00	0-0-0 0.00	0-0-0 0.00	0-0-0 0.00	0-0-0 0.00	0-0-0 0.00	0-0-0 0.00
51	14.491	8.371	1.456	51-83 4.395	51-0 0.000	51-0 0.000	51-0 0.000	0-0-0 0.00	0-0-0 0.00	0-0-0 0.00	0-0-0 0.00	0-0-0 0.00	0-0-0 0.00	0-0-0 0.00	0-0-0 0.00
53	10.868	14.642	1.438	53-85 4.398	53-0 0.000	53-0 0.000	53-0 0.000	0-0-0 0.00	0-0-0 0.00	0-0-0 0.00	0-0-0 0.00	0-0-0 0.00	0-0-0 0.00	0-0-0 0.00	0-0-0 0.00
55	21.740	-4.183	1.457	55-87 4.390	55-0 0.000	55-0 0.000	55-0 0.000	0-0-0 0.00	0-0-0 0.00	0-0-0 0.00	0-0-0 0.00	0-0-0 0.00	0-0-0 0.00	0-0-0 0.00	0-0-0 0.00
57	-3.645	2.079	1.410	57-89 4.383	57-0 0.000	57-0 0.000	57-0 0.000	0-0-0 0.00	0-0-0 0.00	0-0-0 0.00	0-0-0 0.00	0-0-0 0.00	0-0-0 0.00	0-0-0 0.00	0-0-0 0.00
59	-7.249	8.365	1.479	59-91 4.433	59-0 0.000	59-0 0.000	59-0 0.000	0-0-0 0.00	0-0-0 0.00	0-0-0 0.00	0-0-0 0.00	0-0-0 0.00	0-0-0 0.00	0-0-0 0.00	0-0-0 0.00
61	-10.867	14.642	1.448	61-93 4.400	61-0 0.000	61-0 0.000	61-0 0.000	0-0-0 0.00	0-0-0 0.00	0-0-0 0.00	0-0-0 0.00	0-0-0 0.00	0-0-0 0.00	0-0-0 0.00	0-0-0 0.00
63	0.001	-4.182	1.443	63-95 4.400	63-0 0.000	63-0 0.000	63-0 0.000	0-0-0 0.00	0-0-0 0.00	0-0-0 0.00	0-0-0 0.00	0-0-0 0.00	0-0-0 0.00	0-0-0 0.00	0-0-0 0.00
65	3.633	2.091	6.012	65-33 4.478	65-97 4.548	65-107 4.581	65-109 4.612	33-65-97 106.48	33-65-107 112.95	33-65-109 114.17	97-65-107 109.24	97-65-109 109.07	97-65-109 104.85	107-65-109 104.85	107-65-109 104.85
67	0.051	8.387	5.611	67-35 4.328	67-97 4.465	67-99 4.423	67-101 4.528	35-67-97 112.06	35-67-99 112.20	35-67-101 111.22	97-67-99 103.56	97-67-101 110.52	97-67-101 106.93	99-67-101 106.93	99-67-101 106.93
69	-3.607	14.719	5.950	69-37 4.452	69-99 4.548	69-105 4.578	69-111 4.593	37-69-99 106.21	37-69-105 113.95	37-69-111 114.36	99-69-105 109.00	99-69-111 108.09	99-69-111 105.69-111	105-69-111 105.06	105-69-111 105.06
71	7.249	-4.166	5.854	71-39 4.397	71-107 4.579	71-113 4.597	71-0 0.000	39-71-107 115.06	39-71-113 114.49	107-71-113 104.19	0-0-0 0.00	0-0-0 0.00	0-0-0 0.00	0-0-0 0.00	0-0-0 0.00

Nr.	coordinates [a.u.]			bondlength [a.u.]				bondangles						
	x	y	z	73-41	73-109	73-113	73-115	41-73-109	41-73-113	41-73-115	109-73-113	109-73-115	113-73-115	
73	10.886	2.093	5.843	4.389	4.626	4.573	4.580	116.21	114.52	114.72	102.78	102.84	104.13	
75	7.342	8.327	5.940	4.450	4.501	4.596	4.568	105.09	115.54	114.45	109.21	106.93	105.29	
77	3.635	14.859	5.848	4.412	4.472	4.570	4.552	105.13	116.29	116.04	107.04	105.96	105.61	
79	14.484	-4.123	5.847	4.398	4.569	4.579	0.000	115.00	114.91	104.50	0.00	0.00	0.00	
81	18.082	2.089	5.851	4.402	4.568	4.576	0.000	114.81	114.60	104.41	0.00	0.00	0.00	
83	14.511	8.368	5.851	4.395	4.594	4.578	0.000	114.37	114.56	104.10	0.00	0.00	0.00	
85	10.880	14.656	5.836	4.398	4.605	4.610	0.000	114.67	114.52	104.90	0.00	0.00	0.00	
87	21.745	-4.154	5.847	4.390	4.605	0.000	0.000	114.60	0.00	0.00	0.00	0.00	0.00	
89	-3.727	2.037	5.792	4.383	4.489	4.587	4.562	108.67	116.28	115.81	104.39	106.71	104.02	
91	-7.297	8.314	5.911	4.433	4.521	4.586	4.578	106.99	114.65	114.22	106.98	108.41	105.25	
93	-10.858	14.645	5.848	4.400	4.606	4.606	4.598	114.97	114.69	114.25	104.43	103.41	103.70	
95	0.003	-4.175	5.843	4.400	4.601	4.604	0.000	115.12	114.37	104.34	0.00	0.00	0.00	
97	-0.142	4.266	7.318	4.548	4.465	4.489	4.554	107.20	109.14	123.53	111.28	104.63	100.79	
99	-3.521	10.377	7.298	4.423	4.548	4.521	4.536	109.38	110.65	94.19	109.21	117.73	114.62	
101	3.668	10.598	7.205	4.528	4.501	4.472	4.338	107.86	110.64	83.36	113.66	114.71	121.52	
103	2.053	9.433	11.059	4.338	4.461	4.185	0.000	118.17	116.19	104.77	0.00	0.00	0.00	
105	-7.263	16.777	7.783	4.578	4.606	0.000	0.000	104.32	0.00	0.00	0.00	0.00	0.00	
107	3.634	-2.130	7.791	4.581	4.579	4.601	0.000	104.22	104.17	104.26	0.00	0.00	0.00	
109	7.296	4.167	7.894	4.612	4.626	4.596	0.000	103.52	104.01	102.10	0.00	0.00	0.00	
111	0.016	16.857	7.795	4.593	4.570	0.000	0.000	104.48	0.00	0.00	0.00	0.00	0.00	

Nr.	coordinates [a.u.]			bondlength [a.u.]					bondangles				
	x	y	z	113-71	113-73	113-79	113-0	71-113-73	71-113-79	73-113-79	0-0-0	0-0-0	0-0-0
113	10.874	-2.065	7.745	4.597	4.573	4.569	0.000	104.27	104.26	103.57	0.00	0.00	0.00
115	14.491	4.183	7.744	115-73	115-81	115-83	115-0	73-115-81	73-115-83	81-115-83	0-0-0	0-0-0	0-0-0
				4.580	4.568	4.594	0.000	103.74	104.36	104.09	0.00	0.00	0.00
117	10.931	10.478	7.771	117-75	117-83	117-85	117-0	75-117-83	75-117-85	83-117-85	0-0-0	0-0-0	0-0-0
				4.568	4.578	4.605	0.000	103.25	104.49	104.51	0.00	0.00	0.00
119	7.282	16.807	7.753	119-77	119-85	119-0	119-0	77-119-85	0-0-0	0-0-0	0-0-0	0-0-0	0-0-0
				4.552	4.610	0.000	0.000	104.58	0.00	0.00	0.00	0.00	0.00
121	18.107	-2.072	7.754	121-79	121-81	121-87	121-0	79-121-81	79-121-87	81-121-87	0-0-0	0-0-0	0-0-0
				4.579	4.576	4.605	0.000	103.28	104.48	104.07	0.00	0.00	0.00
123	-7.297	4.125	7.777	123-89	123-91	123-0	123-0	89-123-91	0-0-0	0-0-0	0-0-0	0-0-0	0-0-0
				4.587	4.586	0.000	0.000	103.88	0.00	0.00	0.00	0.00	0.00
125	-10.886	10.462	7.775	125-91	125-93	125-0	125-0	91-125-93	0-0-0	0-0-0	0-0-0	0-0-0	0-0-0
				4.578	4.606	0.000	0.000	104.54	0.00	0.00	0.00	0.00	0.00
127	-14.486	16.741	7.743	127-93	127-0	127-0	127-0	0-0-0	0-0-0	0-0-0	0-0-0	0-0-0	0-0-0
				4.598	0.000	0.000	0.000	0.00	0.00	0.00	0.00	0.00	0.00
129	-3.636	-2.087	7.741	129-89	129-95	129-0	129-0	89-129-95	0-0-0	0-0-0	0-0-0	0-0-0	0-0-0
				4.562	4.604	0.000	0.000	104.46	0.00	0.00	0.00	0.00	0.00
131	-1.311	4.880	11.676	131-97	131-133	131-135	131-0	97-131-133	97-131-135	133-131-135	0-0-0	0-0-0	0-0-0
				4.554	4.765	4.681	0.000	100.02	86.66	92.98	0.00	0.00	0.00
133	-2.374	9.524	11.603	133-99	133-103	133-131	133-0	99-133-103	99-133-131	103-133-131	0-0-0	0-0-0	0-0-0
				4.536	4.461	4.765	0.000	98.00	104.73	76.15	0.00	0.00	0.00
135	3.227	5.682	12.496	135-103	135-131	135-0	135-0	103-135-131	0-0-0	0-0-0	0-0-0	0-0-0	0-0-0
				4.185	4.681	0.000	0.000	79.71	0.00	0.00	0.00	0.00	0.00

Bibliography

- [Bar61] J. Bardeen. Tunneling from a many-particle point of view. *Phys. Rev. Lett.*, 6:57, 1961.
- [Ber00] R. Berger. Nic-workshop “molecular dynamics on parallel computers”. *World Scientific*, page 185, 2000.
- [Ber01] R. Berger. PhD thesis, RWTH Aachen, 2001.
- [BG80] U. von Barth and C.D. Gelatt. Validity of the frozen-core approximation and pseudopotential theory for cohesive energy calculations. *Phys. Rev. B*, 21(6):2222, 1980.
- [BH72] U. von Barth and L. Hedin. A local exchange-correlation potential for the spin-polarized case. *J. Phys. Chem.*, 5:1629, 1972.
- [BHS82] G.B. Bachelet, D.R. Hamann, and M. Schlüter. Pseudopotentials that work: From H to Pu. *Phys. Rev. B*, 26(8):4199, 1982.
- [Blü88] S. Blügel. *First Principles Calculations of the Electronic Structure of Magnetic Overlayers on Transition Metal Surfaces*. PhD thesis, RWTH Aachen, 1988.
- [BRGW82] G. Binnig, H. Rohrer, C. Gerber, and E. Weibel. Surface Studies by Scanning Tunneling Microscopy. *Phys. Rev. Lett.*, 49:57–61, 1982.
- [Bri] Encyclopaedia Britannica.
- [BS88] A. Banerjea and J.R. Smith. Origins of the universal binding-energy relation. *Phys. Rev. B*, 37:6632, 1988.
- [CA80] D.M. Ceperley and B.J. Alder. Ground State of the Electron Gas by a Stochastic Method. *Phys. Rev. Lett.*, 45:566, 1980.
- [CC73] D.J. Chadi and M.L. Cohen. Special Points in the Brillouin Zone. *Phys. Rev. B*, 8:5747, 1973.
- [CK97] K. Cho and E. Kaxiras. Intermittent diffusion on the reconstructed Si(111) surface. *Europhys. Lett.*, 39(3):287–292, August 1997.

- [CK98] K. Cho and E. Kaxiras. Diffusion of adsorbate atoms on the reconstructed Si(111) surface. *Surf. Sci.*, 396:L261–L266, October 1998.
- [CP85] R. Car and M. Parrinello. Unified Approach for Molecular Dynamics and Density-Functional Theory. *Phys. Rev. Lett.*, 55:2471, 1985.
- [Dav75] W.E. Davidson. The iterative calculation of a Few of the Lowest Eigenvalues and Corresponding Eigenvectors of Large Real-Symmetric Matrices. *J. Comput. Phys.*, 17:87, 1975.
- [Eng92a] B. Engels. *Ab initio Berechnung der (110) Oberfläche von II-V Halbleitern: Simulation von Rastertunnelmikroskopie-Aufnahmen*. PhD thesis, RWTH Aachen, 1992.
- [Eng92b] B. Engels. Konstruktion von glatten, normerhaltenden Pseudopotentialen. Master’s thesis, RWTH Aachen, 1992.
- [Ewa21] P.P. Ewald. Die Berechnung optischer und elektrostatischer Gitterpotentiale. *Ann. Phys.*, 64:253, 1921.
- [Fee94] R.M. Feenstra. Scanning tunneling spectroscopy. *Surf. Sci.*, 299/300:965–979, 1994.
- [Fri98] D. Frielinghaus. Ab initio Berechnung von BeSe und BeTe (100)-Oberflächen. Master’s thesis, RWTH Aachen, 1998.
- [Har28] D.R. Hartree. *Proceedings of the Cambridge Philosophical Society*, 24:89, 1928.
- [HCT⁺94] M. Horn-von Hoegen, M Copel, J.C. Tsang, M.C. Reuter, and R.M. Tromp. Surfactant-mediated growth of Ge on Si(111). *Phys. Rev. B*, 50(15):10811–10822, October 1994.
- [Hoe94] M. Horn von Hoegen. Surfactants: Perfect heteroepitaxy of Ge on Si(111). *Appl. Phys. A*, 59:503–515, June 1994.
- [IZC79] J. Ihm, A. Zunger, and M.L. Cohen. Momentum-space formalism for the total energy of solids. *J. Phys. Chem.: Solid State Physics*, 12:4409, 1979.
- [JC73] J.D. Joannopoulos and M.L. Cohen. Electronic charge densities for ZnS in the wurtzite and zincblende structures. *J. Phys. C*, 6:1572, 1973.
- [JG89] R.O. Jones and O. Gunnarson. The density functional formalism, its applications and prospects. *Rev. Mod. Phys.*, 61(3):689–746, 1989.

- [Kax93] E. Kaxiras. Interplay of Strain and Chemical Bonding in Surfactant Monolayers. *Europhys. Lett.*, 21(6):685–690, 1993.
- [Kax95] E. Kaxiras. Atomic structure of surfactant monolayers and its role in epitaxial growth. *Mat. Sci. Eng.*, 30:175–186, 1995.
- [Kax96] E. Kaxiras. Atomistic aspects of diffusion and growth on the Si and Ge(111) surfaces. *Thin Solid Films*, 272:386–398, 1996.
- [KB82] L. Kleinman and D.M. Bylander. Efficient Form for Model Pseudopotentials. *Phys. Rev. Lett.*, 48(20):1425, 1982.
- [KK95] E. Kaxiras and D. Kandel. Surfactant Mediated Crystal Growth of Semiconductors. *Phys. Rev. Lett.*, 75(14):2742–2745, October 1995.
- [Kro01] W. Kromen. *Die Projector Augmented Wave-Methode: Ein schnelles Allelektronenverfahren für die ab-initio-Molekulardynamik*. PhD thesis, RWTH Aachen, 2001.
- [KS65] W. Kohn and L.J. Sham. Self-Consistent Equations Including Exchange and Correlation Effects. *Phys. Rev. A*, 140(4):1133–1138, 1965.
- [Ler98] E.J. Lerner. The end of the road for Moore’s Law? *IBM Research magazin*, 3, 1998.
- [Lev79] M. Levy. Universal variational functionals of electron densities, first-order density matrices, and natural spin-orbitals and solutions of the v -representability problem. *Proc. Natl. Acad. Sci.*, 76:6062, 1979.
- [Liu78] B. Liu. Numerical Algorithms in Chemistry: Algebraic methods. *Report on Workshop*, 1978.
- [MA88] G. Meyer and N.M. Ammer. Novel optical approach to atomic force microscopy. *Appl. Phys. Lett.*, 53:1045–1047;2400–2402, 1988.
- [Mar94] I. Markov. Kinetics of surfactant-mediated growth. *Phys. Rev. B*, 50(15):11271–11274, October 1994.
- [Mar96] I. Markov. Kinetics of nucleation in surfactant mediated epitaxy. *Phys. Rev. B*, 53(7):4148–4155, February 1996.
- [MJW80] V.L. Moruzzi, J.F. Janak, and A.R. Williams. Calculated Electronic Properties of Metals. *Pergamon, New York*, 1980.
- [MV89] R.D. Meade and D. Vanderbilt. Origins of Stress on Elemental and Chemisorbed Semiconductor Surfaces. *Phys. Rev. Lett.*, 63(13):1404–1407, September 1989.

- [MVV⁺95a] J.A. Meyer, J. Vrijmoeth, H.A. van der Vegt, E. Vlieg, and R.J. Behm. Importance of the additional step-edge barrier in determining film morphology during epitaxial growth. *Phys. Rev. B*, 51(20):14790–14793, May 1995.
- [MVV⁺95b] J.A. Meyer, J. Vrijmoeth, H.A. van der Vegt, E. Vlieg, and R.J. Behm. Importance of the additional step-edge barrier in determining film morphology during epitaxial growth. *Phys. Rev. B*, 51(20):14790–14793, May 1995.
- [Pay87] M.C. Payne. An *ab initio* investigation of the Takayanagi reconstruction. *Solid State Physics*, 20:L983–L987, 1987.
- [PM77] J.D. Pack and H.J. Monkhorst. "Special points for Brillouin-zone integrations" – a reply. *Phys. Rev. B*, 16:1748, 1977.
- [Ric93] P. Richard. Iterative Lösung der Schrödingergleichung für große Systeme. Master's thesis, RWTH Aachen, 1993.
- [Ric96] P. Richard. *Banddiskontinuitäten an III-V Halbleitergrenzflächen: Verspannungsabhängigkeit und Einfluß von Zwischenschichten*. PhD thesis, RWTH Aachen, 1996.
- [RKH⁺99] D. Reinking, L. Kammler, N. Hoffmann, Horn-Von Hoegen, and K.R. Hofmann. Fabrication of high-mobility Ge p-channel MOS-FETs on Si substrates. *Electr. Lett.*, 35:503, 1999.
- [Roh00] L. Rohlfig. Structural and Optical Properties of the Ge(111)(2 × 1) Surface. *Phys. Rev. Lett.*, 85:5440, 2000.
- [SAB⁺00] K. Schroeder, A. Antons, B. Berger, W. Kromen, and S. Blügel. Surface Diffusion and Models for the Kinetics of Epitaxial Growth. *Proc. Int. Sym. Str. Dyn. Het. Sys.*, pages 71–94, February 2000.
- [SABB00] K. Schroeder, A. Antons, B. Berger, and S. Blügel. Understanding surfactant-mediated growth, contributions from *ab initio* calculations. *acc. at Phase Trans.*, 2000.
- [SER98] K. Schroeder, B. Engels, and S. Richard, P. adn Blügel. Reexchanged Controlled Diffusion in Surfactant-Mediated Epitaxial Growth: Si on As-Terminated Si(111). *Phys. Rev. Lett.*, 80(13):2873–2876, March 1998.
- [SKI00] T. Sato, S. Kitamura, and M. Iwatsuki. Initial adsorption process of Si atoms on Si(111)7 × 7 surface studied by scanning tunneling microscopy. *Surf. Sci.*, 445:130–137, 2000.

- [SPKSL92] I. Stich, M.C. Payne, R.D. King-Smith, and J-S. Lin. *Ab initio* Total-Energy Calculations for Extremely Large Systems: Application to the Takayanagi Reconstruction of Si(111). *Phys. Rev. Lett.*, 68(9):1351–1358, March 1992.
- [TH85] T. Tersoff and D.R. Hamann. Theory of the scanning tunneling microscope. *Phys. Rev. B*, 31:805, 1985.
- [The00] N. Theuerkauf. *Rastertunnelmikroskopische und -spektroskopische Untersuchungen an strukturierten Ge/Si(111)-Oberflächen*. PhD thesis, RWTH Aachen, 2000.
- [TTTT85] K. Takayanagi, Y. Tanishiro, S. Takahashi, and M. Takahashi. Structure Analysis of Si(111)- 7×7 reconstructed Surface by Transmission Electron Diffraction. *Surf. Sci.*, 164(367), 1985.
- [Voi] B. Voigtländer. private communications.
- [VPL⁺92] H.A. van der Vegt, H.M. van Pinxteren, M. Lohmeier, E. Vlieg, and J.M.C. Thornton. Surfactant induced layer-by-layer growth of Ag on Ag(111). *Phys. Rev. Lett.*, pages 3335–3338, 1992.
- [VSH84] J.A. Venables, G.D. Spiller, and M. Hanbücken. Nucleation and growth of thin films. *Rep. Prog. Phys.*, 47:399–459, 1984.
- [VWN80] S.H. Vosko, L. Wilk, and N. Nussair. Accurate spin-dependent electron liquid correlation energies for local spin density calculations: a critical analysis. *Can. J. Phys.*, 58:1200, 1980.
- [VZ93] B. Voigtländer and A. Zinner. Influence of surfactants on the growth-kinetics of Si on Si(111). *Surf. Sci. Lett.*, 292:775–780, 1993.
- [VZ96] B. Voigtländer and A. Zinner. Structure of the Stranski-Krastanov layer in surfactant-mediated Sb/Ge/Si(111) epitaxy. *Surf. Sci.*, 351:L233–L238, 1996.
- [VZWB95] B. Voigtländer, A. Zinner, T. Weber, and H.P. Bonzel. Modification of growth kinetics in surfactant-mediated epitaxy. *Phys. Rev. B*, 51(12):7583–7591, March 1995.
- [Wal62] D. Walton. *J. Chem. Phys.*, 37:2182, 1962.
- [Wig34] E. Wigner. On the Interaction of Electrons in Metals. *Phys. Rev.*, 46:1002, 1934.
- [ZL94] Z. Zhang and M. G. Lagally. Atomic-Scale Mechanism for Surfactant-Mediated Layer-by-Layer Growth in Homoepitaxy. *Phys. Rev. Lett.*, 72(5):693–696, January 1994.

- [ZO97] T.C. Zhao and M. Overmars. *A Graphical User Interface Toolkit for X*. 1997.

Danksagung

An dieser Stelle möchte ich all denen danken, die das Gelingen dieser Arbeit ermöglicht haben:

An erster Stelle möchte ich meinem Betreuer Prof. Dr. Kurt Schroeder für die intensive Unterstützung dieser Arbeit danken. Von den zahllosen Diskussionen habe ich stets profitiert und neue Anregungen erhalten. Auch für die freundliche Atmosphäre, die er verbreitet hat, möchte ich ihm danken.

Herrn Dr. Stefan Blügel danke ich für die fortwährende Betreuung und Unterstützung dieser Arbeit

Herrn Prof. Dr. P.H. Dederichs danke ich für die freundliche Übernahme des Korreferats.

Herrn Prof. Dr. H. Müller-Krumbhaar danke ich für die Möglichkeit, an seinem Institut diese Doktorarbeit erstellen zu dürfen.

Ralf Berger und Winfried Kromen danke ich für die Geduld mit der sie sich meiner vielen Fragen, vor allem während der Einarbeitungszeit in das Programm, angenommen haben.

Ohne sie namentlich aufzuzählen möchte ich mich bei allen Mitarbeitern des Instituts Theorie-III für die Hilfsbereitschaft und für die angenehme Atmosphäre bedanken.

Nicht zuletzt danke ich meiner Mutter, die mich über die Jahre hinweg immer unterstützt hat, nicht nur während der Promotion, sondern während meiner gesamten Ausbildung. Dadurch kommt ihr ein besonderer Anteil an der Entstehung dieser Arbeit zu.

Lebenslauf

Persönliche Daten

Name: Armin Antons
Geburtsdatum: 18.09.1964
Geburtsort: Jülich
Staatsangehörigkeit: deutsch
Familienstand: ledig
email: a.antons@fz-juelich.de

Schulbildung

'71 - '75 katholische Grundschule Jülich
'75 - '81 Realschule Jülich
Juli '81 mittlere Reife
'87 - '90 Abendgymnasium Aachen
Dez. '90 Abitur

Ausbildung

'81 - '84 Biologielaborant, Kernforschungsanlage Jülich
Juni '84 Abschluss

Arbeitsverhältnisse

Juni '84 - Dez. '84 Biologielaborant, Kernforschungsanlage Jülich
Jan. '85 - März '85 Biologielaborant, Henkel KGaA
Juli '86 - Sep. '91 Biologielaborant, Henkel KGaA

Wehrdienst

Apr. '85 - Juni '86 Grundwehrdienst,
1. Flugkörperstaffel Flugkörpergeschwader 2

Studium

Okt. '91 Studium der Physik
März '95 Vordiplom in Physik
März '97 - März '98 Diplomarbeit bei Prof. Dr. Müller-Krumhaar
zum Thema *Simulation eines neuen
neuen Strukturierungsverfahren für Silizide
basierend auf lokaler Oxidation*
Mai '98 Diplom in Physik
Aug. '98 Beginn der Promotion bei Prof. Dr. Schroeder am
Institut für Festkörperforschung im Forschungs-
zentrum Jülich